Structure and Properties of Charged Colloidal Systems

Structure and Properties of Charged Colloidal Systems

A dissertation presented

by

Emily Ruth Russell

to

The Department of Physics

in partial fulfillment of the requirements

for the degree of

Doctor of Philosophy

in the subject of

Physics

Harvard University

Cambridge, Massachussetts

April 2014

Dissertation Advisor: Professor David Weitz Emily Ruth Russell

Structure and Properties of Charged Colloidal Systems

Abstract

This dissertation explores the changes in structure of colloidal systems on the introduction of repulsive interactions. Colloidal gels are well understood when all particle interactions are attractive, but their structure is fundamentally changed when repulsive interactions compete with those attractive interactions, as in the case of a binary gel of oppositely charged particles. Similarly, colloidal crystals are well understood when interactions are approximately hard-sphere, but again, the structure and material properties change when a long-range repulsion is introduced, giving a colloidal 'Wigner' crystal. My research quantitatively investigates these effects in experimental model systems. I use confocal microscopy to directly image in three dimensions suspensions of micron-scale colloidal particles which are monodisperse, index- and density-matched, fluorescent, and electrostatically charged. I use standard image-processing techniques to obtain the precise location of each particle in the imaging volume in order to analyze both global and local structure. In the case of the binary gel, I observe gelation of oppositely charged particles, controlled by varying the total particle volume fraction, the interaction strength, and the mixing ratio of the two particle species. I find that contrary to commonly studied purely attractive gels, in which weakly quenched gels are more compact and less tenuous, particles in these binary gels form fewer contacts and the gels become more tenuous as we approach the gel line, and the average attractive bond number emerges as a critical parameter for gelation. This suggests that a different mechanism governs gel formation and structure in binary gels, in which attractive and repulsive interactions compete. In the case of the long-range-repulsive colloidal 'Wigner' crystals, I find a body-centered-cubic crystalline phase at particle volume fractions near 15%, in contrast to the face-centered-cubic crystalline phase found at volume fractions above 50% for hard spheres. The soft interactions in these repulsive crystals permit large fluctuations, with typical particle displacements up to 20% of the nearest-neighbor spacing. I determine the three independent crystalline elastic constants, and find that the crystals are very compliant ($c \approx$ 5-40mPa), and strongly anisotropic at all volume fractions studied. I also observe a sharp interface between the fluid and crystalline phases.

Contents

List of Figures

Acknowledgements

The long and arduous journey of the PhD is only possible with the help of a great many people – I cannot individually thank everyone who helped me along the way, and to try would threaten to rob of its meaning my thanks to those who were the most influential. I will call out here the most important.

First there are those people who help directly with the work itself, as collaborators or as advisors. Of course this work would have been impossible without the resources provided by my graduate advisor, Dave Weitz. A few others stand out as well. I do not think I would have earned my PhD without the advice and support of Frans Spaepen, who has been for me a model of generosity and scholarship. On the experimental front, Tom Kodger's wizardly skills in chemistry and in engineering made possible many of my experiments (beginning with synthesizing the particles and going on from there); he is one of the most talented experimentalists I know, and one of the most friendly and helpful. Kate Jensen taught me much of what I know about particle location and tracking, among other things, and her ever positive and cheerful attitude was an inspiration. Joris Sprakel got me started in the group and in the field, both teaching me experimental techniques, and providing advice and discussions of physical ideas.

The rest of my committee – Michael Brenner and Vinny Manoharan – have been less directly and frequently involved, but I have benefited from the conversations I have had with them. Others have also helped with experiments and with understanding my system, particularly Joe McDermott, Hyerim Hwang, Emily Redston, Rodrigo Guerra, Zsolt Terdik, Tina Lin, and Nick Schade. Several 'outsiders' have also contributed: thanks to Jeroen Appel for synthesizing my PMMA particles, and to Yongxiang Gao and Maria Kilfoil for the use of their publicly-available particle locating code.

There are those who make things go: Christina Andujar did an impressive job of keeping the Weitzlab running for most of my time here, making administrative tasks as easy as

possible for those of us in the lab. Sheila Ferguson and Lisa Cacciabaudo performed the same magic in the physics department, and were always amazingly responsive, effective, and friendly.

And then there are those who did not contribute directly to the work described in this dissertation, but who nonetheless were influential during my time at Harvard. Foremost among these is Melissa Franklin, whose advice and support as director of graduate studies, as department chair, and as a friend and mentor, were invaluable to my getting through graduate school. Others who have made my time at Harvard more pleasant and fulfilling have been John Girash, Virginia Maurer, and the entire Departmental TF program; Jacob Barandes; David Morin; Kathryn Hollar; Carol Davis; Stan Cotreau; and Masahiro Morii. Among my fellow junior scientists, in addition to those already mentioned, Becca Perry, Kate Wooley-Brown, Alexis Harrison, Adrian Pegoraro, Suzanne Pittman, Esther Amstad, Lloyd Ung, and Jack DiSciacca have all made Harvard a more welcoming place.

Yet the most important people in this journey have been those outside of Harvard. The one person who has done the most to make this possible has been my husband Dale Winter – I cannot express my gratitude and appreciation for his unfailing patience and support over the past six years, no matter how stressed I have been. My parents, my sister Kirby, and my grandparents have also been great sources of encouragement and comfort. My housemates – Lusann Yang, Alan Morse, Tom Dimiduk – have provided a warm environment to go home to, and great conversation, both scientific and otherwise. The Boston Change Ringers likewise have made Boston a home for me. And finally, my old college friends, the Blacker Physics Mafia – Jeff, Emma, Yuliya, Klimka, Jay, and now Shachar – gave me every so often a respite from trying to impress people in graduate school, and reminded me of the fun of physics.

Thomas Kuhn, Karl Popper, and Benjamin Franklin have been sources of inspiration, and encouragement that it is possible to write about deep scientific ideas in a style that is worth reading.

And let me close by acknowledging the sources of funding that made my PhD possible: this material is based upon work supported by the NSF through the Graduate Research Fellowship and the Harvard MRSEC. Thanks NSF for paying most of my stipend, and also to the Harvard Physics Department for financial support during my first year and while I was teaching!

Preamble

A doctoral thesis is not an easy document to write. It is not easy even to articulate clearly the goal of the thesis (and indeed, the perceived goal depends heavily on who is trying to articulate it). I may as well bring into the open the common knowledge that almost no-one will read the thesis in its entirety. The main scientific results are already published, or in the process of being published. What, then, the purpose of this long document? Is it merely to fulfill an obsolete requirement, one which perhaps exists more through inertia than for the value it adds today?

I confess I am not fully convinced by my own answer to that question. Yet I entered graduate school with the idea that the thesis was the central product of the PhD, and should be something more than simply my publications 'stapled together', as it is said – and so for my own sake, I have endeavoured to make it a work in its own right. Writing this thesis has indeed made me think a little more deeply about my work than did writing the papers, and organize my thoughts a little more clearly and coherently, particularly regarding the background to my work. It has thus been an educational experience for me.

I write this thesis not only for myself, but also for those who follow me, in the optimistic hope that younger students may learn something from its pages. To this end, I have tried to start more or less at the beginning, to lay out everything I have learned, elementary though it may seem from my perspective now. Colloidal physics is not an easy field to enter, in that it is not well delineated, and I hope that this thesis may elucidate at least a corner of it to those who are new to the field.

The goal of this thesis, then, is to present as a single whole the story of what I have learned in my graduate research. Even as I write it I know I do not achieve this goal completely – I realize that I do not even know the full story, as details remain hidden from me at every step of the way. Yet I hope that the narrative here is clear enough for any who are interested to learn something from me about colloids.

Let me invite you, then, into my world of tiny dancing particles, and tell you what I have found intriguing about them. Happy reading.

Chapter 1

Introduction

Why do we study colloidal systems? What, to start with an even more basic question, is a colloidal system?

Broadly speaking, the study of colloids encompasses a wide range of systems in which constituents are small, but not too small, and in which thermal energy is important, but not too important. This turns out to include not only artificial model systems of uniform spheres in simple liquids, but also to touch closely on most things biological. The study of colloidal systems is the epitome of seeking to understand the emergent behavior of complex systems through the interactions of constituent parts.

This introduction will address the above questions in fairly general terms, and start to narrow in to explore the particular topics in colloids which have been the study of my thesis. I also give a few quantitative definitions which will be heavily relied upon in the rest of the thesis. In the next chapter, I will go into more explicit detail on recent work in colloidal systems.

1.1 Colloids as model systems

Robert Brown peered into a microscope in the mid-1800's, and discovered a hithertofore unseen world of tiny dancing particles in a humble drop of pond water. These motes seemed to move about in a drunk and random fashion, almost like living things. These pollen grains were the first colloidal particles, suspended in a liquid, their motion and behavior governed by the motion of the liquid molecules. Brown's name is enshrined in the term *Brownian motion*, describing that jiggling dance of a small particle in a bath.

What is a colloidal system? It is not easy to give a concrete definition, as the boundaries are blurred and indistinct. Roughly, a colloidal system comprises a liquid, and particles suspended in that liquid. The liquid is commonly water (in which case we describe the system by the adjective 'aqueous'), but need not be – oils and other solvents can provide the suspending medium for a colloidal system. The particles may be simple solids, such as tiny pieces of plastic or glass; they may be globules of another liquid that does not mix with the first; they may be biological, such as proteins, viruses, bacteria, or other cells; or they may be physical associations made of up smaller molecules, bound less strongly than in a solid, but still coming together to form aggregates. Colloidal particles range in size from several nanometers to hundreds of microns.

Our favorite real-world example of a colloidal system is milk. Milk is mostly water, but its cloudy appearance (so distinctive as to warrant the creation of the adjective 'milky') and slightly thick texture are the result of the colloidal particles suspended in the water. Milkfat is contained in tiny globules floating in the water, just a few microns across and visible in a microscope – these globules are concentrated to obtain cream, or broken up and combined to make butter. Milk proteins also make up colloidal particles, forming loose associations called *micelles*, only tens of nanometers across and invisible – yet it is the sticking together of these particles which gives yogurts and cheeses.

But let us go back to Brown, back to the first observations that water could contain small particles which seemed to move about. Brown's pollen grains were probably tens of microns across. In the century and a half since, the colloidal world has expanded to cover orders of magnitude in size, from nanometer-scale molecular associations to comparatively massive particles just on the edge of being visible to the naked eye. Furthermore, our description of the behavior of colloids has evolved: in his *annus mirabilis*, Einstein lifted colloidal motion from the qualitative description Brown had made, into the mathematical language of the random walk, bringing the study of colloidal systems into the realm of physics.

A Brownian particle is bumped around by collisions with individual liquid molecules, pushing it now one way and now another. Over time, the pushes average out – the liquid isn't pushing the particle anywhere in particular. But the collisions are also noisy – we speak of *thermal energy*, the intrinsic randomness of any system at non-zero temperature, and the *fluctuations* attendant with that thermal energy. Although the pushes from the liquid molecules cancel out on average, they will not necessarily cancel to exactly zero for one single particle – the particle will, by chance, be pushed a little more from one direction

than from another, and will move a little in the direction of the net push.

Considering Brownian motion as a *random walk*, a particle's motion over time can be considered as the sum of many tiny displacements, each too small to measure individually, but producing a net motion in aggregate. Since each step is stochastic, random, their combination is best described by a probability distribution of the displacement of a particle after a given time interval. In one dimension, we approximate the random walk by saying that in each timestep δt, a particle will move by a distance δx, to the right or to the left with equal probability. Where is the particle after n timesteps? With probability $P(m) = \binom{n}{(n+m)/2} \cdot \binom{n}{(n-m)/2} \cdot (1/2)^n$, the particle has moved $(n+m)/2$ steps to the right, and $(n-m)/2$ steps to the left, so that its net displacement is m steps to the right, or a total displacement of $\Delta x = m \cdot \delta x$. For large n – that is, for experimental times much longer than the timescale on which the particle's path is ballistic – this binomial distribution fast approaches a Gaussian distribution. On average, the expected displacement $E(\Delta x) = 0$, but there is a wide spread, with a typical displacement given by the root-mean-*squared* displacement $\sqrt{E(\Delta x^2)} = \sqrt{D \cdot \Delta t}$, and the probability of any displacement $P(\Delta x) \propto \exp(\Delta x^2)$. The *diffusion constant* D gives a measure of the 'speed' of a diffusing particle. Small values of D mean that a particle is very likely to stay near its original position for a long time, such as particles in 'thick', viscous liquids such as corn syrup. Large values of D permit a particle to move farther from its original position in a shorter time, such as aromatic molecules moving through air. D is determined by the viscosity of the liquid; the size of the particle; and the temperature of the system, which after all is the source of the energy which allows the particle to move at all.

Any single particle provides just one point on a probability distribution – to examine the full distribution, we must consider an ensemble, typically by looking at the displacements of many particles, or one particle's trajectory over a long time, or both. Such an ensemble average gives a good measure of the random, thermal Brownian motion in a liquid.

As an aside, while diffusive Brownian motion has now been studied for over a century, it is only recently that the ballistic regime of thermal motion has been measured. This is the regime on the scale of the δt timestep used in the rough derivation above, over which a particle moves at a constant velocity in a straight line until it undergoes enough collisions to randomize its motion. In a lovely recent paper, Li *et al.* were able to access this very short timescale motion of a single particle suspended in air, measuring its ballistic motion on the scale of tens of microseconds [37].

But why in the end do we care about Brownian motion? The thermal motion of tiny colloidal particles allows us to use them as model systems to draw analogies to atoms and molecules. Because of their thermal Brownian motion, colloidal particles are able to explore the space available to them – after a reasonable equilibration time, they will have had a chance to sample different locations, and different configurations relative to other particles so that they access different interactions. 'Reasonable equilibration times' can be on experimental timescales of seconds to days, so that we can (sometimes) study the particles in *thermal equilibrium*, the state where they have been able to reach the lowest free energy available. Without thermal motion, they might be stuck in higher-energy states.

We need models for atoms and molecules because those entities are so small as to be technically challenging to study directly themselves. An optical microscope can only resolve objects a little smaller than the wavelength of the light used – hundreds of nanometers, compared to sub-nanometer atoms and molecules. Thus we cannot use a light microscope to study the structure of single molecules in a crystal. Over the past century, a great assortment of tricks have allowed us to use other tools to come closer and closer, from X-ray diffraction to electron microscopes. Yet none of these tools yet allow real-time, real-space visualization of the structure and dynamics of individual molecules.

Colloidal particles, on the other hand, reach the micron length scale, large enough to be imaged directly by an optical microscope. Where scattering experiments access mainly bulk averages, optical microscopy gives local information, and where electron microscopy requires variously freezing, drying, or coating a sample, optical microscopy accesses the particles in a natural, dynamic environment. Thus using colloidal particles allows real-time, real-space visualization of a system. If this colloidal system can be made to behave like an atomic or molecular system in crucial ways, it can be studied as a proxy for or model of that less-accessible system.

In short, then, colloidal particles are large enough to directly visualize in space and time, yet small enough to explore space through Brownian motion to reach thermal equilibrium. They inhabit the 'happy medium' in size between atoms and molecules, and macroscopic objects, so that the physics describing them can be connected to physics on smaller scales, yet they are relatively easy and intuitive to measure in the laboratory. Colloidal physics is a benchtop sort of physics, where we can carry out experiments with a handful of tools which take up a small amount of space relative to the colliders of particle physics or the telescopes of astrophysics, at room temperature. Colloids thus make a convenient and interesting

model system with which to study deeper physical questions.

1.1.1 The Boltzmann distribution

I have mentioned thermal equilibrium of colloidal particles – it is worth quantifying in at least the most basic way what this means. Thermal equilibrium is characterized by a *Boltzmann distribution* of energies. The energy of a particle in a system is determined by its state: its position (e.g. in a gravitational field), its velocity (e.g. giving its kinetic energy), and by various internal states (e.g. excited states of atoms). We consider a system with many possible states with different energies, and many particles, and ask how this system can minimize its free energy. Energetic considerations drive particles to the lowest energy states. Entropic considerations drive particles to be evenly distributed across energy states. *Temperature* is a measure of the relative importance of these two opposite driving forces – at a given temperature, the lowest free energy is found by distributing particles among the possible states according to the aforementioned Boltzmann distribution, where the probability of being in a state with energy E is:

$$P(E) \propto \exp\left(-E/k_B T\right)$$

where k_B is Boltzmann's constant, an empirically determined constant of nature.

In a colloidal system, the energy E of a state may be affected by any number of considerations. In most cases, for example, there is an external gravitational field, so that gravitational potential energy depends on the height h of the particle above some reference position: $E = (\Delta\rho)Vgh$, with $\Delta\rho$ the difference in mass density between the particle and the solvent, and V the particle volume. Invoking the Boltzmann distribution implies that particles will follow a number density profile $n \propto \exp\left(-h/h_0\right)$, where $h_0 = \left((\Delta\rho)Vg/k_B T\right)^{-1}$ is known as the *gravitational height*. Another common source of energy are electrostatic interactions – these are important enough that they will be treated in more detail shortly in Section 1.2.

Note that the Boltzmann distribution applies only under *equilibrium* conditions. Colloidal systems often undergo *kinetic arrest*, becoming trapped in a non-equilibrium state because of a large energy barrier between the current state and equilibrium. In such *non-equilibrium* situations, the Boltzmann distribution need not apply.

1.1.2 The confocal microscope

I have also referenced the relative ease of observing colloidal particles, compared to atoms and molecules. In the past few decades, the *confocal microscope* in particular has become a powerful tool for studying in detail the three-dimensional structure and dynamics of colloidal systems. I will give a very brief description here of its strengths, and discuss the technicalities at greater length in Section 3.2.

An optical microscope uses lenses to magnify a small field of view, making small entities visible to the eye. Only one narrow two-dimensional plane is brought into focus by the magnifying optics. Anything above or below that plane appears out of focus and blurred, and if there is too much of this blur, then the sharp in-focus image may be obscured. There are a few ways to avoid excessive blur. One can study a very dilute system, where there is only a small concentration of particles. One can study a two-dimensional system, so that everything can be in focus. To study a three-dimensional system, one can *section* a sample, slicing it into very thin pieces so that each nearly two-dimensional slice can be imaged individually. But none of these strategies permit us to study concentrated, three-dimensional samples in which the particles remain free to move in all three dimensions, as we would like to do with our colloidal models.

Enter the confocal microscope. This technique has been developed mainly for biology, but has been co-opted by colloid scientists over the past decade or so, as we discovered its power for three-dimensional imaging. The essential principle of the confocal microscope is that it sections a sample into thin slices *optically* instead of physically (Fig. 1.1). This is achieved by using a *pinhole*, both before the illumination reaches the sample, and after the imaging light leaves the sample. The pinhole selects out only the light coming from the plane of focus, blocking light from out-of-focus planes, so that (almost) no blur reaches the imaging optics. By moving either the sample or the optics, the microscope can then collect light from a new plane of focus. By stacking two-dimensional images taken at different planes of focus, we can build up a three-dimensional image 'stack'.

There are two main classes of confocal microscope, which differ in how the two-dimensional pixels are determined. In a *spinning-disk* confocal, the light passes through an array of many pinholes in a disk; this disk spins rapidly, and as the pinholes move with the disk, the many small illuminated regions move over the sample. The returning light is collected simultaneously on a many-pixel camera. In a *laser-scanning* confocal, in contrast, a single laser

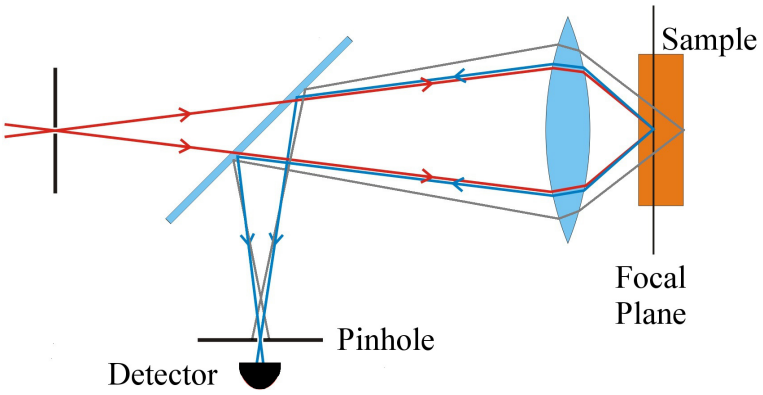

Figure 1.1: Principle of confocal microscopy. Illumination (red rays) enters from the left and passes through a pinhole on its way to the sample. The returning light (blue rays) passes through another pinhole on the bottom before it reaches the detector; this pinhole blocks out the light from out-of-focus planes (grey lines). (Image adapted from Wikimedia Commons.)

beam is deflected by mirrors to a single pixel on the sample; these mirrors are rapidly repositioned to scan the beam over the two-dimensional field of view. The returning light is collected by a single detector (or possibly a few detectors, each for a different range of the light spectrum), and the two-dimensional image is built up by the rapid sequence of pixels.

Confocal microscopes are growing to be quite fast (e.g. scanning back and forth across the image thousands of times per second), and the speed of the confocal microscope means that we can 'scan through' a three-dimensional volume of a colloidal sample, imaging every particle in sharp focus, and then take another snapshot seconds later, so that we get full information on the structure and dynamics of the sample.

1.2 Colloidal interactions and charged colloids

Colloidal particles can take on a wide range of shapes and sizes, even within a single system. As physicists, of course, we make simplifying assumptions until we have a system we can understand and describe more completely – we might approach this by averaging out the variation in shape to a statistical distribution, or, as in this thesis, by avoiding complex shapes and approximating particles as being of the same simple shape and the same size.

Even a 'simple' shape can mean many things – spheres, plates, rods, ellipsoids, dumbbells, 'pac-men', or polygons, to name a few. The shape determines a great deal about the way particles pack and interact. The simplest shape is of course the smooth, isotropic sphere – and as there is plenty of interesting physics to be found even in such simple systems, it is

this simplest system which I have studied.

Of course, having selected monodisperse (same-sized) spheres as our model system, we still have some choice of *interaction*, and the details of the interaction will drive a range of behaviors. The simplest interaction – at least intuitively – is a hard-sphere interaction, in which there is no force between particles until they come into contact, and there is an infinitely steep 'wall' at contact which prevents the particles from overlapping. These are the microscopic versions of the billiard ball or the ball bearing. Dull as this may sound, even the behavior of the lowly hard-sphere has been deeply studied. The most important parameter in a monodisperse hard-sphere system is the concentration of particles (most often reported as the normalized *volume fraction*, that is, the ratio of the total volume of the particles to the total volume of the system, $\phi = V_{\text{particles}}/V_{\text{system}}$). For $\phi \lesssim 0.492$, hard-spheres form a diffusive fluid; for $0.543 \lesssim \phi < \pi/(3\sqrt{2}) \approx 0.740$, the equlibrium phase is a face-centered cubic (f.c.c.) crystal (the limit $\pi/(3\sqrt{2})$ represents the closest packing geometrically possible for monodisperse hard spheres in three dimensions); samples with an average volume fraction between the freezing density $\phi_f \approx 0.492$ and the melting density $\phi_m \approx 0.543$ will phase-separate into coexisting crystal and fluid phases. (Note that even the exact values of these freezing and melting densities are still subjects of study; because of the singularity of the 'infinite wall', the phase diagram cannot be determined analytically, but rather must be calculated numerically through simulations; several approximate equations of state give results very close, but not identical, to the best simulation result [55].) Hard-spheres can also form disordered solid glasses at larger densities, above a glass transition density of $\phi_g \approx 0.58$, if the volume fraction is increased quickly enough. Beyond the phase diagram, the structure of hard-sphere systems within the fluid and glass regimes are also of great interest, and still being actively studied.

Practically speaking, a perfect hard sphere is not physically realizable, although we can come very close – in any real system, the 'hard' sphere can be slightly deformed (so that the wall is not infinitely sharp), and there are interactions before particles come into contact. One of the most successful simple models for the interactions of real colloids is *DLVO theory*, named for its inventors Derjaguin and Landau in Russia, and Verwey and Overbeek in the Netherlands. The DLVO potential has two parts. The first part is an attractive well, due to the *van der Waals* attraction[1]; this well is deep, but short-range, with signficant

[1]The van der Waals attraction is generally described as the attraction due to fluctuating induced electric dipoles in the two particles.

interaction strengths usually only over the range of nanometers. It is always present; thus if two particles come into very close contact, they will essentially never come apart again. With this 'primary' well, it seems that all colloidal particles will simply aggregate and there's an end to any interesting kinetics. The second part of the DLVO potential is a longer-range electrostatic interaction, due to charge on the surface of the particles; for like-charged particles, this interaction provides an energy barrier to contact, stabilizing the particles against aggregation. We will elaborate on this electrostatic interaction in the next subsection.

Additional stability – preventing particles from falling into the primary minimum and aggregating irreversibly – is also often achieved through a *steric* interaction. A thin (nanometer-scale) layer, or *brush*, of small, flexible polymer molecules is attached to the surfaces of the particles, either by chemical covalent bonds, or by physical adsorption. These polymer brushes repel one another at short range, due to entropic considerations: overlap of two polymer brushes as particles approach one another increases the local polymer density, which is entropically unfavorable. This 'steric' stabilization is on the molecular scale, rather than over the longer range of charge stabilization, but the range is still long enough that the repulsive energy barrier prevents particles from approaching close enough for the van der Waals attraction to dominate.

1.2.1 Electrostatic interactions in solution

As we have mentioned, colloidal particles often carry an electric charge, introducing electrostatic interactions between them. The colloidal solutions also carry small electrolytes, e.g. salt ions, being charged, arrange themselves in the electric field of the larger charged particles, and actually *screen* that field. In the limiting case, a charged particle will acquire a layer of oppositely-charged microions on its surface so as to exactly cancel out the charge, so that it does not interact electrostatically with other particles at all.

The exact electric potential and distribution of charges can be derived by solving the *Poisson-Boltzmann equation*. (I will follow here the argument of [18], the textbook which I sat down to read to study for my qualifying exam, but there are many sources which will cover this equation, not least of them the Feynman lectures.) We start with the Poisson equation for the electric potential in a dielectric:

$$\epsilon_r \epsilon_0 \nabla^2 \Phi = -\rho$$

where ϵ_0 is the electric permittivity of free space; ϵ_r the *dielectric constant* of the solvent, which quantifies the response of the solvent to electromagnetic fields[2]; Φ is the electric potential; and ρ the density of free charges. This takes a distribution of free charges, and gives an equation for the electric potential.

We also use the Boltzmann distribution, given in Section 1.1.1:

$$P(E) \propto \exp\left(-E/kT\right)$$

Here, we take the energy as that of a charge in an electric potential, $E = z_i e\Phi$, and reinterpret the probability as a concentration c_i, in which case the Boltzmann equation is translated to

$$c_i = c_{i,0} \exp\left(-z_i e\Phi/kT\right)$$

where $c_{i,0}$ sets the overall concentration. We now have an equation for the ion concentration, that is, the distribution of free charge, in terms of the potential.

The next step is to make these two equations self-consistent:

$$\epsilon_r \epsilon_0 \nabla^2 \Phi = -e \sum_i z_i c_{i,0} \exp\left(-z_i e\Phi/kT\right)$$

where the sum is over species of ions (in particular, in almost all circumstances there is at least one positively-charged species and one negatively-charged species in order to preserve overall charge neutrality). Already, writing this equation makes use of a mean-field approximation that the concentration is smooth; this is usually, though not always, harmless. Even with this approximation, the Poisson-Boltzmann equation is hard to solve exactly; it is generally simplified by making further approximations. In particular, if we consider the potential due to a charged sphere in an ion solution, and invoke spherical symmetry, we obtain (see [18] for derivation)

$$\Phi(r) \propto \frac{\exp\left(-\kappa r\right)}{r}$$

[2]If one is not too careful, one may try to claim that the dielectric constant is directly related to the index of refraction; the solution of Maxwell's equations for the velocity of an electromagnetic wave gives $n = \sqrt{\epsilon_r \mu_r}$, with μ_r the relative magnetic permeability of the material, and as usually $\mu_r \approx 1$, this gives $\epsilon_r = n^2$. Yet an examination of the values given for water, $\epsilon_r \approx 80$ [18] and $n = 1.333$ [84], gives this the lie. What's going on? It is essential to remember that the dielectric constant varies with frequency. The dielectric constant relevant to electrostatics is the low-frequency limit, $\epsilon_r = \epsilon_r(\omega = 0)$, while the index of refraction is reported for visible light, $n = n(\omega \approx 3 \times 10^{15} s^{-1})$.

with

$$\kappa^{-1} = \sqrt{\frac{\epsilon_r \epsilon_0 k_B T}{\sum_i (z_i e)^2 c_{i,0}}}$$

the *Debye screening length*[3].

Let's take a step back and look at what this means. In free space, the potential of a charge falls off inversely with distance, $\Phi(r) \propto 1/r$. In an ion solution, this falloff is modified by an additional factor of $\exp(-\kappa r)$, which means that the potential – and hence the field – falls off much more quickly. This is because counterions in the solution are attracted near the surface of fixed charge; they form what is known as an *electric double layer*, until enough excess counterions have congregated near the particle surface that a particle at a greater distance sees the sum of the particle and its double layer as nearly electrically neutral; that is, the counterions *screen* the field at larger distances. While electrostatic interactions are long-range in free space, their range is shortened in solution.

This form of the potential, $\Phi(r) \propto \exp(-\kappa r)/r$, is termed the *screened-Coulomb* or *Yukawa* potential, and is frequently used in theory and models of colloidal interactions.

How short is the interaction range? This depends on the value of the screening length κ^{-1}; roughly speaking, the 'interaction range' is equated with the screening length – the effect of electrostatics at more than a few screening lengths' distance will be small. The screening length itself has some interesting and important dependencies. There is a dependence on temperature: all else equal, $\kappa^{-1} \propto \sqrt{T}$, so that screening length increases with temperature. At higher temperatures, thermal energy allows the counterions to move further from the charged surface, as entropy drives the system toward uniform ion concentration; thus the 'double layer' extends further; in constrast, in the limit $T \to 0$, the counterions go to the particle surface, so that the particle charge is perfectly canceled by a very thin layer of counterions, $\kappa^{-1} \to 0$, and there is no interaction. This is more intellectually interesting than practically interesting, however, as in the majority of colloidal experiments, T is fairly constant around room temperature. The most important determinant of κ^{-1} is the ionic strength, $\sum_i (z_i e)^2 c_{i,0}$. The larger the concentrations of the charge carriers, the shorter becomes the screening length, $\kappa^{-1} \propto 1/\sqrt{(c_{i,0})}$. Thus in an experimental system, we control the screening length by the ionic strength, adding charge carriers to shorten the screening length and approach hard-sphere interactions, and reducing the ionic strength to

[3]The reason for giving the symbol κ to the *inverse* screening length, that is, the coefficient of r, is lost in the mists of time. I shall try to be consistent in considering the screening length κ^{-1}, as I find it more intuitive, but the literature varies in its language, whether it chooses to consider κ or κ^{-1}.

obtain long-range charge interactions.

This screening length κ^{-1} is an important parameter in describing even the qualitative nature of particle interactions. For a very short screening length compared to the particle size, like-charged particles act roughly as hard-spheres – non-interacting at most ranges, with a repulsive contact interaction. Oppositely charged particles act as 'sticky hard-spheres' – again, non-interacting at long range, but attractive at very short range, so that if they come into contact, they will stick together, reversibly or irreversibly depending on the strength of the attraction. In contrast, for screening lengths which are similar to or larger than the particle size, long-range charge interactions are possible, so that like-charged particles repel one another and keep their distance, while oppositely-charged particles feel an attraction over long distances rather than sticking only on chance contact. Both of these regimes are important in my work.

The overall magnitude of the interactions between micron-scale charged particles depends on the source of the charge. Charged colloidal particles generally carry *surface* (rather than body) charges, with charged groups on the surface of the particle dissociating to exchange ions with the solvent. Thus the details of charging will of course also depend very sensitively both on the surface density and on the nature of these charge groups – their ease of dissociation and any chemistry between the charge groups and the other solutes.

Further details specific to my experimental systems will be given in Section 2.1. For now, I will leave the question of specific colloidal interactions, and turn to discuss some of the interesting structures formed by colloidal particles.

1.2.2 Depletion interactions

The *depletion interaction* is a sufficiently common and elegant method of introducing a *reversible* attraction between colloidal particles that I will take a moment to describe it here; it will prove relevant in Section 2.2.

The depletion interaction comes about when 'depletant' particles – typically nanometer-scale polymer molecules which are added to the solution – are excluded from the volume between the (usually much larger) primary particles, resulting in an attractive force between the primary particles. There are two conceptual descriptions of the nature of this force: a pressure argument and an entropy argument. I first came to think of the effect as one of pressure due to a 'gas' of depletant particles. When two primary particles are far apart,

each feels an isotropic pressure due to collisions with depletant particles. When the primary particles come close to each other, the depletant particles cannot fit between them; the pressure vanishes on the facing surfaces, no longer balancing the pressure on the far surfaces, so that the net pressure on each particle is inward, giving an attractive force.

Another argument – from which it is easier to derive the mathematical form of the attraction – is one of the entropy of the depletant particles. If the depletant particles have a radius r_{dep}, there is a spherical shell of thickness r_{dep} around each primary particle which is forbidden to the center of a depletant particle; the total volume available to a depletant particle is thus reduced by this *excluded volume*. If the surfaces of two primary particles approach within $2r_{\mathrm{dep}}$ of one another, their excluded volumes overlap – the total excluded volume is thus reduced by the overlap amount, and the available volume to depletant particles correspondingly increased. The increase in *entropy* due to this available volume increase decreases the free energy, giving an effective attractive force between the two primary particles.

The depletion interaction provides two tuning parameters. The strength of the interaction – the depth of the potential well – is roughly proportional to the concentration of depletant particles; the interaction can be made stronger by adding more depletant. The range of interaction, as described above, is roughly speaking the radius of the depletant particles; the interaction can be made longer or shorter range by using larger or smaller depletant particles.

1.3 Gels

One primary thread of my thesis work has been to study colloidal gels. So let us ask: what is a gel? You probably think first of goopy, squishy products such as hair gel or medicine capsules, or perhaps Jello. What gives these products their curious physical properties? These are all excellent examples of *polymer gels*. The most important constituent molecules are *polymers*, such as proteins or complex sugars – long, stringy molecules, made up of many small repeating building blocks, which act much like tiny pieces of rope. Many of these polymers will tangle up – our favorite analogy is to a bowl of spaghetti, in which any strand winds through gaps between many other strands, until it is difficult to pull a single strand free. To make a gel of such a polymer tangle, we introduce *cross-links* at some of the points where two strands cross (or in some cases where a strand crosses itself). These

cross-links bind the two strands together so that they can no longer slide past one another, but rather a force exerted on one strand will also be transferred through the cross-link to the second strand – these are much like the nodes of a spiderweb, or the knots of a net. The presence of these cross-links means that on a macroscopic scale, the entire *network* of microscopic polymers behaves as a single solid, by which we mean that it will propagate forces and support stress: if you squish or stretch a gel, it pushes or pulls back, rather than flowing like a liquid. What is remarkable about gels is that they are solid even though the stress-supporting polymer molecules usually make up only a very small fraction of the total material in the gel: a typical gel is mostly (say about 95%) water, or some other solvent. Yet the gel network, embedded in the fluid, responds as a solid, and furthermore traps the fluid so that it does not flow. Polymer gels are common in food (fruits, jams, jellies, jello), cosmetics (shampoos, hair gels), medicines (gel capsules, intravenous fluids), medical implants, toys, etc.

Similar networks can be formed by solid particles instead of long stringy polymers – these are *colloidal gels*. Particles which stick to one another can form clusters and chains, which eventually grow into a network which spans across the system. *Percolation* is the property of forming a path from any boundary of the system to another through connected particles[4]; when the network of particle bonds percolates, and supports stress, so that a force exerted on a particle on one side of the network propagates through the network to the other side, we have a colloidal gel. Colloidal gels are typically weaker than polymer gels (essentially this is because the particles are larger than the molecular-scale polymers, and so there is a lower density of stress-supporting bonds in a colloidal gel than in a polymer gel), but are also ubiquitous. It is in part the formation of a colloidal gel which keeps wet paint from flowing off a wall, or wet ink from spreading too far on a piece of paper – or, in a less constructive situation, which may cause ink to clog a printer, or soot to clog an engine. Colloidal gels are also found in food: yogurt and cheese are colloidal gels, formed when small particles of the protein casein are destabilized (by acid or by bacteria) so that they stick together [43].

These real-world colloidal gels are, of course, complicated systems, with funny-shaped and differently sized particles, not to mention many components other than the gel-forming particles and solvent. So again, we physicists abstract and simplify to model systems, once

[4]To most, the term is more familiar in the context of a coffee percolator; here, it is the spaces between coffee grounds which exhibit percolation, so that the water can find a path from the top to the bottom.

again often (though not always) turning to monodisperse spherical colloids. The formation of a model colloidal gel and its properties are then controlled by the particle concentration and by the nature of the interactions between particles. For a gel to form, there must be some attractive interaction driving the particles to stick to one another, but its range and strength may vary, and it may compete with repulsive interactions as well.

The properties of a gel – how stiff or compliant it is, how easily broken, flowed, and reformed – depend also on the particles and their interactions, and on the structure within the gel. How many bonds does a particle in the gel make with other particles, and how much do those bonds constrain its motion – can bonds rotate? How dense are the cross-links which hold strands and chains together, and how long are the sections between these cross-linked nodes? How thick and how flexible are the strands? Is the gel homogeneous and smooth, or is it heterogeneous and clumpy? All of these questions must be considered in order to understand from physical principles the properties of the gel.

Thus the study of gelation is the study of how microscopic particles at low concentration can form a macroscopic, if squishy, solid, and how the details of those particles, their interactions, and the structure of the gel determine the macroscopic properties of the solid. This is a beautiful example of the general aim of physics to explain as many things as possible as completely as possible from a small set of fundamental principles.

1.4 Crystals

Gels are messy and complicated. On the opposite end of the spectrum we have crystals: regular, ordered structures in which atoms, molecules, or particles fall on a periodic lattice, repeating a pattern over and over again in space. Of course, the structure within a crystal can become quite complex – as an extreme, think of protein crystallization, and the difficulty both of creating crystals, and then also of analyzing the substructure of the single protein. Not so far from ordinary crystals are also liquid crystals – with orientational order but not full translational order – and quasicrystals, with a predictable but non-repeating structure.

What defines a crystal? By crystalline ordering, we mean that the structure of a crystal repeats itself exactly and periodically in space. In particular, for a d-dimensional crystal, there are d independent *lattice vectors*, $\bar{\mathbf{v}}_1$, $\bar{\mathbf{v}}_2$, ... $\bar{\mathbf{v}}_d$, so that if there is a particle at position $\bar{\mathbf{r}}$, then for any integers $\{n_1, n_2, ...n_d\} \in \mathbb{Z}$, there is an identical particle at position $(\bar{\mathbf{r}} + n_1\bar{\mathbf{v}}_1 + n_2\bar{\mathbf{v}}_2 + ... + n_d\bar{\mathbf{v}}_d)$. Under this description, a *unit cell* is the parallelogram

formed by the lattice vectors. There may be arbitrarily many particles *within* this unit cell, of different species, with any structure – but the unit cell repeats in an entirely regular fashion.[5]

In physics, we mainly deal with two- and three-dimensional crystals – I'll speak almost entirely about three-dimensional crystals. Often in three dimensions, we see crystals with cubic symmetry: the unit cell is a cube, so that the three lattice vectors have the same length and are mutually orthogonal. The structure within the unit cube may vary. Consider the case of a simple lattice with only one particle type. In a *simple cubic* structure, there is a single particle in the unit cube (whether it is positioned at the center or a corner, or indeed anywhere else in the cube, is irrelevant up to a simple translation of the entire lattice). In a *body-centered cubic (b.c.c.)* structure, there is a particle positioned at each of the eight corners of the cube, and an additional particle precisely at the center of the cube; since each of the corner particles is shared among eight unit cells, this gives a total of two particles per unit cell. In a *face-centered cubic (f.c.c.)* structure, we again have particles at each corner, and an additional six particles, one in the center of each face of the cube; these face-centered particles are shared between two unit cells, so we have a total of four particles per unit cell. Both the b.c.c. and the f.c.c. structures can be alternatively represented by a unit cell containing only one particle, but which is not cubic; most typically, the cubic cell is used. The f.c.c. structure can also be looked at from a different angle (literally), as consisting of two-dimensional close-packed planes with *hexagonal* symmetry, layered on top of one another so that the structure repeats every third layer. Closely related to the f.c.c. structure is the *hexagonal close-packed (h.c.p.)* structure, in which these same hexagonal layers are present, but repeat every *second* layer. For monodisperse hard spheres, the f.c.c. structure and h.c.p. structure both give the densest possible packing fraction, $\phi = \pi/(3\sqrt{2}) \approx 0.740$; the b.c.c. structure has a smaller maximum packing fraction of $\phi_{bcc} = (\pi\sqrt{3})/8 \approx 0.680$.

The selection of crystal lattice vectors is in fact a fundamental example of *symmetry breaking*. The particle interactions may be completely isotropic – that is, the same in every direction – but three particular directions in space, indicated by the lattice vectors, have been chosen, which look different from every other direction. This *anisotropy* (lack of isotropy) is propagated from the structure to various material properties of the crystal. Slight fluctuations of particles from their position in the crystal are easier along some di-

[5]Note that there are many, indeed infinitely many, possible choices of lattice vectors; each choice of lattice vectors will define a different structure within the unit cell.

rections than along others; sound waves will propagate at different velocities depending on the direction; and the crystal is easier to stretch, squish, or shear along some directions than along others. This directional dependence proves to be a key feature of a crystal; the symmetry-breaking is an important, and not well understood, aspect of the liquid-to-solid freezing transition. Crystalline freezing not only transforms a liquid into a solid, but transforms an isotropic system with no preferred directions into an anisotropic solid, and this symmetry-breaking has implications for the nature of the transition.

Even this briefest of introductions to crystals must mention defects and dislocations – errors in the perfect ordering. The simplest – and those I will consider – are *point defects*. These come in two flavors. A *vacancy* is a missing particle, an empty gap in the lattice where ordinarily a particle should appear according to the regular pattern. One can also find an extra particle that does not fit into the regular lattice – these often appear as *interstitials*, particles squeezed awkwardly into positions between the regular lattice positions. (Interstitials are not possible for close-packed, monodisperse hard spheres, due to simple volume constraints, but with softer interactions, they become viable.) Two particles might also share a lattice position, so that there is an extra particle, but neither particle can be identified as an off-lattice interstitial.

Extended disruptions in the crystal ordering can also occur, called *dislocations*. At a dislocation, for example, an extra plane of particles may suddenly insert itself – far from the insertion line, the crystal appears undisturbed, but at the insertion line itself, at the dislocation, the perfect ordering is disrupted. Dislocations and their motion are critical for stress release and plasticity of crystalline materials, and have been extensively studied.

Of course, no single crystal can extend forever, and most crystalline materials are *polycrystalline*, with many crystalline grains, each with a different orientation, and separated by *grain boundaries*. Single crystals free of such grain boundaries find many important applications, from solar cells to wind turbine blades, but are difficult to grow to large sizes.

Finally, we must elaborate on fluctuations in the crystal. I have so far spoken of the crystal as static, every particle in its proper position (except for defects), but in fact, in any system with nonzero temperature, thermal energy drives particles to fluctuate away from their minimum-energy position. Thus particles in a crystal will deviate slightly from the perfect lattice. These fluctuations grow with temperature until the crystal melts; indeed, the melting temperature is often correlated with the size of the fluctuations within the crystal, as I will discuss further in Section 2.5.1.

1.5 Material properties and rheology

This is 'squishy physics' – we squish, stretch, squeeze, and otherwise deform our systems, and would like to quantify those squishes and squeezes. I'll here give a brief review of strains, stresses, and the elastic moduli which relate them. This will be familiar to those who work with these material properties and deformations, but the details may be useful to those who are new to squishy physics.

1.5.1 Strain

First let me briefly review the definition of strain, for the dear reader who like me has not much dealt with strains quantitatively before. (I will essentially condense the treatment in Kittel [31].) Consider a square in the xy plane. I can deform this square in two fundamental ways. I might grab the two sides of the square and stretch it out into a rectangle: then a point at (x, y) on the original square has moved to $(x', y') = (x + u(x), y)$. We define $\epsilon_{xx} \equiv \partial u/\partial x$, and the *tensile strain* $e_{xx} = \epsilon_{xx}$. For a *uniform* strain, meaning that e_{xx} is constant everywhere, $x' = x(1 + \epsilon_{xx})$: the square has been stretched by a factor $(1 + \epsilon_{xx})$, so that $e_{xx} = \Delta L/L$ where L is the side of the square and ΔL the change in length. Note that I could also compress the square, in which case e_{xx} is defined in exactly the same way and would be negative. We define the other tensile strain components, e_{yy} and, in three dimensions, e_{zz}, in the same way.

I can deform the square in a second way, as well. This time grabbing the top and bottom of the square, instead of stretching them apart, I can move them parallel to themselves and in opposite directions, skewing the square into a rhombus. A point at (x, y) on the original square has moved to $(x', y') = (x + u(y), y)$. We define $\epsilon_{xy} = \partial u/\partial y$, and the *shear strain* $e_{xy} = \epsilon_{xy} + \epsilon_{yx}$ (in this case, $\epsilon_{yx} = 0$, so $e_{xy} = \epsilon_{xy}$, but this need not be true in general). For a uniform strain, $x' = x + y \cdot \epsilon_{xy}$, and $e_{xy} = \Delta x/L$ with Δx, L as shown in Fig. 1.2. Note that if I had pushed the top and bottom in the other directions, I would get a negative value of e_{xy}. If I had taken the two sides instead, I would have ϵ_{yx} nonzero instead of ϵ_{xy}, but the same value of e_{xy} – the rhombus would be the same, but rotated with respect to the first case. Finally, in three dimensions, I define e_{xz} and e_{yz} in the same way.

In general, a deformation is a combination of tensile and shear strains in all directions.

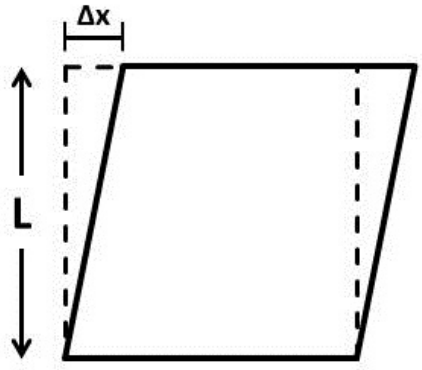

Figure 1.2: Uniform shear strain: $\epsilon_{xy} = \Delta x/L$

For the general displacement, in which a point at (x, y, z) moves to the point

$$(x', y', z') = \big(x + u(\mathbf{r}), y + v(\mathbf{r}), z + w(\mathbf{r})\big)$$

we define $\epsilon_{ij} \equiv \partial u_i/\partial x_j$, and again $e_{ij} = \epsilon_{ij} + \epsilon_{ji}$ for $i \neq j$.

1.5.2 Stress

We have quantified the deformation of a material via the strain, but how do we physically generate such a deformation? We push or pull on the material, which we quantify by *stress*; stress is essentially a generalization of pressure, or force/area.

Like strain, stress comes in two flavors, tensile and shear – indeed, in most materials, a tensile stress generates tensile strains, while a shear stress generates shear strains. A force F_x exerted normal to a surface and over area A_x produces a tensile stress $\sigma_{xx} \equiv F_x/A_x$, which squeezes or stretches the material. Likewise, a force F_x which is instead exerted parallel to a surface in the XZ plane and with area A_y produces a shear stress $\sigma_{xy} \equiv F_x/A_y$, which skews or shears the material. In general, the total stress on a material is made up of tensile and shear stresses in all directions,[6] with $\sigma_{ij} = F_i/A_j$.

1.5.3 Elastic moduli in isotropic materials

If strains are material responses to stress, how are these strains determined? The relation between stress and strain is governed by the *elastic moduli* of a material. Here I will

[6] We measure the stress in the rest frame of the body, so that the sum of the *forces* and the sum of the torques are each zero; but a force pushing on one side balanced by the force pushing on the other generates a net stress tending to squeeze the body.

discuss the simplest case of isotropic linear materials, where the strain components and stress components are related by simple linear transformations. Then an elastic modulus μ is just the coefficient of this linear relationship: the stress required to generate a strain e is $\sigma = \mu e$.

The elastic modulus takes on different values depending on which components of stress and strain are considered. In an isotropic medium, there are two independent elastic moduli. *Young's modulus* Y (sometimes also denoted E) governs deformation in response to stretching and squeezing (tension and compression), giving the tensile stress σ_{ii} required to generate a tensile strain e_{ii} in the same direction: $\sigma_{ii} = Y e_{ii}$. The *shear* modulus governs deformation in response to skewing (shear), giving the shear stress σ_{ij} required to generate a shear strain e_{ij} in the same direction: $\sigma_{ij} = G e_{ij}$.[7]

Stretching a material in one direction also causes a deformation in perpendicular directions; *Poisson's ratio* ν gives the relationship between the perpendicular deformation and the parallel deformation, $\nu = -e_{jj}/e_{ii}$, when a stress σ_{ii} is applied. In an isotropic medium, Possion's ratio is determined by Young's modulus and the shear modulus as $\nu = Y/2G - 1$ [84] (in fact, any one of these quantities can be determined from the other two).

Also frequently used is the *bulk modulus* B (sometimes also denoted K, as is its inverse the compressibility), which governs the response to an isotropic stress or pressure, $P = B\delta$ where δ is the total dilatation or volume change. This can also be expressed in terms of the other moduli, $B = YG/\big(3(3G - Y)\big) = Y/3(1 - 2\nu)$ [84].

The elastic moduli also determine the energy density required to generate a strain. A shear strain e_{xy}, for example, requires an energy density $u = \frac{1}{2} G e_{xy}^2$, while the energy density for an isotropic change in volume is $u = \frac{1}{2} B \delta^2$.

1.5.4 Elastic constants in crystals

While two elastic moduli are sufficient to describe the response of an isotropic material, the situation is not so simple in an anisotropic material. The response in an anisotropic system depends on direction; the coupling of each stress component to each strain component may

[7] This is often given as G' when oscillatory shears are considered: then the response has both an in-phase elastic component, and an out-of-phase dissipative component. The 'storage modulus' G' is the coefficient of the in-phase strain, while the 'loss modulus' G'' is the coefficient of the out-of-phase strain; both G' and G'' are functions of the frequency of oscillation. The elastic modulus G is the low-frequency limit of G', while G'' is related to the viscosity of the material.

be different, giving up to 21 different elastic moduli.[8]

Crystals are, as discussed, anisotropic. For a cubic crystal, symmetries actually reduce the number of independent elastic constants to just three, commonly named as c_{11}, c_{12}, and c_{44} (the indices refer to the stress/strain components: $1 \to xx$, $2 \to yy$, and $4 \to xy$). c_{11} corresponds to Young's modulus along the cubic axes of the crystal; c_{44} is the shear modulus also with respect to the cubic axes; and c_{12} couples a tensile stress along one cubic axis to a strain along another axis. Thus the total strain energy density is expressed as (see e.g. Kittel [31], p. 78)

$$u = \frac{1}{2}c_{11}(e_{xx}^2 + e_{yy}^2 + e_{zz}^2) + c_{12}(e_{xx}e_{yy} + e_{xx}e_{zz} + e_{yy}e_{zz}) + \frac{1}{2}c_{44}(e_{xy}^2 + e_{xz}^2 + e_{yz}^2)$$

where the x, y, and z axes are the *cubic* axes of the crystal.

The anisotropy of the crystal means that along other directions, the elastic moduli take on different values. Consider the shear modulus for example: c_{44} gives the shear modulus in the direction of the cubic axes, but in a coordinate system which is not aligned with those axes, μ_{shear} will take on a different value. In a coordinate system x'-y'-z which is rotated by 45° around the cubic Z axis, a shear strain $e_{x'y'}$ corresponds to a mixture of strains e_{xx} and e_{yy} in the cubic frame: the geometry gives $e_{xx} = \frac{1}{2}e_{x'y'}$, $e_{yy} = -\frac{1}{2}e_{x'y'}$, and $e_{xy} = 0$, so that the energy density contribution is

$$u = \frac{1}{2}c_{11}(e_{xx}^2 + e_{yy}^2) + c_{12}e_{xx}e_{yy} = \frac{1}{2}(\frac{1}{2}c_{11} - \frac{1}{2}c_{12})e_{x'y'}^2$$

I identify what I will call the 'rotated shear modulus' as the second derivative of energy density with respect to the shear in the rotated frame, $\mu'_{\text{shear}} \equiv \partial^2 u/\partial e_{x'y'}^2$; the above formula for the energy yields the expression

$$\mu'_{\text{shear}} = \frac{1}{2}(c_{11} - c_{12})$$

(This is a standard expression; see for example Kittel [31], which gives the wave velocities in various crystalline directions, which are directly proportional to the elastic moduli.)

The bulk modulus B involves an isotropic dilatation, and so has much the same meaning in a crystal as it does in any system. It can also be expressed in terms of the elastic constants.

[8] It may seem that there should be 36 (6 stress components × 6 strain components), but the symmetry imposed by the rest-frame constraint reduces the number to 21.

In particular, consider a uniform dilatation δ, such that $e_{xx} = e_{yy} = e_{zz} = \frac{1}{3}\delta$. Then the total energy contribution is

$$\begin{aligned} u &= \frac{1}{2}c_{11}(e_{xx}^2 + e_{yy}^2 + e_{zz}^2) + c_{12}(e_{xx}e_{yy} + e_{xx}e_{zz} + e_{yy}e_{zz}) \\ &= \frac{1}{2}c_{11} \cdot 3(\frac{1}{3}\delta)^2 + c_{12} \cdot 3(\frac{1}{3}\delta \cdot \frac{1}{3}\delta) \\ &= \frac{1}{2}(\frac{1}{3}c_{11} + \frac{2}{3}c_{12})\delta^2 \end{aligned}$$

Equating this with $u = \frac{1}{2}B\delta^2$, we find that

$$B = \frac{1}{3}(c_{11} + 2c_{12})$$

Again, this is a standard result and can be found directly in Kittel [31] (p. 80) among many other sources.

I will finally mention the *Cauchy relation*, which uses symmetry arguments to put a further constraint on the elastic constants for certain crystals. This relation holds when two conditions are met: first, that the crystalline structure is centrosymmetric, meaning that relative to any lattice position, if there is a particle at (x, y, z), there is an identical particle at $(-x, -y, -z)$; and second, that the interparticle potential can be expressed as a two-body interaction. In this case, $c_{12} = c_{44}$ [80]. In particular, the centrosymmetric condition is met for a single particle species occupying a simple Bravais lattice (that is, a lattice which can be described by a unit cell containing only one particle; the b.c.c. lattice is an example, as mentioned in Section 1.4); if two-body interactions are assumed in such a system, the Cauchy relation is expected to hold. This relation will be quoted later.

1.6 Outline of this thesis

I have here given some rather general musings, introducing some central concepts of the field at an intuitive and qualitative level, and giving just a few preliminary quantitative definitions, those which will be critical moving forward. References have been deliberately thin. The goal of this chapter has been to set the background and the stage for the scientific work I have done, but now it is time to get down to business.

The common thread of my experimental research has been to introduce repulsive charge interactions into colloidal systems which are well understood in the absence of such repulsion:

the two specific systems I have studied are colliodal gels, and colloidal crystals. In both cases, I have used confocal microscopy to study the structure and material properties of experimental systems. In the case of colloidal gels, I identified a change in the gel structure due to the competition of repulsive and attractive interactions. In the case of colloidal crystals, I have expanded our understanding of repulsive crystals at low volume fractions.

In Chapter 2, I will present the literature review, introducing in detail some of the many shoulders on which my work stands, with specific results given – I hope it is clear that none of this is my own work. In Chapter 3, I will give particulars of my model systems and the process of the experiments I carried out. In Chapter 4, I will describe my methods of data analysis. These two chapters of course begin to hint quite heavily at the actual scientific results. Those results are presented fully in Chapters 5 and 6: Chapter 5 presents my work on colloidal gels of oppositely charged particles ('binary gels'), while Chapter 6 presents my work on low volume fraction crystals of long-range repulsive colloids ('colloidal Wigner crystals'). Finally, I will give some final thoughts and summary in Chapter 7.

And so, with the stage set, let the play begin with a lesson in history:

Chapter 2

Background and Literature Review

Having addressed the conceptual basis of my work, and the major (and therefore broad) ideas I learned about during the course of my research, I will now dive into more specific detail in giving the literature review. Let me say outright that I have not read, and am not even aware of, all of the vast body of literature that has come before me. The expert reader may surely wonder why I do not mention so-and-so's work, and all I can say is that I did not have time to read everything. Here, as best I can piece it together, is what I do know of the shoulders I stand on.

I'll start by discussing in Section 2.1 some details of the charge interactions among colloidal particles in the two different systems I use (one in a polar solvent, and one in a nonpolar solvent). In Section 2.2, I'll expand on Section 1.3 to give a whirlwind tour of previous work on attractive colloidal gels and their nature and structure; the background here provides a foil to my new results. Section 2.3 is again directly relevant to the first of my systems, covering some past work with oppositely charged colloids, and earlier observations of the binary gels I study in greater detail. Section 2.4 gives a few examples of other systems in which competition between different interactions drives the structure of gels; again, the background here provides important points of comparison and context for my work on binary gels. In Section 2.5, I will shift to give background to my work on crystals, expanding on Section 1.4 to discuss a couple of general ideas about crystals which I have found useful, continuing in Section 2.6 to give further background about prior work on the

colloidal Wigner crystals which I study.

2.1 Charge in colloidal solutions

A brief warning: there are quite a few charged species in these experiments on charged colloids, and it can sometimes be a challenge to keep them straight if care is not taken. Roughly speaking, I am interested in charge on two scales. The larger scale is that of the particles I study, which have radii of about a micron, and charged surfaces. I'll refer to these as 'charged particles', and in general if I speak of a surface charge, I mean the charge groups covalently bound to the micron-scale particle surface. The smaller scale is that of the sub-microscopic charge carriers in the solution: either free ions on the scale of angstroms, or charged micelles on the scale of nanometers. These I will refer to as 'ions', 'microions', or 'charge carriers'. At both scales, charges may of course be either positive or negative. The condition of electroneutrality requires that the sum of all the charges, microscale and nanoscale, must be zero.

In Section 1.2, I presented the DLVO theory for the interactions of charged particles in solution, where the interaction energy between two particles is expressed as

$$\Phi(r) \propto \frac{\exp(-\kappa r)}{r}$$

with

$$\frac{1}{\kappa} = \sqrt{\frac{\epsilon_r \epsilon_0 kT}{\sum_i (z_i e)^2 c_{i,0}}}$$

I now delve into greater detail on the interactions in my two particular systems: particles with *polyelectrolyte brushes* (that is, surface layers of charged polymers) in both polar and nonpolar solvents. In each of these systems, the detailed chemistry is more subtle than the simple DLVO picture, as you will see.

2.1.1 In polar solvents

In water (at room temperature), $\epsilon_r \approx 80$, so that $\kappa^{-1} \approx 0.3\text{nm}/\sqrt{c_0}$ where c_0 is the molar concentration of a 1:1 electrolyte [18]. In the extreme of deionzied water with an equilibrium concentration of H^+ and OH^-, one can hope to acheive $\kappa \approx 1\mu$m, but the presence of even small amounts of additional electrolyte decreases this screening length. Water is such a

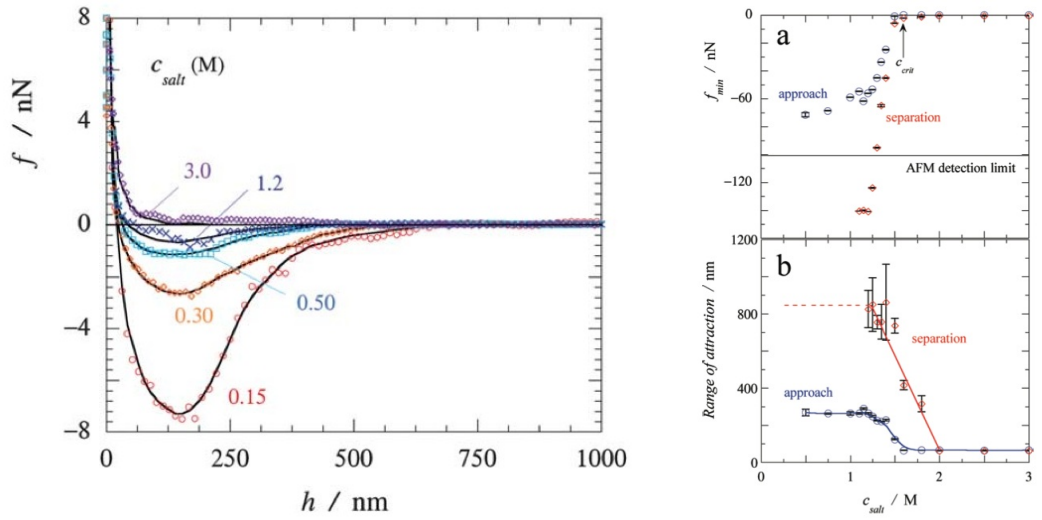

(a) (b)

Figure 2.1: Attractive interaction between oppositely charged colloids. a) Atomic force microscopy force measurements at different salt concentrations, as indicated by the labels. (from [69]) b) Effect of salt concentration on the attractive force minimum. (from [70])

good solvent that it is difficult to obtain screening lengths larger than tens of nanometers.

In the systems I work with, the surface charge groups are on a *polyelectrolyte brush*, where polymers containing charged monomer groups are in some way attatched to the surface of the particle. At distances greater than the extent of the brush, this should look roughly like a surface charge, but it turns out that in attractive, oppositely-charged interactions, the polymer-level entanglement also becomes important.

In many polyelectrolyte-brush systems, the magnitude of the charge on the particles depends sensitively on the pH in the system – the charge groups dissociate to different degree at different values of pH. In fact, in the polar system I used, the polyelectrolytes were very strong acids and bases, and so dissociated almost completely over a very large range of reasonable pH – except at very extreme values, the charge was relatively pH-insensitive.

The strength of attraction, however, still depends heavily on salt concentration. Most of what I know about these interactions is due to excellent work by Evan Spruijt at Wageningen University, who was carrying out detailed experiments on polyelectrolyte brush and particle interactions around the same time I was studying gels made up of those particles [70, 69]. Spruijt measured the force profiles of attraction between two colloidal particles, with results shown in Fig. 2.1.

As the particles approach each other, two effects contribute to their attraction. First is the screened electrostatic attraction between the two effective surface charges, as already

described. Second, the polymer brushes begin to entangle, forming what is known as a *polyelectrolyte complex*; this releases counterions which had been bound close to the brushes into the bulk solvent, increasing their entropy and favoring the complex formation [70]. At higher salt concentrations, the screening is greater, and the entropy gain of going into the bulk solution is smaller, so that the interaction becomes weaker and weaker with increased salt concentration, until past some critical salt concentration, the particles act as hard spheres.

The interaction has a strong hysteresis, in that it is very different on approach and on separation – once the polyelectrolyte brushes have interpenetrated, it takes much greater force to separate them again than the attractive force which drove them together [70]. This force also changes with contact time: the interpenetration of the polyelectrolyte brushes is a gradual process, proceeding over minutes, and so the interaction strength continues to increase with time as the polyelectrolyte complex evolves [70]. Thus the particle interaction cannot be described by a single interaction strength, or even a single potential curve.

The takeaway message, though, is that in a polar solution, salt concentration, here as often, has a strong effect on the *strength* of the electrostatic interactions in the system. The range of interaction is small compared to the micron scale except in very well deionized solvents.

2.1.2 In nonpolar solvents

In nonpolar solvents, the low dielectric constant means that there is a large (e.g. 10s of kT) energy barrier to charge separation, so that the concentration of charge-carriers is typically very low [22]. In fact, the challenge is to get charges to separate at all. The current understanding is that this is best achieved in the presence of some complex charging agent such as a *surfactant*. Surfactants are amphilic molecules with a polar head-group and a nonpolar tail. They will form micelles in a nonpolar solvent, with their head-groups aggregating to produce a small polar core, protected from unfavorable interactions with the solvent by the surrounding tails. These polar cores provide a safe haven for charge, both lowering the energy barrier to charge separation, and providing stabilization against charge recombination. (The terminology is a bit confusing: the term 'micelle' is more often used in aqueous solutions, where the hydrophobic tails form the core surrounded by the head groups, and so the inversion with polar groups inside is then a 'reverse micelle'. Which term

applies in nonpolar solvents has not really been agreed upon – many use 'reverse micelle' as the polar groups are in the core, but I prefer the term 'micelle' to mean the solvophobic groups are in the core. I will, I hope it is apparent, use the term micelle.)

A popular surfactant charging agent is dioctyl sodium sulfosuccinate, commonly called aerosol-OT or AOT. AOT forms micelles comprising about 30 molecules, with a hydrodynamic radius of $a \approx 1.5nm$ (for dry AOT – in the presence of water, these micelles can swell substantially) [22]. The charge behavior of AOT in dodecane, a common nonpolar solvent, was extensively studied in the group by Hsu and Dufresne. Hsu *et al.* considered poly-methyl-methacrylate (PMMA) particles coated with poly-hydroxy-stearic acid (PHSA) – very similar to mine in both composition and size – suspended in dodecane with added AOT surfactant; they used several techniques to elucidate the form of the interparticle interaction. Examination of the structure of quasi-2D samples of particles yielded estimates of the full potential, which fit well to a screened-Coulomb interaction, the screening length determined by the AOT concentration; with a small amount of AOT, they observed screening lengths of up to several microns, much longer than is possible in aqueous solutions. Measurements of the conductivity of AOT solutions (with no particles) corroborated these results, while measurements of the electrophoretic mobility of the particles in dilute solution supported estimates of the surface potential [22]. The result was a consistent story that above the critical micelle concentration (c.m.c.; about 1mM), AOT micelles performed very much as a salt, determining the ionic strength of the solution. From the dependence of the screening length on the AOT concentration (Fig. 2.2a), Hsu *et al.* determined that micelles acquired a charge by exchange of charge between two neutral micelles (rather than by dissociation of an electrolyte; Fig. 2.2b), and that a fraction $\chi \approx 1.2 \times 10^{-5}$ of micelles were ionized [22]. Above the c.m.c., the PMMA particles also acquired a *negative* charge, with a surface potential roughly independent of AOT concentration (although the apparent surface potential depends on the screening length), consistent with a thermodynamic picture of charges on the particle surface exchanging into AOT micelle cores. The surface potential was large: $\zeta \approx 140$mV, similar to the potentials achievable in water, but with fewer charges per particle, on the order of a few hundred (rather than thousands) [22]. The resulting picture is that of AOT micelles acting both as charging agents permitting charging of the particles, and as charge carriers determining the screening length for a screened-Coulomb potential [22]. Very similar results were obtained in a slightly different solvent – a mixture of decahydronaphthalene (decalin) and tetrachloroethylene (t.c.e.) – also in this group, by

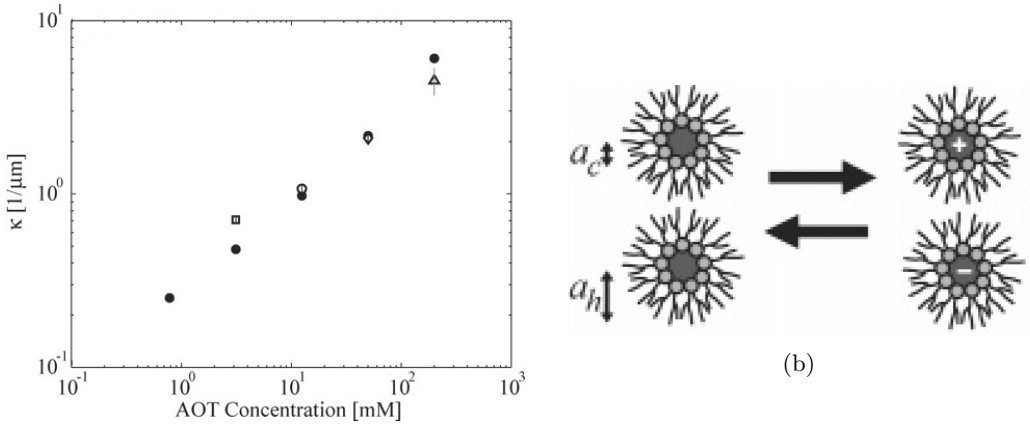

Figure 2.2: a) AOT in dodecane – inverse screening lengths inferred from conductivity measurements (solid circles) and from interparticle potentials determined from radial distribution functions (open symbols). b) Schematic diagram of the two-body process that leads to the creation of charge in the bulk of the solution. (both from [22])

Kanai *et al.* [28].

2.2 Attractive colloidal gels

We shift gears now, leaving charged particles for the time being to discuss the *colloidal gel*. As discusssed in Section 1.3, a colloidal gel is a sparse network of colloidal particles with stress-supporting bonds between them, giving an overall solid structure. The formation and structure of such gels is an intriguing topic with a deep history. Colloidal gels are part of my academic heritage, in that some of the very significant early experimental work in understanding their nature was carried out by my advisor Dave Weitz. I will start with that early work, and move to the aspects of colloidal gels which are particularly relevant to my own work on binary colloidal gels. This section is nothing like a thorough review of a vast literature; for much more information and many more references, I recommend Zaccarelli's relatively recent review [88].

2.2.1 Early observations and fractal nature

David Weitz and others at Exxon performed some of the earliest experiments in which the structure and nature of colloidal gels was directly observed [83]. In this work, the gels were formed by sub-microscopic uniform gold spheres, destabilized and permitted to aggregate by the reduction of the charge stabilization; the resulting clusters were observed in two-

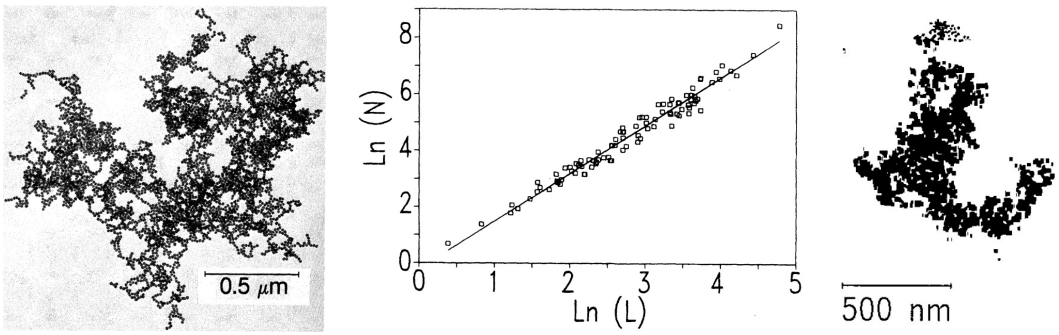

(a) (b) (c)

Figure 2.3: Fractal nature of colloidal gels. a) TEM image of typical gold colloid aggregate. b) N vs. L, where the solid line is a least-squares fit to the data, with the slope giving $D \approx 1.75$. (a,b from [83]) c) TEM image of cluster aggregated by reaction-limited kinetics. (from [82])

dimensional projection using electron microscopy (Fig. 2.3a). Weitz *et al.* identified the *fractal* nature of these gels, that is, the scaling of the number of particles in a cluster N with the spatial extent of the cluster L, found to scale as $N \propto L^D$ with the *fractal dimension* $D = 1.75$ (see Fig. 2.3) [83].

In follow-up experiments, the same group used light-scattering to study the evolution in time of aggregation; comparison with models suggested that the aggregation progressed by *diffusion-limited aggregation (DLA)*, in which particles or clusters would diffuse until they came into contact with another particle or cluster, upon which they would stick irreversibly to form a larger cluster [81]. Importantly, the clusters' diffusion constants were determined by their radius, not their mass, so that the fractal nature of the clusters affected itself the rate of aggregation [81] – this is often referred to as diffusion-limited *cluster* aggregation (DLCA), although the terminology is not always consistent. Denser gels, still fractal but with a larger fractal dimension of $D \approx 2.05$, were also found to form when the particles were only partially destabilized (Fig. 2.3c); this goes by the name of *reaction-limited colloid aggregation* or *reaction-limited cluster aggregation (RLCA)*, in which clusters which come into contact stick only with a certain probability, representing the height of the stabilization barrier [82]. Further studies showed that these two regimes of aggregation are universal across many colloidal systems [38].

2.2.2 Phase diagrams

In theory, when particles have irreversible interactions, a gel will eventually form at arbitrarily low volume fraction, given enough time for the particles to find one another. It is when interactions become *reversible* that things get interesting – the presence of a gel then depends upon the particle volume fraction, and on the shape of the interparticle interaction.[1] Over the past nearly three decades since the early work on fractal gels, quite a bit of effort has gone into determining when a gel will form and when the particles will remain in a fluid phase – that is, determing the state diagram of gelation. I will mention a few such state diagrams I have come across in my studies, particularly those from my predecessors in this group.

The earliest experimental phase diagrams I am aware of hark back to the 1990's, the work of the colloidal greats Pusey and Poon along with Pirie [51, 49]. Pusey *et al.* used the previously described PMMA / PS depletion system, varying both the primary particle (PMMA) volume fraction, and the magnitude of the interaction between the primary particles, via the PS concentration. They identified a range in which the PMMA particles phase-separated into a coexistence between fluid and crystalline phases, and upon increasing the amount of polymer, found that the crystallization was suppressed and that an arrested 'gel' phase formed instead [51, 49]. Lower (primary particle) volume fractions required a larger polymer concentration (hence stronger attractive interaction) to form the gel, while a smaller polymer concentration was adequate at higher volume fractions. Their early experimental phase diagram is reproduced in Fig. 2.4a [51].

The work of Pusey *et al.* had one aspect which is often considered a disadvantage: the PMMA particles were not density-matched to their solvent, so that after some time, the gels would collapse under their own gravitational weight [51]. The practice of using a solvent mixture to density-match the solvent to the particles came about a little later, and an example of colloidal gels using the PMMA / PS system but in a density-matched solvent came out of my group around the turn of the millenium [66]. This work of Segrè *et al.* established a state diagram qualitatively very like that of Pusey *et al.*, showing a critical interaction strength needed to form gels which varies with volume fraction (Fig. 2.4b) [66]. An interesting variation came out of Bristol a few years later, using a similar density-matched PMMA / PS depletion system, but in which the primary particles took on a slight positive

[1] The game also changes when shear stress is applied to the system, a situation of interest to those who think of gelation in the scheme of *jamming* [74], but this is not a dimension I have explored.

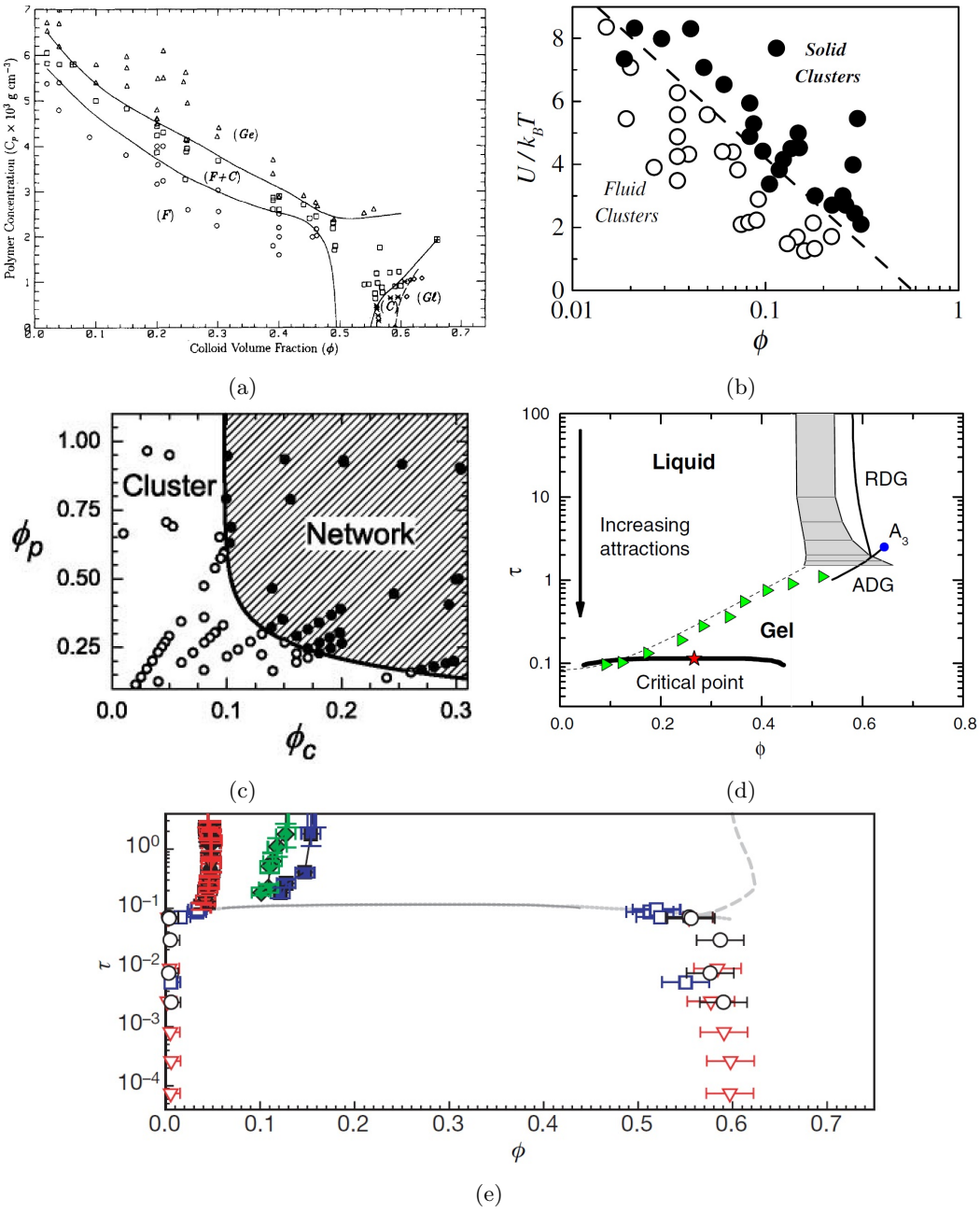

Figure 2.4: Experimental phase diagrams of colloidal gelation. a) Phases observed for a system of PMMA particles with polystyrene depletant, non-density matched; '(Ge)' represents the gel phase. (from [51]) b) Phases observed for a similar system of PMMA particles with polystyrene depletant, but density-matched; here 'solid clusters' corresponds to the gel phase. (from [66]) c) Phases observed for a similar system of PMMA particles with polystyrene depletant, but density-matched and with a slight charge; 'network' represents the gel phase. (from [7]) d) State diagram for a system of silica particles with attraction induced by a coating of octadecyl, not density-matched. (from [17]) e) Phase diagram for a system of PMMA particles with polystyrene depletant, density-matched; open symbols represent gels. (from [41]) In (a) and (c), the y-axis is volume fraction of the depletant, a proxy for interaction strength; in (b) the y-axis is interaction strength scaled by temperature; in (d) and (e), the y-axes is the *Baxter parameter* $\tau = 1/4(B_2^* - 1)$ determined from the reduced second virial coefficient of the interparticle potential.

charge, so that there was a long-range repulsion between particles competing with the short-range attraction. The state diagram for gelation was similar at high volume fractions, but the repulsion did not permit the formation of low volume fraction gels (Fig. 2.4c) [7].

More recently, in an attempt to understand gelation as universal, some groups have shifted to expressing the second dimension of the state diagram not as the polymer concentration or even strength of attraction, but rather as the *Baxter parameter*, $\tau = 1/4(B_2^* - 1)$, where B_2^* is the *reduced second virial coefficient* of the interparticle potential, depending on both the depth and the extent of the attractive well. (E.g., for a square well of extent ϵ and depth U, $\tau = \frac{1}{12\epsilon} \exp(-U/k_BT)$ [17].) Large c_p or U correspond to large B_2^* and hence *small* τ. This conversion allows more direct comparison with general theory and simulation, relating the gel line to equilibrium phase lines. Fig. 2.4d,e show examples of these phase diagrams; (e), by Lu *et al.*, comes out of my group, using nearly the same density-matched PMMA / PS system [41], while (d) shows the result of more recent experiments by Eberle *et al.* at University of Delaware using, for once, a different system of submicron silica particles with an octadecyl brush which mediates the attractive interaction [17]. Both phase diagrams show the equilibrium liquid-vapor coexistence region in addition to the experimental gel line. Lu's work, in particular, is the only one of these phase diagrams to vary not only the strength of the interaction, but also the extent, with one dataset showing results using a depletant of a different size. The size of the polymer changes the critical polymer concentration, but the critical Baxter parameter remains the same [41], emphasizing the usefulness of this parameter.

The general picture that emerges is intuitive: gelation will occur above some critical interaction strength which depends on volume fraction; more dilute particles must stick together more strongly than concentrated ones in order to form a gel. The details of the diagram may be affected by details of the system (e.g. gravitational settling or long-range repulsion). But the comparison to theoretical or simulated lines, begs the question: what is the mechanism of gelation?

2.2.3 Mechanism

There have been a good number of suggestions, and a good amount of debate, over the mechanism of gelation. Again, I shall hardly be able to give a complete story here, but let me try to collect my scattered thoughts on the matter.

One of the more widely accepted mechanisms for gelation is *arrested spinodal decomposition*, as recently strongly argued by Lu *et al.* [41]. *Spinodal decomposition* is a *thermodynamic* phase separation into two coexisting phases, driven by the instability of the intermediate or mixed phase; it is characterized by homogeneous formation of regions of each of the two phases, which grow in extent with a characteristic scaling. Colloidal gelation is potentially understood as stemming from a vapor-liquid spinodal decomposition: the 'vapor' phase corresponds to the nearly particle-free voids in the gel, while the 'liquid' phase corresponds to the volume filled by the strands of the gel. The identification of spinodal-like scaling in the evolution of the structure factor of a particle solution as it gelled was one of the core arguments that this is the driving mechanism for gelation in a depletion system [41]. Within the would-be liquid regions that are the gel strands, the local density is so high as to bring about a glass transition, kinetically arresting the phase separation and 'freezing' the system into a non-equilibrium gel [41].

Yet the book is not closed on the nature of gelation; Lu *et al.* considered only depletion gels, while the work of Eberle *et al.* suggests that in a system with a different physical mechanism for attraction, gels form without phase separation [17]. Instead, the gel line corresponds with the predictions of *percolation theory* – the percolation phenomenon has nothing to do with thermodynamics, but instead describes mathematically the formation of links (bonds) between nodes (particles) in a system, forming joined clusters which at some point will *percolate* across the entire system, forming a spanning network. This theory has been well developed by applied mathematicians over many decades, and applied broadly to all manner of network theories, from the spreading of disease epidemics to the distribution of power and water (not to mention, of course, the filtration of coffee!). Indeed, the idea of percolation has long been applied to gelation. Eberle *et al.* suggest that gelation of attractive particles is not so universal as Lu *et al.* would claim, but that both thermodynamic phase separation and percolation without phase separation may drive gelation under different conditions [17].

Gelation is also closely related to *attractive glasses* and *jamming*. Both Lu *et al.* and Eberle *et al.* connect the moderate volume fraction gelation transition to the high volume fraction attractive glass transition [41, 17]. Segré *et al.* also find glass-like behavior in the evolution of gelation in their earlier work, and extrapolation of their gel line to low attractive strength coincides with the hard-sphere glass transition [66]. Indeed, Trappe *et al.* unified gelation, glasses, and jammed systems into a *jamming diagram* for attractive colloids which

links all of these phenomena closely together as manifestations of the same basic process [74].

2.2.4 Structure within gels

Beyond the formation and state diagram of colloidal gels, there is a great range of properties to study, from structural to dynamic to rheological. I shall focus here on the structural properties, as most relevant to my own work, although I regret the neglect of the others.

The fractal dimension of a gel has already been described, and it is commonly invoked and measured in a great number of papers on colloidal gels. Yet this single parameter loses a great deal of information about the structure in a gel, especially the local structure. The advent of confocal microscopy allowed detailed study of the three-dimensional structures.

A little over a decade ago, a paper out of my group by Dinsmore *et al.* studied the density-matched PMMA / PS depletion gel, and discussed at length gel structures from the point of view of bonds between contacting particles, and the rigidity of chains in the gel provided by multiple contacts [16]. They found that increasing either the primary particle volume fraction or the polymer concentration – that is, forming a more *deeply quenched* gel, one deeper in the gel region of the state diagram – tended to increase the number of bonds per particle, measured in small clusters before the complete formation of the gel (Fig. 2.5a); at longer times, the bond distribution shifted to larger bond numbers [16]. This was explained by the ability of the particles to reorganize by rotating or rolling around a bonded partner; such reorganization will tend to allow particles to form more contacts, increasing the number of bonds n_b. At larger volume fractions, the reorganization is hindered by the formation of larger-scale structure which constrains the particles, while at higher polymer concentrations, the rotational motion itself is kinetically slowed – both effects give rise to gels with lower contact numbers and more rarified structure [16]. The mean cross-sectional area of a chain in the gel similarly decreased with a deeper quench, although the fractal dimension remained the same (Fig. 2.5b) [16].

Dinsmore *et al.* also defined *pivot* particles in the gel, as particles whose bonded neighbors themselves formed multiple disconnected clusters; this allows those clusters of neighbors to move relative to one another by rotating around the pivot particle. In contrast, if multiple bonded neighbors form a connected cluster, their motions are mutually constrained – e.g. in two dimensions, three particles forming a fully-connected triangle are unable to move

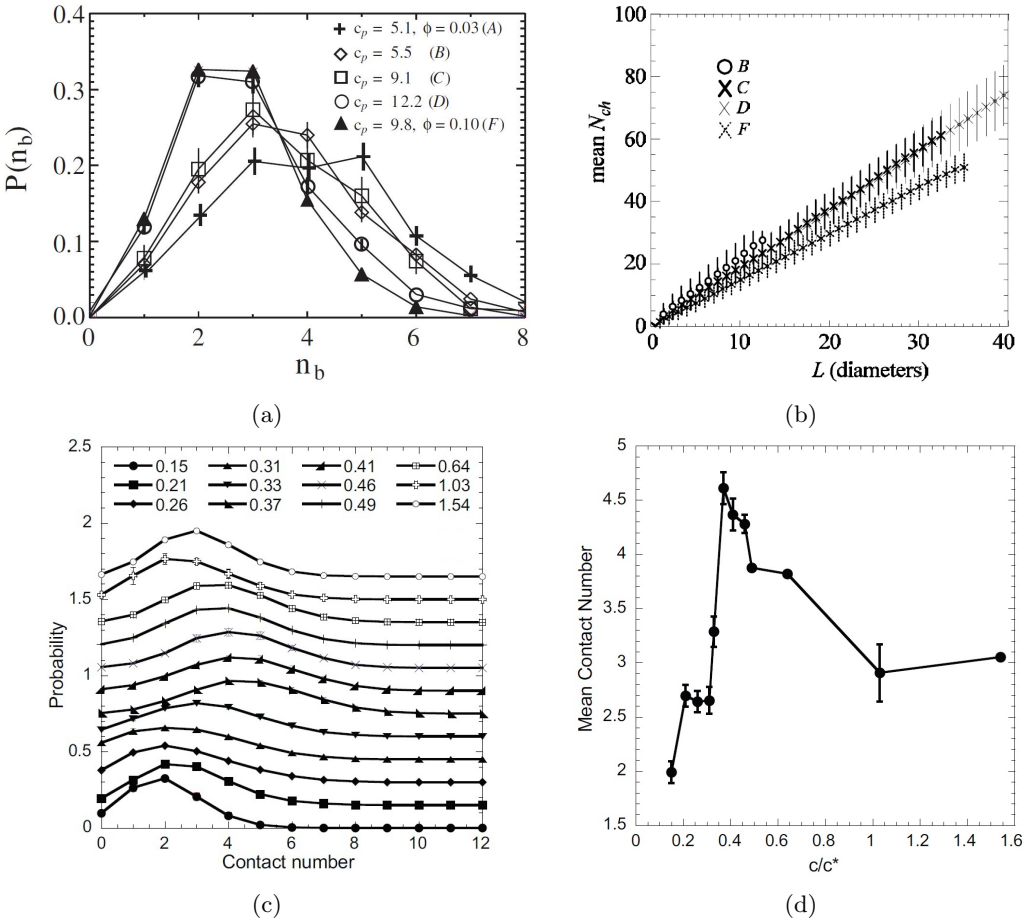

Figure 2.5: Structure within depletion gels. a) Distribution of number of bonds per particle, n_b, in clusters of 20-22 particles before full formation of a gel. Increasing ϕ or c_p tends to reduce n_b. b) Plot of the mean number of particles in a chain, $\langle N_{ch} \rangle$, as a function of chain length L. The slopes of the lines indicate the mean chain cross-sectional area, which decreased as c_p or ϕ increased. (a,b from [16]) c) Contact number distributions for each depletant concentration; the gel transition falls between about $c \approx 0.31$-0.41. Data are offset for clarity. d) Mean contact number distrubition for each $c/c*$. (c,d from [14])

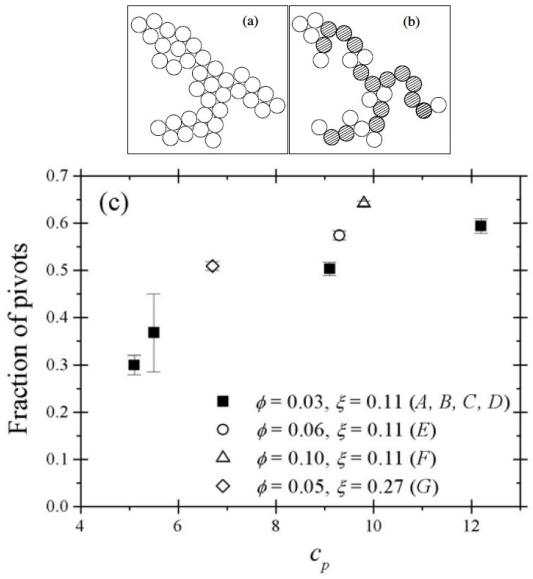

Figure 2.6: Pivot points in the gel. a) An illustration of a two-dimensional gel segment with not pivots. The segement is rigid (for in-plane motion) even if the individual bonds are not. b) An illustration of a gel segement in which 15 out of 28 particles form pivots (shown as cross-hatched circles). c) Plot of the measured fraction of 'pivot' particles as a function of c_p for various ϕ and ξ (the interaction range). The fraction of pivots is systematically greater in samples that lie deeper in the gel region of the phase diagram. (all from [16])

relative to one another. Thus pivot particles represent points of lower rigidity. Dinsmore *et al.* found that while all gels had a significant fraction of pivot particles, that fraction increased for more deeply quenched samples (Fig. 2.6) [16].

More recent work out of Michigan by Dibble *et al.* presents similar findings, also for a PMMA / PS depletion system, and explicitly relate the structural properties to the dynamic properties and gelation. They find that in the fully-formed gel (not small clusters as in the work of Dinsmore *et al.*), the contact number increases at lower polymer concentration, that is, on approach to the gel line, with mean contact number as high as 4.5 for the weakest gel; there is an abrupt drop in mean contact number in the cluster-fluid phase (Fig. 2.5c,d) [14]. The structural heterogeneity also has a significant peak around gelation, as measured by the fluctuations in local particle density; that is, deeply quenched gels at large polymer concentrations are quite homogeneous with evenly-distributed chainlike structure, while gels at low polymer concentration are heterogeneous, with large voids intermixed with dense areas [14].

Both of these works demonstrate that the internal structure of a gel varies over the phase diagram, and gives a broad picture of deeply-quenched gels comprising thin chain-like structures with low connectivity which are homogeneously distributed, while gels close to

the transition comprise thicker bundles with many particle contacts [16, 14].

2.3 Oppositely charged colloids

Most of the work heretofore described has involved a single type of particle with only attractive interactions. Yet taking a step back to consider colloids as models for other systems, we find this is a rather limiting situation. Many 'real-world' systems are heterogeneous in composition, with multiple particle types, and interactions are not always attractive. What can we say about these more complex systems?

The first step we take is to introduce opposite electrostatic charges, and consider systems comprising both positively charged and negatively charged particles. Then the interparticle interaction depends on the nature of the particles: oppositely charged particles will have an attractive interaction, but similarly charged particles a repulsive interaction. This heterogeneity, this non-interchangeability, of both particles and interactions, introduces far more complex behavior into the system.

Certainly these systems are relevant. Drawing some examples from biology, the interaction between DNA and the histone proteins which mediate its folding into the dense, complicated, but ultimately well-organized nucleus, those interactions are substantially governed by the charge interaction between negatively charged DNA and the positively charged histones [4, 53]. The pectin gels that are an important component of cell walls in many plants, the breakdown of which is responsible for the softening of fruit, consist of polysaccharides with negatively charged carboxyl groups, cross-linked by divalent positively charged calcium ions [25]. Structures driven by charge interactions are ubiquitous – and very different from the depletion gels that are so well known.

In the laboratory setting, of course, we vastly simplify matters for ourselves. The main experimental systems I will discuss consist of binary charged spheres, one species positively charged and one negatively charged. The size of the two species may be different, as may the magnitude of the charge on them. I will also give some discussion of polyelectrolyte complexes, formed again by two species, but this time of flexible polymers.

2.3.1 Binary colloidal crystals

This is somewhat of an aside from the discussion of gels, but an important milestone in the study of oppositely charged colloids. Some of the most beautiful work I have seen

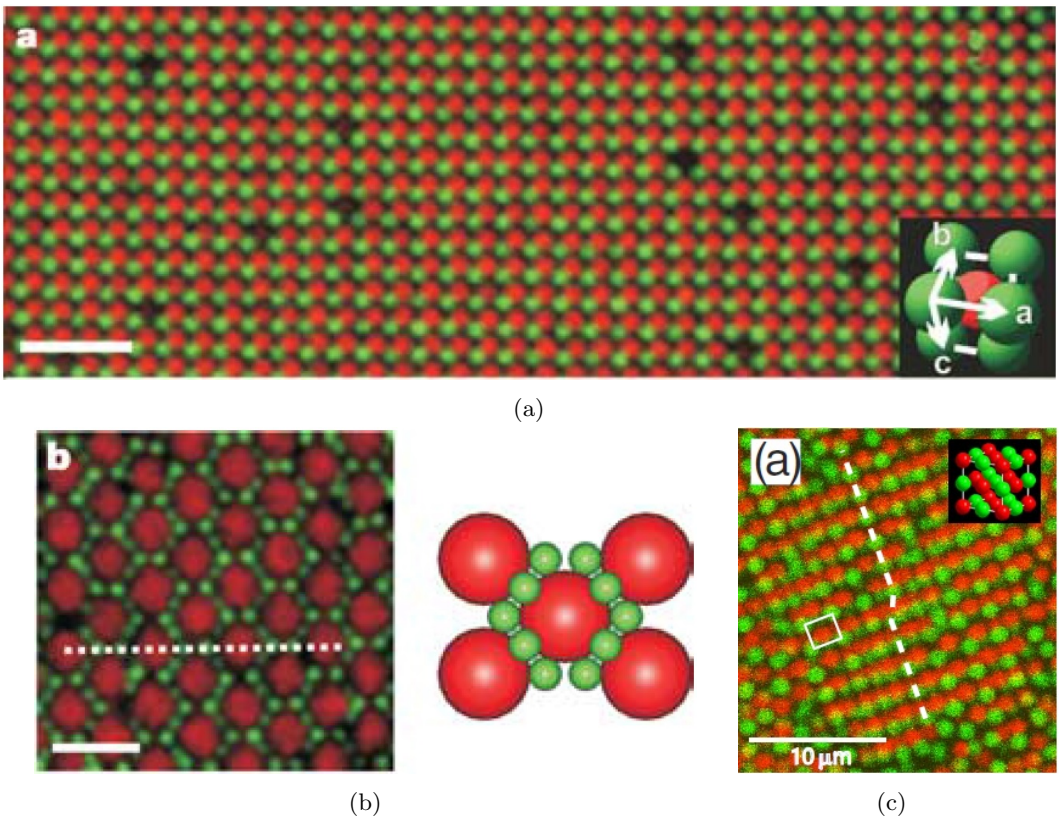

Figure 2.7: Binary colloidal crystals. a) CsCl-type binary crystals; confocal micrograph of a large (100) plane. Inset, the cubic CsCl-type unit cell. Scale bar is 10 μm. b) LS_6-type binary crystals; confocal image and model of a layer of large and several layers of small particles. Scale bar is 4 μm. In both (a) and (b), positive PMMA spheres are red, negative are green. (a,b from [35]) c) Confocal image of tilted (100) plane of sodium chloride superlattice. Inset shows NaCl unit cell. Positive spheres are in green, negative are red. (from [2])

on oppositely-charged colloids came out of Utrecht, the work of Leunissen *et al.* on 'ionic colloidal crystals.' These experiments used PMMA particles in a nonpolar solvent with a small amount of added tetrabutylammonium bromide (TBAB) salt to mediate charging of the particles. Positively and negatively charged particles were labeled with different fluorophores; in this case, the opposite charges were obtained on different batches of particles which supported different charges [35]. The most interesting results came about when the charges were roughly equal in magnitude, and small enough to allow the system to come to equilibrium. Mixtures of similarly-sized particles, then produced crystals with a cesium-chloride structure, with each charge species forming a simple cubic structure, the two species interlocking so that one species would lie at the body-center of the lattice formed by the other (Fig. 2.7a) [35].

Leunissen *et al.* further went on to mix oppositely charged particles of different sizes;

this size asymmetry produced more complicated crystals of LS_6 structure (that is, one large particle to six small particles; Fig. 2.7b), LS_8 structure, and two LS structures when only the large particles were charged [35].

Almost simultaneously, similar work came out of Bristol by Campbell *et al.*, again with differently-dyed PMMA particles. These experiments investigated only same-size particles, but found both the CsCl structure common with Leunissen *et al.*, and, at higher charge magnitude, a sodium-chloride structure in which the overall lattice is simple cubic, with the two species occupying alternating lattice sites (Fig. 2.7c) [2].

These crystals begin to portray the rich structures available when heterogeneous particles and interactions are invoked, along with the effect of such tuning parameters as particle size and charge on those structures.

2.3.2 Polyelectrolyte complexes

From the beautifully ordered crystal lattices of colloidal spheres, we now move to discuss an entirely different beast, *polyelectrolyte complexes* formed by the messy entanglement of oppositely-charged polymers. I bring these up for two reasons: first, because they are one more connection of particular relevance to the phase behavior of binary charged systems; and second, because they turn out to be essential ingredients in the specific interaction between the particles I used (as described in Section 2.1.1).

A polyelectrolyte is any multivalently charged species in solution: most typically polymers with many charge groups, but also colloidal particles (as I use), or smaller molecules. Such a polyelectrolyte is surrounded by a double-layer of counterions. Two complementary polyelectrolytes with opposite charges will often associate to form a complex – this complexation is driven by the nature of the two electrolytes, as well as the micro-ion salt concentration in the solution. When the polyelectrolyte complex phase-separates into concentrated and dilute phases, the concentrated phase is called a *complex coacervate* [77].

The complexation is potentially driven by two effects. The first is energetic. At low micro-ion salt concentrations, the electrostatic energy of the complex is typically lower than that of the free polyelectrolytes, as the charge groups on the polyelectrolytes can associate more closely than do the counterions around the individual polyelectrolytes. At high salt concentrations, however, this energy difference decreases and can even reverse so that complexation is endothermic [77]. The second effect is entropic; counterions are

released from the double layer into the bulk as they are replaced by charges on the oppositely polyelectrolyte, and thereby gain available volume and entropy. The effect is stronger at low salt concentration than at high salt concentration. There is a small entropy loss of configurational entropy of the polyelectrolytes themselves, but this tends to be overwhelmed by the counterion entropy gain [77]. Thus polyelectrolytes will generally complex at low salt concentrations, and remain homogeneous at high salt concentrations.

These qualitative arguments capture very well the behavior of complex coacervates, but a quantitative model incorporating both these and other more subtle effects has proven elusive. Early theoretical work on complex coacervates came from Overbeek and Voorn, using Debye-Hückel theory to calculate the electrical free energy of ions (both multivalent and monovalent) in solution [46]. This Debye-Hückel theory ignores any internal structure of the ions, simply considering the charge and the total molecular volume – essentially treating any ionic species as a sphere. The entropy is simply calculated from the log of the volume fraction. This simplistic treatment gives the major features of coacervation: phase separation into a concentrated and a dilute phase, and the dependence on (micro-ion) salt concentration – see Fig. 2.8a [46].

More recent theoretical work by Biesheuvel and Cohen Stuart in Wageningen gives a more detailed treatment of the energetics, solving the Poission-Boltzmann equation in a *cylindrical* cell around an elongated polyelectrolyte chain, and taking into account the different electrostatic potential near each chain [3]. They also allow for asymmetrical compositions, that is, different concentrations of the anionic and cationic polyelectrolytes, and for different values of the solution pH and the polyelectrolyte pKs, governing the magnitude of the charge on the polyelectrolytes. Salt concentration remains a critical parameter controlling whether complexation occurs, and the densities of the resulting phases. The qualitative behavior is similar (Fig. 2.8b) [3].

Most of what I have learned about polyelectrolyte complexation and complex coacervates come from the group of van der Gucht in Wageningen [77], particularly from the experimental work of Spruijt and others [71, 72, 73]. Spruijt *et al.* measured experimentally the phase diagram of coacervate separation for combinations of polyelectrolytes of varying chain lengths, all of which compare well to the Debye-Hückel model (Fig. 2.8c) [73]. In further experiments, they also measured the interfacial tension between the dense and dilute phases of a complex coacervate, by measuring the capillary force between two silica spheres in a colloidal-probe atomic force microscope, and found that this interfacial tension falls

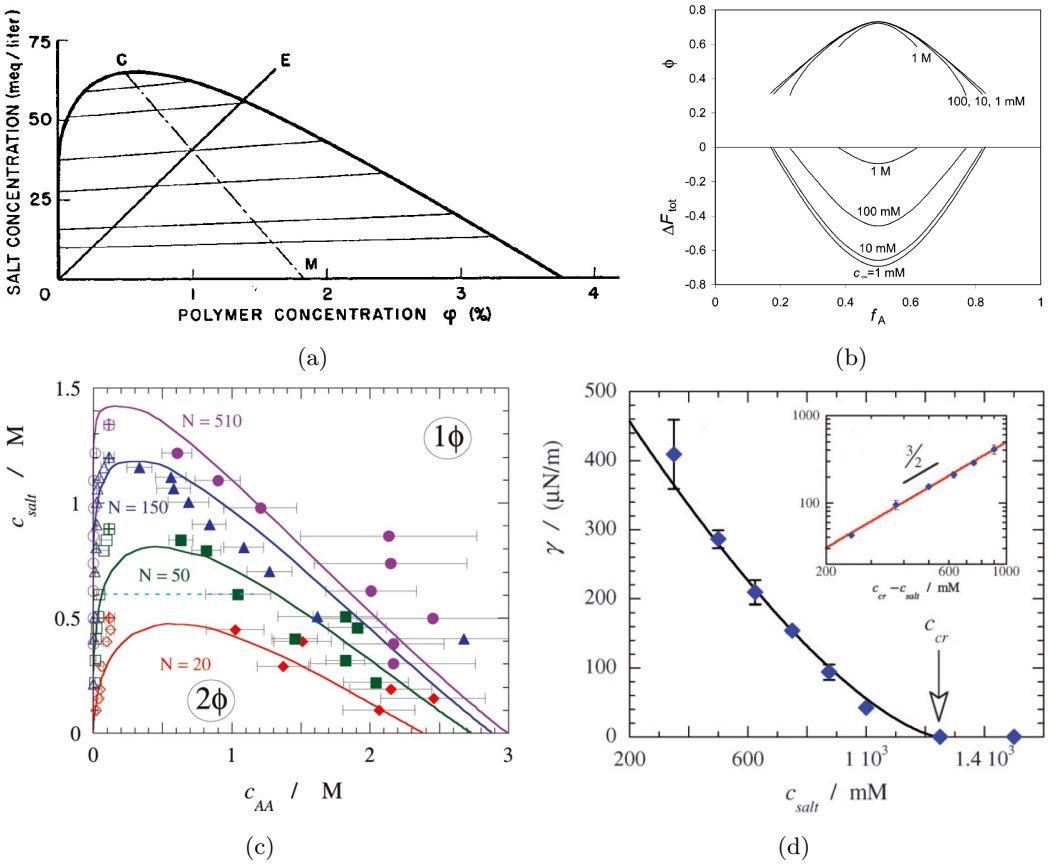

Figure 2.8: Polyelectrolyte complexation. a) Phase diagram for complex coacervation in a system comprising a solvent, polyelectrolytes P and Q, and monovalent salt KA. (from [46]) b) Polyelectrolyte complex density and free energy as a function of salt concentration; the composition f_A is given by the molar fraction of the anionic polyelectrolyte. (from [3]) c) Phase diagram for phase separation between PAA and PDMAEMA at pH 6.5. Symbols indicate experimentally measured binodal compositions of the coexisting phases; solid lines are theoretical predictions of the phase behavior based on the model. The labels N indicate the chain length of the PAA polymer. (from [70]) d) Interfactial tension of complex coacervate phases as a function of salt concentration. The critical salt concentration, above which no capillary force could be measured, is indicated by the arrow. Inset, same data as in the main figure, but plotted against the separation from the critical point on a double logarithmic scale. The solid line is a power-law fit to the experimental data, with an exponent 1.5. (from [71])

off with increasing salt concentration, consistent again with the mean-field Debye-Hückel model (Fig. 2.8d) [71].

Based on their work with coacervates, and extensive measurements on the interactions between colloidal particles with polyelectrolyte brushes, Spruijt *et al.* concluded that the attraction interaction between such oppositely-charged particles is due to the formation of a complex between the two polyelectrolytes, as ion pairs in the two brushes associate [70]. As discussed in Section 2.1.1, this will be important in my experimental system.

2.3.3 Gels of oppositely charged particles

Experiments

There is some previous work on gels of oppositely-charged particles, both theoretical and experimental. Among the earliest work I am aware of are measurements by Kitano *et al.* in Tokyo of the association rate between oppositely-charged particles, finding that dimerization of a very dilute mixture of latex particles ($\phi_{anionic} \approx 10^{-4}$, $\phi_{cationic} \approx 10^{-3}$) proceeded in a diffusion-limited fashion [29]. The association rate seemed to confirm that there was little long-range attraction, but that only the charges quite local to the particle contact played a role [30]. At longer times, Kitano *et al.* observed larger aggregates forming [30].

From dimer association we move to the aggregation of full gel networks. Experiments along these lines have been done only quite recently. In early work in Almeria, Romero-Cano *et al.* mixed oppositely charged latex particles and made macroscopic observations of the phase as they varied both particle volume fraction, and added (micro-ion) salt concentration; they identified a solid gel phase at low salt concentrations, giving way to a gas-liquid phase separation at slightly higher salt concentrations and finally a homogeneous fluid (Fig. 2.9b) [58]. The critical salt concentration for formation of the gel depended weakly on volume fraction [58].

The step from macroscopic to microscopic observations was made a couple of years later by Sanz *et al.* in Utrecht. These experiments used 2μm-diameter PMMA particles floures-cently labeled to be visible in a confocal microscope; at the particular salt concentration of 1.0μM of TBAB salt, two particle species with different fluophores carried opposite charges. Sanz *et al.* observed a gel at a total volume fraction of $\phi = 0.05$, with thin branches coars-ening as the gel formed over time (Fig. 2.9a) [62]. Comparison to simulations suggested that this process represented an interrupted spinodal decomposition [62], similar to the

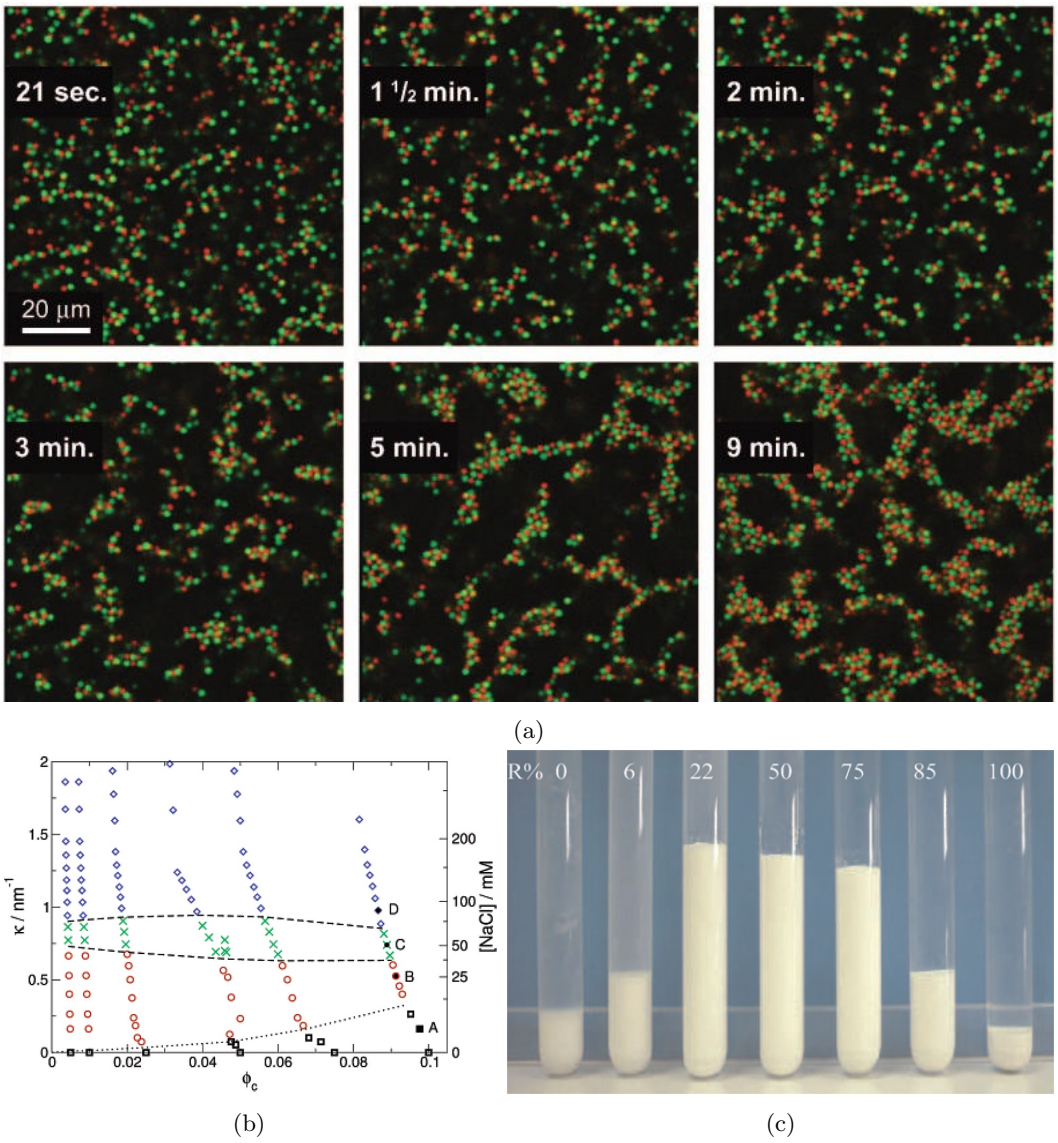

Figure 2.9: Binary gelation of oppositely charged particles. a) Sequence of confocal snapshots illustrating the formation of a binary gel in a system of PMMA particles. Red particles are positively charged, and green particles are negatively charged. (from [62]) b) Phase diagram of a binary mixture in κ (inverse screening length) vs. ϕ_c (volume fraction) in a system of PS latex particles. By increasing the salt concentration, a fluid phase is observed at low κ (black circles), followed by a gel phase (red circles), liquid-gas separation (green crosses), and a homogeneous fluid (blue diamonds). (from [58]) c) Effect of gravitational stress on binary gels at different mixing ratios, after two months of sedimentation in a mixture of silica and alumina particles. The values of R give the mass fraction of negatively-charged silica particles relative to the total mass; note that symmetric mixtures form strong gels which support their weight, while highly asymmetric mixtures are weaker and less stress-supporting. (from [8])

process found in purely-attractive depletion gels. Examination of the structure of the gels showed about nine oppositely-charged particles in the first coordination shell of a particle, with like-charged particles appearing further away [62]. These binary gels were resistant to gravitational collapse – moreso than depletion gels – persisting for months after formation [62].

Even more recently, oppositely-charged gels have been observed at asymmetric mixing of the positively charged and negatively charged species. Experiments done by Cerbelaud *et al.* in Limoges studied mixtures of irregular and differently-sized alumina and silica particles at varying compositions, observing the sedimentation of mixtures over time; where single-species samples formed a dense sediment over months, mixed samples arrested within hours to weeks, with a tall supported sediment indicating a low-volume fraction solid, that is, a gel. The more nearly symmetric mixtures produced taller sediments (Fig.2.9c) [8]. In follow-on experiments, Piechowiak *et al.* synthesized particles closer in size, and used confocal microscopy to directly examine the structure of the gels. Qualitatively they found the same results, and were also able to measure the contacts of particles in a 2-dimensional slice of the sediments (Fig. 2.10a-c) [48].

The Wageningen group which did so much work on coacervation and on the polyeletrolyte brush interactions also studied aggregation of oppositely charged colloids, in this case polystyrene with polyelectrolyte brushes [69], a system closely approaching the one I used. Here, Spruijt *et al.* demonstrated reversibility of the aggregation, controlled by salt concentration. They further examined the structure of the gels, finding partial radial distribution functions much like those of Sanz *et al.* (Fig. 2.10d), and also showing that the fractal dimension of the aggregates depended both on the depth of the quench (again determined by salt concentration) and on time (Fig. 2.10e) [69].

Simulations and Theory

I have so far focused on the experimental work in the literature, revealing my own bias as an experimentalist. Of course, there is also a good bit of theoretical and simulation work. Several of the experiments already mentioned were accompanied by fairly extensive simulations [62, 8, 48]. Simulations allow a much wider exploration of the phase diagram – for example different charges or interaction strengths inaccessible in the finely-tuned experimental systems.

Simulations have taken various forms. Many aim to directly model colloidal systems, and

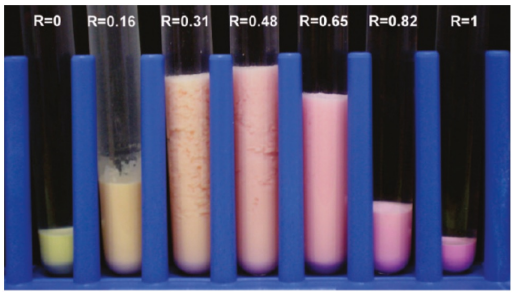

(a)

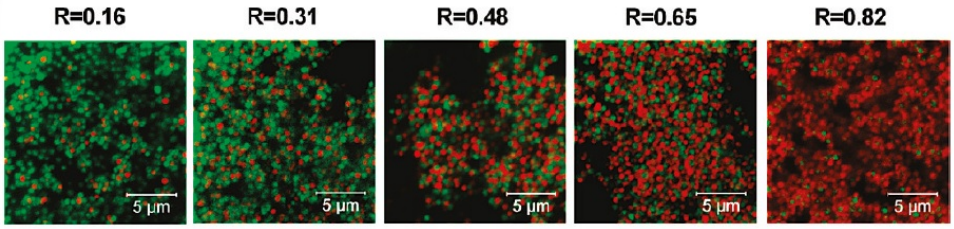

(b)

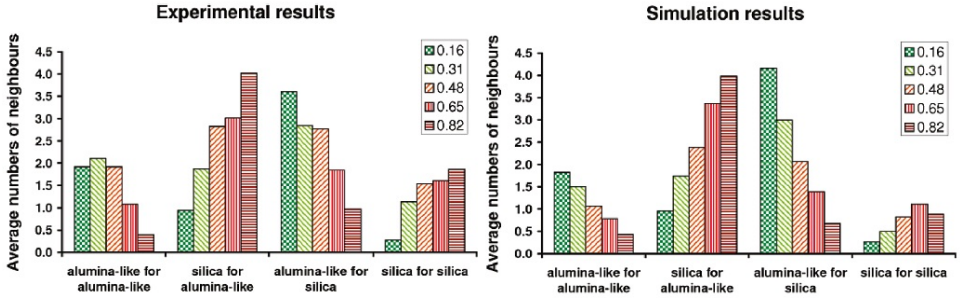

(c)

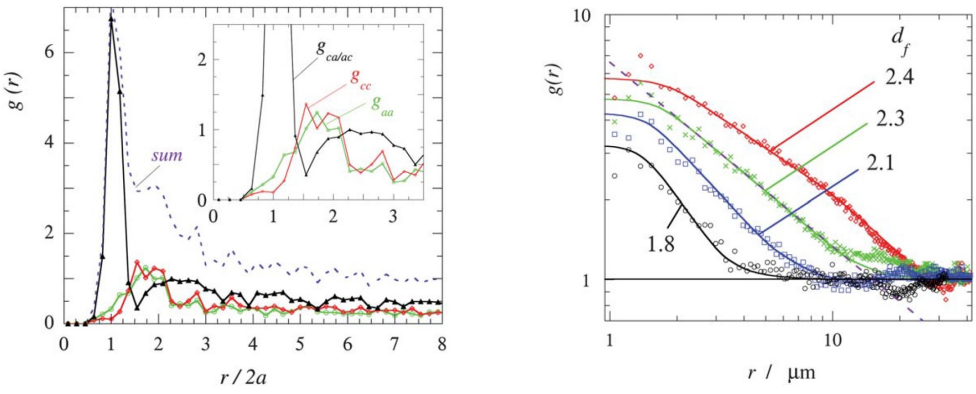

(d) (e)

Figure 2.10: Structure within asymmetric binary gels. a) Sedimentation tests after 1 month, with R as in Fig. 2.9e; total initial volume fraction $\phi = 3\%$. b) Confocal laser scanning microscopy images of alumina-like/silica suspensions as a function of the mass ratio R; negatively charged silica particles in red, positively charged alumina-coated particles in green. c) average number of neighbors in 2D slices. (a-c from [48]) d) 2D partial radial distribution functions of aggregates of oppositely charged particles at 1.5 M KCl salt. e) Radial distribution function of quenched suspensions of oppositely charged polystyrene particles; symbols represent different quench parameters. Labels d_f indicate the fractal dimension. (d,e from [69])

consider spherical particles interacting via a Derjaguin-Landau-Verwey-Overbeek (DLVO) potential; some simplify this to hard spheres with a screened-Coulomb or Yukawa potential. Simulation techniques range from Monte Carlo simulations to Brownian or molecular dynamics.

Many simulations have studied the equlibrium phase diagram of oppositely charged particles, mapping out the different crystalline phases. More recent simulations have examined *non-equilibrium* aggregation and arrested states – that is, gels and glasses. Simulations of the gas-liquid transition are also of interest, as arrested spinodal decomposition remains a significant hypothesis for the formation of binary gels as well as depletion gels [62, 63].

Early Monte Carlo simulations of a symmetric screened-Coulomb system with $\kappa\sigma = 6$ (that is, an interaction range $1/6$ of the particle diameter) identified the gas-liquid transition and critical point, with the freezing line at high volume fractions (Fig. 2.11a) [6]. Later, very similar simulations by Hynninen *et al.* in Utrecht found that this gas-liquid coexistence is in fact metastable with respect to the gas-crystal coexistence (Fig. 2.11b) [24]; upon further simulations at different values of the screening length, they found that the gas-liquid is metastable when $\kappa\sigma > 4$, and stable for $\kappa\sigma \leq 4$ [24].

Using Brownian dynamics to investigate not just the equilibrium diagram, but also non-equilibrium dynamics, the same group found that this metastable gas-liquid coexistence led to spinodal decomposition, which arrested before the liquid phase was able to crystallize, leading to a 'percolating network of amorphous branches', that is, a gel [63]. Thus these simulations lead to the important hypothesis that gelation of oppositely charged colloids is driven by arrested spinodal decomposition, just as in depletion gels [62, 63].

Theoretical results on a 'primitive model' (using a Coulomb rather than a screened-Coulomb interaction) were presented by Sanchez-Diaz *et al.* in San Luis Potosí, determining the arrested state diagram, with an arrested gel at low effective temperatures, the critical temperature varying with volume fraction [61]. Including a size asymmetry or a charge asymmetry introduced novel phases with only one particle type arrested, and the other mobile (Fig. 2.11c) [61].

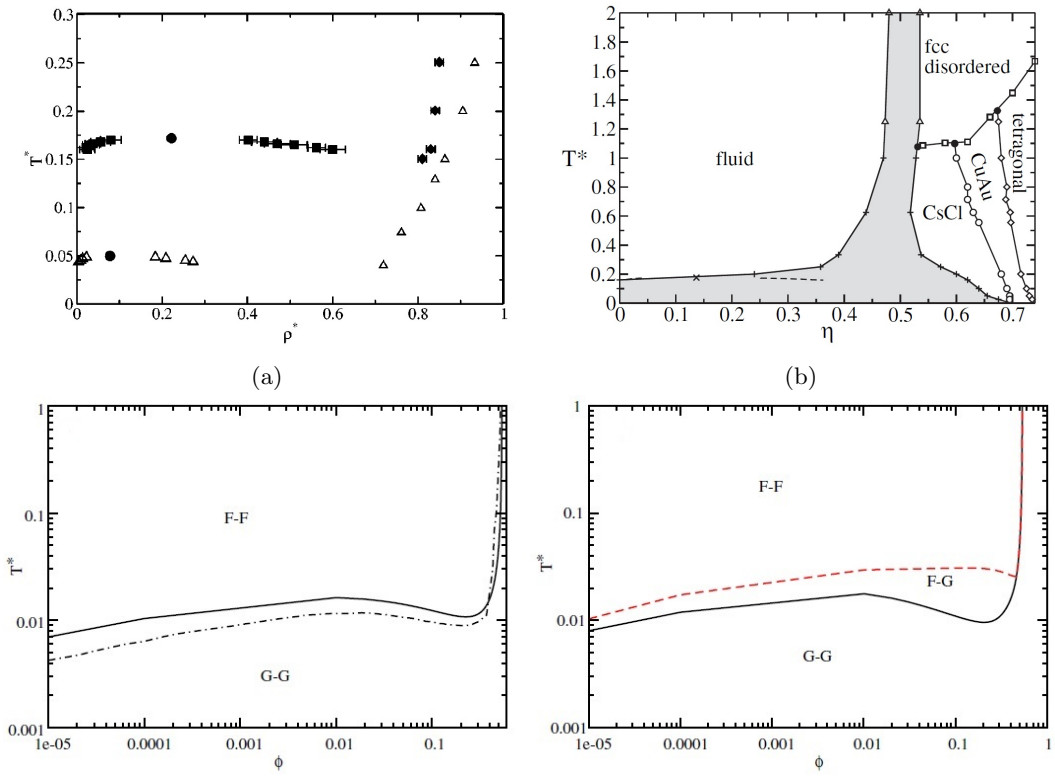

Figure 2.11: Theoretical phase diagrams for binary gels. a) Phase diagram for colloidal mixture showing liquid-gas transition (squares) and freezing line (diamonds); filled circles depict the critical points. Triangles represent the restricted primitive model for Coulomb interactions. (from [6]) b) Phase diagram of screened Coulomb particles with $\kappa\sigma = 6$. The dashed line and the cross show the mestastable gas-liuquid phase envelope and the critical point, respectively. (from [24]) c) Dynamic arrest phase diagram of the binary primitive model for the symmetric case (left) and a charge-asymmetric system with $-q_1/q_2 = 1/3$. (from [61])

2.4 Other models of colloidal gelation with competing interactions

There are a few other examples of colloidal gelation with competing interactions other than oppositely-charged binary gels, but which exhibit some similar properties and are worth mentioning.

A related system is a two-species system where one species is attractive, and the other species is repulsive, as studied experimentally by Mohraz *et al.* in Urbana-Champaign, using silica particles where one species was made attractive by coating with hydrophobic n-octayldimethylchlorosilane [44]. This 'biphasic' mixture formed a gel, but only the attractive particles participated in the gel network, while the repulsive particles remained free and diffusive. The presence of those repulsive particles changed the structure of the gel of attractive particles, however, reducing the bond number and making the gel more homogeneous and tenuous than those formed in the absence of the repulsive particles (Fig. 2.12a) – Mohraz *et al.* suggested that the repulsive particles frustrated the gel formation, preventing the evolution of a more heterogeneous structure [44].

Interesting structural changes can also be acheived with a single-species system where interactions are no longer isotropic; Del Gado in Zürich with Kob in Montpellier used molecular dynamics simulations to study a system of spheres with 'sticky points' and with a three-body interaction term making small bond angles energetically costly [13, 12]. This system formed a percolated network in the absence of phase separation [13]. There was furthermore a marked difference in structure between systems which were slowly cooled and those which underwent a fast quench to low temperature: when quenched rapidly, the structure was more highly connected and locally dense than when slowly cooled (to the extent that not all simulations ended in a percolated gel, but rather in a collection of dense clusters). This is in direct contrast to the typical behavior of istropically attractive gels, which are more space-filling for deeper quenches [12], as discussed in Section 2.2.4.

Another patchy-particle model was recently studied by Roldán-Vargas *et al.* in Rome: they used Monte Carlo and molecular dynamics simulations to investigate a binary mixture with one particle species (A) having four attractive patches, and the second species (B) only one: thus the A particles alone formed a gel network, but this network formation was frustrated by the presence of B particles which blocked the A bonding sites [56, 57]. The system parameters were chosen such that the A gel was entropically favored, while AB bonds

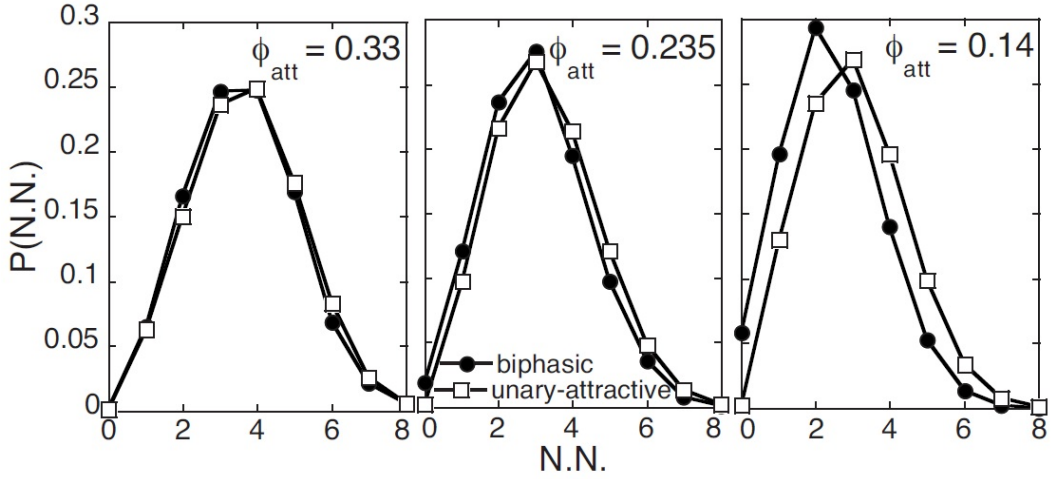

(a)

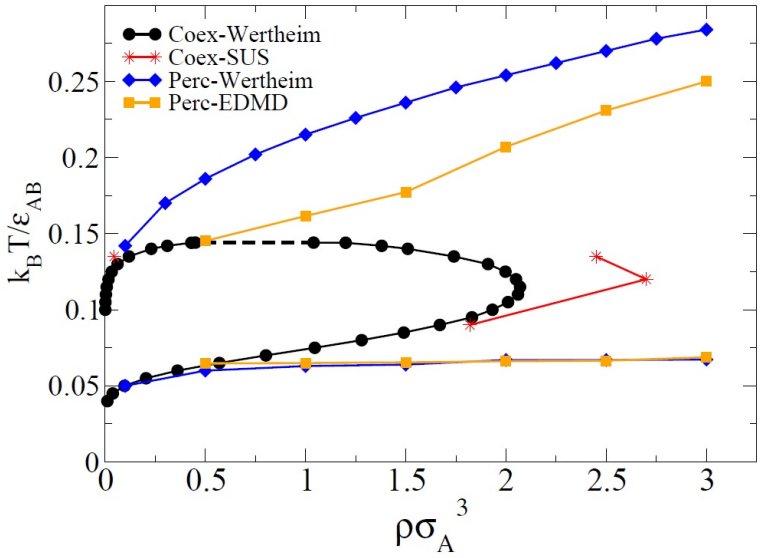

(b)

Figure 2.12: Phase behavior and structure of gels with other competing interactions. a) Probability distribution of the number of interparticle bonds per particle, for gels assembled from biphasic ($\phi_{total} = 0.47$) and unary ($\phi_{repulsive} = 0$) systems. (from [44]) b) Two dimensional cut of the phase diagram showing temperature versus total number density for a fixed composition $x_A = 0.2$. The black dots are the coexistence points according to Wertheim's theory. the figure also shows those coexisting points computed by successive umbrella sampling for $T = 0.09, 0.12, 0.135\ \epsilon_{AB}/k_B$ (red stars). Black and red solid lines connecting the points are guides for the eye. The black dashed line is a guide to the eye to connect the two branches of the Wertheim's coexistence region. Also included are the (upper and lower) percolation lines as obtained by Wertheim's theory (blue diamonds connected by solid lines) and those obtained from molecular dynamics simulations (orange squares connected by solid lines). (from [57])

were energetically favored. Indeed, they found a *re-entrant gel*, where in a given density range, the gel formed only at intermediate temperatures, while at low temperature, the gel fragmented into a fluid of energetically preferred 'flower' structures consisting of an A particle saturated by four bonded B particles (Fig. 2.12b; the 'coexistence' region represents separation into, typically, a percolated gel phase and a B-rich fluid phase) [56, 57].

2.5 Some ideas about crystals

We now turn from non-equilibrium arrested gels to equilibrium crystals. Here, colloidal particles serve as a model, which we seek to use to understand the nature of atomic and molecular crystals as well. There are, of course, books on crystals in the hundreds if not thousands, with knowledge gained over centuries, and I can hardly even scratch the surface. This section then will address just two particular topics which are most directly relevant to my project on colloidal Wigner crystals.

2.5.1 Melting criteria

Let me consider first the idea of melting. Though it may seem simple at first glance, the nature of crystal melting as a thermodynamic phase transition is not fully understood. Free-energy calculations will pin down under what conditions the crystal or the fluid is more stable, that is, where in the phase diagram a crystal will melt, but say nothing about *how* the crystal melts – how the transition proceeds from a solid with long-range order and localized particles to a disordered, mobile fluid.

One of the earliest and most often-cited criteria for melting is the so-called Lindemann criterion, named for Frederick Lindemann, who proposed in 1910 (though I have, to my disappointment, not been able to access the original paper) that a crystal would melt when the fluctuations of an atom or molecule about its average position exceeded about 10% of the spacing between nearest neighbors. The intuitive picture here is that the crystal 'shakes itself apart'. Experiments show a good correlation, with the critical 'Lindemann parameter', the fluctuation lengthscale normalized by the lattice spacing, varying slightly from about 7% to about 11% for various metals. Yet this is only a correlation; it does not, in the end, explain the mechanism of melting. Furthermore, the critical value of $\approx 10\%$ seems to be purely empirical.

It was nearly thirty years before Max Born – better remembered today for his role in the

development of quantum mechanics – took up the problem of melting in his 1939 paper [5]; he cites several other formulae and theories developed in the intervening years, though most of those have since fallen out of favor (or at least out of common language). Born states that the nature of the melting transition is the *loss of stability under shear stress*; that is, a crystal melts because a shear perturbation becomes energetically *favorable* relative to the undeformed lattice. Born calculates the free energy of a lattice of atoms with a homogeneous deformation, which is quadratic in the strain components; the coefficient of the quadratic terms in the shear strains gives the elastic constant c_{44}. According to Born, then, the melting transition is defined by the point at which $c_{44} = 0$ [5].

The value of c_{44} is, of course, determined by the particular structure of the lattice; the nature and form of the interaction between the atoms or components of the crystal; the pressure (which determines the lattice constant); and the temperature. Born proceeds to calculate explicitly the melting transition for the particular case of atoms on a b.c.c. lattice (considering only interactions with nearest-neighbors) and interacting via a two-body Lennard-Jones potential; as he remarks, this was a sightly unfortunate choice as the b.c.c. lattice with these approximations is actually unstable to a different perturbation, but the results concerning shear stability are interesting nonetheless. Born finds that c_{44} is not a single-valued function of temperature (Fig. 2.13a); he identifies the region of temperature where c_{44} takes on multiple values as at best metastable or overheated, and determines that the equilibrium value of c_{44} will jump by a finite discontinuity at melting [5].

Born explicitly neglects any surface effects [5] – his calculations are relevant to homogeneous bulk melting of the crystal. It turns out to be quite a challenge to melt a crystal homogeneously, or, indeed, to freeze a liquid via homogeneous nucleation: these phase transitions tend to proceed from surfaces, interfaces or defects. Thus melting is almost never so elegant as to see an entire crystal lose its stability to shear and fall apart at once; rather the melting front propagates through the crystal, with atoms or molecules successively joining the growing fluid phase. Bulk 'Born melting' is a difficult phenomenon to study, with only a few examples I am aware of.

A final melting criterion I shall mention – not because I employ it myself, but because it has come up several times in the relevant literature – is that of Hansen and Verlet, proposed another thirty years after Born in their 1969 paper calculating the phase transitions of a Lennard-Jones fluid [21]. They relate the behavior of the Lennard-Jones system to that of a hard-sphere system, and suggest a universal "law" that crystallization occurs when the max-

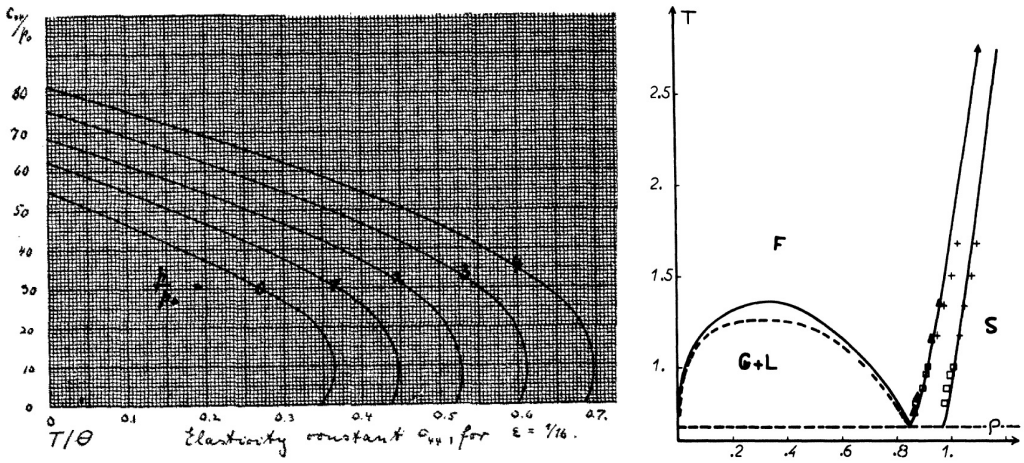

(a) (b)

Figure 2.13: Classical melting criteria for crystals. a) Elastic constant c_{44} as a function of temperature T/Θ for different hydrostatic pressures. (The parameter ϵ is the value of a particular integral which Born was unable to calculate; here he used the estimate $\epsilon = 1/16$, and he notes that it was later numerically calculated to be $\epsilon = 2.15/16$.) Born identifies the region where c_{44} is not single-valued as at best metastable, 'overheated' states. (from [5]) b) Coexistence curve for the Lennard-Jones system. The solid line gives the theoretical results of Hansen and Verlet. The broken line gives an experimental argon liquid-gas coexistence line; the circles experimental argon melting data; and the crosses further experimental data. The triangles indicate the rystallization densities according to the "law" stating that crystallisation occurs whenever $S(k_0)$ reaches the value 2.85. (from [21])

imum value of the structure factor in the fluid, $S(k_0)$, exceeds the value 2.85 [21]. Roughly speaking, this maximum value indicates the weight of the most prominent periodicity in the system; for a completely disordered system with no periodicity, the structure factor will be flat, while it will approach a series of delta functions for a perfectly periodic system. Thus a growing value of $S(k_0)$ indicates the formation of periodicity or order. This criterion works well for structure factors calculated in their paper, as well as, they note, experimental work with argon [21], and it has been cited in the decades since as a good correlation. Yet like the Lindemann parameter, it is more of a correlation than a causation, and while the value 2.85 can be computed for hard-spheres, it is still more phenomenological than a fundamental parameter of the theory.

2.5.2 Preferred crystal structures

The most common simple crystal structures (found e.g. in pure metals) are body-centeredcubic (b.c.c.) and face-centered cubic (f.c.c.), as discussed in Section 1.4. As you will see, both of these structures are of interest in colloidal crystals, as is the discussion of their relative

stability. As with crystal melting, there is a good deal here which is well developed and also much which is still not fully understood. I will mention here one general-theory paper which touches on the question, which question will rise again in the colloidal-crystal context.

Quite a few metals exhibit a b.c.c. phase at intermediate temperatures and an f.c.c. phase at lower temperatures, begging the question of what controls the crystalline phase. Alexander and McTague at UCLA use a mean-field theory to estimate the difference in free energy between an isotropic liquid and a periodically perturbed structure, and find that at the lowest order, the symmetry group of the b.c.c. structures means that fluctuations contribute to the free energy, while those in the f.c.c. structure do not, so that the b.c.c. phase is entropically favorable [1]. Other phases such as f.c.c. may become more favorable by the contribution of higher-order terms, governed by specific interparticle forces. Yet the b.c.c. phase is chosen as the most 'natural' crystalline phase, and when the freezing transition is not too strongly first-order, the b.c.c. phase will be favored near melting. This sheds light on the observation that for some metals, the b.c.c. phase forms initially on freezing even though it is only metastable with respect to the f.c.c. phase [1]. Indeed, it has been found that the b.c.c. lattice has a lower nucleation barrier than the f.c.c. lattice for the r^{-12} Lennard-Jones potential often used to simulate atomic interactions, even when the f.c.c. lattice is more stable [47]. Thus the general picture is that symmetry and entropy favor the b.c.c. phase generally, so that the b.c.c. phase will often be metastable if not stable, and that the f.c.c. phase requires energetic contributions to be stable.

2.6 Colloidal crystals

With this brief introduction to general ideas – which will reappear – I will now turn to colloidal crystals, and discuss the past work understanding this models.

2.6.1 Born melting in colloidal crystals

Although my main focus will be on the next section on charged-sphere colloidal crystals, there is one result which is too beautiful to leave out. I started off my project hoping to study Born's paradigm for melting in colloidal Wigner crystals – while I have since moved away from that question to study instead the properties of the crystals themselves, the one experimental realization of colloidal Born melting I am aware of bears mentioning.

Recent experiments by Wang *et al.* in Hong Kong showed the first direct evidence of

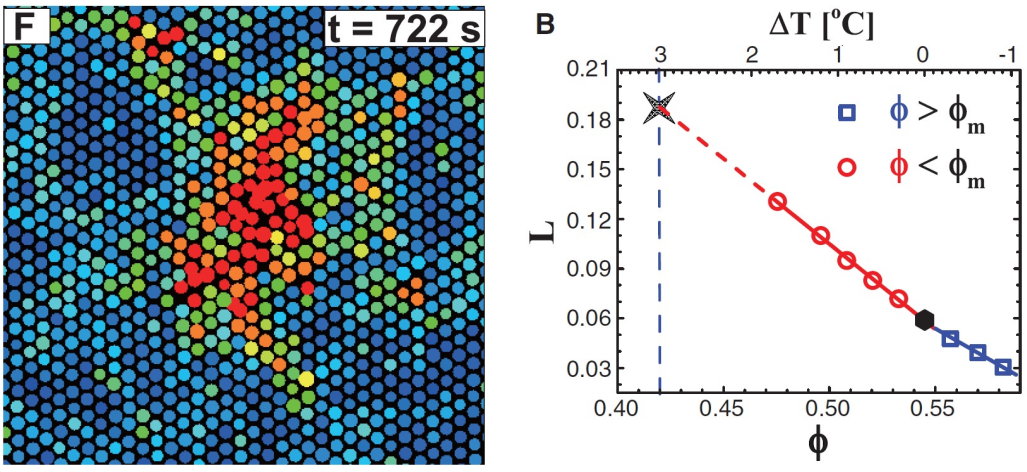

(a) (b)

Figure 2.14: Born melting in colloidal crystals. a) A typical nucleation process at $\phi = 52.0\%$. The heating light was turned on at $t = 0$s. The colors represent different values of the Lindemann parameter. Liquid particles labeled in red are defined by the orientation order parameter. This image shows the liquid nucleus as it reaches critical size. b) The Lindemann parameter is extrapolated to the superheat limit $\phi_s = 42\%$. (both from [79])

Born melting in a 3D bulk system. They used thermosenstive NIPA microgel particles; local heating in a small region inside a bulk crystal, using light, decreased the effective volume fraction of the particles and induced melting, away from any interfaces. Wang *et al.* observed rearrangements of particles in the lattice, followed by formation of liquid nuclei surrounded by regions of 'hot' particles with large Lindemann parameter (see Fig. 2.14a) [79]; measurements of the critical radius for the nuclei matched free-energy predictions. Below a superheat limit of volume fraction, the entire region melted catastrophically, consistent with the Born picture of melting, and also with the Lindemann criterion (Fig. 2.14b) [79].

2.6.2 Charged-sphere colloidal crystals

Many colloid scientists are most familiar with hard-sphere, or nearly-hard-sphere, colloidal crystals, which form at volume fractions $\phi \gtrsim 0.494$, with the particles nearly in contact. I shall here consider, however, the colloidal crystals formed by charged particles, in which repulsive interactions drive crystallization at lower volume fractions.

Experimental phase diagram in aqueous solutions

The first determination of the *structure* of a low volume fraction colloidal crystal was made by Williams and Crandall in Princeton; they measured the Bragg reflection angles of a

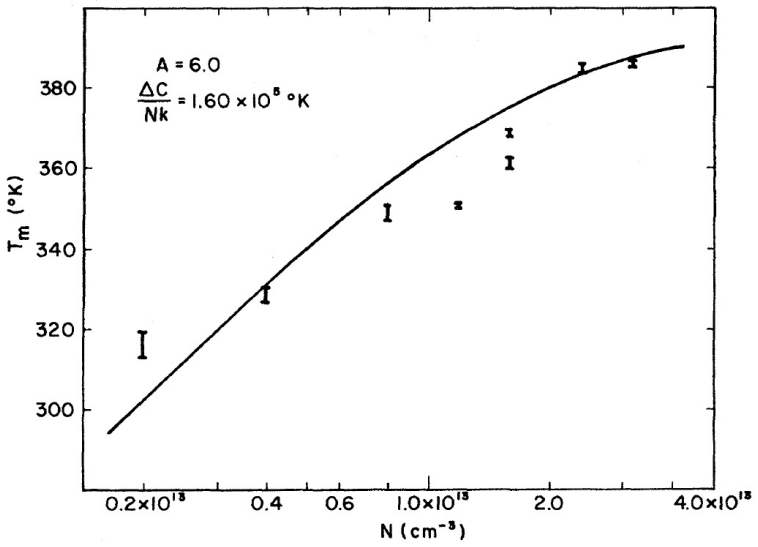

Figure 2.15: Melting temperature, T_m, as a function of the particle concentration. The vertical error bars indicate the temperature range over which melting took place. (from [86])

visible-wavelength laser off crystals of 100nm-diameter polystyrene spheres in deionized water, and from the scattering angles deduced that the crystalline structure was b.c.c. at volume fractions as low as 0.10%, with a mixture of f.c.c. crystals at higher volume fractions ($0.50 - 1.0\%$). These crystals were destroyed by the addition of salt, leading Williams and Crandall to identify the Coulomb repulsion as essential to the ordering, and to draw the parallel to the electron Wigner crystal [85]. In follow-up experiments, they determined the melting temperature of these colloidal crystals as a function of volume fraction, comparing their result to a simple free-energy model predicting the functional form of the scaling (Fig. 2.15) [86].

Similar experiments were carried out by Cotter and Clark in Boulder about a decade later, using an almost identical system, but here allowing annealing of the crystals over months, over which time a density gradient developed in the sample (probably driven by gravitational settling) so that b.c.c. crystals were observed in coexistence with a colloidal fluid, separated by a sharp interface [9]. Cotter and Clark used light-scattering to measure the full structure factor $S(q,t)$, in both the liquid and the crystal phases, and to study the longitudinal fluctuations in both phases; their most interesting results actually regarded the liquid phase [9].

In both of these sets of experiments, the samples were deionized quite thoroughly, yielding long screening lengths, in order to observe any ordering at such low volume fractions; the

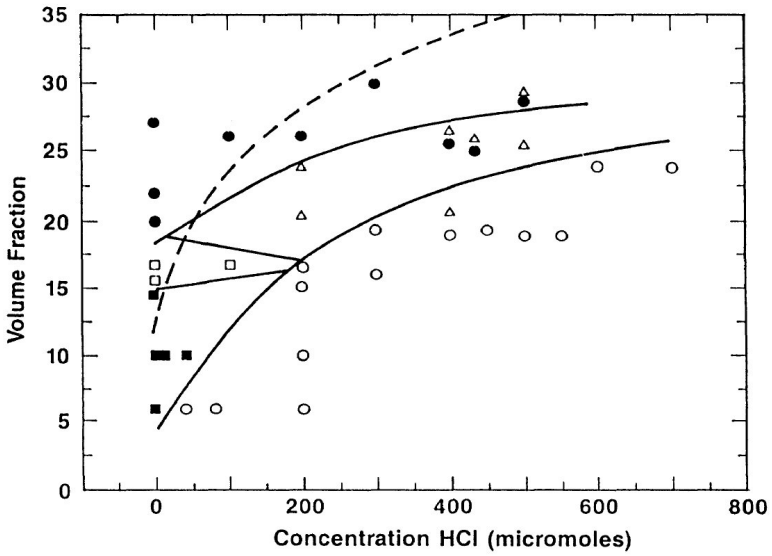

Figure 2.16: Phase diagram for polystyrene spheres as a function of concentration ϕ and electrolyte concentration C_{HCl}. Solid squares, bcc crystal; open triangles, fcc crystal; open squares, fcc+bcc coexistence; closed circles, glass; open circles, liquid. Solid lines are "guide to the eye" phase boundaries. Dashed line is the fcc-liquid theoretical phase boundary for a similar point-charge Yukawa system. (from [67])

phase was determined only by volume fraction. At somewhat higher volume fractions, the crystals remain stable even with the addition of small amounts of salt, as found by Sirota *et al.* at Exxon shortly later [67]. These experiments used slightly smaller polystyrene spheres, about 90nm-diameter, in a slightly different solvent, a mixture of methanol and water, and used x-ray scattering instead of visible light-scattering to determine the structures; the major difference, however, was the addition of HCl to explore a two-dimensional phase diagram in both volume fraction and, effectively, screening length (Fig. 2.16) [67]. They reproduced the b.c.c. phase at the longest screening lengths (little or no added HCl) and low volume fractions, with again a coexistence with an f.c.c. phase at higher volume fractions. Decreasing the screening length narrowed the range of volume fractions at which b.c.c. phases were observed, until the b.c.c. phase disappeared and only the f.c.c. phase was observed at higher salt concentrations [67].

Sirota *et al.* also explicitly discussed both the Lindemann and Hansen-Verlet criteria for the liquid-solid transition. They found the Lindemann parameter near the melting curve to be $\delta_L \approx 0.17$, *larger* than the usual Lindemann criterion of $\delta_{L,c} \approx 0.10$; they still claim that 'the Lindmann [criterion] ... [seems] to be obeyed', in that although the critical value of δ_L is larger, it is constant along the melting curve. The Hansen-Verlet criterion is also met, in that the peak of $S(q)$ is less than 2.8 for all fluid samples [67].

Although Sirota *et al.* draw comparisons between their experiments and simulations using a screened-Coulomb potential [34, 54], they find only qualitative rather than quantitative agreement, and note that at these moderate volume fractions, when the proximity of particle surfaces affects the effective charge calculations and stiffens the potential [67].

Material properties in aqueous solution

Crandall and Williams continued their work to make the first measurements of not only the phase, but the material properties of colloidal Wigner crystals. They noted that the gravitational pressure due to the slight mismatch in density between polystyrene and water ($\Delta\rho \approx 0.5 g/cm^3$) itself causes a variation in the lattice constant with height within a given sample, the lattice at the bottom of the sample being compressed to have a smaller lattice constant relative to the lattice at the top. Young's modulus Y is determined from the magnitude of the variation in lattice constant with height by a simple elastic equation, $e = NV_{particle}\rho_{eff}g\Delta z/Y$. Crandall and Williams used Bragg scattering to measure the lattice constant as a function of height for samples at several volume fractions in the b.c.c. phase, in both water and in heavy (deuterated) water, in which $\Delta\rho$ became negative, and determined Young's modulus as a function of volume fraction (Fig. 2.17a). They found Y to be small – about 1 dyne/cm^2, or 100 mPa – in line with order-of-magnitude estimates; to increase with particle density N as expected; and to be larger than the modulus of an ideal gas at the same number density by about an order of magnitude, demonstrating the importance of the Coulomb repulsion in determining the elasticity of the crystal [10]. They argue that the small value of Y compared to metallic crystals is due mainly to the much lower particle number density; the interaction strengths between particles in the colloidal crystal and atoms in a metallic crystal are actually not much different [10].

The shear modulus of a similar system was measured some five years later by Lindsay and Chaikin at UCLA. In their 1982 paper, Lindsay and Chaikin describe elegant experiments to measure the shear modulus of a suspension, from the resonant frequencies of an rotating bobbin which drives standing shear modes in the crystal [39]. They vary the particle volume fraction, finding the by now familiar b.c.c. crystals at lower volume fraction and f.c.c. at higher volume fraction, with shear modulus increasing with volume fraction (Fig. 2.17b). They also vary the added salt concentration; the addition of HCl decreases the shear modulus, with a discontinuous drop to zero as the crystal melts (Fig. 2.17c), indicating a first-order transition. They interpret their results in the context of a Debye-Hückel

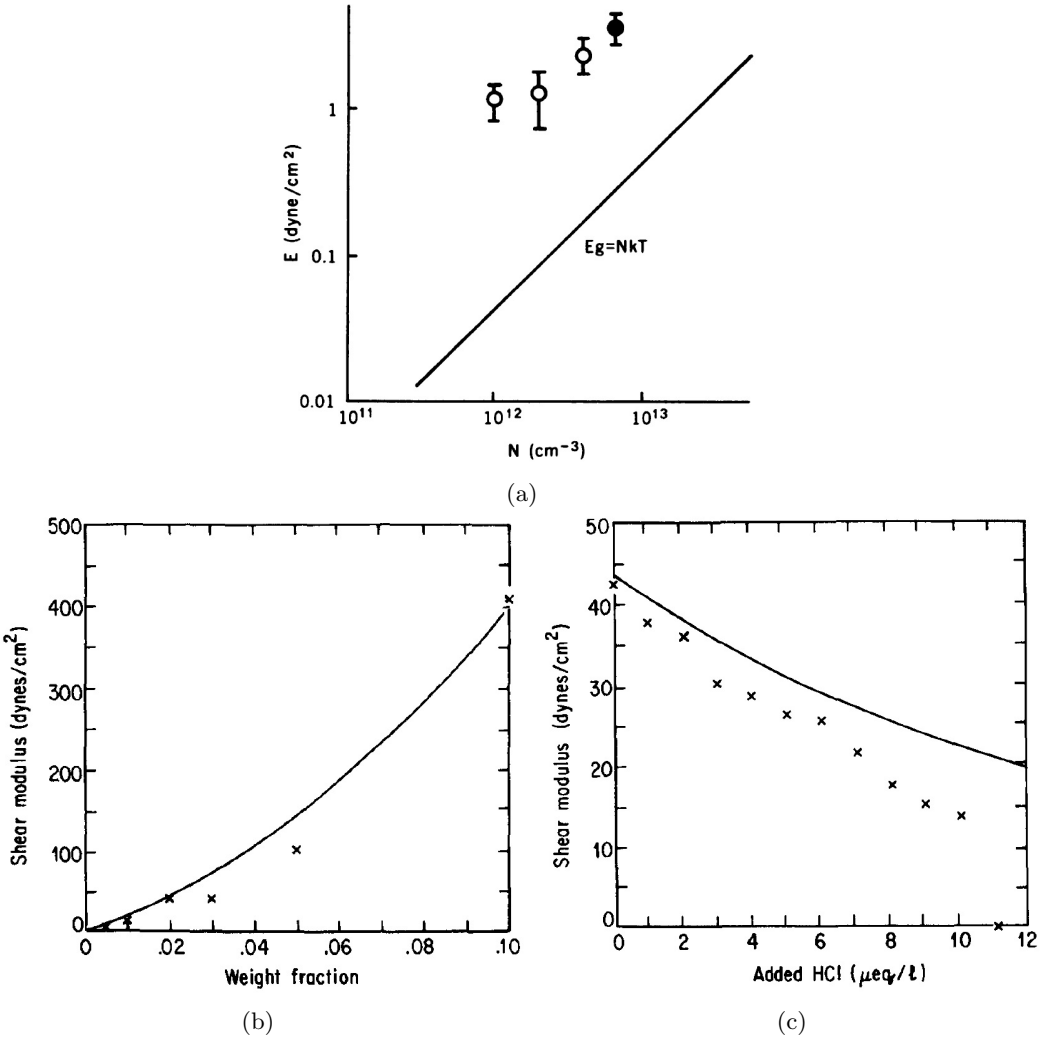

Figure 2.17: Elastic moduli of Wigner crystals. a) Young's modulus, Y, as a function of N. The points are the measured values of Y in H_2O (open circles) and D_2O (filled circles). The error bars refer to different measurements on the same sample. The solid line shows E_g, the elastic modulus for an ideal gas at room temperature. (from [10]) b) Shear modulus of deionized latices of 0.109 μm spheres as a function of weight fraction. c) Shear modulus of a sample of 0.109 μm spheres, $n = 2.8 \times 10^{13}$ particles/cm^3, $\phi = 0.02$, as a function of HCL concentration. (b,c from [39])

or screened-Coulomb model, and find qualitative agreement, but quantitative inaccuracies at higher volume fractions [39].

At the same time, indirect measurements of the elastic constants were made by Hurd *et al.* in Colorado Boulder, by inferring lattice dynamics from the intensity autocorrelations of scattered light. These experiments were carried out on slightly larger particles, some 230nm in diameter, at a single volume fraction of 0.5%, in a thin sample cell; fits to the autocorrelation curves yielded estimates of the spring constants between nearest- and next-nearest-neighbors (k_1 and k_2, respectively). From these spring constants were calculated the crystalline elastic constants, $c_{11} = \frac{3}{2}\frac{k_1+3k_2}{R_0} = 6.96$ dyne/cm^2, and $c_{12} = c_{44} = \frac{3}{2}\frac{k_1}{R_0} = 2.43$ dyne/cm^2 [23]. Young's modulus, calculated from c_{11} and c_{12}, is $Y = 6.08$ dyne/cm^2 [23]. These values are similar to those found by Crandall and Williams (for Y) and Linday and Chaikin (c_{44} is at the lower end of the range of G' which they measured, but this is consistent with a correspondingly low number density). Hurd *et al.* state that these results demonstrate the elastic anisotropy of the lattice [23].

Theory and simulations

The phase-diagram experiments of Sirota *et al.* were carried out in collaboration with simulations by colleagues at Exxon, using molecular dynamics to study a screened-Coulomb or Yukawa system [34, 54]. Where the experimental tuning parameters were salt concentration and volume fraction, the simulations considered the phase diagram in, roughly speaking, screening length and temperature.[2]

The simulated phase diagram is, as mentioned, qualitatively similar to the experimental results: at low temperature and long screening lengths, the b.c.c. phase is the most stable, while f.c.c. is preferred at shorter screening lengths; increasing the temperature will melt either crystalline phase (Fig. 2.18a) [34, 54]. Note that the region of stability of the b.c.c. phase increases with temperature; this means that for $2 \lesssim \lambda \lesssim 5$, an f.c.c. phase at low temperature will transform to b.c.c. at higher temperature before melting, behavior mimicking that of many elemental metals [34, 54]. The melting transition is found to be strongly first-order, with a latent heat around 0.6-0.8kT_m [54].

[2]In fact, the dimensionless quantity $\lambda \equiv \kappa n^{1/3}$ gives the natural lengthscale determined by the volume fraction expressed in units of the screening length; small λ means the screening length is long compared to the interparticle spacing, while large λ means the screening length is comparatively short. The relation between the experimental and theoretical parameters is very roughly $\lambda \propto C_{HCl}$. The dimensionless temperature is scaled by both a measure of the interaction strength, and some factors of λ. The relation between experimental volume fraction at fixed temperature, and theoretical temperature at fixed volume fraction, is less clear, but essentially, low volume fraction corresponds to high temperature.

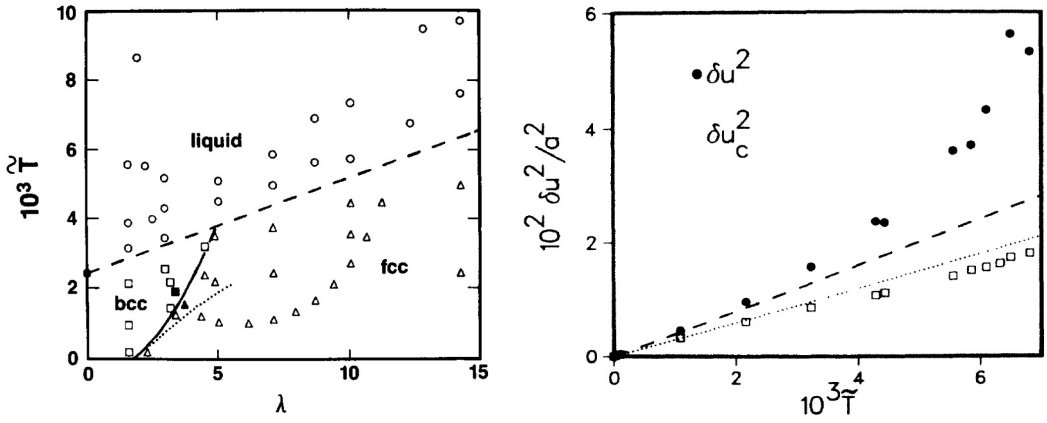

(a) (b)

Figure 2.18: a) The phase diagram of Yukawa systems. Open circles indicate points where the liquid phase is stable. Points where the fcc and bcc phase are stable are indicated by triangles and squares, respectively. The solid square and triangle indicate cases that crystallized from the melt. The dashed line separating liquid and solid phases indicates the value of $\widetilde{T}$ where the rms displacement reached 19% of $a \equiv \rho^{-1/3}$. The dotted line is the harmonic result for the bcc to fcc phase transition, and the solid line interpolates our MD results for this transition. (from [54]) b) The variation of $\langle \delta u^2/a^2 \rangle$ and the displacement relative to nearest neighbors δu_c^2 with $\widetilde{T}$, for $\lambda = 5$. The dashed and dotted lines show the respective quantities in the harmonic approximation. (from [34])

The melting line is qualitatively consistent with the melting criteria of both Lindemann and Hansen-Verlet, although the critical values are quantitatively different. In the case of the Hansen-Verlet criterion, which states that the peak value of $S(q)$ is constant at melting, Robbins *et al.* find that this holds true, but suggest a slightly larger value for that critical value of $S(q)$: 3.0 instead of Hansen-Verlet's 2.85 [54]. The Lindemann criterion puts the melting line at a critical value of the root-mean-square displacement in units of the nearest-neighbor spacing; again, the simulations find that this criterion is met, with a critical value of $\langle \delta u^2 \rangle^{1/2}/\rho^{-1/3} \approx 0.19$, as shown by the dashed line in Fig. 2.18a [34, 54]. This is larger than the usual Lindemann criterion $\delta_L \approx 0.10$, which the authors ascribe to the anharmonicity of the potential [34, 54].

While the Lindemann parameter, determined by the displacements of single particles from their average positions, grows large, the authors find that the displacement of a particle relative to its nearest neighbors is limited to smaller values (Fig. 2.18b) [34]. This suggests *collective motion* of particles with their neighbors, which may enable the large fluctuations manifested in the large value of the critical Lindemann parameter [34, 54].

Robbins *et al.* also use lattice dynamics calculations to consider the elastic constants (obtained from the sound velocities evaluated from the phonon spectrum). Their tabulated

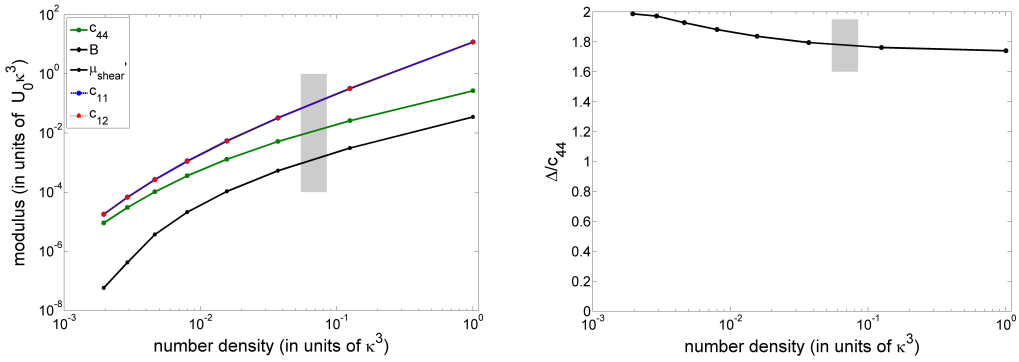

(a) (b)

Figure 2.19: a) Elastic constants and b) Δ/c_{44} as a function of volume fraction for a Yukawa system in the b.c.c. phase, from values given in Table III of [54]. Values for K, c_{11}, c_{12}, c_{44}, and Δ/c_{44} were given as a function of $\lambda = \kappa a$ and normalized by U_0/a^3 ($a = \rho^{-1/3}$); I have fixed κ and U_0 constant and scaled the x-axis as $n \propto \lambda^{-3}$ and the y-axis as $\mu * \lambda^{-3}$, in order to be able to plot the results in more familiar form. $\mu'_{\rm shear}$ is calculated as $\frac{1}{2}(c_{11} - c_{12})$. The grey box shows the approximate range of volume fractions for my experimental system, assuming $\kappa \approx 1(\mu\text{m})^{-1}$.

results are shown in Fig. 2.19 [54]. These results show that generally $B \approx c_{11} \approx c_{12}$; c_{44} varies from about $1/2$ c_{11} at large λ (short screening length or small volume fraction) to almost two orders of magnitude smaller than c_{11} at $\lambda = 1$ (screening length equal to typical particle spacing). The shear modulus along the (110) plane is $\mu'_{\rm shear} = 1/2(c_{11} - c_{12})$; Robbins *et al.* compare the two shear moduli via the quantity $\Delta/c_{44} \equiv (2c_{44} - (c_{11} - c_{12}))/c_{44}$, which takes on a maximum value of 2 when $\mu'_{\rm shear} \ll c_{44}$, while $\Delta = 0$ corresponds to an *isotropic* shear modulus. Robbins *et al.* find that Δ/c_{44} varies from very nearly its maximum value of 2 at large lambda, where $\mu'_{\rm shear}$ is more than two orders of magnitude smaller than c_{44}, to a still-large value of 1.74 when $\mu'_{\rm shear}$ is slightly more than 10% of c_{44} at $\lambda = 1$ – thus in all cases, the simulated crystal is strongly anisotropic [54].

As somewhat of an aside, but an interesting one, Robbins *et al.* also give an interesting discussion of the contributions to the stability of the two crystalline phases, and the nature of the f.c.c. to b.c.c. transition. In the f.c.c. crystal, shear stability is provided by nearest-neighbor interactions. In the b.c.c. crystal, in contrast, nearest-neighbor 'bonds' form square structures which are not stable to shear; stability requires next-nearest-neighbor interactions [54]. Because these next-nearest-neighbor interactions are relatively weaker, the shear modes in the b.c.c. crystal are softer (lower energy) than those in the f.c.c. crystal, giving the b.c.c. crystal a higher entropy, at all screening lengths. This higher entropy enhances the stability of the b.c.c. crystal relative to the f.c.c. crystal, as discussed by Alexander *et*

al. [1, 34, 54] At shorter screening lengths, however, the next-nearest-neighbor interactions become too weak to support shear in the b.c.c. crystal, and only the f.c.c. phase is stable [54]; the f.c.c. crystal is also energetically favored when nearest-neighbor interactions dominate, as the nearest-neighbor distance is longer than that in a b.c.c. crystal at the same volume fraction, and so the repulsive energy is smaller [34]. The overall picture is that the entropic considerations of the soft shear modes permitted by the b.c.c. structure are important to its stability.

In nonpolar solvents

The experiments described so far were carried out in aqueous solvents with high dielectric constant, in order to easily obtain strong charging; as discussed in Section 2.1.1, this limits the screening length to $1/\kappa \lesssim 1\mu$m, and typically much smaller. Thus in order to study systems where the screening length is on the order of the particle size, we are typically limited to submicroscopic particles which are difficult to image directly; all of these experiments were carried out using scattering (or bulk mechanical measurements). In order to directly visualize individual particles in a system with similar behavior, we move to nonpolar solvents, where longer screening lengths are possible (as described in Section 2.1.2).

The first work I am aware of studying low volume fraction colloidal crystals in nonpolar solvents using direct imaging is that of Yethiraj and van Blaaderen in Utrecht in 2003. Their system is quite familiar to many colloid physicists: PMMA particles in a density-matched solvent mixture of decalin and either cyclohexyl or cycloheptyl bromide, with added tetrabutylammonium chloride (TBAC) salt to control the screening length, and imaged using confocal microscopy. They observed fluid, b.c.c., and f.c.c. phases as in the simulated and aqueous systems, along with a random-close-packed (r.c.p.) phase in the nearly-hard-sphere regime (Fig. 2.20); in particular, at $\kappa R \approx 2$, they reproduce the fluid-to-b.c.c.-to-f.c.c. phase sequence [87]. Further work on the system by Royall *et al.* from the same group examines the fluid-f.c.c. transition at $\kappa\sigma \approx 5$ in more detail and in company with Monte Carlo simulations, finding f.c.c. crystals down to volume fractions of $\eta = 0.101$, but did not access the b.c.c. regime [59]. Royall *et al.* also estimated the spring constants of particles in their potential wells from fluctuations over time for one sample, the first step in the direction of studying the material properties [59].

Leunissen and van Blaaderen in Utrecht used a very similar system (without added salt), and compressed the suspension dynamically using an 'eletric bottle' – in a high-frequency

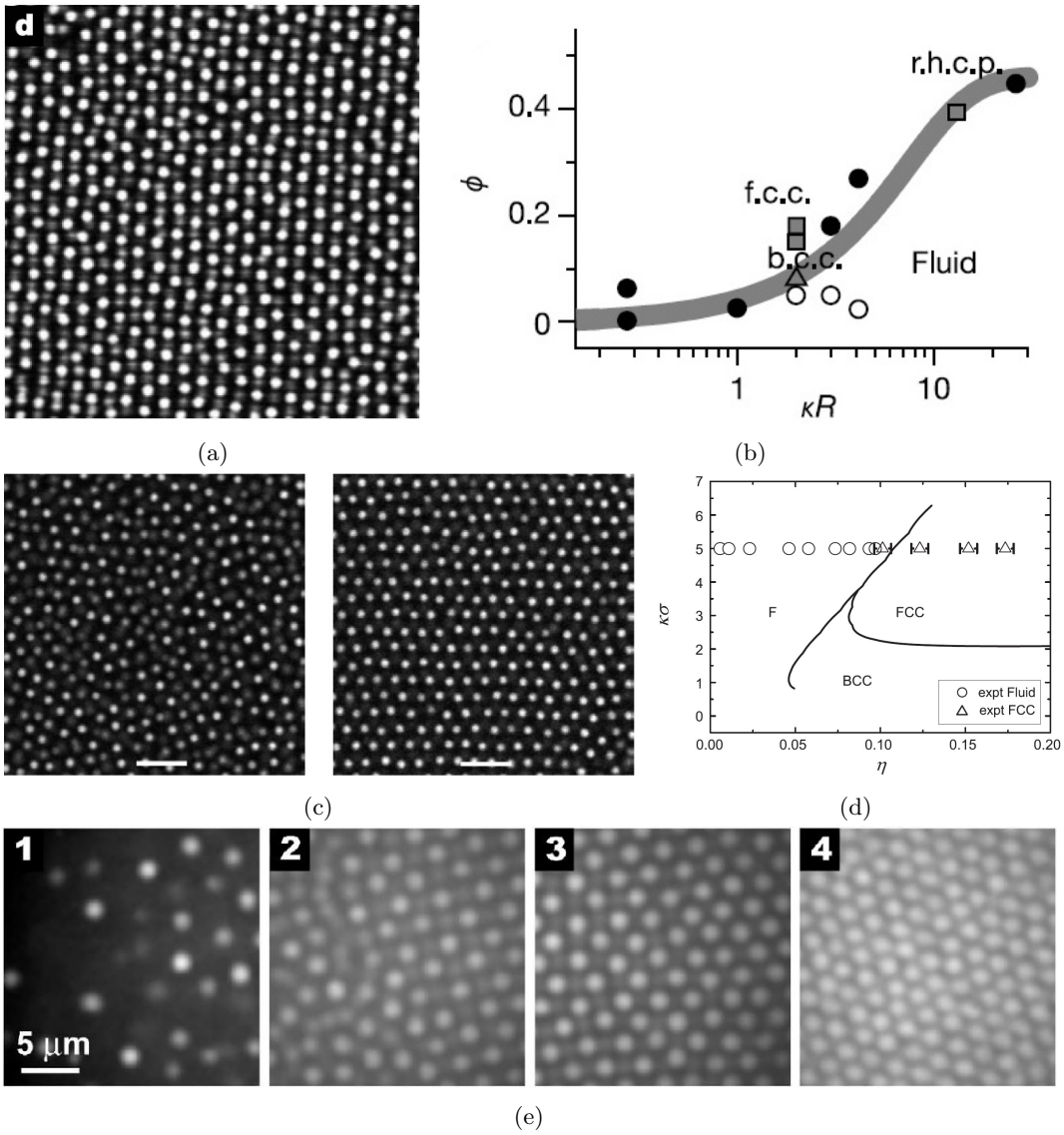

Figure 2.20: Confocal images and phase diagrams for colloidal Wigner crystals in nonpolar solvents. a) x-y confocal image of (110) face (not a hexagonal plane) of b.c.c. crystal. b) Phase diagram as function of softness, κR. The grey triangle (b.c.c.) and squares (f.c.c.) are data for 1-μm spheres in cycloheptyl bromide-*cis*-decalin; (pure and at $c = 260\mu$M); the circles are for 2-μm spheres in cyclohexyl bromide-*cis*-decalin, pure and $c =$ 10-260μM. Open circles are fluid and closed circles are solid close to fluid-solid coexistence. Thick grey line is our best estimate of the phase boundary. (a,b from [87]) c) Confocal images of 2 μm NBD-PMMA spheres in density-matched CHB-decalin mixtures at $\eta = 0.094$ (left) and $\eta = 0.101$ (right). Scale bars are 10 μm. d) Experimental results mapped onto the theoretical phase diagram, for $\beta\varepsilon = 140$. F is fluid, FCC and BCC are face- and body-centereed cubic crystals respectively. The black circles and triangles denote experimental fluids and FCC crystals. (c,d from [59]) e) Confocal microscopy images of a soft-sphere suspension in the electric bottle, after compression for 336 h at $V_{rms} = 21.2$V. The numbers correspond to different positions along the particle-density profile, which approximately were at the slit edge (1) and 200 μm (2), 500 μm (3), and 800 μm (4) into the electrode-free slit. (from [36])

AC electric field gradient, dielectrophoretic forces drove the particles to regions of low field, so that the particle volume fraction was increased. They obtained two different screening lengths in slightly different systems, accessing both a fluid-r.h.c.p. transition, and a fluid-b.c.c. transition for $\kappa\sigma \approx 1.2$, exhibiting large b.c.c. crystals at volume fractions down to $\phi \approx 0.15$ (Fig. 2.20e) [36].

Recent work carried out primarily by Kanai *et al.* in my own group, considered a similar system, of PMMA particles in a solvent mixture this time of decalin and tetrachloroethylene, with aerosol-OT (AOT) added as a screening agent. As in the aqueous systems and simulation, they observed a fluid crystallizing into a b.c.c. phase at low volume fraction, depending on the screening length (here crystals were observed down to $\phi \approx 0.09$), with a transition to an f.c.c. phase at shorter screening lengths. They also found, however, a markedly different behavior at the lowest AOT concentrations – that is, the longest screening lengths – where they found reentrant melting. This behavior is explained by the dual nature of the AOT micelles, as described in Section 2.1.2, which both determine the ionic strength and so the screening length in the solution, and also allow the charging of the particles themselves; at the lowest AOT concentrations, the particle charge is small, and the interactions are too weak to drive crystallization [28]. I wish I could show Kanai *et al.*'s phase diagram, but while I am happy to cite the results, it is hardly appropriate that someone else's unpublished data should appear for the first time in my thesis, and so you will have to wait for Kanai *et al.*'s paper to be published.

Further work on this system has been done by Joris Sprakel, whose project was the jumping-off point for my own. Sprakel fixed the AOT concentration and took a detailed cut along the volume fraction axis of the phase diagram, and began studying not only the phase behavior, but the detailed properties of the crystals. He found that the average Lindemann parameter in the crystals exceeded the usual critical value, and identified a population of 'hot' particles, those which demonstrated particularly large displacements, and which formed clusters which grew as the system approached the melting transition. He also determined the shear modulus G' and the elastic constant c_{44} (from spring constant estimates), and saw an abrupt drop in these quantities at the melting transition [68]. Sprakel's observations informed my own interest in this system, and gave me a starting point from which to study different aspects of the structure and properties.

Chapter 3

Experimental Methods

At its most interesting and inspirational, physics is an abstraction from a real-world physical system to a simplified description which captures the essentials without getting stuck in the gory details. Yet the experiments themselves do depend on those gory details, and in the end, the tests of physics cannot escape from them. This chapter, therefore, covers most of the experimental details. I will lay out how I carried out the experiments which are analyzed in later chapters, some challenges I came across, and tricks I learned. The chapter is broadly separated into two sections: the first on the details of the sample preparation, and the second on the details of data collection, mainly using the confocal microscope.

3.1 Sample preparation

While the two threads of my doctoral research – one on binary gels, and one on crystals – are quite different in the abstracted physics, they largely come together in the experimental details. In both cases, micron-scale polymer particles were charged via a polyelectrolyte brush grown from the particle surface, and suspended in a solvent with added electrolyte to control the charge screening. We chose a solvent mixture both to match the mass density of the particles (to minimize the effect of gravity), and to approximately match the index of refraction of the particles (to minimize scattering, thereby improving image quality). I prepared closed samples with fixed parameters, such as volume fraction, which were allowed to equilibrate before collecting data, primarily using the confocal microscope.

I will describe the nature of the particles in more detail; the solvent preparation; the process of density-matching; and the preparation of closed samples.

3.1.1 Particles

I have used two distinct systems in my research: a binary system of oppositely charged particles in a polar solvent, and a one-species system of negatively-charged particles in a nonpolar solvent.

The first system is the binary system used to study the gelation of oppositely charged particles. The synthesis of these particles must be entirely credited to Tom Kodger, my academic 'elder brother': Tom, along with Joris Sprakel and Rodrigo Guerra, developed and refined the synthesis technique over many trials to attain admirable control over particle size and charge, and Tom synthesized the particular particle batch I used. Since none of this is my own work, I will not describe the synthesis in detail, but will give here a brief summary of the synthesis protocol and a description of the resulting particles; a more thorough treatment by Tom *et al.* of the process and more information on the chemistry involved is forthcoming [32].

The particle synthesis occured in three steps. The first step was the synthesis of neutral, monodisperse seed particles. In the second step, a single batch of seed particles was split in half; each half was differently charged by growing a polyelectrolyte brush from the surface, carrying either a positive or a negative charge. Finally, in the third step, each species was fluorescently dyed to enable visualization in the confocal microscope, using distinct fluorophores to color-code the two species.

The seed particles consisted of a random copolymer of trifluoro ethyl methacrylate (FEMA) and tert-butyl methacrylate (tBMA). The molar ratio of monomers was chosen to tune the mass density and the index of refraction of the particles. The initial particle synthesis was carried out by *dispersion polymerization*: a chemical initiator seeded the polymerization of polymer molecules, which collapsed into a dense particle after reaching a critical length determined by the solvent conditions; a stabilizer (here, polyvinylpyrrolidone (PVP)) was adsorbed on the surface of these particles to sterically stabilize them against aggregation. Polymerization took on the order of a day at elevated temperature (about 55°C). The solvent was a mixture of water and methanol; the ratio of these two solvents determined the size of the final particles. Also included in the polymer chains was a small fraction of initiator-monomer, or 'inimer', a molecule similar to the methacrylate monomers, so that it was included in the polymer chain, but with an active group which, crucially, acted as an initiator in the next step of polyelectrolyte growth. The result of this first polymerization

step was a suspension of monodisperse, stabilized, uncharged polymer particles of about 2μm diameter.

In the second step, this initial seed batch was split in two, and each portion was given a distinct charge by growing a polyelectrolyte brush from the surface. Using the same seed batch for both charged species ensured that the size distribution and mass density of the two particle species would be identical. The polyelectrolyte brush was again a random copolymer, this time of a neutral monomer (N,N-dimethylacrylamide), and a charged monomer (one of sodium 2-acrylamido-2-methyl-1-propanesulfonate (negative), or 3-acrylamidopropyl-trimethylammonium chloride (positive)); the molar ratio of the neutral and charged monomers helped determine the magnitude of the final particle surface charge. Both of these charge groups are quite strong (acid and base, respectively), so that the charge is constant over a large range of pH. Polymerization proceeded from the 'inimer' groups present on the particle surface, which acted as anchors for the new polymer; copper then catalyzed an *atom-transfer radical polymerization (ATRP)* reaction, successively adding monomers to the polymer chain. The reaction time (here about 20 minutes) controlled the size of the polymers, and so the magnitude of the particle charge; it was critical that the reaction conditions for the two species were much the same in order to achieve equal charge magnitudes. On completion of this step, each particle had a polyelectrolyte brush a few nanometers thick covalently bound to the particle.

The final step was to dye the particles. A boron-dipyrromethene (BODIPY)-class fluorescent dye was introduced into the particles: the dye was dissolved in carbon tetrachloride and emulsified, and this emulsion combined with the particle solution. The carbon tetrachloride swelled the particles, introducing the dye molecules into the particles. After several days, the carbon tetrachloride was evaporated – as the dyes have low solubility in water or other polar solvents, they remained trapped inside the particles. Two different dyes were used, one for the negatively charged particles, and another for the positively charged particles, with different excitation and emission spectra, so that the particle type could be distinguished by the fluorescence color alone.

After each of these three steps, the particles were filtered through a coffee filter, and glass wool if available, to remove chunks of particles which may have aggregated; the remaining particles, at the end of the synthesis, were monodisperse, relatively uniformly charged (positively or negatively) by a polyelectrolyte brush, and fluorescently dyed. They were also easily index- and density-matched to a solvent mixture as described in the next section.

The second system I used was of a single species of negatively-charged particles in nonpolar solvents. These particles were synthesized by Jeroen Appel of University of Wageningen. The particles were composed of polymethylmethacrylate (PMMA), with a polymer brush of polyhydroxystearic acid (PHSA), and again fluorescently dyed to be readily visible; like the binary system, they were quite monodisperse, and index- and density-matched to a solvent mixture. They were very similar to the particles synthesized by Andrew Schofield, which have been used extensively in the literature over the past decades (e.g. in many of the results discussed in Chapter 2).

3.1.2 Storage, cleaning, and solvent preparation

Of course, the particles themselves were not the only ingredient for our experiments; the solvent in which they were suspended was also important. Several steps of cleaning and solvent preparation were therefore needed.

First a brief note on the storage of particles. For the tBMA/FEMA particles, we found it best to store them in water or in a water/methanol mixture. The particles are quite stable in these solvents, whereas we have seen evidence of a slow degradation in the experimental solvent of formamide/sulfolane (described below), resulting in loss of charge. For similar reasons, the PMMA particles should not be stored in a solvent containing tetrachloroethylene, although this is used in the experiments. Finally, to minimize bleaching of the fluorescent dye, it is encouraged to store the particles in a dark place (e.g. in a drawer), although these particles are quite bright and so this is probably not critical for storage times on the order of at least months.

I will refer repeatedly to 'washing' particles in a solvent. This indicates centrifuging the particles to sediment them, and pouring off the supernatant, then resuspending the particles in the fresh solvent, usually replacing about $^2/_3$-$^3/_4$ of the volume with each wash. Centrifugation in storage solvents (water/methanol for the tBMA/FEMA, or decalin for the PMMA) can often be done at about $1000g$ for 10 minutes or thereabouts, as the density difference is large. For tBMA/FEMA particles being washed in formamide, the difference is smaller, and sedimenting may require up to $3000g$ for 2 hours.

I learned to be quite conservative about resuspending particles. In the early days, I would cheerfully use the vortexer to quickly resuspend a sediment. As time went on and I became more and more concerned about degradation of the brushes, I would resuspend

particles by tumbling them slowly on a rotating wheel, for hours or sometimes a day. In reality, this was probably overly conservative, and I expect the particles would do just fine being vortexed more often.

To have as clean a system as possible, I treated the solvents before use. In the case of the tBMA/FEMA particles, the chosen solvent was a mixture of formamide and sulfolane, with sodium chloride (NaCl) added as an indifferent electrolyte. Sulfolane is actually solid at room temperature, so I would heat the sulfolane gently to melt it, and mix it with formamide at a ratio of 90% sulfolane to 10% formamide, adequate for the mixture to remain liquid. To this bottle, and to a bottle of some hundreds of mL of plain formamide, I would add ion-exchange resins, to deionize the solvent, and 4Å molecular sieves, to remove water. I would allow these each to sit for some days, and then pass the solvents through a syringe filter to obtain clean, deionized solvents; these I would store in closed tubes covered in aluminum foil to protect them from light-induced degradation. I would prepare a vial of formamide with NaCl added to a concentration of 1M.

I washed each particle species several times in water/methanol to remove any traces of excess reactants from the synthesis process; washed several times in untreated formamide; and then washed 3-4 times in deionized and filtered formamide. I then split each particle batch in two; to half of each species, I would add the 90% sulfolane / 10% formamide mixture, and to the other, formamide with NaCl, until the solvent for each stock was density-matched to the particles (this is elaborated in the next section). I ended with four particle solutions: for each particle species (positive and negative), a solution in a mixture of deionized formamide/sulfolane, and a solution in formamide with added NaCl. These solutions could be mixed at will to obtain the desired salt concentration and ratio of positive/negative particles.

For the PMMA particles, the solvent choice was a mixture of decalin and tetrachloroethylene (t.c.e.), with aerosol-OT (AOT) surfactant added as a charging agent and screening electrolyte. In some experiments I used a mixture of cis- and trans-decalin, while for others I used pure cis-decalin. Because these organic solvents tend to dissolve many plastics, I did not filter the solvents before use, and was careful to use only glass vials and pipettes to handle them. I would prepare a vial of a few tens of mL of each solvent, and add AOT to a concentration of 10mM. After dissolving the AOT by tumbling the vials overnight, I would add 4Å molecular sieves to capture water, and store these vials in a dark drawer.

I would wash the particles several times in untreated mixed decalin to remove any syn-

thesis reactants. I would then suspend them in a roughly 6:5 mixture of decalin/t.c.e. with added AOT, and tumble them slowly in an oven at 40-65°C for a few hours; this heating allowed the t.c.e. to swell into the particles, which are slightly soluble in t.c.e. I repeated this wash in the decalin/t.c.e. mixture 2-3 times, heating each time; resuspsend a final time without heating; and then add decalin or t.c.e. as necessary to density-match the solvent.

In both systems, there was a small population of clumps comprising two or more particles which had adhered during the synthesis or storage. In order to filter these out, I would, before adding the second solvent to density-match, centrifuge the solution briefly, e.g. at $3000g$ (for the tBMA/FEMA in formamide) or $1000g$ (for the PMMA in decalin, with a larger density difference) for about 30s. This is not long enough to sediment single particles significantly, but would preferentially sediment the larger clumps, concentrating these impurities into the lower portion of the vial, which would often appear as a thin layer of 'sludge.' I would then recover the bulk of the solution, discarding the concentrated portion at the bottom, thus filtering out many of the impurities. Two or three repetitions of this process would noticeably improve the monodispersity of my particles, although, as you will see, I was never able to fully remove the impurities.

3.1.3 Density matching

An important aspect of my experiments was carefully matching the mass densities of particles and solvents, so that the particles would not settle under gravity. Gravitational stresses and pressure gradients can significantly change the structure of particle gels [65], and so it was desirable to avoid them as much as possible.

This density-matching was achieved by carefully tuning the ratios of the two solvents used in the mixture (formamide and sulfolane in one case, and decalin and tce in the other). Simple calculations give a reasonable guess of the density-matching ratio, but 1) it is difficult to precisely realize this ratio, especially when the particles are not dry, and 2) the ideal ratio turned out to be slightly different from this estimate, due to effects such as tce swelling the PMMA particles. Thus the density-match was realized phenomenologically by successively adding small amounts of one solvent or another until the desired density was achieved.

How to determine if the solvent density was indeed that desired? Checking the density match was done by centrifuging the solution, speeding up the settling or creaming of the particles. The basic outline of the density-matching process was thus to centrifuge, starting

with perhaps half an hour at $1000g$; if the particles sedimented, then I would add more of the heavier solvent (90% sulfolane; formamide with NaCl; or tce), while if they creamed, I would add the lighter solvent (formamide or decalin). I would then centrifuge again and repeat. If the particles did not seem either to sediment or to cream, I would increase the speed or the time of centrifugation, until the final density match was checked by centrifuing at $4500g$ for 4 hours. As I progressed, I could also make rough estimates of the quantities of solvent to add based on the magnitude of the change due to previous additions, until the final steps of density-matching involved the addition of only one or a few drops of solvent.

There are some tricks to the details of this process. A key observation is that the density match depends fairly sensitively on temperature. The thermal coefficients of expansion of the particles and of the solvent are different, with the solvent having a larger coefficient, so that its density changes faster with temperature than that of the particles. Thus by increasing the temperature, the solvent expands and becomes relatively less dense than the particles so that the particles sediment, while by decreasing the temperature, the solvent becomes relatively more dense and the particles will cream.

Thus it is essential that the temperature of the centrifuge during density-matching be chosen such that the particles will be density-matched under the experimental conditions. Note that if the temperature sensor in the centrifuge is not well calibrated, the setting may not be identical with the actual temperature, so take care in choosing the setting. For my experiments, I used a centrifuge temperature of 23°C at the sample (the 'air' setting produced different results), which worked well.

For the tBMA/FEMA system, I encountered a second and more interesting challenge. As I have mentioned, one of the tuning parameters I used in this system was the concentration of NaCl. It turns out that – and this is no surprise – the addition of NaCl increases the mass density of the solution, and can do so quite significantly. The particles were density-matched in a mixture of either 82% formamide / 18% sulfolane, *or* formamide with about 420mM added NaCl. The experimental range of salt concentrations was mainly 100mM-150mM, that is, mixing about one part of formamide with added NaCl with two to three parts of formamide/sulfolane.

But the mixing introduced the complication that the mass densities did not combine linearly: that is, although the two stocks were matched to the same density, the interactions between the sulfolane and the NaCl changed the density of the mixture, generally to be slightly lighter than either stock. Indeed the density of the mixture varied with the pro-

portions, so that if the system were well density-matched at 100mM, the particles would sediment slightly at 150mM mixed using the same stocks.

In truth, in most of the reported experiments, the particle stocks were density-matched, and this variation of the mixture was not taken into account. I shall still describe the process I developed for improving the density-match. The robust way around this issue would have been to carefully density-match each salt concentration independently – this would have been an enormous hassle, and not even remotely worthwhile. I thus chose that the density match should be around 120mM of NaCl, where the behavior of the system was most interesting, and near the middle of my experimental range. I then had to density-match the NaCl-only and sulfolane-only stocks at a slightly higher temperature, that is, to tune their density so that the solvents were slightly too heavy at room temperature, giving the appropriate density of the mixture.

In deciphering the degree of density change during mixing, I developed an even more precise method of determining the quality of the density match than simple centrifugation. I loaded a small amount of solution into a sample cell, and allowed it to equilibrate for an hour or so. I then collected 3D images on the confocal microscope, and I ran a very cursory particle-location analysis. By histogramming the z-positions of the particles in the sample, I obtained a measure of the density match, and in particular an estimate of the gravitational height ($h_0 = \left((\Delta\rho)Vg/k_BT\right)^{-1}$, as defined in Section 1.1.1). The goal is that $h_0 \to \infty$.

A representative example of the gravitational height as a function of salt concentration, mixing a NaCl-only stock and a sulfolane-only stock, is given in Figure 3.1. Checking this gravitational height gave the best measure of the quality of the density-match, and, as with centrifugation, permitted successive refinements of the density match by addition of solvent.

3.1.4 Volume fraction determination

There was one last step in preparing the particle solutions before they were quite ready for experiments, and that is getting the density-matched particles to the desired volume fraction. I always density-matched at low volume fraction, to ensure that I would have extra solvent and be able to prepare samples at different volume fractions.

I would concentrate the particles by sedimenting them in the centrifuge at typically 35°C and 4500g for 4 hours – recall from the density-matching discussion that changing the temperature changes the density-match, so that this increase of 10-12 degrees broke the

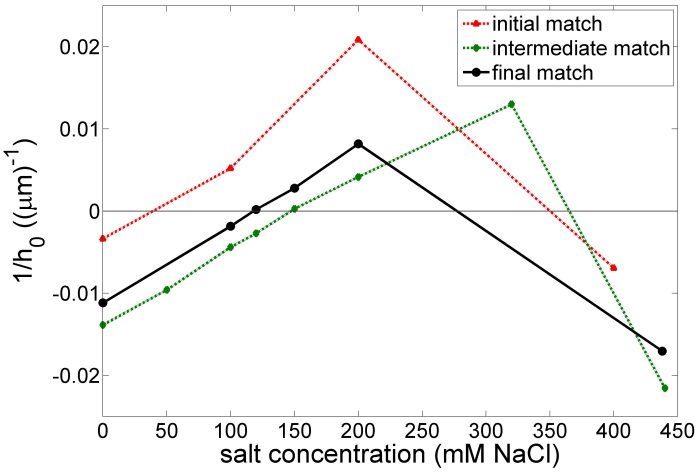

Figure 3.1: Dependence of gravitational height on salt concentration for tBMA/FEMA particles in formamide/sulfolane mixtures. Solvents at 0mM salt are a mixture of formamide and sulfolane; solvents at the highest salt concentration shown for each curve are NaCl dissolved in formamide (with no sulfolane); and intermediate points are obtained by mixing the stocks at these two extremes. Inverse gravitational height is obtained as the coefficient in an exponential fit of particle density with height in the sample (so that $P(h) \propto \exp(-h/h_0)$), determined by locating particles in a 3D confocal image, and is proportional to the density difference between particles and solvent; zero inverse gravitational height corresponds to a perfect density match. Curves are shown at several iterations of density-matching; the final match is chosen as optimal for $1/h_0 \approx 0$ at $c = 120$mM. Lines are given as guides to the eye.

density match and allowed the particles to sediment. I would then extract the bulk of the supernatant, storing this as the density-matched solvent, and resuspend the particles in the remaining supernatant (generally about the same volume as I had of particle sediment, as all of my experiments were at volume fractions well under 30%).

For the tBMA/FEMA particles, I cared less about the precise volume fraction, and more that all four of my stocks were at the same volume fraction around 20%. I would thus prepare a sample of each stock, gather confocal data, and use again a cursory particle-location to count the number of particles in a standard imaging volume. I would add the appropriate amount of solvent to each stock to try to achieve the volume fraction of the least concentrated stock, and repeat this successively until all stocks were at the same volume fraction, within the counting error.

For the PMMA particles, I was interested in the specific range of volume fractions bracketing the transition between b.c.c. crystals and fluid. I determined approximately where this boundary was in the first few experiments I did by trial and error, until I had a reasonable estimate of the volume fraction. For later experiments, for which the data is

reported, I would thus prepare two stocks, at the boundaries of the range of interest. I would set aside a small amount of more concentrated particles, and split the remaining stock in two. For each stock, I would repeat the procedure described above of counting particles, and adding either solvent or concentrated particles to eventually home in on the desired volume fractions, one above and one below the volume fraction of crystallization.

3.1.5 Sample preparation

The preparation steps so far gave density-matched particle stocks at roughly known volume fraction, ready for experiments. It remains of course to vary the volume fraction of our particles, prepare different mixtures of salt concentrations or positive/negative particles, and to move our particles from the stock vials into sample cells suitable for confocal microscopy.

My standard sample cell was easily fabricated from a 22mm×50mm microscope slide and three 18mm×18mm 1-½ thickness (150 μm) microscope cover slips. The slide provided a rigid base for the sample. Two coverslips were adhered to the slide, with a gap of around 0.5cm between them, using Norland optical glue.[1] The third coverslip was then glued over the first two, spanning the gap.[2] The glue was cured under a UV lamp for 5-6 minutes to set. I never observed any indication of the solvents interacting with the cured optical glue.

It was important that the sample cells be clean. My cleaning protocol was to immerse the cells in a 3% solution of Helmanex in water for an hour or more, and then to rinse several times with deionized water. The effect of washing is shown in Fig. 3.2.

For the tBMA/FEMA system, the sample cells were also coated with a polyelectrolyte layer, to prevent the particles from sticking to the surfaces. The cells were immersed for an hour or more in a 1-2% solution of polyethylene oxide (PEO; molecular weight $1,000,000$), with a few drops of hydrochloric acid added to decrease the pH; rinsed several more times with deionized water; and finally dried, first using a compressed-gas 'duster', and then in a 65°C oven overnight.

I varied three parameters in the binary gel experiments: each sample was prepared with a specific NaCl salt concentration, total particle volume fraction, and mixing ratio between negatively charged and positively charged particles. These mixtures were obtained

[1] I generally used either Norland 81 or 68, loading the glue into a syringe and using a thin needle to apply 7-8 drops to the slide, then gently dropping the coverslip over the drop; the weight of the coverslip combined with capillary forces in most cases spread the glue over the entire underside of the coverslip.

[2] For this coverslip, I applied three small drops of glue on the edge of each lower coverslip, and dropped the third coverslip gently over them.

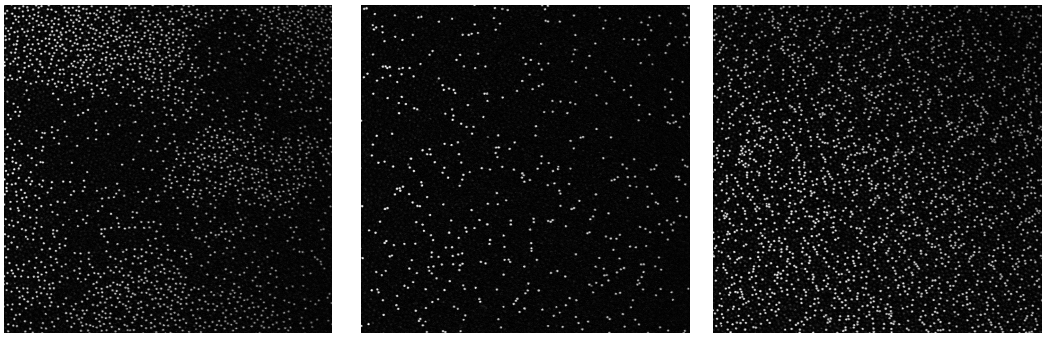

(a) (b) (c)

Figure 3.2: Effect of sample cell cleaning treatment. a) Layer of PMMA particles at the lower coverslip of a sample cell with no cleaning treatment; note that the layer is quite heterogeneous. b) Layer of PMMA particles at the coverslip of a sample cell which has been washed with Helmanex and water, then dried; note that fewer particles stick and the layer is more uniform. c) Layer of PMMA particles at the coverslip of a sample cell which has been washed with Helmanex, water, and isopropanol, then dried; note again that the layer is quite uniform, although more dense than in (b). All images are 230μm $\times$ 230μm.

by mixing together eight different stock solutions: for each of the positively and negatively charged particles, I had particle stocks with sulfolane only and with added NaCl; and for each of these four particle stocks, a corresponding particle-free solvent. The preparation was done by successively combining pairs of stocks to determine first salt concentration and then total particle volume fraction, and then finally mixing the positively and negatively charged particles together. That is, for each particle species, I would first mix the two particle stocks in proportion to obtain the desired salt concentration, as well as mixing the corresponding particle-free solvents in the same proportion. I would briefly vortex each of these four mixtures to ensure full mixing. I would then use the mixed solvent to dilute out the particle stock to the desired volume fraction, vortexing again, for each of the two particle species. Finally, I would mix small amounts (total 100μL) of the positively charged and negatively charged particles, always adding the minority type to the majority type, and vortexing a final time to fully intermix the particle species.

It was best to load and seal the samples as quickly as possible, to which end I would prepare the sealing epoxy immediately before loading the sample cells. To close the sample cells, I used DevCon 5-minute epoxy, which comes in two parts to be mixed in a 1:1 ratio, air-curing in a few minutes after mixing. I would thus mix the two components together and then proceed with sample loading.

I exploited capillary forces to load the samples, simply using a pipettor to slowly release the solution at one entrance to the channel of the sample cell and allowing the capillary

force to pull the solution fully into the channel. It was important to load slowly to prevent the introduction of small air bubbles. 25 μL was more than adequate to fill a sample cell. I would then use a Kimwipe to gently and quickly wipe away excess solution from the outside of the sample cell, to improve the bonding of the epoxy to the glass.

I would then seal the cell, using a thin wooden applicator first to cover one end of the channel, then wiping away any solvent from the second end before covering it with epoxy as well. I would extend the epoxy seal along the edge of the uppermost coverslip to ensure a complete sealing. Even with great care, some samples did not seal completely.

This sealant was not entirely ideal – while it seemed to perform well over the short periods of the experiment, samples left for a few weeks would exhibit peeling away of the epoxy from the glass, eventually breaking the seal and allowing the solution to evaporate. It was, however, adequate for the experiments.

After preparation, I would allow the sample to equilibrate for about one day before collecting images on the confocal microscope.

The process for the PMMA samples was similar, and somewhat simpler. No coating was needed on the sample cells; I cleaned the sample cells using Helmanex as already described, and after rinsing several times with deionized water, rinsed several more with isopropanol, in order to remove any water from the system. I then dried in the 65°C oven as already described before loading the samples.

For the PMMA system, volume fraction was my sole tuning parameter. I would mix evenly-spaced combinations of my high-volume-fraction and low-volume-fraction stocks to obtain a range of volume fractions, e.g. 13 different volume fractions. Generally I would mix larger amounts of one to three benchmarks (e.g. 1:3 ratio, 1:1 ratio, and 3:1 ratio), and then use these intermediate stocks to generate the more finely-spaced volume fractions.

I loaded the samples in the same way, being careful to use a glass pipettor. Again I used the 5-minute epoxy as a sealant, mixed immediately before loading – I would often use two applicators and both hands to attempt to close off both ends of the sample at once, to minimize flow of the epoxy into the sample chamber, which appeared to be a greater issue with this system than with the formamide/sulfolane system. A masters student in the group from before my time had found that this 5-minute epoxy had some interaction with decalin [45]; my experience has been that samples would remain well-sealed for over a year, although I cannot rule out small amounts of the epoxy dissolving into the decalin.

I was more careful in the storage and equilibration of these samples, as I expected the

soft crystals I was studying to be more fragile to external disturbances than the binary gels. I was thus careful to store the samples in the orientation on which they would go onto the microscope, i.e. cover-slips down, in the same room as the microscope, so that they equilibrated at the experimental temperature (one of my fellow students, Rodrigo Guerra, had made measurements of the temperature stability in the room and found it to be quite good). I stored the samples in a box, to provide a dark environment and prevent either light-induced degradation or photobleaching.

The question of equilibration time for the Wigner crystal samples is, unfortunately, a tricky one, to which I have not yet come up with a satisfying answer. At my most enthusiastic, I would collect data on the same samples after one day, two days, four days, six days, eight days, etc. I did see changes over this time, not only in that some samples took up to two weeks to crystallize, but also in the dynamics of the fluid samples. I do therefore suspect some change over time of the chemical environment in the system – hypotheses include slow reorganization of the charge groups on the surface of the particles due to softening of the particles by the tce solvent, or leaching of charge from the glass or epoxy.

For the data I report, I consider only data collected on the same day for samples which had been prepared on the same day from the same stock solutions. Data collected on a different day or samples prepared on a different day I will treat separately; and of course the preparation of a stock is never precisely identical, so I am not surprised by small variations in, for example, volume fraction of crystallization from one batch to another.

With these sealed and (perhaps) equilibrated samples in hand, it is time to turn to describe the workhorse instrument of my doctoral research, the confocal laser-scanning microscope.

3.2 Confocal microscopy

As briefly described in the introduction, the confocal microscope is a powerful tool for visualizing particles in three dimensions in real time. It is actually fascinating to be able to watch the particles jiggling and dancing about under the microscope, scanning up and down in the sample to fully elucidate the structure instead of only being able to access a two-dimensional system. A full and detailed description of the microscope does not seem appropriate here, but I'll try to give adequate information to operate the microscope.

The microscope I used almost exclusively was a Leica SP5 confocal laser-scanning micro-

scope. The *laser scanning* moniker (in contrast to, for example, a spinning-disk confocal), refers to the scanning of an excitation laser pixel by pixel over the two-dimensional field of view. The laser is aimed along its path by mirrors, which can rapidly change their angle to scan first in the x-direction, and then down a row in the y-direction. The speed with which the microscope can scan is an important component of how quickly data can be obtained. I used the microscope in 'resonant mode' at 8 kHz, the fastest setting available.

Several different lasers can be attached to the microscope to provide different excitation wavelengths; multiple lasers can be used simultaneously, and the choice of which laser(s) to use depends on the excitation spectra of the fluorescent agent(s) used. For the two-colored tBMA/FEMA system, I used two lasers simultaneously: a helium-neon laser at 543nm, and an argon laser at 488nm. For the single-species PMMA system, I used the 543nm laser only.

In the most common use, the scanning laser excites fluorescent dyes – in my case, the dyes in the particles – and it is the emission light, at a different wavelength, which is actually imaged. This emission light travels back through the optics, through a dichroic or multichroic mirror which can be chosen to exclude any reflected laser light, and then is processed by a serious of mirrors and blocks to direct certain chosen wavelengths to one or more photomultiplier tubes (PMTs). The wavelengths collected by the PMTs are selected by the user, and so can be chosen to match the emission spectrum of the fluorescent agents (and excluding the laser wavelength). For the tBMA/FEMA system, I would use the band between 500nm - 525nm to image the yellow (negatively charged) particles, and 555nm - 625nm to image the red (positively charged) particles. The emission spectra of the yellow particles extended far enough that faint images were picked up in the red channel, but at low enough intensity to be easily filtered out. For the PMMA system, I used one PMT on the 555nm - 625nm band.

As with most microscope imaging, the settings on the PMTs were generally optimized to use the full dynamic range without saturating either extreme. Thus I would adjust the gain in each PMT to see the occasional over-exposed pixel in the bright center of particles, and the offset to see the occasional under-exposed pixel in the dark background. The laser power was adjusted coarsely so that the optimum gain fell around 500-600 on this instrument, the range in which my colleagues assured me the response was most linear. A complication was that the solvent was reasonably well but not perfectly index-matched to the particles, so that there was some scattering, and the brightness of the particles decreased the further into the sample I was imaging. The microscope offered compensation for this, allowing the user

to pin the gain at different depths in the sample and then interpolating between these as it scanned. For some data I used this, but I found that it actually slowed scanning down, and so eventually stopped using this feature. I would instead set my gain somewhere near the middle of my intended three-dimensional imaging volume, so that the bottom was slightly over-exposed and the top slightly under-exposed, but never had any indication that these small deviations caused issue in the data analysis.

As mentioned previously, the 'confocal' aspect of the microscope is embodied in the pinhole which restricts both the excitation light and the collected imaging light, giving a tight plane of focus. The size of the pinhole can be controlled, a larger pinhole giving a thicker imaging slice. I would typically use the 'Airy 1' setting for the pinhole, which set the pinhole to optimize for the narrowest focus given diffraction limits, giving a plane of focus about 1μm thick; for some 2D fast timeseries, I would set the pinhole wider by 20% or so to capture particles which were near but slightly out of the narrower plane of focus.

The plane of focus can be moved in the z-direction through the sample in one of two ways: by moving the entire objective turret (the 'z-wide' setting), or by using a galvanometer stage to move the sample itself ('z-galvo' setting). I almost exclusively used the z-galvo, to take advantage of the much faster speed available. The mechanical scanning in z is perhaps the rate-limiting step of imaging using this microscope, and to see dynamics of mobile particles in three dimensions required pushing the microscope almost as fast as it could go.

The confocal microscope can provide several varieties of image 'stacks'. An image of a single plane of focus is generally referred to as an XY slice. If this single plane is imaged repeatedly over time, we have an XYT stack or XYT series, or sometimes just a T series. A collection of images at closely-spaced Z positions constitutes an XYZ stack, or a Z stack. Finally, if such a Z stack is imaged repeatedly over time (that is, the microscope scans through the Z-dimension, returns to the bottom of the imaging volume, and scans through again), then we have an XYZT stack or ZT stack.

I generally worked with a 40x oil-immersion objective lens, which provided adequate zoom that I would be able to get good particle locations from the data. My pixel resolution was essentially set by the requirements of the location algorithm (described in the next chapter) – in order to have > 7 pixels per particle, I generally used 160nm resolution in the x- and y- dimensions for slow single Z-scans, and 200nm resolution in ZT scans with time. Since the z-dimension scans most slowly, I compromised with 210nm (Z-scans) or 250nm (ZT-scans) resolution in z (but see below for a note about the calibration of this resolution).

Image sizes were chosen to compromise between volume and speed. I would use 512 × 512 pixels in XY for slower Z-scans, giving images about 80 μm on a side, and generally scan through 40 μm in Z, corresponding to 191 pixels. For fast ZT-scans, I found that I could push the stack acquisition time below 2s by reducing the image size to 256×128×81 pixels, or roughly 50×25×20 μm. Speed could be further increased by using the 'bidirectional' setting, in which the microscope collected data as it scanned in both directions in X, which required calibrating the phase offset to line up alternate rows with one another; this phase drifted slightly after first turning on the instrument, but settled down after typically half an hour. With these settings, the claimed minimum time possible between images was slightly over 1s. I found that using this minimum setting gave artifacts at the start of each stack, and so would choose timesteps of 2s or, later, 1.5s or 1.1s, but always slightly larger than the claimed minimum.

For a typical experiment, I would mount a sample cell on the microscope, find the coverslip by the first plane at which particles appeared, and collect several stacks, starting 20 or 30 μm into the sample to avoid boundary effects as much as possible. For the binary gel system, the data I used were several (e.g. 8) Z-stacks per sample, at different positions in the sample, and a 10- to 12-minute T-stack, following particles in only 2 dimensions but at 100ms timesteps. For the Wigner crystal system, the key data is in ZT-stacks, typically one or two per sample for 12 minutes.

3.2.1 Calibration of Z pixel size

The microscope software's nominal conversion from pixels to microns along the optical axis (referred to as the z-direction) proved to be unreliable - the first suggestion I noticed of this was a substantial difference in the apparent localization lengths in xy and in z. My colleague Kate Jensen also noticed an error, and investigated more thoroughly, developing a small device with which to calibrate the conversion [27]. Briefly, a square array of dots with a known spacing of 1.63 microns was etched on a glass slide, which was positioned at a 30° angle to the horizontal. The space below this reference was filled with a solvent dyed with fluorescin, allowing imaging of the reference. The spacing of the array in each axis was then used to obtain the calibration [27]. Using this device, I determined the correct conversion factors of 0.1953 microns/pixel (nominal 0.2098) and 0.2276 microns/pixel (nominal 0.2518). The data was somewhat too noisy to obtain a good calibration at the fast scan speeds I

use for my experiments; therefore I carried out the calibration with slower scans at a range of speeds, and extrapolated to the fast speed to obtain my final conversion factor. In the case of a nominal spacing of 0.21 microns/pixel, the actual conversion was independent of scan speed; for the nominal spacing of 0.25 micron/pixel, there was a slight decrease in the conversion value with increasing scan speed.

3.2.2 Upright configuration

Very recently, one more experimental capability has been added to our lab repertoire: the confocal microscope in an upright configuration. The development of this setup is almost entirely due to Tom Kodger; he designed all of the extra parts and helped me set up the system.

In the typical use of the confocal microscope, the direction of gravity and the optical axis are parallel – and in particular, the sample can only be imaged over a small distance along this axis, due to the working distance of the objective lens. Tom saw the use for a system in which these directions were decoupled, allowing observation over a large range of Z. In a non-density-matched system, the gravitational pressure varies with height in the sample, so that sampling at different Z positions corresponds to sampling different values of pressure.

Since we cannot reasonably change the direction of gravity, in order to realize this decoupling, Tom changed the direction of the optical axis. He managed this by inserting a mirror between the objective lens and the rest of the microscope optics, shown in Fig. 3.3 – the mirror is at an angle of 45°, enclosed in the black box to which the objective is immediately attached. The objective is also supported on a lens tube which allows it to be positioned in (gravitationally defined) Z over a wider range.

In order to enable collection of three-dimensional image stacks, we still needed the sample to be able to move rapidly parallel to the optical axis (the motion of the objective turret remains in the gravitational Z-direction); to acheive this, Tom mounted the z-galvo stage on a rigid frame, perpendicular to its usual orientation, so that its direction of motion is parallel to the optical axis of the objective. With a sample on the z-galvo stage, the position of the objective in the perpendicular plane can be controlled using the usual x-axis control, and the lens tube or the z-wide control for the height of the objective; the depth of the plane of focus is controlled coarsely by the 'y-axis' control, and rapidly by the z-galvo stage. This configuration permits us to do most of what we could do in the typical configuration (e.g.

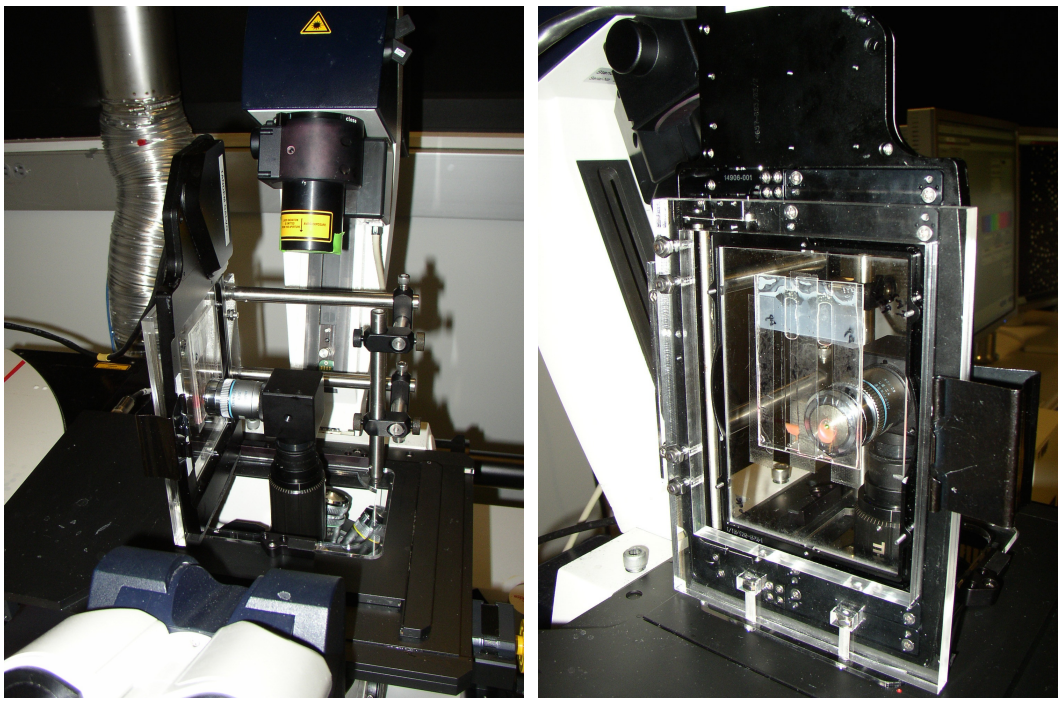

(a) (b)

Figure 3.3: Upright confocal configuration. a) The Leica confocal in the upright configuration. The objective lens can be seen in the center of the image, attached directly to a box containing a mirror set at 45° to the horizontal, and supported on an adjustable lens tube which attaches to the microscope optics. The Z-galvo stage, on the left, is screwed to a plastic frame (seen at better advantage in (b)); the metal posts making up the rest of the frame stabilize the stage. b) View of the same setup from the back of the sample. The wide plastic inset is screwed directly to the Z-galvo stage, and the sample is adhered to this inset with three strips of double-sided tape. The colloidal suspension appears pink due to the fluorescent dye; the objective lens is visible through the transparent sample cell.

XYZT stacks), but enables us to move the objective over about 8mm in Z (more if we use the lens tube) and access different gravitational pressures.

A few notes about this setup. We used a much more viscous immersion oil (Cargille Type B), to encourage the immersion oil to remain between the sample and the objective lens rather than dripping down. This worked well.

The main drawback to this configuration is that Z-stacks cannot be obtained quite so rapidly as in the original configuration. We noticed that when the z-galvo stage is asked to make a large jump (e.g. 20μm) in the plane of focus, it jumps perhaps $^2/_3$ of the way quickly and then slowly relaxes the rest of the way over a couple of seconds. Thus if the time between Z-stacks is set to a minimum, when jumping from the top back to the bottom of the stack, the instrument does not reach its claimed plane of focus before it takes the image, and the Z-stack is substantially compressed. We found the best way to avoid this issue was to leave about 2s additional time between Z-stacks.

It is not clear exactly the source of this issue. The z-galvo may reasonably be unhappy that we are asking it to operate with gravity in a different direction than it was designed for, and with torques on the galvo stage to which it is also unaccustomed. The lag of 2 seconds was observed with the z-calibrator as the sample: between the roughly 90g z-calibrator and the roughly 25g plastic inset, the total weight added to the z-galvo stage was around 115g; it may be that the lag is smaller when the loading is smaller, such as the 50g or so expected for the actual sample. It may also be that hydrodynamics of the viscous immersion oil are damping the motion of the stage.

In any case, drawbacks aside, this configuration allowed for a new type of experiment. I took a sample of the density-matched PMMA system of about a milliliter, and added three drops of dried cis-decalin, to make the solvent just slightly less dense than the particles. This sample was loaded into a sample cell of Tom's making, cut from plastic to be about 7cm tall, 1cm wide, and a few mm in depth, with a coverslip glued on as one surface. A small air gap was left above the sample, and the cell sealed using the same 5-minute DevCon epoxy. This sample was gently centrifuged at $10g$ for about a day and a half, during which the particles sedimented about half the length of the sample, and then left to equilibrate, upright (that is, the 7cm dimension parallel to the direction of gravity), for another roughly two months. The sample was moved onto the confocal microscope in the upright configuration, and left for another 2.5 days to re-equilibrate before data were taken.

3.3 Other instruments

While the majority of my data, and by far the best-analyzed, were from the confocal microscope, I made us of a few other tools, and will briefly describe that data collection.

3.3.1 Rheology

The colloidal gels formed by oppositely charged particles, or 'binary gels', were of course solids, and had in fact measurable elastic moduli. To confirm and explore the bulk solidity of these gels, I also carried out some experiments on an Anton-Paar rheometer, aided by Joris Sprakel.

Again, I will not go into great detail on the workings of a rheometer, but will give a brief description. The rheometer measures the stress-strain relations of a material, that is, how a material deforms in response to stresses. In the geometry I used, a small sample of binary gel was sandwiched in a narrow gap between two plates: one flat, and one with a slight conical shape. The flat plate was fixed, while the conical plate could be rotated, and both its position and the force required to rotate it accurately measured by the rheometer. Rotating the upper plate exerted a shear stress tangentially on the upper surface of the gel; the viscoelastic gel deforms in response to this shear, and the strain, or relative deformation, is measured by the instrument. For an oscillatory stress of a fixed frequency, this response has two components: the in-phase component represents the solid-like elastic response, giving the 'storage modulus' G', while the out-of-phase component represents the liquid-like viscous response, giving the 'loss modulus' G", related to the viscosity η. Generally, a material is considered to be behaving as a solid if $G' > G''$, and as a liquid if $G' < G''$. The moduli can be dependent on the amplitude of the strain (how much the material is being deformed) and on the strain rate (how fast the material has to respond to the stress). For my purposes, the most interesting behavior was at low strain rates, that is, very slow oscillations, where a liquid would have plenty of time to flow, giving a negligible storage modulus, whereas a true solid would sustain a deformation over a long time, giving a finite storage modulus.

To measure the rheological properties of my binary gels, I used a stress-controlled rheometer (Anton Paar MCR 501) in a cone-plate geometry, with an angle of 4° and a 50 mm diameter. This necessitated using 650 μL of gel sample per measurement – a large amount in comparison to the 25 μL per microscopy sample, so that I measured only a few samples using the rheometer. I would mix the sample shortly before loading it into the

geometry, then pipetted the (easily yielding) gel onto the lower plate, then allowed the instrument to slowly lower the upper cone, slowly and freely spinning, to contact the sample and squeeze it to fill the entire gap. I used a solvent trap to minimize evaporation of the solvent: this is essentially a cap which goes around the rod supporting the cone, and a thin layer of silicone oil provides a seal between the trap and the lower support of the instrument.

Having loaded the sample, I applied a large pre-shear, rotating the cone through a large angle, to break up any clusters or networks formed during loading. Reducing the amplitude of this oscillatory shear over two minutes minimized the imposition of a preferred direction into the sample, so that after the ramped pre-shear, the hope is that the sample is essentially homogeneous. I then allowed the system to sit nearly quiescent for 30 minutes in order to allow the gel to form; during this period, I applied a very small oscillation in order to measure the evolution of the elastic moduli, seeing that the storage modulus increased and appeared to plateau. After this equilibration stage, I carried out the reported experiment, a frequency sweep. This sweep holds a fixed, small strain amplitude (0.1%), and varies the frequency of oscillation, measuring G' and G'' at a range of frequencies spanning several decades.

With Joe McDermott, I also used the same instrument to measure the precise viscosity of the decalin/tce density-matched solvent with AOT. For this measurement, we used a Couette geometry: a cylindrical bob inside a cup with a thin gap, to maximize the surface area.

3.3.2 Macroscopic imaging

While the confocal microscope gives beautiful data on the local, single-particle-level structure and dynamics, we also have the potential to learn something from the larger-scale behavior of the samples. I noted early in the Wigner crystal experiments that I could easily see by eye whether a sample was crystalline or disordered: the imperfect index-matching of the particles to the solvent allows for Bragg scattering off crystallites, so that where a disordered system appeared a featureless pink (the coloration due to the dye), a crystallite appeared iridescent, with individual crystallites distinguishable by eye. Based on these most rudimentary observations, I distinguished that the rate of crystallization in the sample cells varied with volume fraction – after a delay of typically a few days, the higher volume fraction samples would crystallize overnight, while the samples at the two lowest volume fractions

showed a transient but long-lasting coexistence between fluid and crystalline regions as they crystallized more slowly. These observations begged for more robust measurements.

With this in mind, I set up a macroscopic imaging system, with a good deal of assistance from Tom Kodger. I adapted a larger version of the single sample cell, with thin spacers cut from coverslips separating 14 separate channels, each of the same aspect as the single sample cells, so that I could image 14 different volume fractions simultaneously. This sample cell was loaded, sealed, and then mounted upright, by taping to a base used for mounting optics elements. I lit the sample from behind and to the side using a very bright LED, with a mirror opposite the LED aimed toward the sample to even the illumination; with some tweaking, this provided enough discrimination between disordered and crystalline regions. I imaged using a simple CCD camera, and verified (using an old, already-crystallized sample) that I could indeed distinguish disordered and crystalline regions on the camera images; set up a Matlab program to capture and save an image every 10 minutes; and left this setup to collected data for some three months. From these images I was able to see the initiation and progression of crystallization at different volume fractions.

3.3.3 Laser scattering

Finally, in the spirit of many experiments past, I set up a very rough laser-scattering experiment, passing a HeNe laser through the same samples used for the macroscopic experiment described above; using a sheet of semi-translucent paper to capture the resulting (forward-scattered) scattering image; and imaging this paper from the back using the same camera as above.

3.3.4 Electrosonic analyzer

In order to get a rough measure of the zeta-potential of my PMMA particles, Joe McDermott and I employed a Field Electrosonic Analayzer or ESA (PA Partikel-Analytik-Meßgeräte). This instrument applies a high-frequency ($\approx$1MHz) electric field pulse across a small sample of the particle suspension; charged particles are thus excited to oscillate in response, generating ultrasonic pressure waves in the medium, which are detected by a transducer. The amplitude of these sound waves is determined by the effective zeta-potential of the particles (in addition to the particle mass fraction in the solution; the density difference between the particles and the solvent; and the solvent viscosity and dielectric constant).

We made these measurements in pure decalin, since a significant density mis-match between the particles and the solvent was necessary to form a pressure wave that could be detected by the transducer. We prepared a suspension of particles at volume fraction $\phi \approx 12\%$ in pure decalin, and titrated in decalin with 500mM dissolved AOT, measuring the zeta-potential at various values of AOT concentration.

Because we used very approximate values for several of the parameters going into the conversion from sound amplitude to zeta-potential, our results should only be trusted qualitatively rather than quantitatively. The zeta-potential may also be different in the decalin/t.c.e. solvent used in the main experiments than in pure decalin. Furthermore at low ionic strength, when the screening length (which can be thought of as the extent of the electric 'double-layer' of AOT micelles surrounding each particle) is smaller than or similar to the particle separation, the hydrodynamic response of the particles may differ from that assumed in calculating the conversion between pressure amplitude and zeta-potential. In spite of these systematic uncertainties, the results should be of the right order of magnitude, and the qualitative behavior of the zeta-potential as a function of AOT concentration remains of interest.

3.3.5 Dynamic light scattering

My best determination of the physical size of my PMMA particles was made using a dynamic light scattering (DLS) apparatus (Scitech Instruments ST-100 Variable Angle Light-Scattering Instrument). Nick Schade helped me with these measurements. The DLS measures the time correlation of a laser scattered by a dilute particle sample: roughly speaking, the timescale of the decorrelation gives the timescale of motion of the scattering bodies, that is, the particles. The particle radius is calculated by assuming Stokes-Einstein drag and modeling the correlation, given the viscosity and refractive index of the solvent. Measurements at different scattering angles can be combined to give a more accurate result.

I frankly used the DLS setup as more or less a black box, leaning on Nick's experience. We took some time to re-align the laser input to increase the intensity. I prepared a very dilute particle suspension (about 0.01% if I recall correctly) in my density-matched solvent with AOT, in a carefully cleaned glass vial. We set the DLS to measure eight different angles over a total measurement time of several hours, and then fit the resulting curves; with two repetitions, some seven curves provided good fits, and we used the aggregate of

these results to determine the particle radius.

3.3.6 Refractometer

The final instrument I will mention is the Abbe refractometer used to determine the refractive index of my density-matched solvent with AOT (the refractive index is a necessary parameter to the model for sizing using DLS, as it enters into the scattering angle). Thanks to Sujit Datta for demonstrating how to use the apparatus, although I took the measurements myself.

The Abbe refractometer (unfortunately the specific machine has since broken and been discarded, so I cannot look up the exact model) is a lovely little instrument. A thin film of the sample fluid is placed between two prisms, and a bright light passed through the prisms and sample. A block provides a sharp shadow; the precise position of the shadow depends on the refractive index of the sample. The instrument is set up so that the user scans a field of view to identify the shadow, and can then read out the refractive index required to achieve that position.

Chapter 4

Analysis

This chapter covers the data analysis I performed on the images from the confocal microscope. Data analysis was done entirely using Matlab. Of course many of the algorithms are not my own; for the particle location code, I am indebted to Yongxiang Gao and Maria Kilfoil, whose code can be found on Kilfoil's website[1], and which code I used nearly unaltered. For the particle tracking code, I am indebted to Kate Jensen, who wrote the core function to link particle trajectories. For the strain calculations, I relied heavily on Kate's code as well.

The data analysis can be broken down into roughly two parts. The first stage of analysis is particle location and tracking, using several steps of image-processing to extract precise location as a function of time for each particle from a 'stack' of raw images. With these particle locations in hand, we then move to the second stage, computing assorted structural and dynamical measures of the system. These measures constitute the vocabulary used to discuss the interesting physics in these systems.

I intend to curate my data analysis codes into a package which will I hope be at least somewhat useful to others who wish to use Matlab to study colloidal systems – as mentioned above, the core location codes are widely available and commonly used, but I have also taken some time to make parts of the subsequent analysis robust and efficient, and there is no point in others inventing the wheel if they would find these algorithms useful.

[1] people.umass.edu/kilfoil/downloads.html

4.1 Particle location and tracking

Though the terms are often used interchangeably, I will draw a clear distinction between particle *location* and particle *tracking*. Particle location considers an image at a snapshot in time – either a single 2D XY slice, or a full 3D XYZ stack – and extracts the precise positions of every particle in that image alone. Particle tracking considers these precise particle positions at multiple times, and identifies the trajectory of each individual particle, linking its position at time t_1 to its position at time t_2, etc.

4.1.1 Locations: general principles

The standard algorithms for locating colloidal particles were developed by John Crocker and David Grier in the 1990's [11]; their original IDL codes have been translated into other programming languages, adapted, and extended, but in the end, most particle location algorithms trace back directly to their work. I'll summarize here the general principles of the algorithm (full details are of course available in their paper, or by reading any of the codes); later sections will provide fuller details for my particular system and method of analysis.

The algorithm begins with a two-component image processing step to clean up the images, making the particle features more distinct. Short-wavelength pixel noise is filtered out by convolution with a Gaussian kernel. Long-wavelength variations in brightness are filtered out by subtracting off a background, determined by a wide boxcar averaging. These two steps take a noisy camera image to an image in which bright, smooth particles are readily apparent against a black background.

The local maxima of this filtered image are then used as the first estimates of the particle locations. (Local maxima are quickly identified by a fairly clever method: the image is 'dilated', that is, each pixel is reassigned the value of the brightest pixel within a certain distance, and the local maxima are then those pixels which have the same value in the dilated image as in the filtered image.) This estimate is refined by identifying the center of mass of brightness of a disk around that central pixel, with a size to encompass the particle. This refinement allows sub-pixel resolution in the particle locations, which is key to accurately calculating structural measures of the system.

The original Crocker and Grier codes deals with the 3$^{\text{rd}}$ dimension (Z) in a different manner. The image resolution in Z tends to be much poorer than the XY resolution, so

that a particle spans many more pixels in XY than in Z. The Crocker and Grier method thus calculates the XY position of a particle in each slice independently, and then estimates the Z-coordinate of the particle based on how its brightness varies with slice.

Yongxiang Gao and Maria Kilfoil implemented a 3D location algorithm which treats the Z-dimension more equally with the X- and Y-dimensions, applying the filters and calculating the center of mass in full three dimensions rather than two dimensions [20]. This method is more computationally intensive (read: slower), but there is good evidence that it gives greater location accuracy.

Gao and Kilfoil also introduced further refinement steps in the center of mass calculations. Having estimated the center of mass, they actually perform a 'fracshift' to redefine the pixels of their image, so that the calculated center of the particle is at the center of a newly-defined pixel. The brightness of each new pixel is computed by a weighted average of the original pixels overlapping it. The center-of-mass is then recalculated again using these frame-shifted pixels, and the refinement iterated. Gao and Kilfoil demonstrated that this iteration significantly improved accuracy, with about 20 iterations needed for the best results [20].

Using this algorithm, the typical (r.m.s.) error in particle locations is reported to be less than 1/11 pixels in X and Y, and about 1/20 pixels in Z [20]. This can translate to locations accurate to within a few nanometers.

These are not the only changes to be made to the original Crocker and Grier codes; codes can be found written in many other programming languages, and with many other modifications and improvements. There is of course a trade-off between speed and accuracy – the Gao and Kilfoil codes are slower than many others, but provide higher accuracy. Different detailed methods will also be more or less appropriate depending on the volume fraction of the system, and quality of the images.

4.1.2 Locations in two dimensions

General principles are all well and good, but here I will include some nitty-gritty details of the parameters that go into these algorithms, and how to choose the optimum values for these parameters. Locating in two dimensions (for XYT stacks) is rather different from locating in three dimensions (XYZ and XYZT stacks), so I will describe each separately.

For 2D locations, I used Gao and Kilfoil's `feature2D` function. The noise lengthscale I

set by default to 1 pixel. The primary parameters I adjusted were the radius of the mask used to locate particles, and a brightness cutoff.

The given mask radius (the variable `w` in the Kilfoil code) should be slightly larger than the radius of the particles, in pixel units, and must have an integer value. With too large a value, a mask may overlap a neighboring particle, so that the calculated locations of nearby particles appear to be pulled toward one another. With too small a value, the mask does not capture the entire particle, and so is not using the full information available and will be more sensitive to noise and tend not to acheive good sub-pixel results. I generally estimated the mask radius just by counting pixels across a particle by eye, and then test the location algorithm on a single image using a few values of mask radius near this estimate. By superimposing particle locations, calculated with different parameters, over either the raw or the filtered images, I could almost always spot by eye which locations were more accurate and use this value for the radius.

As a sanity check, I also histogrammed the fractional part of the particle locations in the X and in the Y dimensions (see Fig. 4.1). If the accuracy is in fact sub-pixel, these histograms should be uniform (unless there is a truly remarkable coincidence of periodicity in the particle locations and the pixel size), that is, a particle should be equally likely to be positioned at any offset from the nearest pixel center. If the radius is ill-chosen, there may be a bias in these fractional histograms – generally a tendency either to preferentially locate particles at half-pixel values, or at full-pixel values. The presence of this 'pixel bias' usually indicates that the chosen radius is too small. Of course, an absence of pixel bias is no guarantee that the radius is well chosen, so it should only be used in conjunction with common-sense checks such as eyeballing the accuracy of the location, but checking the pixel bias can sometimes raise a red flag.

For the binary system, I used particles of about 2μm diameter, and an XY pixel resolution of 0.1802μm; my chosen mask radius for this system was 7 pixels, slightly larger than the 6 pixels predicted by simple geometry. Similarly, for the Wigner system I used particles of about 1.7μm diameter, and an XY pixel resolution of 0.1600μm, also with a mask radiuis of 7 pixels. The mask radius is probably slightly large 1) to ensure that the entire particle is captured even when the center estimate is slightly off; and 2) because the point-spread function of the microscope means that the particle image is blurred by a pixel or so.

Having chosen the mask radius, I also found it useful to impose a cutoff in brightness, so that fainter particle images are discarded. These faint images are almost always particles

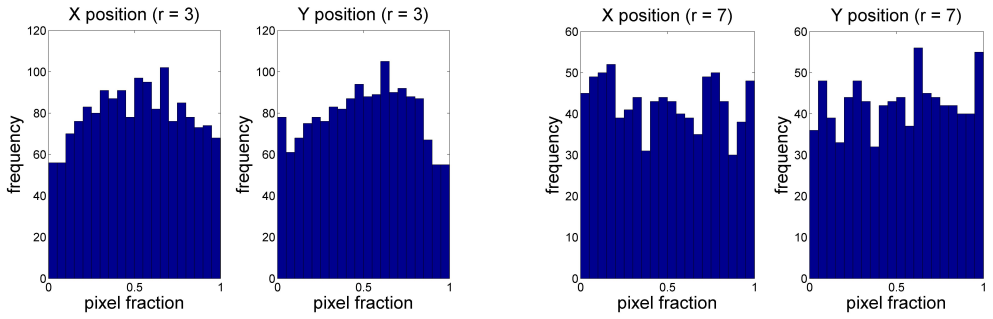

Figure 4.1: Pixel bias in 2D locations, showing the effect of the mask radius on location accuracy. a) Histogram of the fractional part of particle locations obtained using a mask radius of 3 pixels; note that the distributions show a distinct peak at a fraction 0.5, meaning that particles are more likely to be located near the center of a pixel than near the edge of a pixel. This 'pixel bias' indicates that the mask radius is too small. b) Histogram of the fractional part of particles locations obtained using a mask radius of 7 pixels, for the same original image as in (a); note that the distrubutions are quite flat. This is encouraging that the mask radius is large enough, although other checks should be used to verify a good mask radius.

which are nearly out of the plane of focus, so that only a small cross-section is visible in the XY slice. Discarding such images reduced the evil of trying to locate two particles which appear to coincide in XY, one being well above and the other well below the plane of focus. Such a particle pair may appear as an elongated splotch, so that neither can be accurately located; it is best to not even try and to count the particle as having left the field of view. Even faint single-particles will often be poorly located simply because of poor signal-to-noise ratio. The cutoff is in the peak brightness of a feature; any potential particle whose brightest pixel is below the cutoff is discarded. I typically chose the mask radius without using the brightness cutoff, and then increase the cutoff in steps, always visualizing to compare which potential particles were discarded, until by eye I reckoned that I was losing most of the double or poorly located faint particles, while keeping most of the particles which were well located. For 8-bit images, where the maximimum possible pixel values is 255, with the full dynamic range used, I generally found that a brightness cutoff in the range 70-100 worked best.

In some analysis, I also used a cutoff in eccentricity of a particle, which is calculated by the `feature2D` function. Any cut of a spherical particle should of course be a circular disk of zero eccentricity; a substantially nonzero eccentricity generally indicates a double-particle, either real or apparent. Applying an eccentricity cutoff served a similar purpose to the brightness cutoff, getting rid of particles which were poorly located due to being

superimposed in XY on another particle. As with the brightness cutoff, I set the maximum eccentricity by changing the cutoff (this time starting from 1 and decreasing the cutoff) and visualizing the results, until a change in eccentricity resulted in losing more well-located particles than poorly-located. I typically ended up using a value of about 0.25.

With these two cutoffs, in brightness and in eccentricity, I would lose a few particles which would potentially have been well-located, losing structural information in two dimensions; however, I felt this a good trade-off to be able to trust the dynamical information. By being conservative and allowing particles to be 'lost' out of the plane of focus a little more easily, I could be more certain that the trajectories of particles I did locate and track were more reliable.

I generally determined the location parameters using a single image of an XYT timeseries; I then applied these location parameters to all images in the series. If there had been significant changes in brightness, for example, over that time, this might not be appropriate; however in my experiments this tended to work quite well.

4.1.3 Locations in three dimensions

In two dimensions, there were really only two or three parameters to vary in calculating the locations. In three dimensions, the algorithm is rather more sophisticated, and a greater number of parameters are left to the user's control. I will here give a fairly detailed description of how each one affects the results, and how I went about setting them.

First note that most of the parameters are given as three-element vectors, giving dimensions in X, Y, and Z. Generally these dimensions should be the same in real-space units; however for the location algorithm, they must be given in pixel units, and so it is essential to take into account the possible difference in pixel sizes in each dimension. The X and Y values are almost always the same, and since I do most of the visualization in the XY plane, I generally defined the X and Y value, and then calculated the necessary Z value from the ratio of the XY and Z pixel sizes. So for the mask size, I converted the scalar `mask_size` to the vector `masksz` = `mask_size` $*$ [1 1 (`xy_pix_to_micron`/`z_pix_to_micron`)], where `xy_pix_to_micron` and `z_pix_to_micron` are respectively the XY and Z pixel sizes in microns.

While the image filtering and the location algorithm are amalgamated in the `feature2D` function, they are separated for the 3D locations, with the image filtering being done by the

`bpass3dMB` function, and the locations by the `feature3dMB` function. This separation gives us our first new parameter, the filter size.

As described in Section 4.1.1, the image is filtered for short-wavelength pixel noise, and for long-wavelength background levels; each of these filters is governed by a lengthscale in each dimension. For the pixel noise, I set the lengthscale by default to be one pixel in each dimension.[2] For the background subtraction, the filter size should be roughly the typical separation between particles, if not a little larger. The background at each pixel is calculated as the average value over a box around it, so it is best that this box include a good amount of empty space. In the extreme of choosing too small a filter size, the particles may artificially appear ring-shaped in the filtered image, as the 'background' at the particle center consists mostly of bright pixels, while the 'background' at the rim includes many empty pixels (see Figure 4.2).

The quality of my images was such that they generally had quite uniform backgrounds, and so I did not need the background subtraction to compensate for large changes in brightness across the image. Therefore in my earlier data analysis, I chose the filter size by starting with a large filter size (e.g. 50 pixels), and then decreasing this size until the typical change in particle locations was larger than some desired limit. I realized after some time that this was overly conservative and resulting in larger filter sizes than necessary (which slows down data analysis), and changed to select the filter size rather by eyeballing the separation between particles, and calculating the locations using several values around this estimate.

In the 3D analysis, the mask size is given as the diameter of the particles (rather than the radius), and may take on any value, integer or non-integer. I always scaled my mask size to be spherical in real space dimensions, requiring that the mask size given in pixels in Z be scaled relative to the mask size in XY pixels. To choose the mask size, I first made an estimate based on geometry and/or counting pixels in an image. I then calculated particle locations using a range of mask sizes, from so small as to introduce pixel bias, to so large as to visibly be skewing the locations toward neighboring particles. I compared the net change in computed locations as I varied the mask size, and chose the mask size where this change was a local minimum, suggesting stability of the location result with respect to the parameter value (and subject to sanity checks such as pixel bias and visual

[2] In earlier versions of my data analysis, I scaled the lengthscale in Z to be the same physical dimension as the X and Y lengthscales; however, I realized that since the pixel noise is determined by the imaging resolution more than by physical dimensions, this is not appropriate. If one is very precise and careful, one probably should take into account the thickness of the slice in Z, governed by the pinhole aperture, in determining this lengthscale.

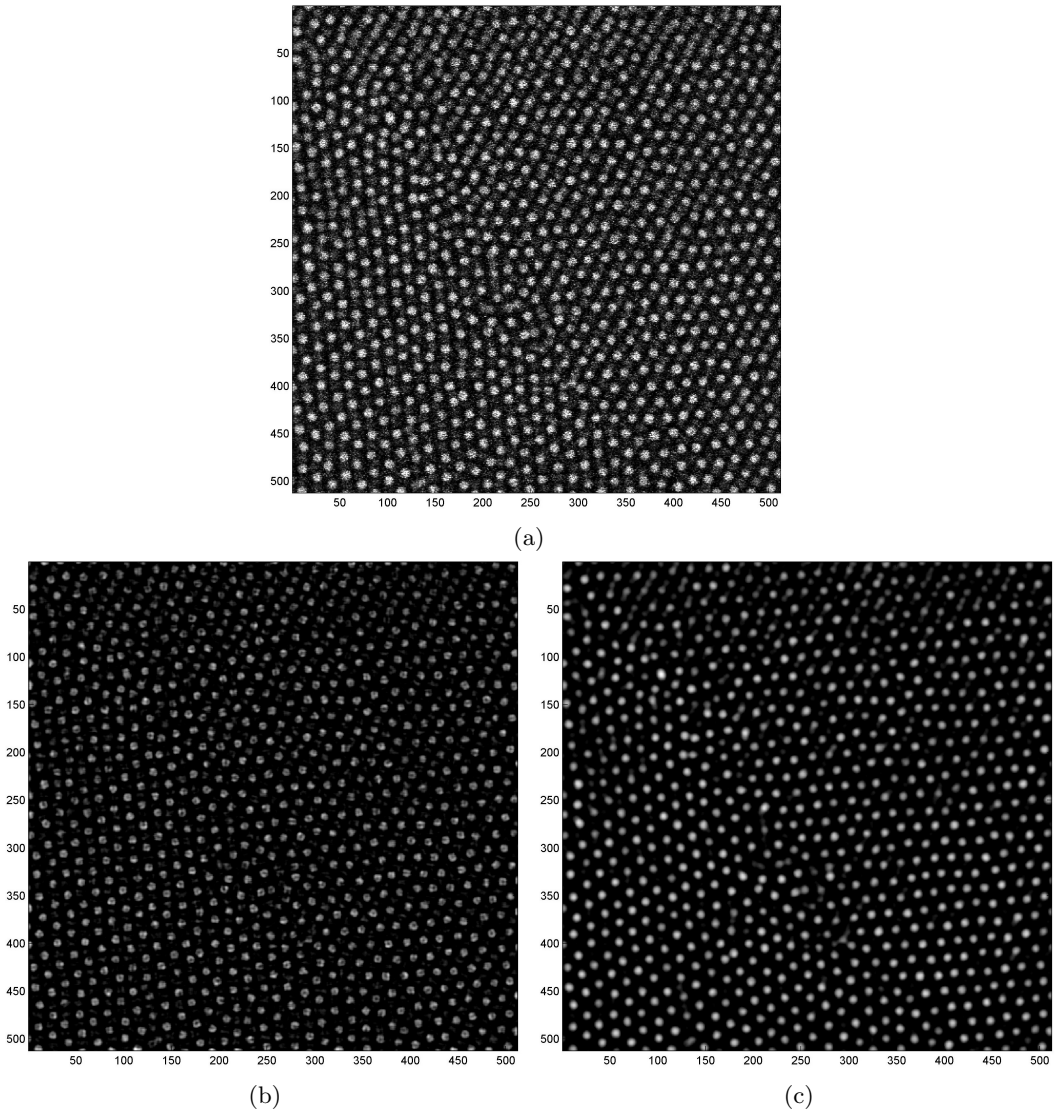

Figure 4.2: Effect of image filter size in 3D locations. a) Single raw XY image of a confocal XYZ stack. b) Same XY slice of image after (3D) filtering using a 'boxcar' size of 3 pixels in XY; note that most particles have a dark center and many no longer appear round. This indicates that the filter size is too small. c) Same XY slice of image after (3D) filtering using a 'boxcar' size of 22 pixels; note that the particles appear bright and smooth against a dark background. This is encouraging that the filter size is not too small. All images are 82μm across.

confirmation). I generally iterated several times, using successively smaller increments of mask size, ultimately choosing the mask size to within about 0.1-0.2 pixels.

For the binary gel system, I typically took Z-stacks using an 0.18μm pixel size in XY, and a mask size of 13.2 pixels. For the Wigner crystal system, I took Z-stacks with an 0.16μm pixel size, and a mask size of 11.8 pixels; and ZT stacks with a 0.20μm pixel size, and a mask size of 8.6 pixels.

The next most important parameter in particle locations is the maximum separation allowed between particles. I generally set this to about 1/2 - 2/3 of the mask size. Too large an enforced separation, and some particles would be lost, being too close to a neighbor (especially, in the Wigner system, those participating in a dimer). Too small an enforced separation, and particles would be double-counted, if noise introduced two local brightness maxima in a single particle. I generally estimated this at about 2/3 the mask size, and then checked a few nearby values to make sure I was not losing or double-counting too many particles, determining the final value to within only about a pixel.

I will mention briefly the other two available parameters, mainly to argue that they were not very useful in my application. There is the option of a cutoff in integrated brightness (note this is different from the peak brightness cutoff in 2D). This generally only excluded particles around the boundaries of the image, which I dealt with at a later stage of the analysis (see Section 4.1.5), and so my results were generally equally good whether I used the cutoff or not. I generally set a very low cutoff just to get rid of one or two blips of noise. The Kilfoil code also includes a parameter named `diameter`; this parameter did not affect the actual locations, so long as it was chosen larger than mask-size; all it effected was to also exclude some particles near the boundaries. I generally set it to a couple of pixels larger than the mask size and mainly ignored it.

As in the 2D case, I found it best to check as a very rough verification that there was no pixel bias – note that pixel bias generally appeared in the Z direction sooner than in the XY directions. I furthermore checked visually that the particle locations superimposed on the original image were satisfactory.

Three-dimensional locations do introduce one drawback which was generally not present in the two-dimensional data: particles may change their position over the time it takes for the microscope to scan through a particle. A particle would typically be at least 7 or more pixels in extent in the Z direction, and at the very fastest I ran the microscope, the delay between slices in Z was on the order of 15 milliseconds. In the roughly 100ms to

scan between the bottom and the top of a particle, that particle might move a couple of hundreds of nanometers, so that its image in the scan was not a perfect sphere. This means that for mobile particles – as in the Wigner system, or the softer gels of the binary system – the accuracy of the locations is in fact much poorer than the few nanometers obtainable for static particles. In the strongest gels of the binary system, particles were sufficiently arrested in the gel that this effect was negligible.

As in the two-dimensional case, for a ZT stack, I set these location parameters using the Z-stack at the first timestep, and then use the same parameters for every timestep of a series. This is suitable so long as illumination and brightness do not change too much; I did observe some slight bleaching of particles over time, but not so severe I think as to affect the locations.

4.1.4 Tracking in time

We have done then with the locations – for a time series (either a 2D T-stack or a 3D ZT-stack), we can easily obtain a list of particle locations at each timestep. How now to link together these locations, identifying a single particle from one timestep to the next and determining its trajectory?

The exact algorithm here is almost entirely due to Kate Jensen, based on earlier algorithms, and I used her `particle_tracking` code to carry out the actual particle tracking. In brief, for each particle location at time t_1, the algorithm searches for the particle at the smallest displacement from that reference location at time t_2. If two particles at t_1 would both map to the same particle at t_2, the algorithm chooses the reference particle closer to the particle location at time t_2, and looks for an alternative match for the second reference particle. This ensures that each particle have at most one past and one future. If no consistent match is found within a cutoff distance of the reference location, then the particle is 'lost' to the algorithm – this most often happens near the boundaries of an image as particles move in and out of the imaging volume. A particle is identified by a unique number, and this particle ID is associated with that particle's location at each time, indicating its trajectory through time.

There are essentially two parameters which the user can change. The first is a maximum displacement allowed for a particle between timesteps. (Without such a cutoff, a particle which leaves the imaging volume on one side could be incorrectly identified as the same

particle that enters on the opposite side at a later time!) This cutoff depends on the number density and dynamics of the particles, and on the length of the timestep between images. For true tracking, this timestep must be short enough that particles are unlikely to switch places with each other between consecutive images – that is, particles should not move further than about half the interparticle distance. This is of course ensured even in a dense system if particles do not move more than about a particle radius.

In the earlier stages of my data analysis – for the binary system, for example – I chose the maximum displacement simply by visualizing many particle tracks over a short clip of my timeseries, and adjusted the maximum displacement so that the trajectories agreed with my qualitative impressions. Too short a maximum displacement, and a particle which moved a larger than average distance between timesteps would be lost by the algorithm and its track would end, while my eye could still follow its motion. Too large a maximum displacement, and a track according to the algorithm might appear to me to jump from one particle to what I could identify as another particle. I watched a few tens of particles over a few tens of timesteps, adjusted the maximum displacement, and repeated this several times to determine the best timestep.

For two-dimensional analysis, I tended to be conservative – I would rather 'lose' a particle and have a short track than have a track jump from one particle to another, and so I would set the maximum displacement accordingly. This ended up being about the particle radius, e.g. 1μm.

In later analysis, I developed a more quantitative measure of what should be the appropriate maximum displacement. This was based on the observation that the expected distribution of displacements should fall off smoothly at larger displacements. In a purely Brownian system, this fall-off would be Gaussian; even in the partially arrested systems I study, at timescales comparable to or shorter than the localization timescale, this will still be roughly true, and in any case the fall-off should probably be smooth. Thus plotting the distribution of displacements, an abrupt cutoff is likely to indicate a maximum displacement which is too small, losing those particles with large excursions. A distribution which reaches a plateau or even increases suggests a maximum displacement which is too large – the excess of large displacements in an artifact due to the tracking algorithm incorrectly transferring a label from one physical particle to another. The optimal maximum displacement gives a curve which falls off smoothly to low frequencies (Fig. 4.3c). I verified this choice against videos of particle motion as before.

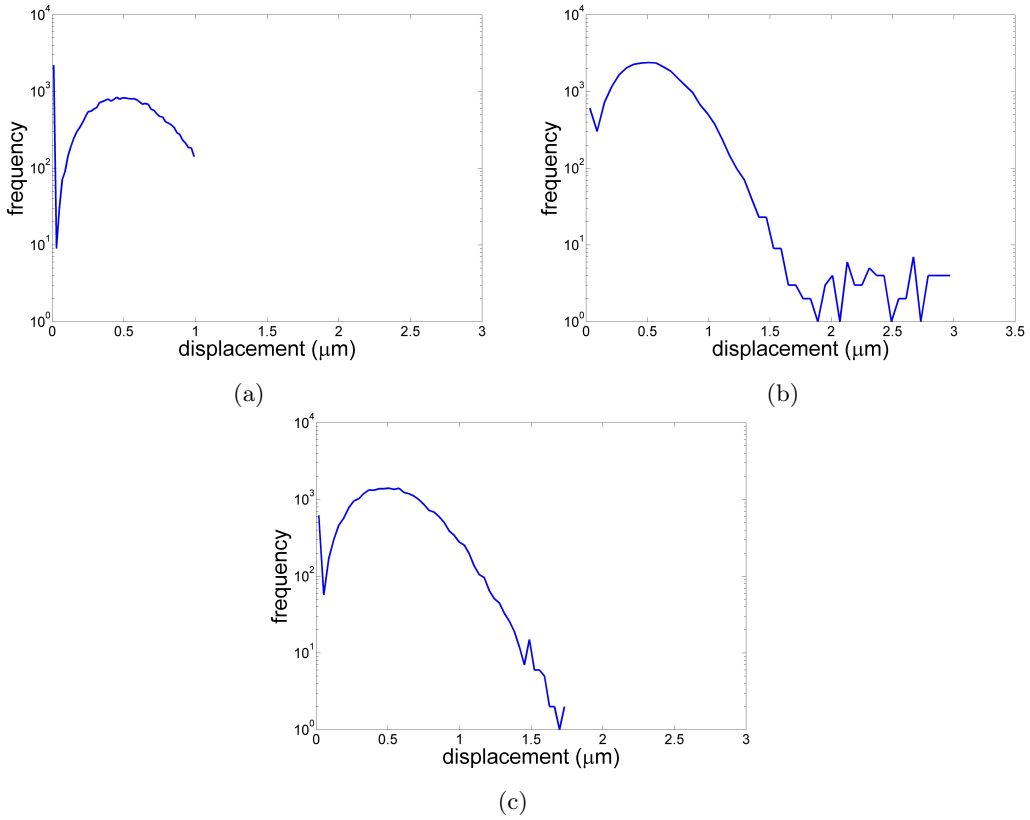

Figure 4.3: Effect of maximum displacement in 3D tracking. a) Distribution of particle displacements from one timestep to the next when tracked imposing a maximum displacement of 1μm; note that the distribution is cut off when the frequency is still quite high. This indicates that the maximum displacement is too small, and particle tracks are being artificially lost. b) Distribution for the same location results but when tracked imposing a maximum displacement of 3μm; note that the distribution has a noisy, nonzero tail at large displacements, above the continuation of the smooth curve. This indicates that the maximum displacement is too large, and particle labels are artificially being transferred from one physical particle to another physical particle. c) Distribution for the same location results but when tracked imposing a maximum displacement of 1.75μm; note that the distribution falls off fairly smoothly to low frequency, with no tail. This indicates that this is the optimum maximum displacement for this sample, neither losing too many particle tracks nor artificially connecting distinct particle tracks.

For ZT stacks in the Wigner system, I generally had a timestep of 2 seconds, and used a maximum displacement around 1.7μm (varying slightly with volume fraction). Note that this is about the particle diameter, and furthermore was larger than half the particle spacing of 2.5μm - 2.9μm. The necessity of such a large maximum displacement indicates that the timestep is a little longer than would be ideal for reliable tracking; this is a weakness of pushing the microscope to the limits of its speed.

Indeed it is this precisely which makes tracking in 3D in a more diffusive system still intractable; we can only attempt the tracking here because the particles are largely localized around their mean positions due to the ordering. In the fluid phase of either the binary system or the Wigner system, I never even tried to track particles in 3D – any tracking in time was done on 2D images.

The second useful parameter in tracking is the number of timesteps a particle is allowed to skip, that is, not be located in, before being 'lost' for good. This is primarily useful for not losing particles which move in and out of an image – either crossing an image boundary, or moving in and out of the plane of focus in a T-series. If a lost particle reappears after too many timesteps, it is considered a new particle and given a new ID number. I generally set this so that over the total *time* it was allowed to skip, I would not expect it to move further than about its own diameter, so that it was unlikely to have swapped places with another particle. Thus for ZT stacks, I generally allowed only one timestep (e.g. 2 seconds) to be skipped, whereas for T-series with shorter timesteps, I allowed more like 8 timesteps (0.8 seconds). Thus a particle could move out of the plane of focus for nearly a second and then re-enter, and still be identified as the same particle. These timescales matched up pretty well with my qualitative impression of watching the videos.

4.1.5 Other considerations

Once the parameters are chosen for location and, if relevant, tracking, we are ready to locate and track entire stacks. One consideration after the location and tracking is to exclude particles too close to image boundaries – if the image of a particle is cut off by the boundary, its location will not be computed accurately. I therefore introduced a gap of 1/2 the mask size, and discarded any particle locations which were closer than this cutoff to any image boundary.

There is a slight advantage to performing this cutoff after tracking: a particle which

moves about near a boundary, in and out of the imaging volume, may have inaccurate locations at some timesteps which nonetheless provide reliable links between adjacent timesteps. Thus even though these inaccurate locations will be thrown away after tracking, their inclusion in the tracking stage may result in a more reliable particle track.

Finally, a brief note on data wrangling. For any experiment, I often took multiple stacks of the same dimensions, but in different locations in the sample. Each stack of course must be located and tracked separately, but I generally combined these lists of particle locations into a single master list, with an extra parameter to indicate which stack a particle belonged to, and ensured that particles in different stacks maintained unique ID numbers. I adopted the standard data format of a two-dimensional array in which each row corresponded to a single particle at a single time, with the columns containing the position, the timestep, the particle ID, and the stack ID. These conventions required some delicacy in later calculations, e.g. ensuring that for purely structural measures, only the relations between particles in the same stack and at the same timestep were used.

Having compressed the raw images into a list of particle trajectories, we are now in a position to calculate characteristics of greater information and interest. The remaining sections of this chapter will describe the measures I used, with notes about how they are calculated.

4.2 Dynamic measures

In both the gel experiments and the crystal experiments, the most fundamental characteristic of a sample was whether it was in a fluid state or in a solid state. Although the most generally accepted distinction between a fluid and a solid is the stability to shear stresses, a good proxy is the mobility of the particles in the system. This mobility is measured by calculating the dynamics of the system, that is, characteristics of the motion of single particles over time.

4.2.1 Mean square displacement

In particular, the dynamic measure I used was the *mean square displacement*, indicating the 'typical' distance moved by a particle over a given period of time. The mean square displacement is calculated as:

$$MSD(\tau) = \left\langle \left(x\left(t+\tau\right) - x\left(t\right) \right)^2 \right\rangle - \left(\left\langle \left(x\left(t+\tau\right) - x\left(t\right) \right) \right\rangle \right)^2$$

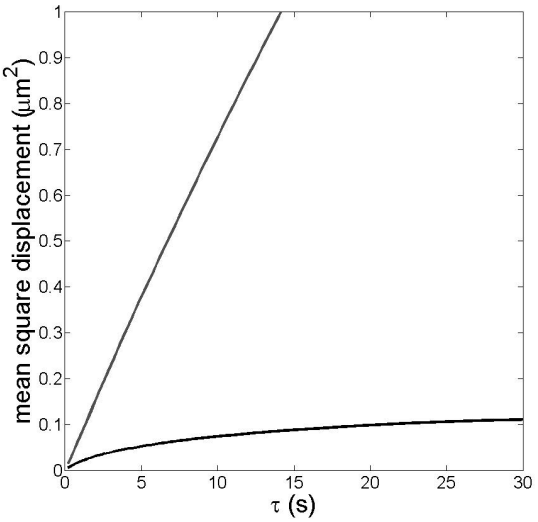

Figure 4.4: Mean-squared displacements in fluids and gels (in one dimension). The upper curve increases linearly with time, indicating free diffusion of particles, and is identified as a fluid. The lower curve increases at early times, but flattens to a plateau, indicating localization of the particles, and is identified as an arrested system, in this case a gel. The distance cutoff of $1(\mu\text{m})^2$ represents the thickness in Z of the confocal image slice, and therefore the typical distance a particle moves before leaving the plane of focus (for an XYT confocal serires). The behavior of the mean-squared displacement thus provides a means of distinguishing between fluid and arrested samples.

where the average indicated by $\langle\rangle$ is over both starting times t, and over the ensemble of particles. This is equivalent to the expected value of the squared-displacement, $E(\Delta x^2)$, for the ensemble; as discussed in Section 1.1, for a purely diffusive, Brownian system, this quantity should increase linearly with time (the *root* mean square displacement therefore increasing as the square-root of time). For an arrested or solid system, however, particles are localized or caged within the solid, and are able to diffuse only a short distance within that cage before being restored toward their original position by interactions with surrounding particles. Thus the mean square displacement at first increases, but then reaches a plateau, flattening out at some 'localization length' within which the particles are confined (see Fig. 4.4).

The mean square displacement is best calculated independently for each dimension of motion; the total three-dimensional mean-squared displacement is just the sum of the single-dimension mean square displacements. If there is no preferred direction in the system, we expect that the mean square displacement in each dimension should be the same.

Note that the calculation of the mean square displacement includes a correction for the square of the mean displacement. This removes the effect of overall drift in the system;

this typically should be zero, but sometimes slight motion of the sample does take place. It is further worth considering the independence of different displacements included in the average. In particular, the average is taken over all starting times t; yet if the interval τ is many times the timestep Δt, then the displacement of a particle between times t and $(t+\tau)$ is very nearly the same as the displacement between times $(t+\Delta t)$ and $(t+\Delta t+\tau)$, that is, the displacements from adjacent starting times are nearly the same, and not independent. I assumed that only starting times separated by more than $\tau/2$ gave independent points. Mean square displacements then were only reported which were calculated using at least 1000 *independent* displacements in the average.

While the mean square displacement is an absolutely standard measure used widely in the literature, I expended some effort in developing the code to perform the actual calculation to run quickly in Matlab. In order to speed up the calculation, I would interpolate missing locations in a particle's trajectory; this may introduce some artifacts, but I expect them to be small.

From the mean square displacement curves, two single parameters may be derived. The first, in liquid samples or in the short-time diffusive regime of a solid sample, is the *diffusion constant*, given by the slope of the linear portion of the curve. In general I used this diffusion coconstant no further than to verify that it was of the order of magnitude expected given the particle size and solvent viscosity. The second, in solid samples, is the *localization length*, or the plateau value of the root mean square displacement at long times.

4.3 Structural measures

The second broad class of measures I used are structural measures, which use the relationships among the positions of many distinct particles at a fixed time. Bulk measures such as the radial distribution function indicate interactions and correlations among particles; more local measures such as contact number distributions give finer information about the structures in a system. In this section, I describe several measures used in each system.

4.3.1 Radial distribution function

The most basic structural measure of a system is the *radial distribution function (r.d.f.)*, which measures the relative particle density as a function of distance from a generic reference

particle:

$$g(r) = \rho(r)/\rho_0$$

where ρ_0 is the average particle density. This is computed by finding the likelihood of any two particles being a given distance apart:

$$g(r) = \frac{1}{4\pi r^2} V \left\langle \delta(r - r_{ij}) \right\rangle = \frac{1}{4\pi r^2} \frac{V}{N^2} \sum_{i=1}^{N} \sum_{j=1, j\neq i}^{N} \delta(r - r_{ij})$$

where r_{ij} is the distance between particles i and j, and the average $\langle\rangle$ is taken over all *pairs* of particles. Note that the $4\pi r^2$ scaling converts from number of particles to density by dividing out the volume of a shell of radius r, while the scaling of V the total volume of the system normalizes to the average density.

For a system with a featureless uniform density, that is $\rho(r) = \rho_0$, the r.d.f. is identically $g(r) = 1$. Thus deviations from unity indicate *spatial correlations* among particles. Of course in a colloidal system, the r.d.f. is never perfectly uniform; the finite size of the particles means that $g(r) = 0$ for $r \lesssim D$ the particle diameter. The r.d.f. for a dilute, hard-sphere colloidal fluid (as close as one can get to non-interacting) will thus look something like Fig. 4.5a, with a slight hump at distances slightly larger than a particle diameter, quickly flattening to $g(r) = 1$.

The r.d.f. changes dramatically when interactions are introduced into the system. These interactions cause correlations among particle locations – e.g. when an attractive interaction causes particles to stick together, this is clearly apparent in the r.d.f. as a significant peak in $g(r)$ at $r \approx D$ (see for example Fig. 4.5b). When interactions induce ordering, as in the Wigner system, this is also dramatically visible in the r.d.f. In particular, the correlations become long-range instead of only short-range, as the relative locations of faraway particles are determined by the ordered structure. In a perfect crystal, the r.d.f. would be a series of sharp delta-function peaks at the crystallographically determined distances, indicated by the red lines in Fig. 4.5c. In a real system, these sharp peaks are blurred by thermal fluctuations, but the experimental r.d.f. still shows clear peaks and oscillations out to many particle diameters, indicating the long-range ordering. Indeed, the shape of the r.d.f. for ordered systems can be used to distinguish the crystal structure by comparing the experimental r.d.f. to the theoretical crystal peaks.

The r.d.f. is another very standard measure used widely in colloid physics, but while

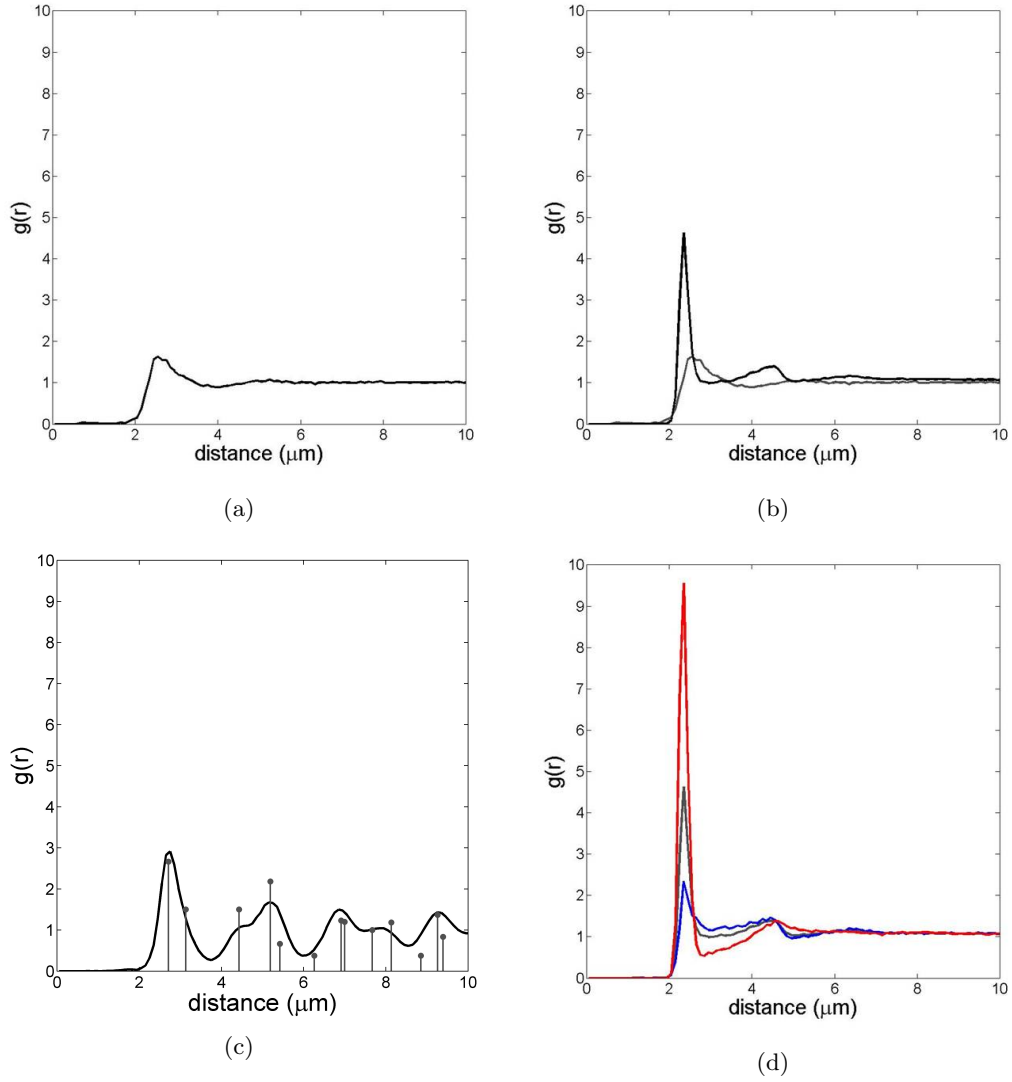

Figure 4.5: Radial distribution functions in fluids, gels, and crystals. (a-c) R.d.f. in a) a hard-sphere colloidal fluid; b) a strong (binary) colloidal gel, and c) a colloidal b.c.c. crystal, with the ideal crystal peaks shown for comparison. (d) Partial radial distribution functions in a binary gel, with $g_{+-}(r)$ shown in red; $g_{++}(r)$ shown in blue; and the species-agnostic $g(r)$ shown in grey. All samples at $\phi_{tot} \approx 0.20$.

its equation is fairly straightforward, there are some tricks to calculating it correctly and efficiently. The first catch is that a naive calculation of the r.d.f. will be affected by image boundaries. Consider a reference particle which is a distance b from an image boundary. For $r \leq b$, we can easily count the density of particles at distance r from the reference particle. But for $r > b$, some of the particles at distance r are outside of the image; we cannot access the full volume, and so our particle count is correspondingly smaller than it would be did we have an infinite imaging volume, or were the particle farther from the boundary. Thus for every reference particle and for every distance $r > b$, we must scale our calculation of the r.d.f. by the fraction of the volume at distance r which is in the imaging volume.

I implemented a strategy for dealing with this which is due to Eric Weeks: I only use as reference particles those particles which are far enough from the image boundaries in x and y that these boundaries will not affect the calculations, that is $b_x < r_{\max}$ and $b_y < r_{\max}$ where $r_{\max}$ is the maximum distance to which I am calculating the r.d.f. Then we need deal only with the effect of the image boundary in z. It is not too challenging an exercise in geometry to find the volume of a spherical cap of radius r, height $r - b$, and thickness dr; the contribution to the r.d.f. from this reference particle is then scaled by the volume of the spherical shell which is within the imaging volume for each value of r.

As with the mean square displacement calculations, I also put some effort into speeding up the r.d.f. algorithm in Matlab.

Partial radial distribution function

In the binary system, the r.d.f. can be refined to take into account the nature of the particles: instead of measuring the density of all particles as a function of distance from a reference, we can measure the density of particles of the same species as the reference or of the unlike species. We define the *partial radial distribution function* for particles of type a and b by

$$g_{ab}(r) = \frac{1}{4\pi r^2} \left\langle \frac{1}{n_b} \sum_b \delta(r - r_{ab}) \right\rangle_a$$

where $\langle\rangle_a$ indicates an average over all particles of type a; n_b is the number density of particles of type b; and r_{ab} is the distance between two particles a and b. Note that $g_{ab}(r) = g_{ba}(r)$ (with potential small differences in the calculation due to the finite imaging volume).

Since the interaction between like and unlike species are different, the partial r.d.f.s for like particles $g_{aa}(r)$ and $g_{bb}(r)$ may be very different indeed from the partial r.d.f. for

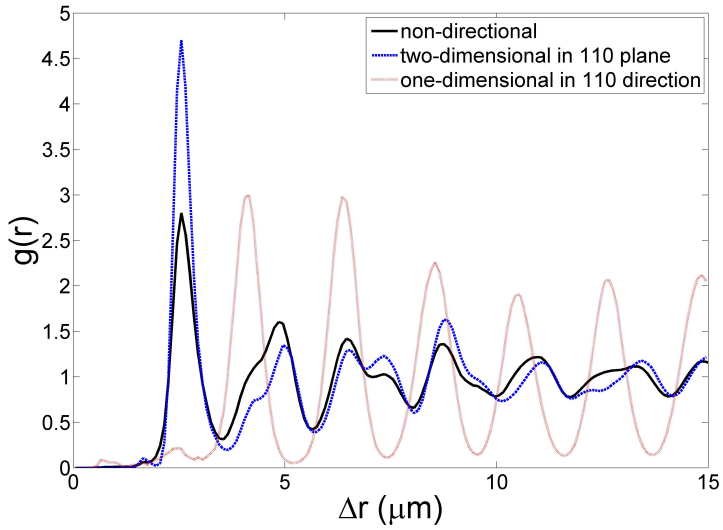

Figure 4.6: Directional radial distribution functions in a b.c.c. crystal sample. The solid black curve shows the overall, non-directional r.d.f. The blue dashed line shows a two-dimensional directional r.d.f. in a (110) plane; this is similar in overall shape, but the height and position of some peaks changes – note particularly the enhanced nearest-neighbor peak. The red dotted line shows a one-dimensional directional r.d.f. in the [110] direction; here we see clearly the regular layering of the (110) planes.

unlike particles $g_{ab}(r)$, and indeed from each other. For the binary system I studied, the two particles species are of course positively and negatively charged; there is an attraction between oppositely-charged particles, but like-charged particles have a nearly hard-sphere interaction. Thus $g_{++}(r)$ and $g_{--}(r)$ are flattened relative to the overall species-agnostic r.d.f., while the unlike correlation is much stronger, so that $g_{+-}(r)$ shows a particularly sharp first peak – see Fig. 4.5d.

Directional radial distribution function

So far we have expressed the radial distribution function as a single-variable function of distance from the reference particle, ignoring orientation or direction. This is appropriate for an isotropic system, but for a nonisotropic system such as the Wigner crystal, there is some information lost which can be recovered by considering *directional* radial distribution functions. These are calculated by restricting the volume over which the sum is taken, e.g. to a narrow cone or cylinder for a one-dimensional directional r.d.f., or a plane for a two-dimensional directional r.d.f. In Fig. 4.6, for example, the crystalline layers become clear when we consider the one-dimensional directional r.d.f. in the 110 direction.

4.3.2 Contact number distribution

The radial distribution function is, like the mean-squared displacement described in the previous section, still essentially a bulk measure. While I use particle-by-particle location information to compute the r.d.f., it can also be calculated from the Fourier transform of the scattering function $S(q)$, that is, from a bulk measurement when data on individual particles are not available. Yet one of the much-touted advantages of using confocal microscopy to study colloidal systems is the ability to obtain just that single-particle-level data. What can we do with this data that we cannot do in bulk?

The first *local* structural measure I use is the *contact number distribution* of particles in a gel or other locally dense system. This simply counts how many particles are in contact with each reference particle. The average contact number can be deduced from the radial distribution function – in particular from the integral of the first peak – but local information is retained in the full distribution.

Of course, to compute the contact number distribution, we must define when two particles are 'in contact'. I used a cutoff distance set at the first minimum of the radial distribution function, thus capturing the nearest-neighbor shell. This cutoff distance is typically larger than the particle diameter by about 40%, allowing for some polydispersity in the sample and noise in the locations.

In a noninteracting system, contact number will be determined by the particle density, while attractive interactions will cause additional contacts to form and move the distribution to higher contact numbers. Geometry caps the number of contacts at 12 for a monodisperse system, but this limit can only be achieved by particles which are able to rearrange and equilibrate; the contact number is necessarily lower, usually much lower, for an arrested gel.

In the binary system, we can of course distinguish contacts between like and unlike particles. Contacts between unlike or oppositely charged particles are attractive, and therefore act as bonds in the gel.

4.3.3 Clusters

Once particle contacts have been defined, we can also define *clusters* of particles, by saying that any two particles in contact are members of the same cluster. Thus the cluster identity can be propagated out to neighbor after neighbor, and a continuous cluster defined. Indeed, one potential definition of a colloidal gel is a system with a cluster which spans the volume

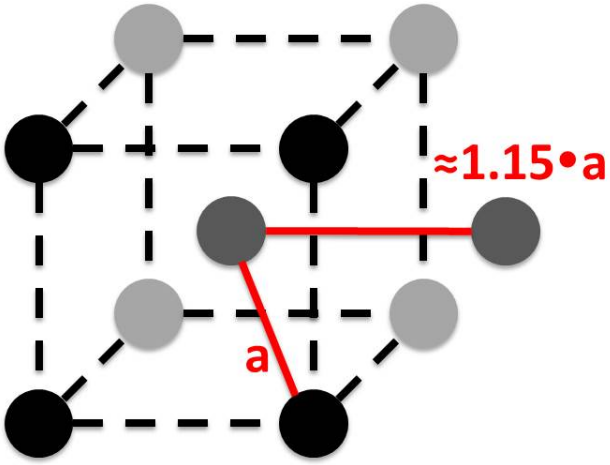

Figure 4.7: Neighborhood of a particle in a b.c.c. crystal. Shading indicates depth. The body-centered particle (dark grey) has eight nearest-neighbors at the corners of the cube, and six next-nearest-neighbors (only one shown) at the body-centers of the adjacent cubes; the next-nearest-neighbor distance is $(2/\sqrt{3})\,a \approx 1.15a$, only slightly greater than the nearest-neighbor distance.

in all dimensions.

4.3.4 Crystallographic neighbors

These last two measures, of contact number distribution and cluster identification, were relevant to the binary system in which I was interested in locally dense gels, and fluids of clusters which approached a gel. In the Wigner system, in contrast, the repulsive interactions among all particles preclude particle contacts as such. The structures of interest are not the locally dense clusters, but rather the *crystalline lattice* formed by the particles even at relatively low volume fraction.

In particular, I found it useful to distinguish crystallographically the nearest-neighbors and next-nearest-neighbors of a particle. In a perfect b.c.c. lattice, a particle has eight nearest-neighbors, and six next-nearest-neighbors, which are only 15% further away than the nearest-neighbors (Fig. 4.7). In the fluctuating Wigner system, these nearest-neighbor and next-nearest-neighbor shells overlap, so that on occasion, a particle in the nearest-neighbor position is farther away than a particle in the next-nearest-neighbor position. Thus to study the crystal, it is essential to identify neighbors not by distance, but by position in the crystal.

This is easy to do visually, and not too challenging to translate into a quantitative method. As far as I am aware, this is not analysis that has been done before in experimental colloid science, and so the algorithms, while straightforward, are all original. I identify the

neighbors in three steps: approximate the nearest-neighbors and next-nearest-neighbors by distances; from these approximate assignments, identify the most frequent angles at which nearest-neighbors and next-nearest-neighbors appear; and then use these angles to identify true crystallographic nearest-neighbors and next-nearest-neighbors.

The first step, approximating nearest- and next-nearest-neighbors by distance, is straightforward. Much as in the first step of calculating the r.d.f., for each particle I first calculate the distance to every other particle. The eight closest particles are tentatively identified as nearest-neighbors, while the next six are tentatively identified as next-nearest-neighbors. As hinted at above, some of these tentative definitions turn out to be incorrect – nearest-neighbors fluctuate farther from the particle as next-nearest-neighbors fluctuate closer, and particles near an image boundary or defect may have an incomplete complement of neighbors, so that farther neighbors are counted among the closest fourteen. Still, in all cases I tried but one, this tentative assignment was more than adequate.

The next step is to identify the angles (θ, ϕ) describing the position of each of these fourteen neighbors relative to the reference particle. Histogramming the angles of the eight closest neighbors exhibits eight bright peaks, corresponding to the angles of crystallographic nearest neighbors (Fig. 4.8a). Several fainter peaks correspond to next-nearest-neighbors which had fluctuated into the nearest-neighbor shell. Histogramming the angles of the next six closest neighbors brings out the same peaks that appeared faintly in Fig. 4.8a, corresponding to the angles of crystallographic next-nearest-neighbors (Fig. 4.8b). Again, faint peaks represent both nearest-neighbors which fluctuated far away, and further neighbors which had fluctuated close, or been counted among the fourteen closest due to missing neighbors. This of course only works for single-crystal images; if there is a grain boundary in the imaging volume, the histogram will show a mixture of the angles for the two crystal orientations, and be much more difficult to interpret.

We pick out quantitatively these brightest peaks, by calculating the mass of each peak, that is, the total brightness over a region around the maximum value.[3] The center-of-mass of each peak is identified as a 'typical angle' for nearest-neighbors (eight brightest peaks of the histogram from the eight closest neighbors) or next-nearest-neighbors (six brightest peaks of the histogram from the next six closest neighbors).

[3]We fairly arbitrarily use a 39x39 histogram, and 5x5 squares to calculate the mass. Histogramming spherical angles into equal bins in each angular component is of course geometrically nonsense, and as of writing, peaks near edges of the histogram are simply cut off rather than wrapping around the sphere to the opposite edge; however, the results of these calculations are 'good enough' to identify neighbors.

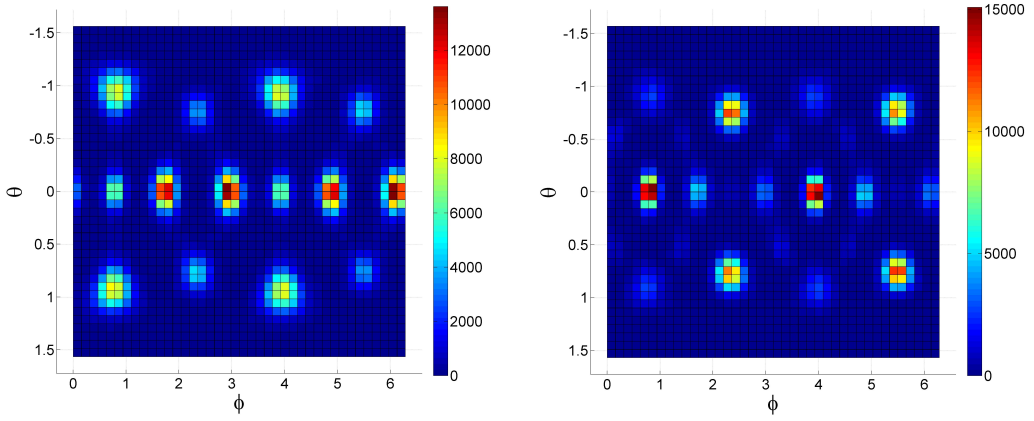

(a) (b)

Figure 4.8: Close neighbor orientations in a crystal. a) Histogram of the spherical angles (θ, ϕ) (relative to the imaging coordinates) giving the directions from a reference particle to its eight closest neighbors. Note that there are eight bright peaks containing most of the total mass, which correspond to the eight nearest-neighbor directions in the b.c.c. lattice. Six fainter peaks hint at next-nearest-neighbors which are included in the eight closest neighbors either due to fluctuations or due to missing nearest-neighbors (e.g. at the image boundaries). b) Histogram of the spherical angles giving the directions from a reference particle to its next six closest neighbors. Note the six bright peaks corresponding to the six next-nearest-neighbor directions in the b.c.c. lattice. The nearest-neighbor peaks in (a) also appear in (b) – hinting at fluctuations of nearest-neighbors to greater distances – as do several faint peaks at third-nearest-neighbor directions. These fourteen peaks are used to define the 'typical angles' to identify the crystallographic nature of neighbors in the b.c.c. lattice.

With these fourteen 'typical angles' in hand, we go back to the list of the fourteen closest neighbors of each particle. For each neighbor, we determine whether the angle of the displacement to that neighbor falls sufficiently close to one of the typical neighbor angles; if so, we identify it with that crystallographic position, and so as a nearest- or next-nearest-neighbor. If the angle is too far from any of the typical angles, we classify the neighbor as falling outside these two nearest shells (e.g. it may be a next-next-nearest neighbor). We thus have an identification of crystallographic nearest-neighbors and next-nearest-neighbors based upon position in the crystal, rather than on distance alone.

4.3.5 Average lattice

The identification of crystallographic neighbors is a local definition of crystalline ordering; the next extension is to identify the global ordering, the *average lattice* of the crystalline sample. While this average lattice is easy to identify by eye, it takes several steps to define quantitatively. I will here describe the process of calculating the average lattice from a set of particle locations. As with the neighbor identification, this is the first example I have seen of explicitly calculating an average lattice for an experimental colloidal system.

Parameters of a lattice

A generic three-dimensional crystal is defined by three lattice vectors defining the edges of a unit cell, requiring a total of nine components. There may also be an offset between the origin of the measurement frame and that of the crystalline frame, requiring three additional components, for a total of twelve parameters to describe the crystalline lattice. Finally, if there is more than one particle per unit cell, the structure within the unit cell must be specified, defining the location of each particle in the unit cell, and giving three more components per additional particle.

In fact, I reduce the number of free parameters for my lattice by imposing the constraint of a b.c.c. structure – this is justified both visually and by the r.d.f., and confirmed by the goodness of the resulting average lattice. I define the unit cell to be the *cubic* cell containing two particles: one particle at the corner of the cell, $(0, 0, 0)$, and the second particle at the body center at lattice coordinates $(1/2, 1/2, 1/2)$. The cubic cell has only four free parameters instead of nine: the lattice vectors are required to be of the same length (reducing three length parameters to one), and orthonormal (reducing the six angles needed to describe the

three lattice vectors to only three). The overall offset of the origin still requires an additional three components.

Describing the lattice explicitly by three angles is awkward; I instead define the lattice by its rotation matrix, which takes the X, Y, and Z directions of the imaging frame to the directions of the lattice cubic axes. The description is equivalent, in that the rotation matrix and three angles can be determined from one another.

Thus I define a lattice by three quantities: 1) the *cube side*, which gives the single length scale, the length of an edge of the cubic lattice; 2) the *rotation matrix*, a 3x3 orthonormal matrix defining the rotation from the imaging frame to the lattice coordinates; and 3) the *offset*, a 3-element vector giving the origin of the lattice in the coordinates of the imaging frame. In total, these comprise seven free parameters that must be calculated from typically 1000-2000 three-dimensional particle locations.

Note that this description is equally good for any cubic lattice; only the structure within the unit cell will differ. The algorithms I wrote are thus generalizable to e.g. f.c.c. crystals, with the unit cell structure a parameter which can be specified by the user.

We now have two reference frames, which can require some attention to keep straight: the 'imaging coordinates', measured in microns, with the X and Y directions defining the plane of the 2D confocal slices, and the Z direction the optical axis; and the 'lattice coordinates', measured in multiples of the lattice cube side l, with the X, Y, and Z directions along the cubic axes of the lattice. The lattice parameters are defined so that the geometric transformations between one frame or coordinate system and the other are given by:

$$\begin{pmatrix} x_{\text{lattice}} \\ y_{\text{lattice}} \\ z_{\text{lattice}} \end{pmatrix} = \frac{1}{l} \cdot \mathcal{R} \cdot \left[\begin{pmatrix} x_{\text{image}} \\ y_{\text{image}} \\ z_{\text{image}} \end{pmatrix} - \begin{pmatrix} x_{\text{offset}} \\ y_{\text{offset}} \\ z_{\text{offset}} \end{pmatrix} \right]$$

and

$$\begin{pmatrix} x_{\text{image}} \\ y_{\text{image}} \\ z_{\text{image}} \end{pmatrix} = \left[l \cdot \mathcal{R}^{-1} \cdot \begin{pmatrix} x_{\text{lattice}} \\ y_{\text{lattice}} \\ z_{\text{lattice}} \end{pmatrix} \right] + \begin{pmatrix} x_{\text{offset}} \\ y_{\text{offset}} \\ z_{\text{offset}} \end{pmatrix}$$

where l is the lattice cube side, $\mathcal{R}$ the rotation matrix, and $\mathbf{r}_{\text{offset}}$ the offset vector.

Initial estimation

The calculations of the nearest- and next-nearest-neighbors in fact provide a sound basis for an initial estimate of the average lattice. In particular, the next-nearest-neighbors fall on the corners of the lattice cube, and so the 'typical' angles to these next-nearest-neighbors provide estimates for the directions of the (cubic) lattice vectors, which are converted into an estimate for the orthonormal rotation matrix.[4]

The cube side is also obtained from the neighbor calculations. I used the peak of the distribution of distances to nearest-neighbors (mainly because this distribution is sharper than the distribution of distances to next-nearest-neighbors, which could also be used). For a b.c.c. lattice, nearest-neighbor distance a is related to the cube side l by $l = (2/\sqrt{3})\, a$.

For aesthetic reasons, I put the origin of the crystalline frame near the center of the image, and so chose this center as an initial estimate of the offset. This is a fairly empty estimate, but is quickly improved in the refinement process.

Refinement

These initial estimates are not bad (except for the offset), but they are subject to some noise and inaccuracy. We therefore refine the estimate of the average lattice, with a refinement step for each of the three lattice quantities.

Each refinement depends upon identifying each particle to a lattice position: this is done by transforming the imaging coordinates into lattice coordinates and rounding to the nearest lattice point. (Note that as we have a b.c.c. lattice structure, this may be at either (n, m, l) or $(n + 1/2, m + 1/2, l + 1/2)$ in lattice coordinates, with $n, m, l \in \mathbb{Z}$.) We then use the displacement of each particle from its lattice position (given in lattice coordinates) to determine errors in the lattice.

Refinement of the offset is the most straightforward. We posit that the mean displacement of a particle from its lattice position should be zero, averaged over all particles in the image. Thus we take the mean of particle displacements from the lattice, convert this from lattice coordinates to imaging coordinates, and add this mean to the estimated offset,

[4]To give more detail: starting with six typical angles, I first identify opposing pairs; within each pair, I reverse the direction of one of the pair so that they are roughly in the same direction, and then average to obtain the angle defining one of the three cubic lattice axes. I then convert these angles into unit vectors in the (imaging) (X,Y,Z) coordinates. I concatenate these vectors into a 3x3 matrix (identifying the lattice-Z-vector, that is the third column, as the one pointing closest to the imaging-Z-direction, and the lattice-X-vector, that is the first column, as that pointing closest to the imaging-X-direction), ensuring a right-hand-rule relationship among the columns. Finally I orthonormalize this matrix (using, for ease of implementation in Matlab, a QR decomposition) to obtain an estimate for the rotation matrix.

shifting our estimated lattice. If all particles remained associated with the same lattice position, this would result in a zero mean displacement; in fact, the shift of the lattice will generally change the associated lattice position for some particles, so that a recalculation of the lattice positions and displacements may result in a nonzero mean displacement. Particularly if the initial estimate was poor, a refinement may change the lattice assignments quite significantly. The first step of the refinement, then, is to iterate the refinement of the estimated offset a few times until it stabilizes to give only small changes.

Refinement of the cube side is not much more difficult. Consider one lattice direction, say the X-direction. If we have the correct cube side, the displacements of particles from their lattice positions will be random. If the estimate of the cube side is too small relative to the true lattice, this will appear as an apparent dilation: that is, the displacement ΔX from the erroneous lattice position will increase with X. Similarly, if the estimate of the cube side is too large, we will see an apparent compression, with displacement ΔX decreasing with increasing X (actually, ΔX will tend to be negative and increase in magnitude). We thus define the apparent dilation in the X direction as m_X, the best-fit slope to ΔX considered as a function of X. We find the apparent dilations in the Y and Z directions, m_Y and m_Z, in the same way. To refine the cube side, we take the average apparent dilation, $\delta = {}^1\!/_3(m_X + m_Y + m_Z)$, and scale the cube side by a factor $(1 + \delta)$. For a perfect cubic lattice, this should correct the cube side to match the average particle spacing so that there is no overall dilation. If the lattice is not perfectly cubic, and is slightly squeezed in one dimension relative to another, there may still be a nonzero dilation in individual dimensions; this is because we have constrained the lattice to have only one length scale, coupling the three length scales which may in fact differ slightly in an imperfect lattice. (It is also worth noting that this refinement only works well if the initial estimated lattice is already a good enough approximation to the true lattice that the error in the estimate manifests itself as an apparent dilation. For example, if the estimated cube side were half the true cube side, this algorithm would fail; it would interpret only one lattice position in eight as being occupied, but there would be no trend of displacement with position, that is, no apparent dilation.) In my experience, however, the initial estimate from the neighbor distance has almost always been an adequate point from which to refine the cube side.

Finally, we must refine the rotation matrix. The algorithm here is similar to that for the cube side: we calculate and correct for apparent rotatation of the particles relative to the estimated lattice. If the estimated lattice is rotated in the XY plane relative to the

true lattice, this will appear as a trend in displacements ΔX as a function of Y, and an opposite trend of ΔY as a function of X; thus we find the slopes of these trends, $m_{\Delta X,Y}$ and $m_{\Delta Y,X}$. We find the corresponding values for apparent rotations in the XZ and YZ planes, and form the initial correction matrix

$$\mathcal{C} = \text{asymm} \begin{pmatrix} 1 & m_{\Delta X,Y} & m_{\Delta X,Z} \\ m_{\Delta Y,X} & 1 & m_{\Delta Y,Z} \\ m_{\Delta Z,X} & m_{\Delta Z,Y} & 1 \end{pmatrix}$$

Where `asymm` indicates taking the anti-symmetric part, as we expect $m_{\Delta X,Y}$ and $m_{\Delta Y,X}$ to have opposite signs. Finally, we orthonormalize this matrix (much as we did our initial rotation matrix), and take our new estimate of the rotation matrix to be $\mathcal{R}' = \mathcal{R}\mathcal{C}$.

(As a geometrical note, we are essentially equating θ_Z, the rotation angle of the estimated lattice about the Z axis relative to the true lattice, with $1/2$ the Z-component of the mean curl of the apparent displacement field, $\partial(\Delta Y)/\partial(X) - \partial(\Delta X)/\partial Y$ (and likewise for rotations about the X and Y axes). This approximation is valid for small rotation angles.)

As with the refinement of the cube side, we also only expect this rotation refinement to work well if the lattice is already pretty good, but again, I have almost always found the initial estimate to be good enough.

Our overall refinement process, then, is to choose a tolerance to which we wish to refine, so that further refinements will change the parameter values by less than this tolerance. I make the initial estimate, and apply a few cycles of the offset refinement. I then iterate the process of refining the rotation matrix; refining the cube side; and refining the offset, keeping track of the magnitude of each correction, until all corrections are within tolerance. For a typical experiment, a tolerance of 0.1% will result in on the order of 10 iterations to converge on an average lattice.

One final note: most of my crystal experiments consist of ZT stacks, with three-dimensional information as a function of time. I chose to refine the average lattice at each time step independently from the other timesteps. This is not the only sensible choice – one might also ask what is the average lattice that best fits the system at all times, or even allow the offset to change (for drift) but not the cube side and rotation. I will discuss in Chapter 6 some of the results on the stability of the lattice with time.

With this average lattice in hand, we are well equipped to examine a number of measures

of displacements of the particles from their lattice positions; deformation of the average lattice; and defects in the lattice. I will next describe the calculation of local strains using the average lattice; other uses of the lattice will appear in Chapter 6.

4.3.6 Local strain

We now turn to a discussion of *strains* in the system. Indeed we have already begun discussing strains in the context of the lattice refinements, speaking of dilations and shears. So far these have been considered as global strains of the system, but we can also consider the local strain of the neighborhoods of individual particles.

How do we think about the *local* strain around a particle? The method I use is ultimately due to Falk and Langer [19], though I inherited the algorithm and the code from Peter Schall [64] and Kate Jensen [26]. Essentially, in order to define the strain 'of a particle', we consider a neighborhood of that particle, that is, the particle and some set of its close neighbors. We take the positions of the particles in that neighborhood, and some reference positions, and find the best *affine transformation* which describes the deformation from the reference to the true positions – that is, a matrix A so that for each neighbor, $\mathbf{r}' \approx A\mathbf{r}$ with $\mathbf{r}'$ the true position relative to the central particle and $\mathbf{r}$ the reference position. In the small-deformation limit, this transformation consists of rotation, dilation and/or compression, and shear, in each of the three dimensions. We ignore the rotation (the antisymmetric part), but take the dilation and shear components (the symmetric part) to be the *local strain*.

Computationally, the affine transformation matrix is obtained by taking $(\sum \mathbf{r}'.\mathbf{r}) * (\sum \mathbf{r}.\mathbf{r})^{\dagger}$, where . indicates an outer product and the sums are over all the neighbors used. The $\mathbf{r}$ are taken relative to the position of the central particle (which may itself move, introducing a translation). The symmetric part of this matrix is

$$\text{symm } \mathcal{A} = \begin{pmatrix} (1+\epsilon_{xx}) & \epsilon_{xy} & \epsilon_{xz} \\ \epsilon_{yx} & (1+\epsilon_{yy}) & \epsilon_{yz} \\ \epsilon_{zx} & \epsilon_{zy} & (1+\epsilon_{zz}) \end{pmatrix}$$

Note that the off-diagonal elements give ϵ_{ij} rather than e_{ij}; since the symmetry enforces $\epsilon_{ij} = \epsilon_{ji}$, we must simply multiply by a factor of 2 to get $e_{ij} = 2 \cdot \epsilon_{ij}$.

Some considerations to be taken are 1) how to define the neighborhood, and 2) what reference positions to use. As mentioned, I learned this calculation from Kate, who had

been using it on amorphous systems, and both of my considerations are different from hers.

The 'neighborhood' I defined by all particles assigned to lattice positions within one cube side of the central particle – that is, all nearest- and next-nearest-neighbors.[5] This should result in up to 14 neighbors. I required that a particle have at least six such neighbors to perform the calculation, so that some particles near the image boundary were too neighbor-poor to calculate a local strain.

For the reference positions, the identification of the lattice gives the happy result that I can use the lattice positions themselves as the references. Thus the local strain as I calculated it is informing us about the local deformation *from the average lattice*. (This is in contrast to Kate's method of using the particle positions at a previous timestep as references, all that was available for the amorphous case.)

I made one further consideration in reporting results based on local strains: I generally did not consider the strains calculated for particles within the nearest neighbor distance of the image boundaries – I found that this filter step did change the overall distribution of strains, with the particles near the boundaries having generally a broader distribution, hinting at artifacts due to missing neighbors and/or inaccurate positions.

4.4 Elastic moduli

Colloid physicists often estimate a shear elastic modulus, G', from the plateau of the mean-square displacement curve (see, for example, Section 5.5). We can make a more accurate estimate of the elastic modulus using the strain information, as the modulus is in fact defined via the energy required to produce a strain (this argument again follows [64]). The energy density required to generate a strain e is

$$u = \frac{1}{2}\mu e^2$$

where μ is the elastic modulus associated to the strain e. Thus for a volume V with an average strain e, the total energy required is

$$E = \frac{1}{2}\mu e^2 \cdot V$$

[5] If either the central lattice site, or any of the neighboring lattice sites, is occupied by a dimer, then both members of this dimer may be included; this extra particle may affect the strain calculation. As dimers are rare, I hope this does not have a large effect on the distributions of strains.

We now invoke the assumption that my systems are thermally activated: there is no externally imposed stress or strain, and so any strain in the system is driven by the thermal energy k_BT. We thus expect the distribution of strain energies to follow a Boltzmann distribution:

$$P(E) \propto \exp\left(-\frac{E}{k_BT}\right) = \exp\left(-\frac{\mu e^2 \cdot V}{2k_BT}\right)$$

Thus from the distribution of strains-squared, $P(e^2)$, we can determine the elastic constant μ.

To explicitly calculate μ, we first select an averaging volume V, and calculate the *average* strain e_V within each voxel. The elastic modulus will actually vary somewhat with lengthscale, from the continuum limit of large lengthscale down to the discrete limit where the lengthscale is that of the particle separation. The averaging volume should be chosen to access the lengthscale of interest – usually this ends up being a compromise between considering a large lengthscale, where the elastic modulus is more meaningful as we approach the continuum limit, and obtaining adequate statistics from a limited sample volume. For the b.c.c. crystals, I chose a volume $V = (2l)^3$, that is, a cube of side two lattice cube sides, comprising 16 lattice positions. Taking these volume-averaged strains, we subtract off the average value (this is generally very small), and square the strains to obtain a list of e_V^2, which is proportional to the strain energy in each voxel.

We now wish to determine the probability distribution $P(E)$ of these strain energies, and make a fit to the expected exponential form to evaluate the elastic modulus. In principle this sounds straightforward, but in practice, the determination of the distribution proves to have some subtlety. To give the distribution of a finite list of values, we must choose the size of the bins into which we classify the values, that is, the resolution of our histogram. This choice of bin size turned out to have a surprisingly large effect on the final result, the value of the elastic modulus calculated. Too small a bin size, and each bin would contain only a few values, so that the counts $P(E)$ which we are hoping to fit include large Poisson noise. Too large a bin size, and we have only a few bins, so that we are fitting to only a few values. The particular choice of bin size changed the calculated value of the modulus by as much as a factor of two for e.g. a fifty-fold change in bin size, with small bin sizes tending to give larger values of the modulus. Furthermore, the 'best' bin size depends on the size of the list, and on the yet unknown modulus we are trying to calculate!

I thus determined the optimum bin size for each fit by an iterative process. Since

histogramming and fitting is computationally fairly cheap, I started by doing the fit using a range of different bin sizes. I took the R^2 goodness of fit parameter (adjusted for the number of degrees of freedom, returned by the Matlab fitting function) as a metric of the fit. As shown in Fig. 4.9, as we increase the bin size, the modulus drops as the goodness of fit rises, giving way to a region where the modulus is relatively insensitive to bin size (always a good sign!), followed by some fluctuations in the modulus and a sudden drop in both goodness of fit and modulus. Examination of these results suggests that the optimum bin size is somewhere in that stable region of high goodness of fit. We chose the optimum bin size, and then carried out the optimization twice more, with increasingly fine gradations of bin size to narrow in on a good result.

Note that as long as we are in the stable region, the precise bin size does not strongly affect the modulus calculation. In particular, the reported confidence interval on the value of the modulus is larger than the spread of moduli within the stable region, so that the error bars reported contain the small uncertainty due to the bin size selection.

Having at last selected the optimum bin size, we are equipped to carry out the final fit. We first scale the strain-squared by $E/\mu kT = \frac{1}{2}e_V^2 * V/kT$, with $V = (2l)^3$ as described above, and $T = 296$K room temperature. We then histogram these scaled energies to obtain $P(E)$.

Here we note another complication: $P(E)$ appears exponential (that is, linear on a semi-logarithmic plot) for larger values of E, but increases rapidly as $E \to 0$ (see Fig. 4.9c). The reason for this is still not understood. My best understanding is that it is a result of the Falk-and-Langer method of calculating the strains. In particular, the same behavior is evident if I carry out the analysis on a model dataset consisting of a perfect b.c.c. lattice with added, uncorrelated Gaussian noise in the particle locations (the *Einstein model* of a solid). Fig. 4.9c shows a deviation for $e_V^2 \lesssim 0.003$, or $e_V \lesssim 5\%$; over 2 lattice spacings, this corresponds to a displacement of about 370μm, or 20% of the particle diameter, larger than our expected uncertainty in the particle locations.

We use the large-E exponential tail of the $P(E)$ distribution to calculate the elastic modulus, in spite of the mysterious behavior at small-E. The last piece of the calculation then is to define the boundaries of the fit, to restrict to the exponential tail. This definition is somewhat arbitrary, supported by eyeballed estimates: I define the largest bin so as to cut off all bins with a count smaller than 3, and define the smallest bin as 1/4 of the largest, which generally cuts off the small-E region well. I then perform a linear fit to

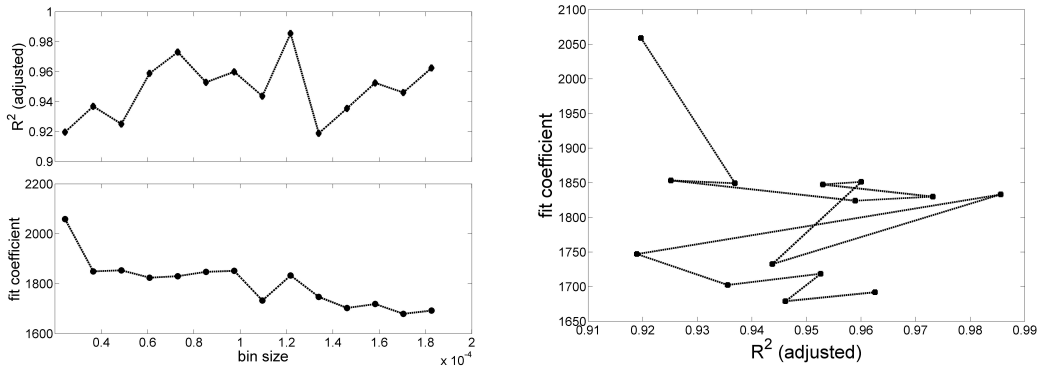

(a)

(b)

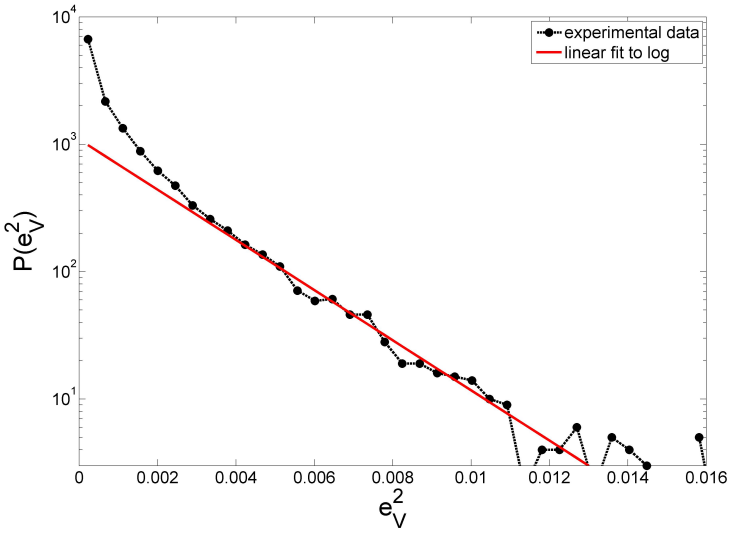

(c)

Figure 4.9: Determination of fit parameters for calculations of elastic moduli. (a-b) Selection of optimum bin size based on goodness-of-fit. a) R^2 goodness-of-fit metric (adjusted for number of degrees of freedom) and fit coefficient (proportional to estimate of modulus) as a function of bin size for an exemplar strain distribution (ϵ_{xy} for a b.c.c. crystal at $n = 0.054(\mu m)^{-3}$). b) Same data as in (a) replotted as coefficient vs. R^2. Note that the fits with the highest R^2 metric have very similar values of the coefficient around ≈ 1850. c) Strain-squared distribution using optimum bin size; note the exponential behavior at large e_V^2, and the deviation for small e_V^2.

$\log(P(E)) = -\mu(E/\mu kT) + P_0$: μ, the negative of the slope, gives the elastic constant (in Pa), while the 95% confidence interval on μ gives the reported error bars. Fig. 4.9c shows an example of this fit.

As mentioned above, the identity of the modulus μ thus calculated depends on the nature of the strains e used in the calculation; this relationship is described in the next subsection. When we have multiple strain components which are expected to correspond to the same modulus (e.g. three independent shear strains e_{xy}, e_{xz}, and e_{yz}), we calculate the modulus from their aggregated distribution; the aggregation is carried out *after* the tiling and the subtraction of the average value.

4.4.1 Crystalline elastic constants and strain components

As discussed in Section 1.5.4, a cubic crystal has three independent elastic constants, c_{11}, c_{12}, and c_{44}; we would like to determine values for each of these constants. Recall the total strain energy density is expressed as (see e.g. Kittel [31], p. 78)

$$u = \frac{1}{2}c_{11}(e_{xx}^2 + e_{yy}^2 + e_{zz}^2) + c_{12}(e_{xx}e_{yy} + e_{xx}e_{zz} + e_{yy}e_{zz}) + \frac{1}{2}c_{44}(e_{xy}^2 + e_{xz}^2 + e_{yz}^2)$$

where the x, y, and z axes are the cubic axes of the crystal.

Note that the shear strains e_{xy}, e_{xz}, e_{yz} each decouple from the other strains. In particular for thermally-excited strains,

$$P(\bar{\bar{e}}) \propto \exp(-uV/k_BT) \propto \exp(-c_{44}e_{xy}^2 V/2k_BT) \cdot f(\text{other strain components})$$

Thus c_{44} can be estimated from the distribution of any of e_{xy}, e_{xz}, or e_{yz} using the process already described, independent of any other strain component.

Not so with the tensile strains e_{xx}, e_{yy}, and e_{zz}; these couple to one another through c_{12}, and so cannot be neatly separated. In order to evaluate c_{11} and c_{12}, therefore, we do not use the distributions of the tensile strains in the same way. Rather, we directly evaluate two other elastic constants: the 'rotated shear modulus', and the bulk modulus.

To calculate the 'rotated shear modulus', we consider a coordinate system which is

rotated by 45° around one of the cubic axes, e.g., we transform the particle coordinates via

$$\begin{pmatrix} x' \\ y' \end{pmatrix} = \frac{1}{\sqrt{2}} \begin{pmatrix} 1 & 1 \\ -1 & 1 \end{pmatrix} \begin{pmatrix} x \\ y \end{pmatrix}$$

We then *recalculate* the strains in this x'-y'-z frame. The 'rotated shear strain' $e_{x'y'}$ again decouples from the other strains, so that

$$P(\bar{\bar{e}}) \propto \exp\left(-\mu_{x'y'}\, e_{x'y'}^2 \cdot V/2k_BT\right) \cdot f(\text{other strain components})$$

This allows us to use the method of fitting the distribution to calculate the rotated shear modulus $\mu_{x'y'}$. As given in Section 1.5.4, this can be expressed in terms of c_{11} and c_{12} as

$$\mu_{x'y'} = \frac{1}{2}(c_{11} - c_{12})$$

We need another strain component which can be decoupled, for which we use the total dilation $\delta = \mathrm{Tr}(\bar{\bar{e}}) = e_{xx} + e_{yy} + e_{zz}$. This dilation is governed by the *bulk modulus* B:

$$u = \frac{1}{2}B\delta^2 + f(\text{other strain components})^6$$

We thus calculate B by fitting the exponential distribution of the dilations-squared δ^2 as above. B can also be expressed in terms of c_{11} and c_{12} as

$$B = \frac{1}{3}(c_{11} + 2c_{12})$$

(see again Section 1.5.4).

From $\mu_{x'y'}$ and B, we can thus immediately obtain

$$c_{11} = B + \frac{4}{3}\mu_{x'y'}$$
$$c_{12} = B - \frac{2}{3}\mu_{x'y'}$$

[6]To explicitly realize the decoupling, we can define $\alpha \equiv e_{xx} - e_{zz}$ and $\beta \equiv e_{yy} - e_{zz}$; then

$$\begin{aligned} u &= \frac{1}{2}B\delta^2 + \frac{1}{2}(c_{11} - B)(\alpha^2 + \beta^2) + (c_{12} - B)\alpha\beta \\ &= \frac{1}{2}c_{11}(e_{xx}^2 + e_{yy}^2 + e_{zz}^2) + c_{12}(e_{xx}e_{yy} + e_{xx}e_{zz} + e_{yy}e_{zz}) \end{aligned}$$

gives the non-shear contribution of the total energy density. Using the expression for B in the text, the equality is confirmed by straightforward algebra. Thus δ is decoupled, although α and β are not.

This discussion has been rather involved, so let me summarize our method of calculating the elastic constants c_{11}, c_{12}, and c_{44} for a colloidal crystal:

- Calculate the strain tensor $\bar{\bar{e}}$ as described in Section 4.3.6.
- Calculate also three strain tensors $\bar{\bar{e}}'_{\{x,y,z\}}$ with the particle coordinates rotated by 45° about the crystalline X, Y, and Z axes respectively.
- Calculate c_{44} from the distribution of shear-strain energies, as the exponential coefficient μ of $P(e^2) \propto \exp(-\mu e^2 \cdot V/2k_BT)$ where $e = \{e_{xy}, e_{xz}, e_{yz}\}$ (shear with respect to crystal axes, aggregate list).
- Calculate μ'_{shear} from the distribution of rotated shear-strain energies as the exponential coefficient μ of $P(e^2) \propto \exp(-\mu e^2 \cdot V/2k_BT)$ where $e = \{e_{x'y'}, e_{x'z'}, e_{y'z'}\}$ (shear in rotated frames, aggregate list).
- Calculate the bulk modulus B from the distribution of dilation energies as the exponential coefficient μ of $P(e^2) \propto \exp(-\mu e^2 \cdot V/2k_BT)$ where $e = \delta = (e_{xx} + e_{yy} + e_{zz})$ (total dilation in original frame).
- Calculate c_{11} and c_{12} from B and μ'_{shear} using the given equations.

4.4.2 Estimation of elastic constants from Yukawa model

We also make back-of-the-envelope numerical calculations of the elastic constants for particles on a b.c.c. lattice interacting via the Yukawa potential, by calculating the energy density as a function of strain. I assume a two-body Yukawa interaction,

$$U(r) = U_0 \frac{\exp(-\kappa r)}{r}$$

with U_0 and κ fixed, and a b.c.c. structure with lattice cube side l. I include the 64 nearest neighbors in the calculation (that is, the first six neighbor shells, containing 8, 6, 12, 24, 8, and 6 neighbors, respectively). Then the total energy per particle, given a strain e, is explicitly computed over a range of e as

$$U(e)/\text{particle} = \frac{1}{2}\sum_{i=1}^{64} U(r_i(e))$$

where $r_i(e)$ is the distance to neighbor i given strain e (see the Appendix for the full expressions). Dividing by the volume per particle gives the energy density $u(e) = 2(U(e)/\text{particle})/l^3$, and taking the (numerical) second derivative of energy density with respect to strain e gives the elastic constant, $\mu = d^2u(e)/de^2$. This calculation is made for a shear strain e_{xy}, giving c_{44}; a tensile strain e_{xx}, giving c_{11}; and an isotropic dilatation, $e_{xx} = e_{yy} = e_{zz} = {}^1\!/_3\,\delta$, giving B. c_{12} and μ'_{shear} are then calculated from B and c_{11}. I then repeat the calculation for different lattice cube sides l (corresponding to different number densities n).

4.5 Correlations

Finally, we approach the collective behavior of the system by calculating *correlations* – a correlation is essentially a measure of, 'If my state is such-and-such, what can I say about the state of that guy over there?' Correlations have of course already been hinted at in the radial distribution functions – a non-unity r.d.f. indicates correlations of position. But what other and more explicit information can we get about 'that guy over there'?

The mathematical calculation of a correlation is straightforward enough; the normalized correlation of quantity x is given by

$$C_x(\mathbf{\Delta r}) = \frac{\Big\langle \Big(x(\mathbf{r}) - \big\langle x(\mathbf{r})\big\rangle\Big) \cdot \Big(x(\mathbf{r}+\mathbf{\Delta r}) - \big\langle x(\mathbf{r})\big\rangle\Big)\Big\rangle}{\Big\langle \Big(x(\mathbf{r}) - \big\langle x(\mathbf{r})\big\rangle\Big)^2\Big\rangle}$$

where the averages are over reference position $\mathbf{r}$. Note that we subtract the mean value of x. The displacement $\mathbf{\Delta r}$ is the relative position of 'that guy over there' – if I know x here, the correlation $C_x(\mathbf{\Delta r})$ tells me what on average is x at a relative position $\mathbf{\Delta r}$ away. A correlation of 1 means that 'that guy over there' always has the same value of $(x - \langle x\rangle)$ as I do, no matter what $\mathbf{r}$ I start from. A correlation of 0 means I have no clue what 'that guy over there' is doing – he could be up to anything. A negative correlation means 'that guy over there' is doing the opposite of whatever I'm doing (relative to the mean).

Of course, in a discrete system of particles, $x(\mathbf{r})$ is not defined for all $\mathbf{r}$; rather it is only defined at particle positions $\{\mathbf{r}_i\}$. Thus the correlation must be calculated for voxels large enough that enough relative displacements of particles $(\mathbf{r}_i - \mathbf{r}_j)$ fall into the voxel to provide a good average.

In calculating correlations on the Wigner system, I again made use of the lattice positions, and generally instead of using the true displacement $(\mathbf{r}_i - \mathbf{r}_j)$, I used the displacement of

the particles' lattice positions. That is, I asked, What is my nearest neighbor doing? or my next-nearest neighbor? where neighbors were defined crystallographically. (This of course made the $\mathbf{\Delta r}$ discrete as well, being simply allowed lattice vectors.)

4.6 How to make Matlab faster

Let me finish by giving a few brief words of advice on lessons I learned in speeding up Matlab codes. Note that because Matlab is built around the array, these tips are specific to the language. They are not deep, but they may be useful to others who wish to use Matlab.

- I will start by reiterating a central tenet of working in Matlab: it is almost always more efficient to do array operations than to do `for` loops. If you have a `for` loop, try everything you can think of to get rid of it. It's not always possible, but it is more often than you may think at first.

- It is a central tenet of computer programming in general that the less you have in your active memory / workspace, the faster things will run. If you are done with a large variable, clear it before carrying on further computations.

- It is faster to subtract a scalar value from an individual row column than to create an array repeating that scalar value and subtract the array. Thus even when I wanted to subtract the same three-element vector from every row of a particle location array, the fastest way to do this was to subtract the corresponding value from each column individually.

- If data are to be discounted for a particular calculation, throw them away as early in the computation as possible, to minimize the size of the data structure(s) which must be manipulated. For example, in identifying particle neighbors, I would discard particles which were 'very far away' before sorting the list of particles by distance – the precise definition of 'very far' was not important, but I was able to speed up the calculation by shortening the list which needed to be sorted.

Chapter 5

Results: Colloidal Gelation of Oppositely Charged Particles

At last we reach the meat of this dissertation: the actual science I have to contribute. In this and the next chapter, I shall describe the results of the experiments and analysis so painstakingly described in the preceeding chapters. There will be some repetition of what has been more throughly treated already, in order that each of these chapters stand on its own.

The majority of this chapter has already been published by the Royal Society of Chemistry in the journal *Soft Matter* as "Colloidal gelation of oppositely charged particles" [60], co-authored with Joris Sprakel, Tom Kodger, and my advisor Dave Weitz. To the text of this paper, I have added Section 5.5, containing extended speculations, observations, and ideas for future directions, which were not included in the published paper, along with a paragraph added to the conclusion discussing the relationship of my results to others' work I have become aware of since publication. The rest of the paper is left intact, including the abstract. The work described was carried out in collaboration with Joris, then a postdoc in the group, and Tom, a fellow graduate student in the group. Tom synthesized the particles which I used, using a technique developed by himself and Joris along with Rodrigo Guerra; I carried out the experiments and analysis, with advice and suggestions from both Tom and Joris, and wrote most of the manuscript, with suggestions from the other co-authors. This chapter is also – like all my analysis – indepted to Kate Jensen for advice on particle location and tracking, and the use of her tracking code.

E. R. Russell, J. Sprakel, T. E. Kodger, and D. A. Weitz. Colloidal gelation of oppositely charged particles. *Soft Matter*, 8:8697–8703, 2012 - Reproduced by permission of The Royal Society of Chemistry.

5.1 Abstract

Colloidal gelation has been extensively studied for the case of purely attractive systems, but little is understood about how colloidal gelation is affected by the presence of repulsive interactions. Here we demonstrate the gelation of a binary system of oppositely charged colloids, in which repulsive interactions compete with attractive interactions. We observe that gelation is controlled by varying the total volume fraction, the interaction strength, and the new tuning parameter of the mixing ratio of the two particle types, and present a state diagram of gelation along all these phase-space coordinates. Contrary to commonly studied purely attractive gels, in which weakly quenched gels are more compact and less tenuous, we find that particles in these binary gels form fewer contacts and become more tenuous as we approach the gel point. This suggests that a different mechanism governs gel formation and ultimate structure in binary gelation: particles are unable to form additional favorable contacts through rearrangements, due to the competition of repulsive interactions between similarly-charged colloids and attractive interactions between oppositely-charged colloids.

5.2 Introduction

Colloidal gels are remarkable materials, their solid-like properties being determined primarily by a network of particles which make up a relatively small fraction of the total volume. The mechanisms controlling the formation and properties of colloidal gels offer interesting fundamental questions which have been extensively studied, and there is now a good understanding of how the formation and structure of purely attractive colloidal gels are governed by the particle volume fraction, depth of attraction, and range of interaction [7, 14, 15, 16, 33, 42, 49, 51, 66, 75, 76, 88]. It is clear that the formation of a space-filling network at low volume fraction requires attractive interparticle interactions in order to form stress-supporting bonds between particles. Surprisingly, colloidal gelation can also take place in systems where repulsive interactions compete with attractive interactions [44, 78]. Several examples of colloidal gels have been observed in binary suspensions of particles which

carry opposite electric charges, in which repulsive interactions between similarly-charged particles are present in addition to the attractive interactions between oppositely-charged particles which drive gelation [8, 48, 58, 62, 69]. Such binary colloidal gels exhibit a rich behavior, yet the conditions under which they form, and the physical mechanisms governing their properties, are not yet well understood.

Here we introduce a new experimental model system which allows us to study the colloidal gelation of oppositely charged particles, and determine the state diagram describing the circumstances under which a gel forms. We demonstrate that the mixing ratio of the two particle types can be used as a tuning parameter, controlling the formation and structure of the gels. Unexpectedly, we find that unlike in purely attractive gels [14, 16], the number of contacts a particle forms in a binary gel decreases as we approach the transition to the fluid state; this decrease in contact number is invariant whether this gel line is approached by changing the interaction strength or by changing the mixing ratio. This suggests that screening of the charges, either through addition of small electrolyte ions, or through microscopically large macro-ions, is the main mechanism tuning the gelation process and final structure of the binary colloidal gels.

5.3 Experimental

Particles with a diameter of 2μm are polymerized from tert-butyl methacrylate and trifluoro ethyl methacrylate [32], a copolymer combination which permits both the refractive index and the density of the particles to be matched by a polar solvent mixture of formamide and sulfolane. Refractive index matching minimizes scattering of light by the particles, allowing us to visualize the interiors of bulk samples, and obtain precise information about the three-dimensional structure and dynamics of these gels, using confocal microscopy. Density matching minimizes the effects of buoyancy, which if present can dramatically alter the structure of a colloidal gel and the location of the gel line [65]. After synthesis, a single batch of seed particles is split in two portions; each portion is then fluorescently dyed, and given either a positive or a negative electric charge by polymerizing a strong polyelectrolyte brush from initiators incorporated on the particle surface [32]. The positively charged brush is a random copolymer of cationic (3-acrylamidopropyl)trimethylammonium and neutral *N,N*-dimethylacrylamide, while the negatively charged brush is a copolymer of anionic 2-acrylamido-2-methyl-1-propanesulfonic acid with the same neutral monomer. Using the

same seed batch for both the positively and negatively charged particles ensures that the two particle types have equal sizes and distributions. Two different fluorophores, both from the BODIPY family, with non-overlapping excitation and emission spectra, are used so that the two populations of particles are readily distinguished in the confocal microscopy experiments, and can thus be tracked and analyzed separately.

Interactions between the polyelectrolyte brushes govern the interparticle interactions, and vary with the addition of an indifferent electrolyte to the solution. Similarly-charged particles are repulsive; in a polar solvent at moderate salt concentrations, the repulsion is primarily due to the steric interaction of the brushes. Only at separation distances smaller than the Debye length, which is in the range of 1nm in the present study, does electrostatic repulsion become important. Oppositely-charged particles experience an attractive interaction; recent AFM work suggests that this attractive interaction is due to the interpenetration of the oppositely-charged brushes as they form a polyelectrolyte complex [70]. The strength of the attraction is tuned by the addition of monovalent salt; at higher concentrations, the salt ions screen the interaction between the charge groups in the polymer brush, and make the formation of the polyelectrolyte complex less favorable.

We use sodium chloride as our indifferent electrolyte, and confirm that our system works as expected: similarly-charged particles do not aggregate at any salt concentration up to $c \approx 1$M, indicating that their stability is indeed due to steric interactions rather than charge repulsion. When we mix oppositely-charged particles in a solution with no added salt, they aggregate strongly, whereas with an added salt concentration of around $c \approx 0.5$M, oppositely-charged particles are stable against aggregation and behave as a hard-sphere fluid. This demonstrates that the attractive interaction can be tuned by salt concentration, and is stronger at lower salt concentrations.

We expect the thickness of the polyelectrolyte brushes to govern the range of the interparticle interactions, so that the range is nearly independent of salt concentration in most of our gel experiments. The polar solvent has a dielectric constant near that of water, $\epsilon \approx 80-100$; thus with the addition of even moderate amounts of salt, as in the experiments reported here, the screening length is on the order of $\kappa^{-1} \lesssim 1$nm, and all electrostatic interactions are short-range. The thickness of the polyelectrolyte brush is a few nanometers, several times longer than the screening length, and will dominate the interaction range. Thus the salt concentration controls only the strength of the attraction between oppositely-charged particles, while the repulsion between similarly-charged particles and the interaction range

are nearly constant over our experiments.

We use a confocal microscope (Leica SP5) to study the dynamics and the three-dimensional structure of binary mixtures of these charged colloids. The positively and negatively charged particles are imaged in separate channels, corresponding to the fluorescence emission spectra of the two fluorophores used. We obtain precise particle locations using standard algorithms to calculate the particle centroids [11, 20]. To analyze the structures, we use particle locations from fully three-dimensional image stacks, while we obtain the dynamics from two-dimensional images, allowing sequential images to be taken rapidly enough to clearly track the motion of individual particles. We vary the total particle volume fraction and the strength of the attraction between oppositely charged particles to compare our results to previous work with purely attractive gels. We also vary the mixing ratio R, defined as the ratio between the number of anionic particles and the number of cationic particles in the system.

For the most deeply quenched, strongest gels, we are also able to measure the viscoelastic moduli of bulk samples. We use a stress-controlled rheometer (Anton-Paar) in a cone-plate geometry. We subject samples to a large oscillatory pre-shear in order to break up networks or large clusters formed during loading; the amplitude of this pre-shear is then gradually decreased so that no preferred direction is imposed on the final structure of the sample. The pre-sheared sample is then equilibrated for 30 minutes with a very small oscillation imposed to measure the evolution of the elastic moduli during the reformation of the gel structure. Finally, a frequency sweep is performed to measure the storage and loss moduli G' and G''.

5.4 Results and discussion

We begin with the symmetric case $R = 1$, in which we mix equal numbers of postively charged and negatively charged particles. At the lowest salt concentrations studied, $c = 100$mM, and for total volume fractions in the range $\phi_{tot} \approx 0.05 - 0.20$, the particles form a colloidal gel, a space-filling network in which particle motion is arrested. Particles aggregate into a large cluster which spans the imaging volume, and very little particle motion occurs over several minutes, with the particles executing only small fluctuations around their average positions (Fig. 5.1a; note that apparently disconnected clusters in the two-dimensional image are connected in the third dimension). As we decrease the strength of the attraction between oppositely-charged particles by increasing the salt concentration

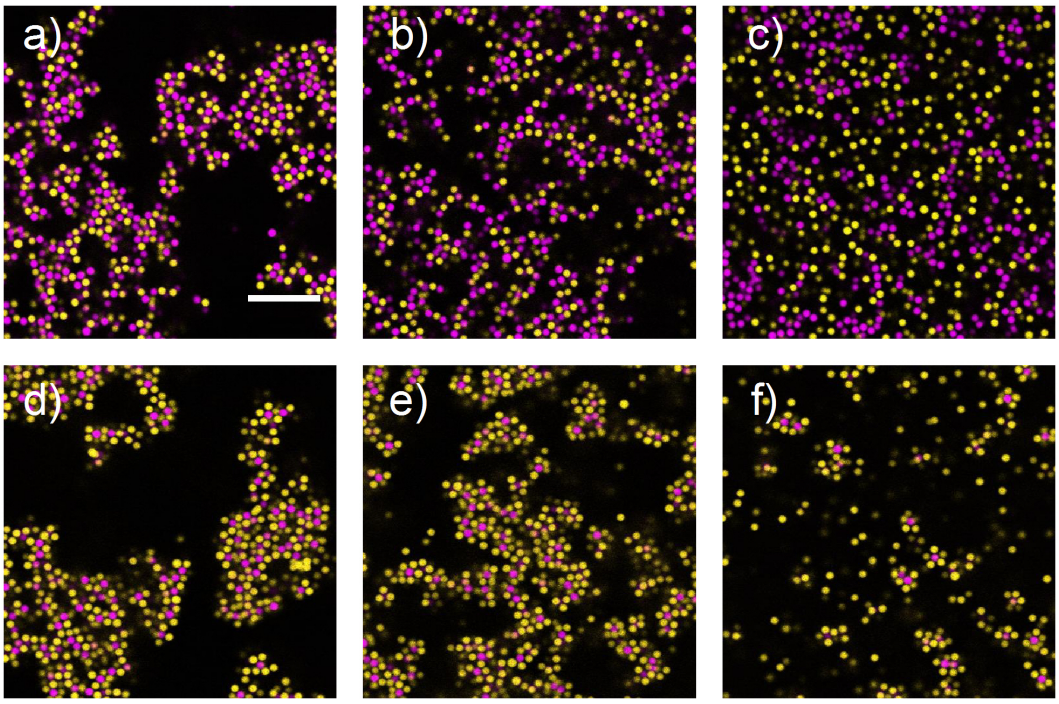

Figure 5.1: Confocal images of binary mixtures of oppositely charged colloids. Negatively charged particles are shown in yellow, and positively charged particles in magenta. Interaction strength decreases in a-c, exhibiting the transition from a gel at high interaction strengths to a fluid at low interaction strengths. Mixing ratio increases in d-f, exhibiting the same transition accessed using a different tuning parameter. a) mixing ratio of anions to cations $R = 1$, added salt concentration $c = 100$mM; b) $R = 1$, $c = 130$mM; c) $R = 1$, $c = 150$mM; d) $R = 4$, $c = 100$mM; e) $R = 6$, $c = 100$mM; f) $R = 8$, $c = 100$mM. $\phi_{tot} \approx 0.1$ and scale bar is 20μm for all samples.

to $c \approx 130$mM, the space-filling network persists, but the amplitude of the particle motion increases, with larger fluctuations easily visible, and some collective motion of larger strands of the gel (Fig. 5.1b). With yet a further decrease in the interaction strength, at $c \approx 150$mM, the space-filling network breaks up into a fluid of free particles and small clusters, in which the particles diffuse rapidly (Fig. 5.1c).

For salt concentrations in the range $c = 130\text{mM} - 150\text{mM}$, we also observe a transition between the gel and fluid states as we vary the total particle volume fraction ϕ_{tot}. At a fixed added salt concentration, we see the formation of a gel at large volume fractions, and a fluid of clusters at low volume fraction, where a spanning cluster is unable to form. These observations allows us to determine the gel line which separates the fluid region of the parameter space from the gel region, and determine the state diagram for colloidal gelation of oppositely charged particles (Fig. 5.2a). These symmetrically mixed binary samples with $R = 1$ show the same qualitative behavior as that established for attractive gels [66, 75, 41]: the formation of gels depends on both volume fraction and interaction strength, with the critical interaction strength required for gelation decreasing for higher particle volume fractions. In our system, this is manifested by the existence of gels at higher salt concentration for higher total volume fractions.

We quantify the behavior of the samples by computing the one-dimensional particle mean-square displacement over time,

$$\Delta x^2(\Delta t) = \left\langle ((x(t + \Delta t) - x(t))^2 \right\rangle$$

(averaged over all particles and over all starting times t), which gives a measure of particle diffusion. In most cases, there is a clear distinction between fluid samples and gel samples, as shown in Fig. 5.2b. Fluids exhibit diffusive dynamics; we define fluids as samples in which the mean-square displacement increases rapidly and roughly linearly with time until the particles leave the imaging plane, indicating that the particles and clusters remain diffusive. Gels show arrested dynamics; we define gels as those samples in which the mean-square displacement reaches a plateau at long times, indicating that the particles are localized and not free to diffuse. These definitions based on measured dynamics match well with the qualitative characterizations obtained by observing the samples by eye over longer periods.

Our identifications of the strongest gels are supported by bulk rheological measurements of the storage modulus G' and loss modulus G'' (Fig. 5.2c). The storage modulus demon-

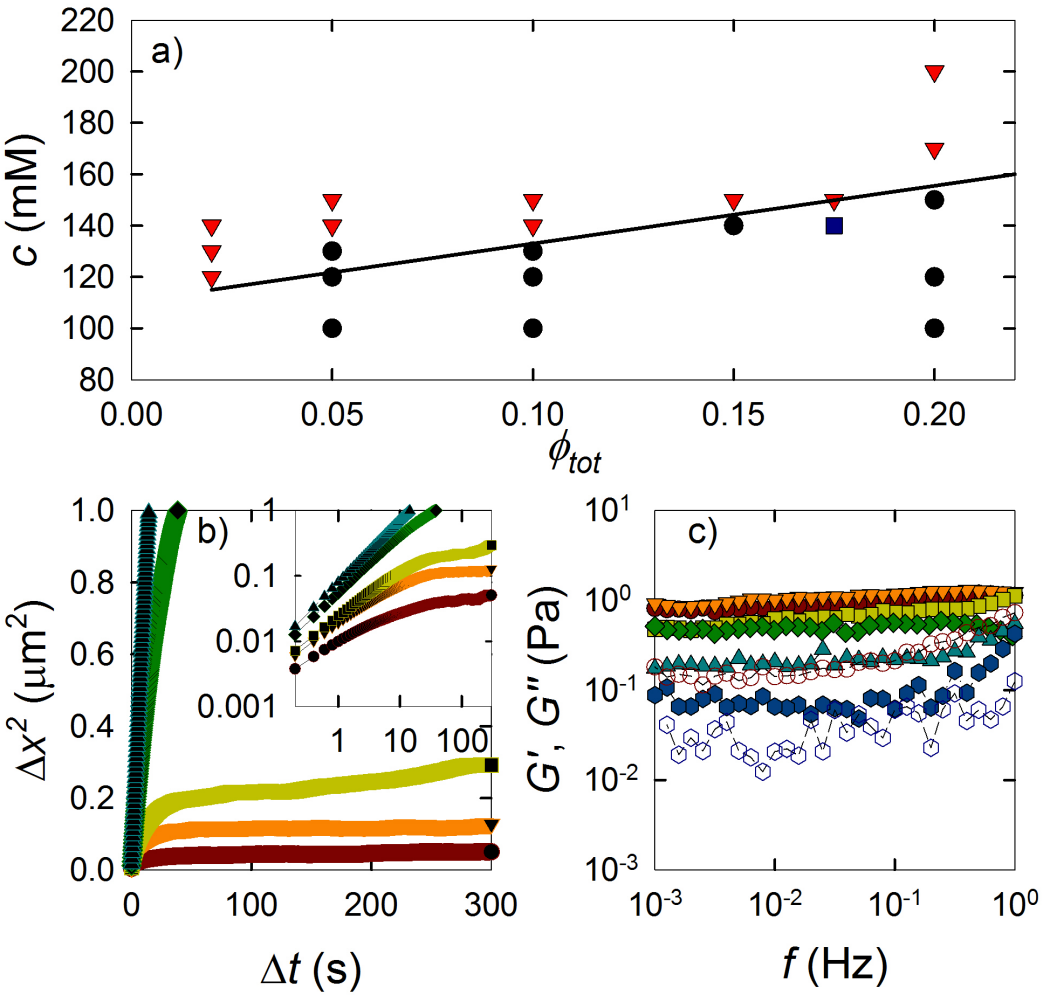

Figure 5.2: a) State diagram for the gel transition of a symmetrically mixed binary charged system; fluid samples are denoted by triangles, and gel samples by circles. The square point could not be identified as gel or fluid using the mean-square displacement criterion. The line is drawn as a guide to the eye. b) One-dimensional mean square displacement curves for samples at several salt concentrations and $\phi_{tot} \approx 0.05$, showing the change from arrested to diffusive behavior. From bottom to top, $c = 100$mM, 120mM, 130mM, 140mM, and 150mM. Inset: the same data on a log-log plot. c) Frequency-sweep measurements for the strongest gels; solid symbols give the storage modulus G', while open symbols give the loss modulus G''. For clarity, only two examples of the loss modulus are shown. $c = 60$mM (circles), 80mM (down-triangles), 90mM (squares), 100mM (diamonds), 110mM (up-triangles), and 120mM (hexagons). $\phi_{tot} \approx 0.2$ and $\gamma = 0.1\%$ for all samples.

strates a plateau at low frequency for several salt concentrations, the hallmark of a solid gel; this further confirms that these samples indeed form macroscopic sample spanning networks of aggregated colloidal particles. The moduli of weaker gels are too small to measure using the rheometer.

To better understand the nature of the gel transition, we examine the structures of the gels, and the change of these structures with interaction strength. The radial distribution function $g(r)$ provides a straightforward measure of the average structure; $g(r)$ quantifies the distribution of interparticle distances relative to a random particle distribution, highlighting correlations between particle positions. As we image positively charged (cationic) and negatively charged (anionic) particles in different spectral channels, we can distinguish between them, and calculate not only the total radial distribution function, but also the partial distribution functions for pairs of particles with similar or opposite charges. This partial radial distribution function is given by:

$$g_{ab}(r) = \frac{1}{4\pi r^2} \left\langle \frac{1}{n_b} \sum_b \delta(r - r_{ab}) \right\rangle_a$$

where each of the indices a and b indicate either positively or negatively charged particles; $\langle\rangle_a$ indicates an average over all particles of type a; n_b is the number density of particles of type b; and r_{ab} is the distance between two particles a and b.

In all gel samples, the partial $g_{-+}(r)$, indicating correlations between oppositely charged particles, shows a strong nearest-neighbor peak at about one particle diameter. In the deeply-quenched cases at low salt concentration, there is also a dip after this nearest-neighbor peak, indicating a region of depletion of oppositely-charged particles relative to the overall average density (Fig. 5.3a). In contrast, the partials $g_{++}(r)$ and $g_{--}(r)$, indicating correlations between similarly charged particles, are suppressed at one particle diameter, but have a slight, broad peak between about one and two particle diameters (Fig. 5.3a). This indicates that similarly charged particles are more likely to be slightly separated but not in direct contact. The partial radial distribution functions thus suggest a typical arrangement of oppositely-charged particles forming contacts, while like-charged contacts are disfavored. This local ordering persists only over short lengthscales of a few particle diameters at most, while the system is disordered at longer lengthscales. Similar results for a different system of oppositely charged particles have been reported in [58]. As the interaction strength between oppositely charged particles decreases, the $g_{-+}(r)$ curves flatten out toward a fea-

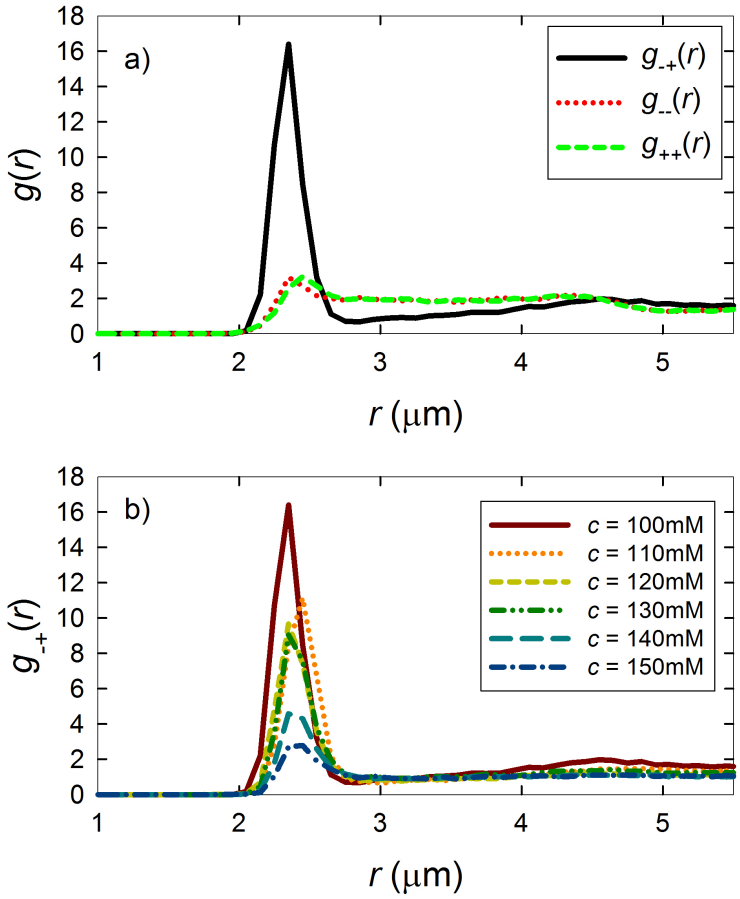

Figure 5.3: a) Partial radial distribution functions for $\phi_{tot} \approx 0.1$ and $c = 100$mM. Note the large nearest-neighbor peak in the partial for oppositely charged particles, and the suppression of this peak in the partial for similarly charged particles. b) Partial radial distribution function for oppositely-charged particles at $\phi_{tot} \approx 0.1$ as salt concentration is varied.

tureless, liquid-like curve, indicating that the particles are becoming less correlated as the gel transitions to a fluid (Fig. 5.3b).

Examining contacts between particles gives more local information than the sample-averaged radial distribution function. We identify contacts between particles from the microscopy data, defining two particles to be in contact if the distance between their centers falls within the first peak of $g_{-+}(r)$. Again, we identify contacts between both similarly-charged and oppositely-charged particles. Attractive contacts between oppositely-charged particles are the bonds which allow formation of a gel network; contacts between similarly-charged particles are not attractive, and so are not expected to contribute to the ability of the gel to support stress. We thus focus our attention on the attractive oppositely-charged bonds. In the strongest gels at high interaction strength, a particle makes on average three

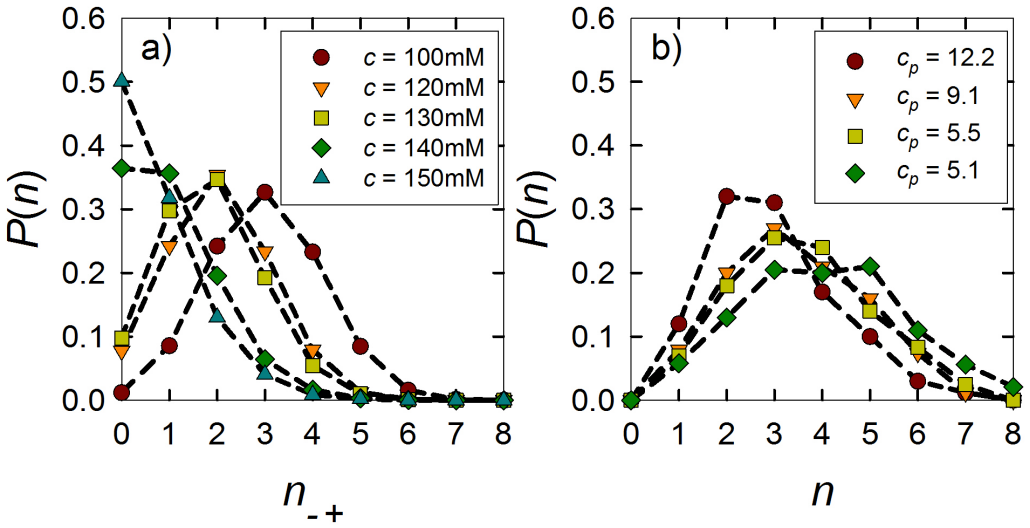

Figure 5.4: a) Distribution of number of cationic contacts of anionic particles in a binary gel as interaction strength is changed. $\phi_{tot} \approx 0.1$ for all samples. b) Distribution of number of contacts in a purely attractive gel as interaction strength is changed. Data taken from Ref. [16] with permission of the authors and IOP. $\phi = 0.3$ for all samples. The labels c_p refer to the concentration of polymer depletant in mg/mL, and are numerically roughly equivalent to the depth of the attractive well in kT [16].

bonds with oppositely-charged particles. As we decrease the interaction strength, the contact number distribution shifts to lower values, as shown in Fig. 5.4a; the gel line is crossed when the average bond number falls below about 1.

This trend is in clear contrast to the case of purely attractive gels, in which stronger gels tend to be more chain-like with fewer contacts, while weaker gels closer to the gel line have thicker strands and more contacts, as shown in Fig. 5.4b (data taken from [16]; see also [14]). In strong attractive gels, a particle attaching to the gel is unable to rearrange, so that the structure of the gel is essentially determined by chance contact events. In contrast, lower interaction strengths allow particle rearrangements within the gel; since all contacts are attractive, it is favorable for particles to form as many contacts as possible, and so rearrangement leads to higher contact numbers [16].

We suggest that in binary gels, local rearrangements are not likely to result in more favorable contacts. Essentially this is because triangles in the binary gel are not favored. In a purely attractive gel, a triangle consisting of three particles in mutual contact involves three attractive bonds; however, in the binary gel, such a triangle involves only two attractive bonds between oppositely charged particles, the third contact being a repulsive contact between similarly charged particles. This is a type of geometric frustration which in part

gives rise to the complexity and richness of the system. Thus triangles do not tend to form in binary gels, and as the interaction strength decreases and particles are more able to rearrange, they are not able to form additional favorable contacts. We suggest that instead, several particles of one charge all contacting the same oppositely-charged particle will tend to spread out around that central particle as far from one another as possible. We do not expect this to be due to charge repulsion, as the short screening length ensures that any charge interactions are very short-range. Rather, the arrangement of the particles farther from each other is likely to be simply an entropic effect. This spreading out blocks other particles from contacting the central particle, thus lowering the average contact number. The lower interaction strength may also allow particles to more readily detach from the gel, making the gel structure more sparse and decreasing the typical contact number within the gel. In a binary gel, in contrast to an attractive gel, the gel line is approached as particles in the gel are no longer able to form enough favorable contacts to sustain a network.

Another striking difference between this binary system and an attractive system is the ability to vary the mixing ratio R of the two particle species. The behavior of the system changes dramatically with mixing ratio, even as the total volume fraction of particles and the added salt concentration are held constant. For a total particle volume fraction of $\phi_{tot} \approx 0.10$ and an added salt concentration $c \approx 100$mM, a sample at $R = 1$ with an equal number of anionic and cationic particles forms a strong gel, with the particles fluctuating over only a small localization length (Fig. 5.1a). With an excess of anionic particles at ratios up to $R = 6$, the amplitude of particle motion increases, as the particles fluctuate farther from their equilibrium positions (Fig. 5.1d,e). As the mixing ratio increases further to $R = 8$, the gel breaks up into smaller clusters which are able to move freely (Fig. 5.1f). Each of these clusters contains several cationic particles coated by excess anionic particles. As the exteriors of these clusters present only anionic particles, the clusters cannot aggregate together into a spanning gel network. The critical mixing ratio for gelation with this high interaction strength is between $R = 6$ and $R = 8$. This is similar to the critical minority number fraction $x \approx 0.15$, corresponding to a mixing ratio of $R = 1/x - 1 \approx 5.7$ reported in simulations for irreversible bonds [40]. As interaction strength decreases, this critical mixing ratio becomes lower (Fig. 5.5).

We consider the structure of these asymmetrically mixed gels by again examining the contact-number distributions. With a larger and larger excess of anionic particles, it is the cationic particles bound to a single anionic particle that become the most relevant contacts

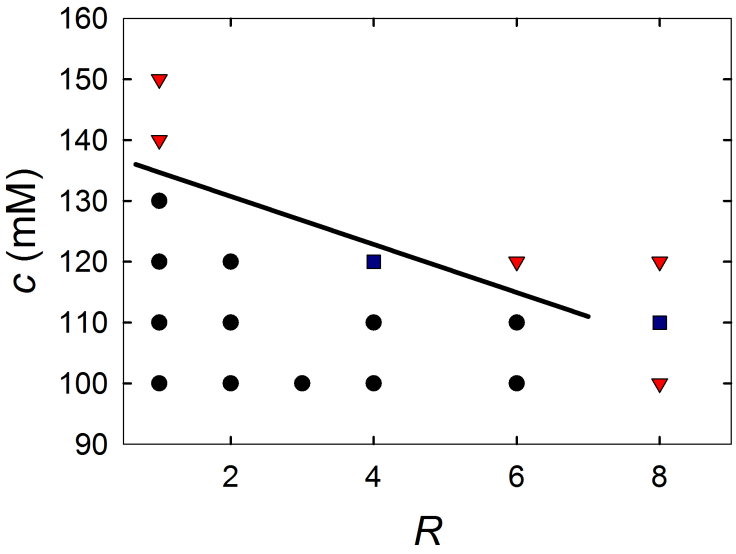

Figure 5.5: State diagram showing the gel transition of the oppositely charged system at fixed total volume fraction ($\phi_{tot} \approx 0.1$); fluid samples are denoted by triangles, and gel samples by circles. The square points could not be identified as gel or fluid using the mean-square displacement criterion. The line is drawn as a guide to the eye.

to the formation of a gel. Essentially the gel consists of cationic particles bound together by anionic particles; an anionic particle is only part of the skeleton of the gel if it makes at least two attractive bonds to cationic particles. The number of anionic particles bonded to a cationic particle is less important, as many of those excess anionic particles will not form an additional attractive bond. As the excess of anionic particles increases, the distribution of n_{-+}, the number of cationic particles bonded to an anionic particle, shifts to lower bond numbers (Fig. 5.6a). The gel line is reached approximately when the average n_{-+} falls below 1.

It is also interesting to note what happens to the distribution of n_{+-}, the number of excess anionic particles bonded to given cationic particle. As the asymmetry increases, so that there is a greater excess, it is unsurprising that the distribution shifts to a cationic particle having more anionic particles bonded to it (Fig. 5.6b). What is unexpected is that this distribution appears to reach a saturation at high asymmetry, with the distributions for $R = 6$ and $R = 8$ appearing quite similar. This saturation coincides with the gel line. This suggests that part of the reason for the concurrent decrease in the number of cationic particles contacting anionic particles is that the cationic particles become overcrowded with anionic particles. At high asymmetries, a typical cationic particle is surrounded by sufficient

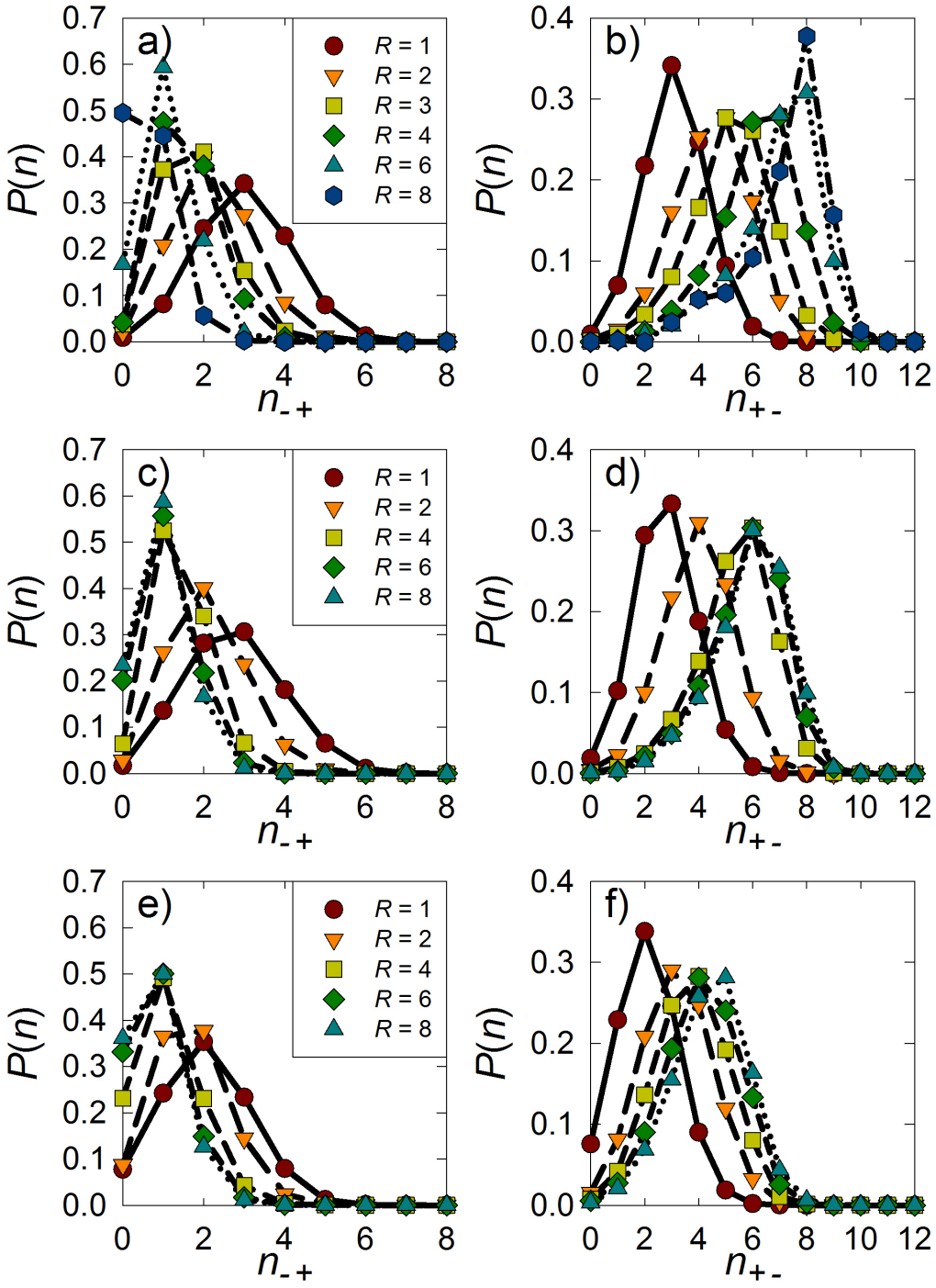

Figure 5.6: Distribution of the number of positively charged contacts of negatively charged particles (a,c,e), and negatively charged contacts of postively charged particles (b,d,f) as the mixing ratio R is changed. a,b: $c = 100$mM; c,d: $c = 110$mM; e,f: $c = 120$mM. Note that the trends in a, c, and e are similar to that in Fig. 5.4a, while in b, d, and f, there seems to be an approach to a saturated distribution at the highest asymmetry. All samples at $\phi_{tot} \approx 0.1$.

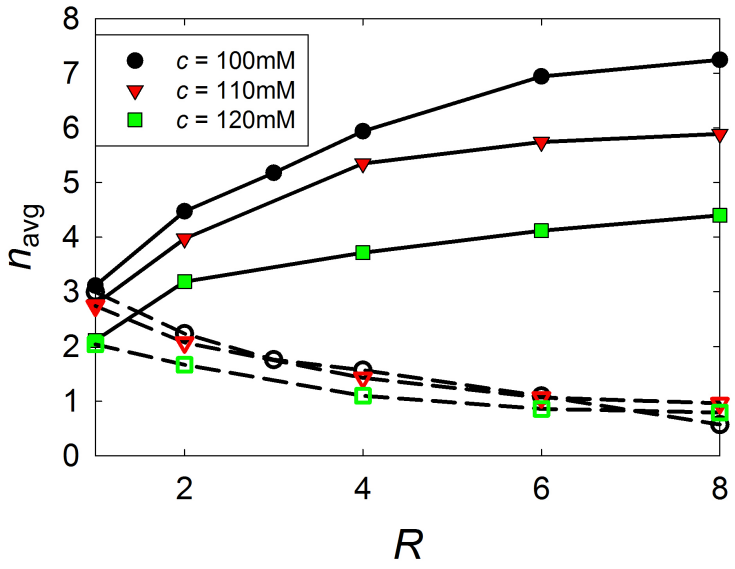

Figure 5.7: Mean number of contacts to oppositely-charged particles as a function of mixing ratio, for several salt concentrations. The lower branches (open symbols, dashed lines) show the average number of cationic particles bonded to an anionic particle; the gel line in all cases is reached at a mean contact number of about 1. The upper branches (filled symbols, solid lines) show the average number of anionic particles bonded to a cationic particle; note the apparent saturation to a plateau, with the saturation value depending on interaction strength. All samples at $\phi_{tot} \approx 0.1$.

anionic particles that there is no opportunity for another anionic particle to make contact. If none of the anionic neighbors is in contact with another cationic particle, there will be no opportunity for a structure-supporting bond to be formed; the cluster consisting of the cationic particle and its surrounding shell of anionic particles will remain stable and not become part of a larger cluster. This situation is analogous to the formation of soluble complexes in the coacervation of oppositely charged polymers [77]. The saturation drives the number of cationic particles that can contact one anionic particle below the critical number for gelation. It remains an interesting question whether the distribution truly saturates below complete coverage, or reaches a close-packed arrangement as the system approaches an infinitely large mixing ratio.

The trends of contact number distributions with mixing ratio remain similar as the interaction strength decreases. At salt concentrations of $c = 110$mM and $c = 120$mM, the mean numbers of cationic particles contacting an anionic particle again decrease with increasing mixing ratio (Fig. 5.6c,e). Again we observe that the gel line coincides with a mean bond number of about 1, although the transition occurs at a different mixing ratio (Fig. 5.7).

The trend of anionic contacts of cationic particles is also the same at different interaction strengths, reaching a saturation distribution which is shifted to lower contact numbers as interaction strength decreases (Fig. 5.6d,f). The mean contact number at a mixing ratio of $R = 8$ is above 7 for a high interaction strength at $c = 100$mM, but decreases to about 6 at $c = 110$mM and is less than 4.5 for $c = 120$mM (Fig. 5.7). This supports our earlier observation that particles form fewer oppositely-charged contacts at lower interaction strengths; this is robust even when there is a large excess of one type of particles. Thus as the interaction strength decreases, the gel weakens not simply because of the weakening of the individual bonds, but because of the reduction in the number of attractive bonds in the gel. This provides a stark contrast to purely attractive gels where failure of individual bonds to carry a stress is the sole cause of instability of the gel at the gel point. We further note that the distribution of contacts between two anionic particles also shifts to lower numbers at higher salt concentrations (data not shown), supporting again the argument that the long-range separation of like charges is not due to charge effects; the screening of charge repulsion would allow more such contacts at high salt concentrations rather than fewer.

5.5 Speculations and further directions

A hint at re-entrant gelation

There is one peculiar point on our experimental state diagram for binary gels (Fig. 5.5): that at $R = 8$, $c = 110$mM, which cannot be definitively identified either as a gel or a fluid. For these parameters, the mean-squared displacement grows slowly to about the slice thickness (taken as 1μm), but at the longest experimental times, shows indications of flattening, suggesting that at yet longer timescales, particles might be arrested. Further note the lower branches in Fig. 5.7; for all $R \leq 6$, the average value of n_{-+} decreases with decreasing interaction strength (increasing salt concentration c), yet for $R = 8$, the average value for $c = 100$mM suddenly drops relative to the values for $c = 110$mM and $c = 120$mM, so that $n_{\mathrm{avg},c=110\mathrm{mM}}$ is the largest, and in fact very close to the proposed critical value of 1. Thus in both dynamics (mean-square displacement, used to determine the state diagram in Fig. 5.5), and in structure (shown in Fig. 5.7), $R = 8$, $c = 110$mM is, if not a gel, closer to being a gel than either $R = 8$, $c = 120$mM (which is not surprising), or $R = 8$, $c = 100$mM (which is).

Why do I say it is surprising? Over the rest of the three-dimensional state diagram, higher interaction strength corresponds to a deeper quench into the gel phase. This is intuitive, and in direct analogy to the case for attractive gels. Yet here, we see that a higher interaction strength at $c = 100$mM relative to $c = 110$mM seems to inhibit the processes leading to gelation, resulting in a *less* gel-like state at higher interaction strength.

Thus this one point gives just the hint of what might be a *re-entrant gelation*, where a gel forms at intermediate interaction strengths, but the system remains fluid at both high and low interaction strengths. It is only a hint: the point is not characterized as a gel, but only as slightly more gel-like than the points at higher and lower interaction strength. Yet perhaps if we examined this point more closely, or studied a slightly lower mixing ratio, we might be able to confirm this hint. Is there truly a re-entrant transition? Sadly this must, for now, remain a question – I do not haven an answer. In spite of some effort, the binary system proved finicky enough that I did not perform the further experiments to investigate it – hence the inclusion of this discussion in the section labeled 'Speculations'. But let me speculate a little further.

My suspicion, based on this one data point, is that there is indeed a re-entrant gelation, with the following physical explanation. At these large mixing ratios, the gelation process

is a competition between the saturation of minority particles with majority particles, and the aggregation of unsaturated clusters into a gel network. A higher interaction strength favors saturation, possibly in two ways: first by increasing the number of majority particles covering a minority particle in equilibrium, as already mentioned and as discussed further below; and second by inhibiting rearrangements of bonded majority particles around a minority central particle, which might allow an extra majority particle – say one already bonded to another minority particle – to make contact. Thus at large mixing ratios, both high and low interaction strength inhibit gel formation – high interaction strength by instead favoring majority-saturated clusters, and low interaction strength by disfavoring aggregation altogether, as in attractive gels. Only at intermediate interaction strength is the gel network able to form before the minority particles become saturated, so that we see a re-entrant gelation. I expect that at higher mixing ratios, this re-entrant region will disappear, so that beyond some critical mixing ratio not far from $R \approx 8$, the system forms a fluid independent of interaction strength.

I must reiterate that this is speculative; it is hinted at by the current data, but further experiments are necessary to observe re-entrance, if indeed it occurs at all. So far as I am aware, such would be the first experimental demonstration of re-entrant gelation. A re-entrant gel of patchy particles has been simulated [56, 57], but requires non-isotropic interactions, and re-entrant attractive glasses at much higher densities are better known. The observation of an experimental system with re-entrant gelation would be quite novel and interesting.

Saturation coverage

I have already commented on the apparent saturation of minority particles with majority particles at large mixing ratio. An intriguing follow-on experiment would be to further examine this saturation by going to yet higher mixing ratio, where I expect to observe saturated clusters rather than gels, as seen in most points at $R = 8$. The nature of the saturation – the saturation number and the arrangement of particles – may depend both on interaction strength and on total volume fraction. Geometrical constraints limit the contact number to a maximum of 12, corresponding to close-packing of the majority particles around the central minority particle in a locally f.c.c. structure. Below this constraint, the saturation condition will be determined, as all things are, by the balance between energy and entropy.

Energetically, bond formation is favored, driving the system toward large saturation coverage – although possibly not to full coverage, as forcing contacts between close-packed, similarly-charged majority particles is energetically unfavorable. Higher interaction strength of course makes the energetic driving stronger. Entropically, majority particles have higher entropy in the bulk, driving the system to low saturation coverage; the magnitude of this effect should depend on the volume fraction of the majority particle, with lower volume fractions giving a larger entropy contribution and so giving a lower saturation coverage. The kinetics of the bonds will also contribute, as the coverage will depend on whether rearrangement is possible, and how quickly it proceeds, both determined by the kinetic barrier.

Further experiments might determine 1) how the saturation coverage at very large mixing ratio depends on both volume fraction and on interaction strength, and 2) how this saturation value is approached as mixing ratio is increased. If these dependences were also modeled theoretically, this could provide a method for estimating the interaction strength (most likely the depth of the attractive well) as a function of the salt concentration.

Bond angle distribution

There is one more speculation already mentioned on which I would like to further elaborate. When multiple similarly-charged particles are bonded to the same central oppositely-charged particle, how do they arrange themselves around that central particle? This is closely related to the saturation coverage number, and similar to the saturation, depends on entropics, and on kinetics. As discussed above, we expect that entropic considerations will drive these particles to arrange randomly over the surface of the central particle; but this is only possible if they are free to rearrange, determined by the kinetic barrier to rearrangement. The typical arrangement of bonded particles has implications for aggregation and the formation of clusters and of gels. Each particle 'blocks' a certain area of the central particle from forming a bond with an additional particle; particles spread uniformly over the surface of the central particle block a larger total area than particles which are near one another so that those blocked areas overlap. Thus the likelihood of an additional particle forming a bond with the central particle is affected by the arrangement of already-bonded particles, and this arrangement will help determine whether a percolated gel is able to form.

One way to quantify the arrangement of particles is by considering 'bond angles', that is the three-body angles formed by one central particle and two of its contacts.[1] How does

[1] In crystalline systems, where these angles are predicted by the crystalline structure, bond angles are

the distribution of bond angles depend on volume fraction, interaction strength, and mixing ratio? There will be nuances to this question – considering separately the distributions for particles with different contact numbers, for example, or the time dependence of the distributions as the system evolves. The variation in these distributions over the state space may given insights into gel formation.

Furthermore, it may be interesting to examine the dynamics of the bond angles in addition to their distribution at a snapshot in time – that is, not only how do particles arrange themselves around a central particle, but how do they move? Is the mobility affected by the interaction strength? I expect the mobility to vary with time – as discussed in Sections 2.1.1, the attraction between particles strengthens with time in contact as a polyelectrolyte complex forms and the polyelectrolyte brushes interpenetrate more deeply. This evolution of the interaction strength will affect the kinetic barrier to rearrangement, that is, the mobility of the particle bonds.

I also expect the bond angles' distribution and dynamics to be very different in small, free clusters than in the gel, where the additional constraints will freeze in structures. Experiments at low volume fraction to study small clusters could prove an interesting contrast to analyzing the structure and dynamics in the gels themselves, and perhaps offer insight into the formation of the gels.

These three potential topics for future study – re-entrance, saturation, and bond angle distribution – are all interrelated, and get at deeper, salient details of the structure of clusters and gels. The introduction of repulsive interactions competing with attraction will dramatically affect all of these phenomena in this binary system compared to the attractive gels already studied, and the changes brought about by this competition will be intimately tied to the nature of the gel transition.

Material properties

I have already made allusion to the shear modulus of these gels, measured in bulk using a rheometer, and shown in Fig. 5.2c. For the strongest gels measured, the shear modulus is $G' \approx 1$Pa. The sensitivity of the rheometer limits our ability to measure moduli much lower than $G' \approx 100$mPa, as measured for the sample at $\phi \approx 0.2$ and $c = 120$mM, but the state diagram (Fig. 5.2a) shows that the system remains a gel at even higher salt concentrations and lower volume fraction, where we expect the shear modulus to fall to even smaller values.

often used to calculate an order parameter for the 'crystallinity' of the neighborhood of a particle.

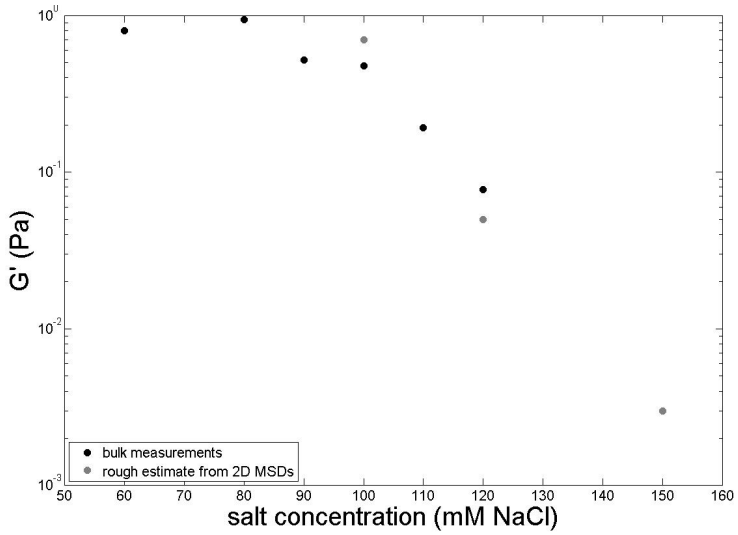

Figure 5.8: Shear modulus estimates in binary gels. Black circles give direct measurements from bulk rheology, but are limited to $G' \gtrsim 0.1$Pa. Grey circles give approximations from one-particle microrheology, $G' \approx k_B T/(\langle \Delta r^2 \rangle L)$. $\phi \approx 0.2$.

How small? We can make a rough estimate of G' from one-particle local microrheology:

$$G' \approx \frac{k_B T}{\langle \Delta r^2 \rangle L}$$

where $\langle \Delta r^2 \rangle$ is the plateau value of the mean-square displacements (e.g. those plotted in Fig. 5.2b), and $L = a/\phi$ is a typical lengthscale of the gel. Using this approximation, we can extend the estimate of G' nearly to the gel line (see Fig. 5.8). The shear modulus drops roughly exponentially with salt concentration over the region 100mM $< c <$ 150mM ($\phi \approx 0.2$), with the lowest value $G' \approx$ 3mPa at the closest point to the gel line. At lower volume fraction, $\phi \approx 0.05$, the lowest estimated modulus is $G' \approx$ 0.8mPa, for $c =$ 130mM, the weakest gel found. Unexpectedly, for the stiffest gels, G' appears to saturate at $G' \approx$ 1Pa for $c \lesssim$ 100mM. (This saturation does not continue indefinitely; with no added salt, the gel is so strong that it is impossible to load into sample cells for microscopy, and it undergoes syneresis, expelling the solvent, when agitated in the rheometer.)

5.6 Conclusion

We have introduced a novel experimental model system of oppositely charged colloidal particles which allows a detailed study of colloidal gelation in the presence of a mixture of attractive and repulsive interparticle interactions, and identified a novel mechanism under-

lying the formation and structure of these binary colloidal gels. The most striking difference between oppositely charged colloidal gels and purely attractive gels is that in the binary case, there appears to be a critical mean bond number of 1 for gelation, which is the same no matter how the gel line is approached. We observe this critical mean bond number in symmetric gels as the interaction strength varies, and in asymmetric gels as mixing ratio varies at several different interaction strengths. With variation of either tuning parameter, particles tend to form fewer structure-supporting bonds as the gel line is approached. Thus over a range of parameters, the presence of a gel correlates with the mean number of attractive bonds a particle makes: if this mean bond number is greater than one, a gel will form, while if it is less than one, the system will form a fluid of clusters.

The similarity in the effects of two very different tuning parameters emphasizes that the structural integrity of a binary gel is determined by the contacts between *oppositely*-charged particles; not all possible particle contacts are favorable or contribute to the ability of the gel to bear stress. This is in clear contrast to the case of purely attractive gels, in which any particle contact stabilizes the gel. In binary gels, unlike in purely attractive gels, rearrangements do not allow for a significant increase in the number of favorable contacts. With a decrease in the interaction strength, particles are more able to rearrange to form string-like structures and are more able to detach from the aggregate, leading to lower contact numbers; with an increase in the mixing ratio, excess particles of one type saturate the minority particle type, preventing further attractive bonds from forming. Either tuning parameter affects the number of attractive bonds, and if this number is below a critical average of about 1, a gel cannot form.

While polyelectrolyte brushes present an interesting and relevant system, they are not the only method of introducing opposite charges on colloidal particles, and it remains an interesting question how the particulars of the interaction might affect our results. Our gels appear to be similar in structure to those formed by oppositely charged particles more nearly described by a bare surface charge with a screened Coulomb or Yukawa interaction [62, 63], suggesting some generality to our results, but we cannot rule out that some details may differ. We expect the interpenetration of the polyelectrolyte brushes to pose a kinetic barrier to the rotation of bonds between oppositely charged particles; we can speculate that this barrier may change in the case of bare surface charges, changing the ability of the particles to rearrange within the gel. The range of the interaction also plays a role in determining the internal gel structure; for example, in experiments with longer-range

interactions, the gel strands became locally crystalline [63], which we did not observe in our short-range system. A related question well worth further investigation is whether the onset of gelation of oppositely-charged colloids is generally driven by a thermodynamic phase separation. In a purely attractive system, gelation appears to be a consequence of arrested gas-liquid spinodal decomposition [41]. Simulations have indicated that spinodal decomposition also drives gelation in a system of oppositely charged particles interacting via a Yukawa potential [62, 63]. We see nothing to suggest that the onset of gelation in our system is not also driven by a thermodynamic phase transition, although we are unable to confirm whether this is the case, due to the difficulty of calculating the equilibrium phase diagram. The relationship between the gel state and the equilibrium phases of this system invites further study.

These binary gels do bear resemblance to other model systems with competing interactions. Simulations of gels with directionally-dependent three-body interactions, introducing an energy cost to small bond angles, have shown that a faster quench gives a more locally connected structure [12]; we find a similar effect in binary gels, where gels with a deeper quench have higher contact numbers. Indeed, we expect small bond angles to be inhibited in our system by the short-range repulsion between like-charged particles both bonded to the same oppositely-charged particle. In another example, re-entrant gelation has been observed in simulations of gels formed by a binary system of 4-valent and monovalent patchy particles, where the monovalent particles act as blockers of binding sites on the 4-valent particles and fragment the gel at low temperature [56, 57]; similarly in our asymmetric system at large mixing ratio, the majority particles can act as blockers of the minority particles, giving an inconclusive but tantalizing hint of re-entrant gelation.

The binary system of oppositely-charged colloidal particles introduced here constitutes a new system valuable for studying a range of new phenomena in gelation which have not been observed in purely attractive gels, and which may bear on other examples of gelation and aggregation driven by opposite electric charges. These binary gels offer the novel parameter of the mixing ratio of the two particle species, which can be used to tune the system between a fluid and a gel, and to control the structure of the gels. Furthermore, we see that the structure of binary gels tends toward lower contact numbers on approach to the gel line whether interaction strength or mixing ratio is varied, in contrast to the opposite trend exhibited in attractive gels. The mechanism of gel formation in a binary gel is thus distinct from that in an attractive gel.

Chapter 6

Results: Colloidal 'Wigner' Crystals

Large portions of this chapter are in preparation for publication; we expect the main results presented here to appear in a journal in the near future, but cannot yet give a reference to the publication-to-be. Even more so than the last chapter, this chapter will include more details and speculations than will the corresponding paper.

This work picks up a system studied by Joris Sprakel when he was a postdoc in the group, and so many of the early ideas were his [68]. The data I report on, however, are my own, as are all the analyses involving the lattice and strains. This chapter in particular is also deeply indebted to Prof. Frans Spaepen, who took an interest in the project and provided a good deal of excellent advice and suggestions as to what calculations would be most interesting to carry out. Tom Kodger helped with the 'upright' confocal experiments. I again made great use of Kate Jensen's codes for particle tracking, and adapted her codes for the strain calculations.

As with Chapter 5 on binary gels, I intend this chapter to stand more or less on its own as a coherent synopsis of this project; there will, therefore, be some repetition of the material covered in previous chapters as it is needed.

I will begin with a preview of the results which will be presented in this chapter. The typical layman (which category probably includes even physicists from fields which do not often deal with crystals) – the typical layman, when asked to think of a crystal, will generally picture something like Fig. 6.1a – a crystal made up of simple molecules, with strong

(a) (b) (c)

Figure 6.1: Examples of crystals. a) Silicate quartz crystals, which have structure and properties very different from the crystals I study (image credit: Didier Descouens, via Wikimedia Commons). b) The central vial shows colloidal hard-sphere crystals at $\phi \approx 49\%$, identified by Bragg scattering from many crystallites (from [52]). c) A confocal image of a colloidal Wigner crystal at $\phi \approx 0.15$; the image is $\approx 80\mu$m across.

attractive bonds making the crystal hard and rigid. A colloid physicist might picture something like Fig. 6.1b – a colloidal hard-sphere crystal, in which particles at volume fractions of $\phi \gtrsim 50\%$ form a crystal with a face-centered-cubic (f.c.c.) structure, in the absense of particle interactions other than a hard-sphere repulsion. The colloidal 'Wigner' crystals I study are yet another beast, formed when particles with a long-range *repulsion* are confined. At only moderate volume fractions (indeed, at arbitrarily small volume fractions if the repulsion be sufficiently strong and long-range), the energetic advantage of maximizing the distance between particles by ordering drives the system into a crystalline phase (Fig. 6.1c). For long enough screening length, the low volume fraction ordered state is a *body-centered cubic (b.c.c.)* crystal, in contrast to the hard-sphere f.c.c. crystal. The term *colloidal Wigner crystal* is in analogy to a state proposed by Eugene Wigner, in which electrons in a metal (or other effective 'electron gas') at low temperature and low density are expected to order into b.c.c. crystals due to Coulomb repulsion.

I demonstrate the formation of colloidal Wigner crystals with extents of hundreds to tens of thousands of lattice spacings, with the crystalline phase tuned by particle volume fraction. I use confocal microscopy to investigate in detail the structure and properties of these crystals. The most outstanding features of these colloidal Wigner crystals are the large fluctuations which are possible, due to the very soft interactions between particles. These large fluctuations stand in stark contrast to the much smaller fluctuations in atomic or molecular crystals, where common lore has it that a crystal will melt when the fluctuations surpass a certain threshold – this is the 'Lindemann criterion' of melting, which, while it represents a true correlation, does not explain the *cause* of melting.

I further probe the material properties of these fluctuating crystals over a range of particle volume fractions. I determine the crystalline elastic constants c_{11}, c_{12}, and c_{44} from the thermal distributions of local strains in the system, and demonstrate their variation with volume fraction. Comparison of the elastic constants emphasizes the anisotrpy of the crystals at all volume fractions. It is also interesting to note that the strain distributions distinguish the nonlinearities in the tensile elastic modulus, with a stiffening for compression and a softening for dilation. Finally, while the crystalline ordering manifests the long-range correlations of particle position, the local strains are correlated on the scale of only about two lattice spacings.

6.1 Introduction

As described more fully in Chapters 1 and 2 (particularly Section 2.6.2), there is a rich background of inquiry into colloidal Wigner crystals harking back to the '70s and '80s. The earliest work was carried out in aqueous systems using light scattering and x-ray scattering, and established the b.c.c. structure and melting properties of low volume fraction charged-sphere crystals [85, 86, 9], culminating the determination of an experimental phase diagram of the b.c.c., f.c.c., and fluid phases as a function of volume fraction and salt concentration [67]. The phase diagram was qualiatitively understood using simulations of a Yukawa potential [34, 54]. Not only the structure, but also the material properties – isotropically averaged elastic moduli, and directional elastic constants – have been investigated using several techniques [10, 23, 39]. With the advent of confocal microscopy to the field of colloid physics came more direct visualization of these low volume fraction crystals in nonpolar solvents, demonstrating again both the b.c.c. and f.c.c. phases at low volume fraction [59, 87, 36]. Previous work in my group, still unpublished, has also established the phase diagram of the nonpolar system [28] and begun to investigate the material properties and the mechanism of melting [68].

Here I present the first study of the detailed *local* structure and material properties of colloidal Wigner crystals. I demonstrate the control of crystalline structure using volume fraction, and measure directly the fluctuations of particles from their positions in the crystalline lattice, and find that these fluctuations can be quite large. From the thermally-activated local strains in the system, I measure the three independent crystalline elastic constants, and determine their dependence on volume fraction. The material properties of

these crystals are strongly anisotropic at all volume fractions accessed; this is the first direct demonstration of this anisotropy. These experiments provide a detailed view of the material properties and local structure of the still incompletely understood colloidal Wigner crystal.

6.2 Experimental

As described in much greater detail in Chapter 3, I suspend 1.8μm diameter poly-methyl-methacrylate (PMMA) particles coated with a brush of poly-hydroxystearic acid (PHSA) in a mixture of decahydronapthalene (decalin) and tetrachloroethylene (t.c.e.). The solvent ratio (roughly 55% decalin / 45% t.c.e. by volume) is chosen to density-match the particles, to minimize the effects of gravitational pressure in the system. The particles are fluorescently dyed, and the refractive index of the solvent mixture is sufficiently close to that of the particles to permit imaging in three dimensions using confocal microscopy.

I induce a long-range repulsion between particles by adding 10mM of the surfactant dioctyl sodium sulfosuccinate (commonly known as aerosol-OT or AOT). Above its critical micelle concenctration (≈1mM), AOT forms micelles, which enable the dissociation of electrolytes into the solution: the polar cores of the micelles provide an environment in which the energy barrier to dissociation is lowered, while the hydrocarbon tails provide stabilization against re-association. In the presence of the AOT micelles, the PHSA groups on the particle surfaces dissociate, with the H^+ counterion going into the core of an AOT micelle, while the negatively-charged acid remains on the particle surface, stabilized by association of additional AOT molecules – thus the particles take on a negative charge. The AOT micelles also act as screening agents in the solution, as a small additional population of the micelles become charged [22]. The 10mM concentration was chosen based on others' past experiments [28, 68] as giving an optimum balance between highly charged particles (at large [AOT]) and long screening lengths (at low [AOT]) to achieve large interparticle spacings. We verify that this is near optimum by using an electrosonic analyzer (ESA) to measure the effective zeta-potential of the same particles in pure decalin as a function of added AOT concentration (Fig. 6.2).

I determine the particle size by dynamic light scattering (DLS) of a dilute suspension in the same solvent, combined with measurements of the solvent viscosity (1.302 mPa·s) using an Anton-Paar rheometer in a Couette geometry, and of the solvent refractive index (1.4877) using an Abbe refractometer. This measurement gives a hydrodynamic diameter

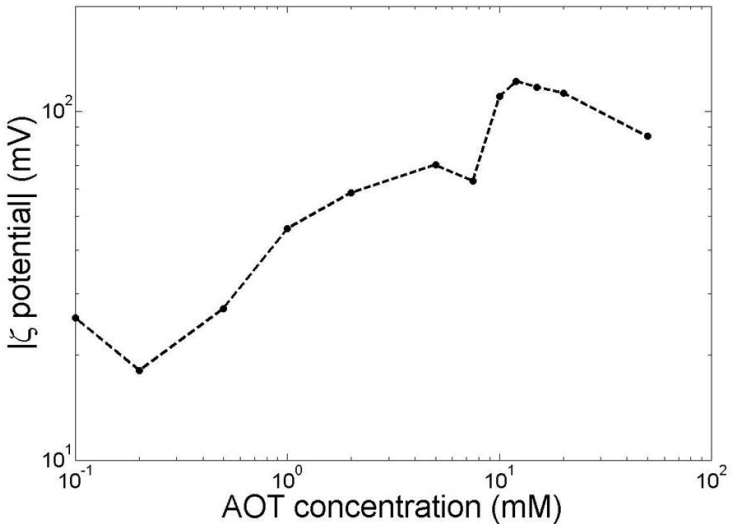

Figure 6.2: Approximate effective zeta-potential of particles in pure decalin as a function of added AOT concentration, obtained using an electrosonic analyzer. As the concentration increases from zero, more and more acid groups on the particle surface dissociate, increasing the particle surface charge and effective potential. At larger AOT concentrations, the surface charging slows, while the screening by ionized micelles becomes stronger, decreasing the effective potential. The peak around [AOT]=10mM was chosen as the optimum concentration to study Wigner crystals.

of 1.79μm.[1]

The bulk behavior is captured by (macroscale) time-lapse video of several samples at fixed volume fractions, obtained over the period of several months to monitor the progression of crystallization over time.

I prepare samples for confocal microscopy at fixed volume fractions, and allow them to equilibrate over eight days[2] before making observations. A typical confocal 'stack' includes roughly 1100-1700 particles (depending on volume fraction), and follows the same imaging volume over a period of 12 minutes. From the confocal microscope images, I use standard analysis techniques [11, 20] to obtain precise locations over time of each particle in the imaging volume.

I also have preliminary results on an experiment with a range of volume fractions in

[1]While I use this value to report approximate volume fractions, it is probably a slight overestimate of the 'hard-sphere' diameter of the particles, as the hydrodynamic diameter includes the effect of the double-layer of AOT micelle counterions near the charged particles. An error in the particle diameter will give a systematic error in reporting volume fraction (determined by the product of the number density and the particle volume); for this reason, most of my results are given in terms of particle number density, which is very well measured, rather than volume fraction.

[2]I observed further evolution of the samples with time after these eight days, of a nature which suggested that not only were the samples not fully equilibrated, but also that the chemical environment in the samples was slowly changing with time. The nature of this chemical change is not understood. Since all data were collected from samples prepared from the same stocks and after the same equilibration time, I expect at least that the effect of any such change in the chemical environment is uniform across the samples reported.

a single sample, achieved by using a slightly different solvent ratio so that the particles sediment, introducing a gravitational pressure gradient. This sample equlibrated for two months, and is then observed using the confocal microscope in an 'upright' configuration, with the objective lens mounted on a mirror so that the optical axis was perpendicular to gravity and the field of view could be moved over nearly 1cm in Z.

6.3 Results and discussion

6.3.1 Process of crystal growth

The macroscale time-lapse video showed the growth process of colloidal Wigner crystals over the timescale of tens of days. At all volume fractions, there was an initial delay time before crystallization began, ranging from about 10 to about 45 days for different samples. At the highest volume fraction, crystallization initiated near the middle of the sample, and the crystal grew outward. In all other samples, the crystal grew from the bottom of the sample; this is probably due to slight sedimentation of the particles over the long experimental time.[3]

Snapshots of the crystallization process are shown in Fig. 6.3a-c. Disordered regions appear a featureless grey; crystalline regions are visible as textured areas, due to Bragg scattering off multiple small crystallites. The speed of crystal growth varied, as seen in Fig. 6.3d, which gives the crystal height as a function of time. A more detailed analysis of this crystal growth is a good prospect for future study: the velocity of the interface as crystallization proceeds can be used to infer the free-energy difference between the crystal and the fluid, and the variation of this free energy with volume fraction is of interest in understanding the system.

The initial volume fraction of the sample determines the lattice spacing of the crystals formed; this is exhibited by the volume-fraction dependence of the Bragg scattering angles, shown in Fig. 6.4.

6.3.2 Control of structure by volume fraction

I observed the formation of body-centered cubic 'colloidal Wigner crystals' over a range of moderate particle volume fractions of about $n = 0.054{-}0.085(\mu\text{m})^{-3}$ (corresponding roughly

[3]While the solvent was nominally density-matched to the particles, this density-match is sensitive to temperature, as mentioned in Section 3.1.3. The sample was continuously illuminated by a bright LED for imaging; I suspect that this illumination heated the sample enough to cause the particles to sediment.

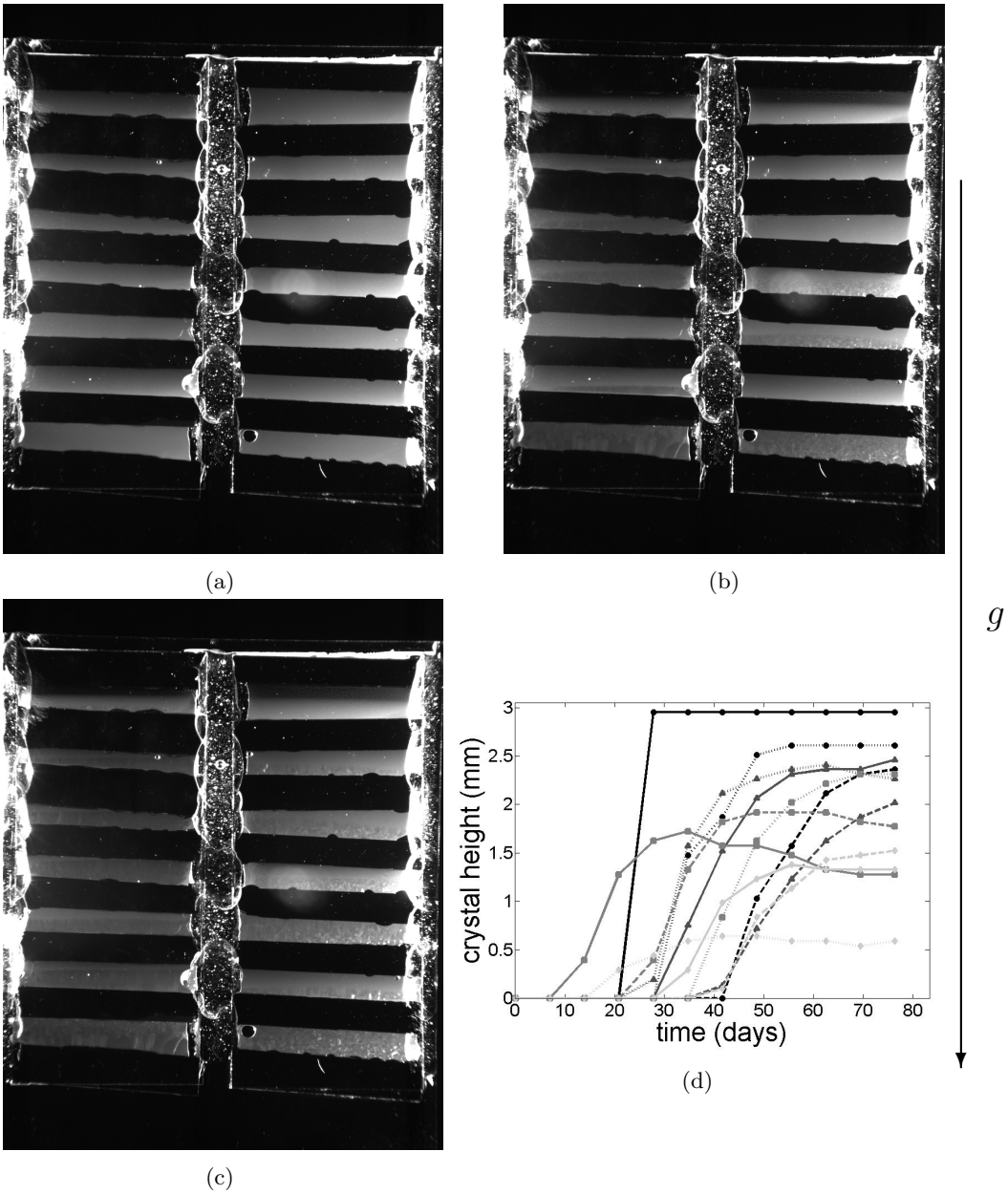

Figure 6.3: Crystal growth at different volume fractions. (a-c) Several timelapse images of crystallization. Gravity is pointing down. Each cell has a different volume fraction, with highest volume fractions at the bottom and lowest volume fractions at the top. Images show the sample after sitting undisturbed for (a) 7, (b) 35, and (c) 56 days. In (a), none of the samples have begun to crystallize. In (b), crystallites are visible as textured regions at the bottom of several cells; crystallization has begun in 9 of the 14 samples, but only the two highest volume fractions (bottommost cells) have fully crystallized. In (c), crystallization has begun in all samples except the lowest volume fraction (upper right), and has propagated across the entire sample in several cases. (d) Crystal height as a function of time for each sample. Volume fraction is indicated by darkness and shading of the curves; dark curves are at higher volume fraction than light curves, and for a fixed darkness, solid lines are at higher volume fraction than dashed lines, which in turn are at higher volume fraction than dotted lines. Note the range of delay times from ≈ 10 days to ≈ 45 days.

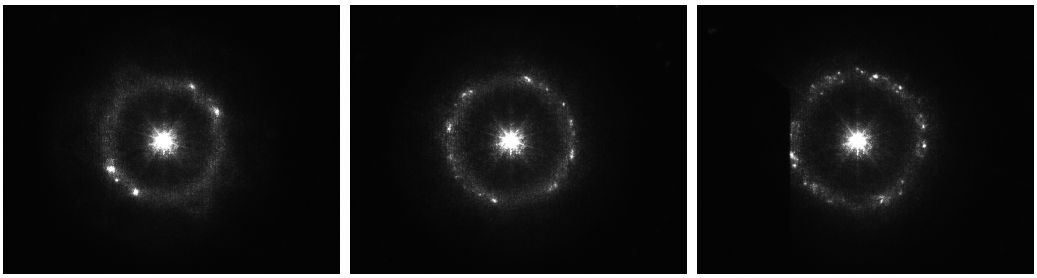

(a) (b) (c)

Figure 6.4: Light-scattering patterns from the samples shown in Fig. 6.3, after 119 days. (a) Low volume fraction; (b) intermediate volume fraction; (c) high volume fraction. All images at the same scale. In each case, the laser is striking multiple crystals, so we see the a clear nearest-neighbor ring, with several bright spots indicating the particular orientation of the dominant crystals. The radius of the ring grows with volume fraction as the lattice spacing decreases.

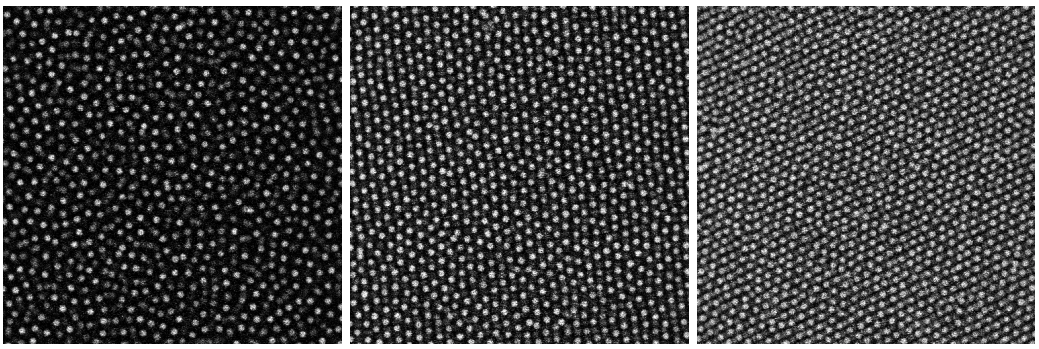

(a) (b) (c)

Figure 6.5: Confocal images of repulsive charged-sphere system at several volume fractions. a) Colloidal fluid at $n = 0.035(\mu\text{m})^{-3}$. b) (110) plane of a b.c.c. crystal at $n = 0.054(\mu\text{m})^{-3}$. c) (110) plane of a b.c.c. crystal at $n = 0.085(\mu\text{m})^{-3}$. All images are 82μm across.

to volume fractions $\phi \approx 15\%$-26%). The process of crystallization was faster and more uniform than in the samples described in the previous section. Most samples crystallized within the space of a day or two, after an initial delay of about 5 days; the two samples at the lowest volume fractions took about 10 and 13 days to crystallize. The crystallinity was visible to the naked eye by the iridescence of Bragg reflection off the macroscopic samples; samples were polycrystalline, with typical grain sizes of hundreds of microns to several millimeters. Under the confocal microscope, the crystalline structure was equally apparent, with examples of single planes shown in Fig. 6.5. The b.c.c. crystals gave way to colloidal fluids at lower volume fractions $n \lesssim 0.045(\mu\text{m})^{-3}$.

The crystals always formed with a (110) plane parallel to the coverslip; this plane has a stretched hexagonal structure and is the closest-packed plane of the b.c.c. crystal. This

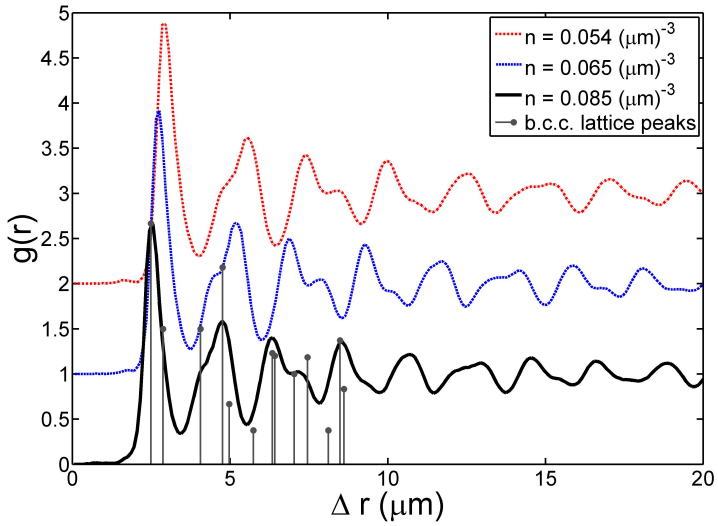

Figure 6.6: Radial distribution functions for experimental b.c.c. crystals at several volume fractions; curves are offset vertically for clarity. Also shown are the r.d.f. peaks for a perfect b.c.c. crystal (with Δr scaled to match the curve at $n = 0.085(\mu\text{m})^{-3}$), read from [50]. The shape of the experimental curves remains distinctly similar, indicative of the persisting b.c.c. structure, even as the lengthscale shifts with volume fraction.

orientation indicates boundary effects in the system and a preferred direction; however, we shall show evidence later which suggests that the effects on the material properties are mild.

It is also worth noting that even in fully polycrystalline samples, the volume fraction was not uniform across the sample. Volume fractions in different crystal grains varied by about $\Delta n \approx 0.002$. Thus while I report eight different volume fractions, these come from only six samples, with two of those samples each contributing two slightly different volume fractions.

The crystallinity was, as mentioned, obvious to the eye, and the particular crystalline structure was identified as b.c.c. supported by the radial distribution functions; a few examples are shown in Fig. 6.6. The shape of the r.d.f. was identical across samples, with only the lengthscale varying with number density, and the peaks lined up nicely with the expected peaks for a perfect b.c.c. crystal (indeed, except for the first peak, the curves were nearly identical to those generated by calculating the r.d.f. for a perfect b.c.c. crystal with artificially added uncorrelated Gaussian noise).

6.3.3 Fluctuations

The crystalline ordering is apparent, but individual particles fluctuate significant distances from their position in the average lattice. This is visible in single snapshots of the crystal

in time (e.g. Fig. 6.1c), where both the average lattice and the deviations of particles from the average lattice are apparent. The dynamics of these fluctuations are also readily visible in real time in the microscope, or in time-lapse movies made from microscope ZT-stacks, as individual particles are seen to 'dance' about their mean lattice position on the timescale of seconds.

One measure of the degree of fluctuation in the system is behavior of the mean-squared displacement (m.s.d.) of particles over a delay time Δt, particularly at long times. Several examples of the mean-squared displacements for crystalline samples are shown in Fig. 6.7a. The m.s.d. increases with time at short times, and then reaches a plateau at long times as particles are localized on the lattice and not free to diffuse far from their lattice position – here, the experimental resolution of 2s is comparable to the localization timescale, so that the short-time increase is barely captured. The value to which the *root*-mean-squared displacement (r.m.s.d.) plateaus, δr_t, can be considered as a 'localization lengthscale' of the fluctuations; Fig. 6.7b gives this lengthscale at different number densities. In some samples, the m.s.d. increases again at later times, suggestive of particles hopping between lattice sites (see Section 6.3.6 for further discussion).

This value of the plateau of the temporal r.m.s.d., δr_t, is related to another localization measure, the root-mean-squared displacement of particles *from their average position*, $\delta r_{\bar{r}}$, by $\delta r_{\bar{r}} = \delta r_t/\sqrt{2}$.[4] I calculate the unitless *Lindemann parameter*, δ_L, which gives the r.m.s.d. from the average position normalized by the nearest-neighbor spacing a: $\delta_L = \delta r_{\bar{r}}/a = \delta r_t/(\sqrt{2}a)$. The name 'Lindemann parameter' comes from the Lindemann criterion for melting, which states that a crystalline material will melt when the Lindemann parameter exceeds ≈ 0.1 – that is, when particles typically fluctuate more than about 10% of the distance to their nearest neighbors. Over the range of volume fractions investigated, the Lindemann parameter appears nearly constant with volume fraction (Fig. 6.7c), with

[4] To see this, consider a snapshot of the crystal at time t_0, with the displacement of each particle i from its average position denoted by $\mathbf{d}_{i,0}$. At a later time t_1, the displacements are $\mathbf{d}_{i,1}$. We assume that $t_1 - t_0$ is sufficiently long that these displacements are uncorrelated. Then the r.m.s.d. from the average position is

$$\delta r_{\bar{r}} = \sqrt{\langle |\mathbf{d}_{i,0}|^2 \rangle} \approx \sqrt{\langle |\mathbf{d}_{i,1}|^2 \rangle}$$

where the average is taken over particles i, while the temporal r.m.s.d. is

$$\begin{aligned}
\delta r_t &= \sqrt{\langle |(\mathbf{d}_{i,1} - \mathbf{d}_{i,0})|^2 \rangle} \\
&\approx \sqrt{\langle |\mathbf{d}_{i,0}|^2 + |\mathbf{d}_{i,1}|^2 - 2|\mathbf{d}_{i,0} \cdot \mathbf{d}_{i,1}| \rangle} \\
&\approx \sqrt{\langle |\mathbf{d}_{i,0}|^2 \rangle + \langle |\mathbf{d}_{i,1}|^2 \rangle} \text{ since } \mathbf{d}_{i,0} \text{ and } \mathbf{d}_{i,1} \text{ are uncorrelated} \\
&\approx \sqrt{2} \times \delta r_{\bar{r}}
\end{aligned}$$

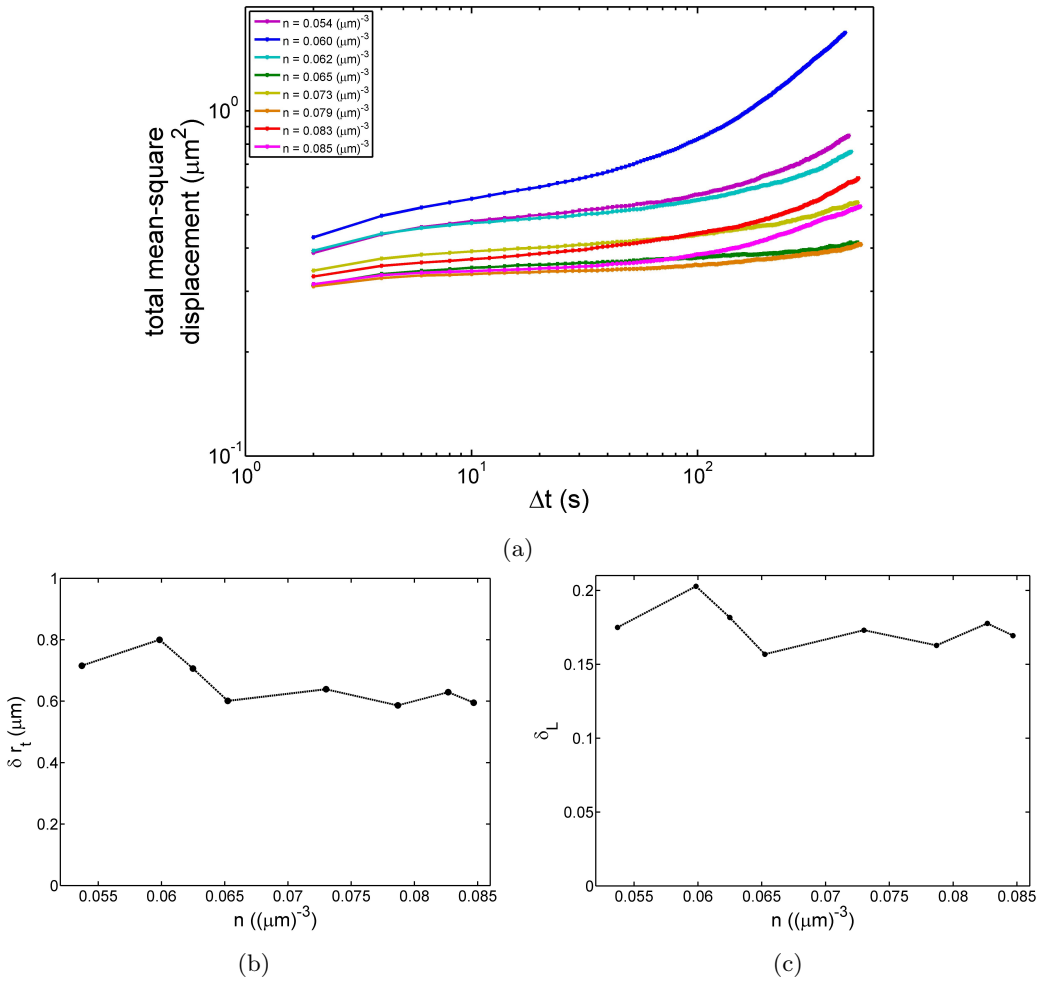

Figure 6.7: Localization of particles in colloidal Wigner crystals. a) Total mean-squared displacements of particles from their average positions for crystalline samples at different volume fractions. Note that, except for one outlier at $n = 0.060(\mu\text{m})^{-3}$, the curves show a distinct plateau at intermediate times, indicating the localization of particles near the lattice positions. For some samples, the increase at later times is suggestive of particles hopping between lattice sites, but this is inconclusive (see Section 6.3.6). b) The square-root of the plateau values of the curves in (a), taken as the mean value between delay times $\Delta t = 6$s and $\Delta t = 60$s, giving the localization lengthscale δr_t. c) The plateau values in (b) scaled to give the unitless Lindemann parameter $\delta_L = \delta r_t/(\sqrt{2}\,a)$. At all volume fractions, δ_L is significantly larger than the critical value for melting usually reported as the Lindemann criterion ($\delta_{L,c} \approx 0.10$). Note that δ_L varies little with volume fraction, with perhaps a slight increase at the lowest volume fractions.

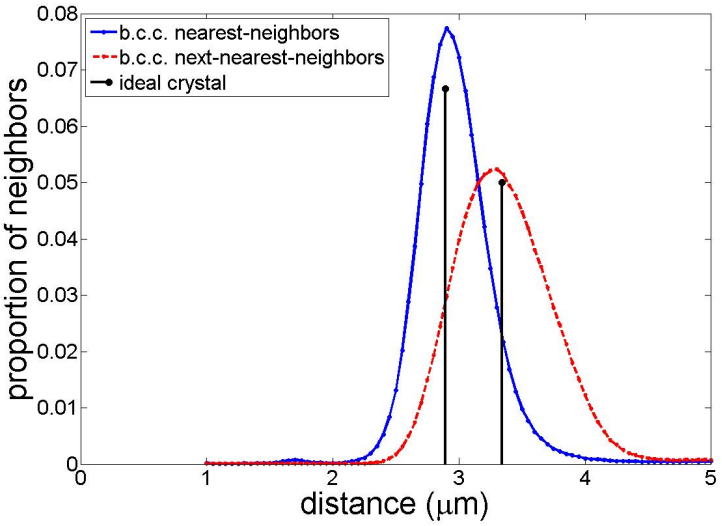

Figure 6.8: Neighbor distances in an experimental Wigner crystal. Neighbors are classified as nearest- or next-nearest-neighbors according to the orientation of the vector connecting the particle centers. Fluctuations are large enough that the distributions of nearest-neighbor distances and next-nearest-neighbor distances overlap significantly. Data are shown for $n = 0.054(\mu\text{m})^{-3}$; the curves are very similar for other number densities.

a slight increase in δ_L at the lowest volume fractions; and at all volume fractions, it is significantly larger than the 0.1 critical value above which a crystal is often expected to melt.

One result of the large fluctuations is that the nearest-neighbor and next-nearest-neighbor shells of these Wigner crystals overlap. As discussed in Section 4.3.4, a particle in a perfect b.c.c. lattice with lattice cube side l has eight nearest-neighbors at a distance $a = (\sqrt{3}/2)\ l$, and six next-nearest-neighbors at distance l, only 15% further away than the nearest-neighbors (see Fig. 4.7 in Section 4.3.4); these two neighbor shells are quite close. Thus with typical fluctuations on the order of $\gtrsim 20\%$ of the nearest-neighbor distance a, some nearest-neighbors will fluctuate further away than the next-nearest-neighbor distance, while some next-nearest-neighbors will fluctuate closer than the nearest-neighbor distance. We classify crystallographic nearest- and next-nearest-neighbors not by distance, but by comparing the *orientation* of the vector connecting the particle centers with characteristic orientations determined from the sample average, as described further in Section 4.3.4. This classification allows us to separate the distributions of nearest-neighbor distances and of next-nearest-neighbor distances (Fig. 6.8). In a perfect b.c.c. lattice, the nearest-neighbors would be represented by a delta function at distance a, and the next-nearest-neighbors by a delta function at l. In the experimental system, however, fluctuations broaden both distributions

until they overlap substantially. The slight skew of both distributions is also notable – it is easier for a neighbor to fluctuate further from the reference particle than closer, so that both distributions show a wider tail toward large distances than toward small.

6.3.4 Lattice analysis

From the particle positions, I explicitly define the *average lattice* (the lattice fitting is described in great detail in Section 4.3.5). I impose the constraint that we have a b.c.c. crystal, enforcing a single lengthscale and orthonormality of the crystal axes. The lattice is then described by seven parameters: one lengthscale, for which we will use the aforementioned *cube side* l, that is, the side length of the cubic unit cell; three angles representing the rotation of the lattice with respect to the imaging coordinates (actually expressed as a 3x3 orthonormal rotation matrix); and the three-component translation of the lattice origin with respect to the origin of the imaging coordinates. These seven parameters are calculated from the 3D locations of typically 1000-2000 particles at each timestep in a single imaging volume.

Let me pause here to remind you of the terminology discussed in Section 4.3.5. 'Imaging coordinates' refer to coordinates in the reference frame determined by the confocal microscope: positions are measured in microns, and the X and Y directions refer to the optical scanning directions in a single 2D confocal image, while the Z direction refers to the physical scanning direction and the optical axis. 'Lattice coordinates', in contrast, refer to coordinates in the reference frame determined by the fitted average lattice: positions are measured in multiples of the lattice cube side l, and the X, Y, and Z directions are along the cubic axes of the lattice. I shall try henceforward to be clear as to which coordinate system I am using, so pay attention.

The fit of the particle positions to a b.c.c. lattice is quite good, but there are some slight deviations. We examine the constraint that the three lengthscales of the crystalline lattice are equal by calculating the overall dilation of the system in each of the three directions (calculated as the best-fit slope of the displacements ΔX_i as a function of X_i, in direct analogy to the dilations used in refining the lattice as described in Section 4.3.5). Taking the sample at $n = 0.054(\mu m)^{-3}$ as an example, we find a slight dilation in the (lattice) X direction, and a slight compression in the (lattice) Z direction, but that the magnitude of the dilation in any dimension is on average less than 1% (Fig. 6.9a), with some variation with time. Similarly, we examine the constraint that the crystalline axes are normal by

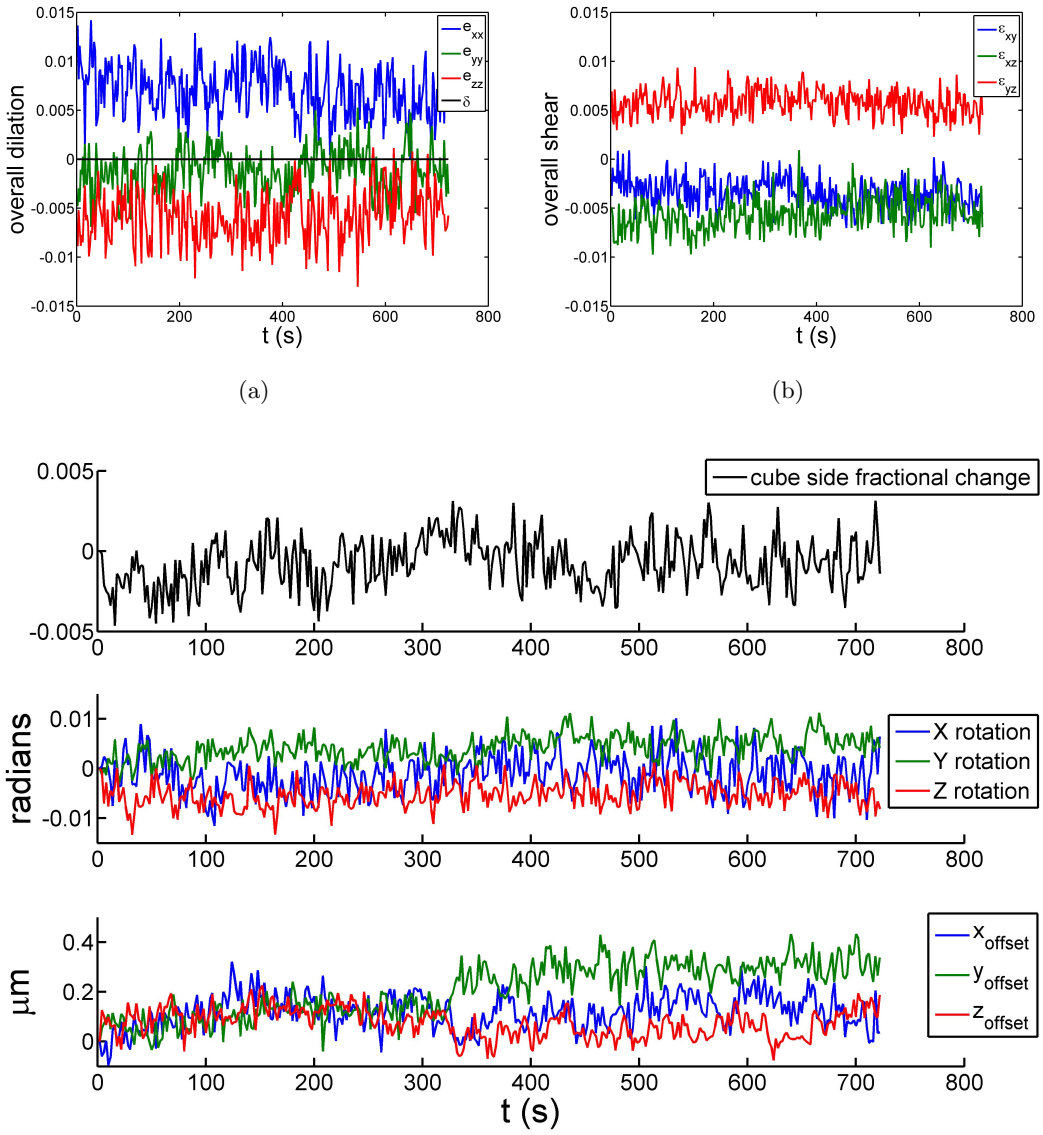

Figure 6.9: Deviations and stability of the average lattice. a-b) Deviations of the overall lattice from a perfect cubic lattice, showing the overall strain components fluctuating in time. a) The overall dilation in each lattice dimension, calculated as the best-fit slope to ΔX_i as a function of X_i; the constraint $\delta = 0$ is enforced by the lattice fitting algorithm. Time-averaged values are $\overline{e_{xx}} = 0.70\%$; $\overline{e_{yy}} = -0.12\%$; $\overline{e_{zz}} = -0.58\%$. b) The shear component in each cubic plane, calculated as the best-fit slope to ΔX_j as a function of X_i. Average values are $\overline{\epsilon_{xy}} = -0.34\%$; $\overline{\epsilon_{xz}} = -0.56\%$; $\overline{\epsilon_{yz}} = 0.57\%$; note that there is no constraint relation. c) Stability of the average lattice over time. Top panel: variation of lengthscale with time, plotted as fractional change from initial frame, showing stability to within 0.5%. Middle panel: variation of rotation angles with time, plotted as the off-diagonal components of $\mathcal{R}(t)\mathcal{R}(t_0)^{-1}$ (relative rotation angle in the small-angle approximation), showing stability of better than 0.01 radians. Bottom panel: variation in offset with time, plotted as change from initial frame, showing both slow drift, and an abrupt jump at around 320-330s, but total displacement of less than 0.5μm in any direction. All data for $n = 0.054(\mu\text{m})^{-3}$

considering the overall shear of the system in each of the three cubic planes (again calculated as a best-fit slope of ΔX_j as a function of X_i in analogy to the lattice refinement). We find slight shears in each component, but again less than 1% at all times (Fig. 6.9b). Thus we are quite confident that our description of the system by an average b.c.c. lattice is valid; deviations from this characterization are nonzero, but small.

We further find that the definition of the average lattice is quite stable with time. The value of the lattice constant fluctuates slightly with time, but changes by less than 0.5% over the 12-minute observation period (Fig. 6.9c, top panel). The rotation angles of the lattice relative to the imaging frame similarly fluctuate, but vary by less than 0.015 radians (Fig. 6.9c, middle panel). The offset between the origin of the imaging frame and that of the lattice frame moves by up to 0.5μm (possibly caused by a slight jogging of the physical sample; Fig. 6.9c, bottom panel). As with the deviation from a perfect cubic lattice, the variation with time is nonzero, but is small enough that we are confident that the average lattice is a good description of the system over time.

Finally, we verify that the calculation of the average lattice does not change signficantly if we use subsets of a 3D image; e.g. the average lattices defined independently in the left half and the right half of the image are very similar. In fact the variation with subset of the image is on the same scale as the variation with time.

Taking this average lattice, I identify each particle to its nearest lattice position, and can calculate its displacement from its lattice position; the root-mean-squared average displacement from the lattice position provides a time-independent measure of the fluctuations in the crystal. This lattice r.m.s.d. is shown for one sample in Fig. 6.10a, in lattice units, as a function of time. Note first that this fluctuates in time by a few percent. Note second that the traces for the three dimensions (in lattice coordinates) are similar, which is further suggestive that the average lattice is valid, and furthermore that the crystalline directions are physically equivalent (e.g. that effects of gravity and boundary effects are small).

I use this r.m.s.d. from the lattice position to calculate the Lindemann parameter, and compare this to the value calculated using the temporal r.m.s.d. (Fig. 6.10b). Curiously, these two measures of the mean-square displacement give slightly different results. It may be that the average particle position does not quite correspond to the lattice position, or that the particle displacements were not indeed uncorrelated on the timescale of the plateau in the temporal r.m.s.d. as assumed. However, both calculations give large values of the Lindemann parameter, and little variation with volume fraction.

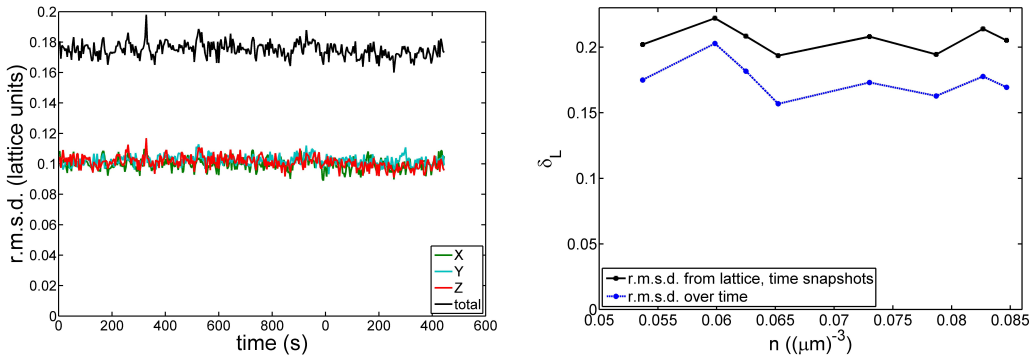

(a) (b)

Figure 6.10: a) Root mean square displacement from the lattice position, for $n = 0.054(\mu\text{m})^{-3}$, shown fluctuating in time. The r.m.s.d. is given in units of the lattice cube side. b) Comparison of the Lindemann parameter calculated using displacements from the lattice position (black curve), and using the temporal displacements (blue curve). Note that while the two measures do not quite agree, both give values larger than the usual Lindemann melting criterion $\delta_{L,c} \approx 0.1$, and both are fairly flat with volume fraction.

6.3.5 Local strains

I also quantify the local deformation of the lattice by the *local strains*. I calculate these strains from the locations of a central particle and its nearest- and next-nearest-neighbors (up to 15 particles in total), by finding the best affine deformation from the particles' reference lattice positions to their measured positions (this method is originally due to Falk and Langer, and explained in more detail in Section 4.3.6) [19, 26, 64]. Two strain components, ϵ_{xx} and ϵ_{xy}, are visualized for one sample in Fig. 6.11. While small strains are most common, strains of up to $\approx 20\%$ are readily observed.

I use the distribution of strains to calculate the elastic constants of the system (as in Refs. [26, 64]; this calculation is described in more detail in Section 4.4). Creation of an average strain e over volume V requires energy $E = \frac{1}{2}\mu e^2 V$, where μ is the elastic constant associated with the strain e, and so for thermal excitations, we expect a Boltzmann distribution with $P(E) \propto \exp(-E/k_B T)$. Thus a linear fit to $\log P(E/\mu k_B T) = \log P(e^2\ V/2k_B T)$ yields the elastic constant μ as the negative of the slope. Here we use an averaging volume of a cube of side two lattice units, so that $V = (2l)^3$, and an averaging volume typically contains 16 particles.[5] The choice to average reflects the idea that the elastic modulus is ultimately a contiuum concept, and so speaking of the elastic modulus on the single-particle lengthscale is less meaningful.

[5]The calculated elastic constants do depend on the averaging volume used – if the un-averaged single-particle strains are used (with $V = 1/2\, l^3$), the resulting elastic constants are larger by about a factor of 5.

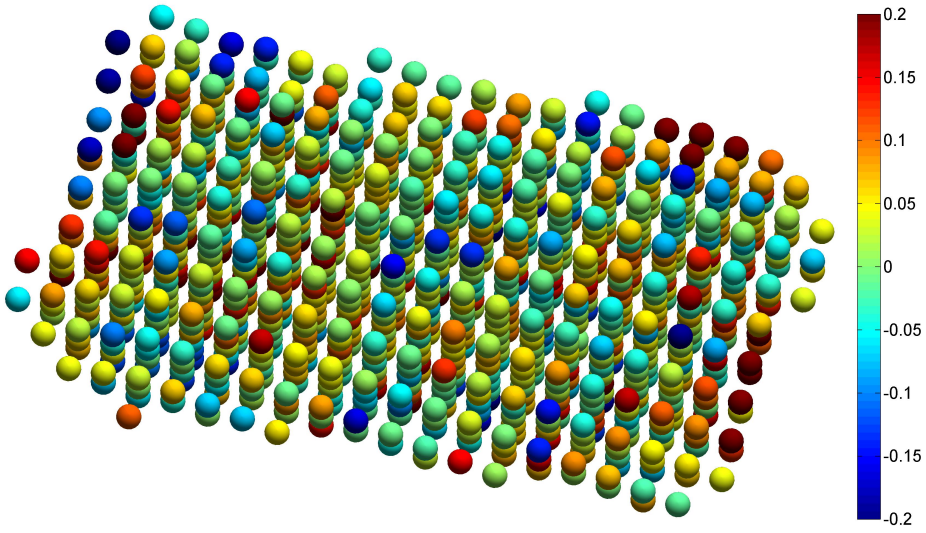

(a)

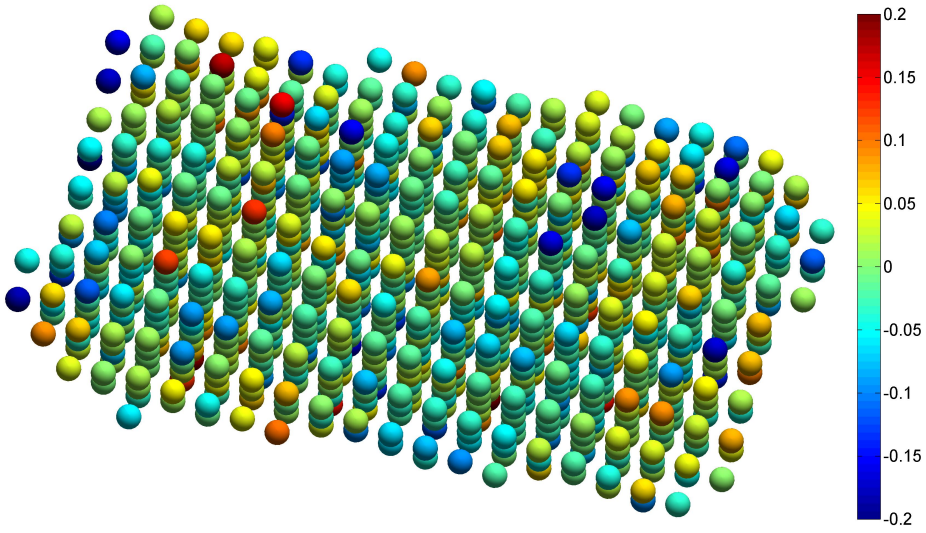

(b)

Figure 6.11: Local strains in a Wigner crystal. Particles are artificially shown on their lattice positions rather than their true positions to make the ordering more clear, and are color-coded according to the local value of a) tensile strain ϵ_{xx} and b) shear strain ϵ_{xy}. $n = 0.054(\mu m)^{-3}$.

A cubic crystal is characterised by three independent elastic constants: c_{11} associated with tensile strains along the cubic lattice directions; c_{44} associated with shear strains in the cubic planes; and c_{12}, which couples a tensile stress in one lattice direction to the tensile strain in a perpendicular lattice direction.[6] The shear constant c_{44} is directly obtained from the distribution of shear strains in the directions of the cubic axes. The other elastic constants, c_{11} and c_{12}, are obtained indirectly from two other moduli: the bulk modulus B, which is calculated from the distribution of dilatation energies; and the shear modulus in a coordinate system rotated by 45° around one of the cubic axes, $\mu'_{\rm shear}$, calculated from the shear energies in the rotated frame. Then

$$c_{11} = B + \frac{4}{3}\mu'_{\rm shear}$$

and

$$c_{12} = B - \frac{2}{3}\mu'_{\rm shear}$$

Example averaged strain energy distributions, are shown in Fig. 6.12a, with the fits giving the elastic constants. For e the total dilatation, $\delta = e_{xx}+e_{yy}+e_{zz}$, the corresponding elastic modulus is the bulk modulus $B \approx 7.7$mPa. For e a shear strain, the shear modulus depends on direction relative to the crystal, from ≈ 5.4mPa to ≈ 13mPa.

These crystalline elastic constants vary with volume fraction (Fig. 6.13a). Always $c_{12} \lesssim c_{44} < c_{11}$, and the elastic constants increase with volume fraction as expected. The crystals are strongly anisotropic at all volume fractions. I quantify the anisotropy by $\Delta \equiv 2c_{44} - (c_{11} - c_{12})$; $\Delta = 0$ for an isotropic system. In fact we find that $\Delta > 0$ at all volume fractions (Fig. 6.13b). There is no decline in anisotropy at lower volume fractions; if anything, there is perhaps a slight *increase* in anisotropy at the lowest volume fraction, although the data are noisy enough that this is inconclusive.

I expect the Cauchy relation to hold and $c_{12} = c_{44}$ for the centrosymmetric b.c.c. lattice with two-body Yukawa interactions [80] (see Section 1.5.4). It is not quite clear whether this is the case for this system; there is the suggestion that $c_{12} < c_{44}$ at most volume fractions, but the uncertainties are too large to draw any conclusion.

We also observe the nonlinearity of the stress-strain relationship in the strain distribu-

[6] As given in Section 1.5.4, the total strain energy density in a cubic crystal is

$$u = {}^1\!/_2\, c_{11}(e_{xx}^2 + e_{yy}^2 + e_{zz}^2) + c_{12}(e_{xx}e_{yy} + e_{xx}e_{zz} + e_{yy}e_{zz}) + {}^1\!/_2\, c_{44}(e_{xy}^2 + e_{xz}^2 + e_{yz}^2)$$

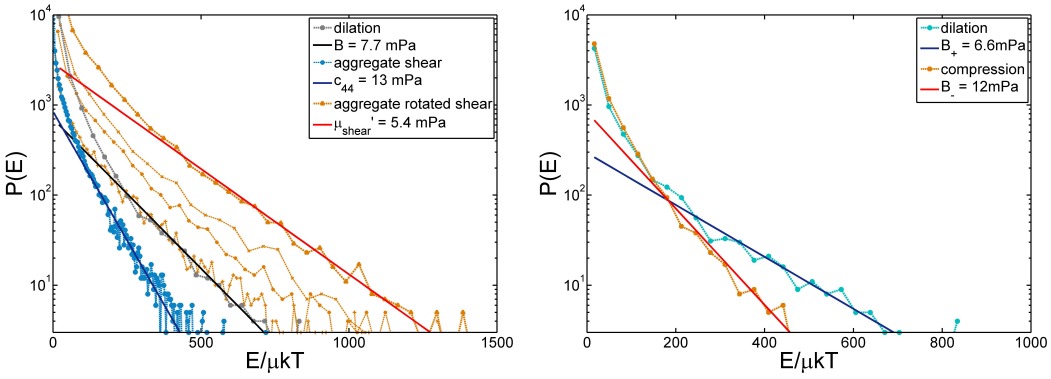

(a) (b)

Figure 6.12: Determination of elastic constants from distribution of strain energies in a Wigner crystal. a) Distribution of strain energies, scaled by $\mu k_B T$, obtained as $E/\mu k_B T = \frac{1}{2} e^2 V/k_B T$ with the averaging volume $V = (2l)^3 \approx 300(\mu\text{m})^3$. Distributions are shown for energy contributions of the total dilatation (grey/black), shear strains relative to the cubic axes (blue), and shear strains relative to a rotated reference frame (orange/red). For the two types of shear strain, the distribution shown is an aggregate of three components; the individual components are shown as thin orange lines for the rotated shear strain. Shown with best-fit lines; the slope of these lines gives the bulk elastic modulus B; the elastic constant c_{44}; and a 'rotated shear modulus' μ'_{shear}, respectively. The deviation from the exponential behavior at small values of $E/\mu kT$ is not yet understood. b) Distribution of strain energies for total dilatation, with positive strains (dilation) and negative strains (compression) distinguished. Shown with best-fit lines, giving approximate bulk modulus for dilation ($B_+ = 6.6$mPa) and for compression ($B_- = 12$mPa). $n = 0.054(\mu m)^{-3}$; distributions are aggregated over all timesteps.

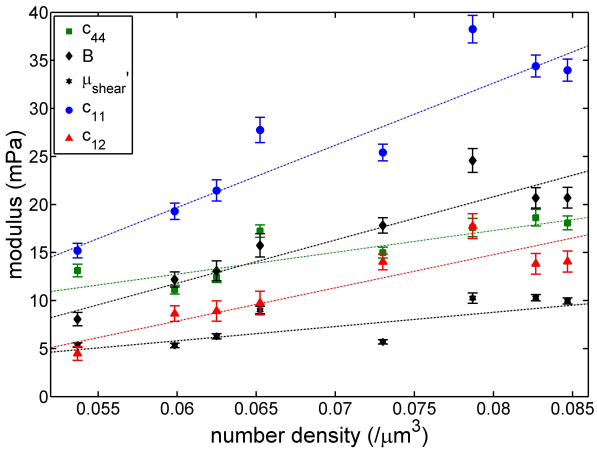

(a)

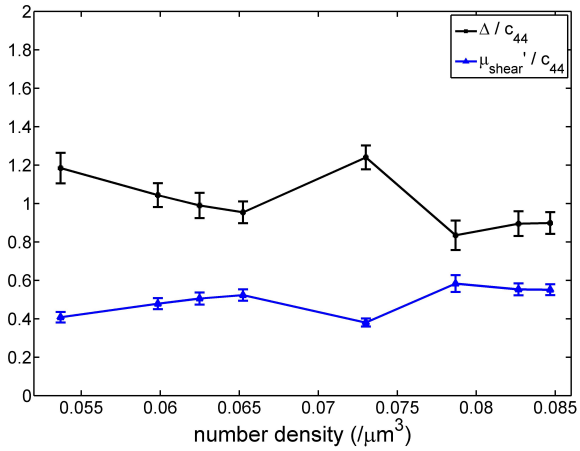

(b)

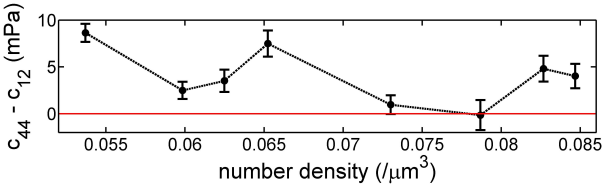

(c)

Figure 6.13: a) Variation of elastic constants with volume fraction. The constant c_{44} is estimated from the exponential region of the distribution of shear squared-strains, in the cubic lattice coordinates; the bulk modulus B is estimated from the exponential region of the distribution of squared total dilatation (sum of the tensile strains); and μ'_{shear} is estimated from the exponential region of the distribution of shear squared-strains in a coordinate system rotated by 45° around one cubic axis. c_{11} and c_{12} are calculated from B and μ'_{shear} by the relations given in the text. Lines are guides to the eye. b) Variation of elastic anisotropy with volume fraction. $\Delta/c_{44} \equiv [2c_{44} - (c_{11} - c_{12})]/c_{44} = 2(1 - \mu'_{\rm shear}/c_{44})$ is 0 for an isotropic system, and larger for an anisotropic system, with a maximum possible value of 2 for a shear-stable system. (The factor of 2 is included to match the definition used by others.) The colloidal Wigner crystal is markedly anisotropic ($\Delta/c_{44} > 0$) at all volume fractions accessed. c) Difference between elastic constants c_{44} and c_{12}; the Cauchy relation says this should be 0 for two-body interactions on a centrosymmetric lattice.

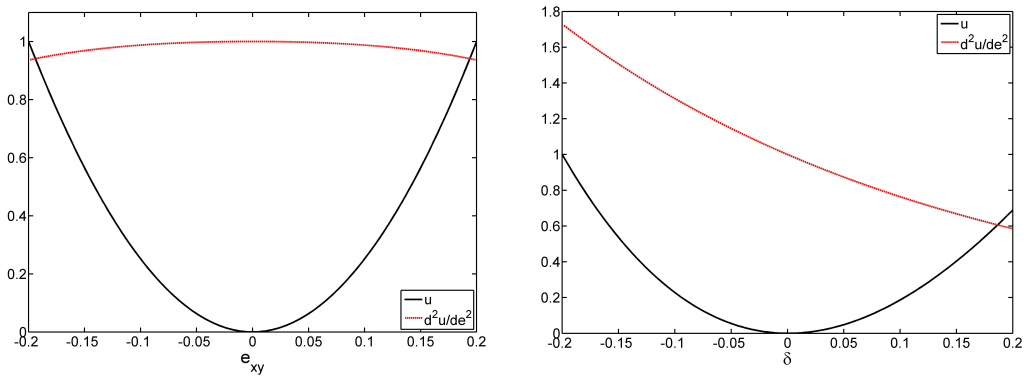

(a) (b)

Figure 6.14: Estimation of strain energies and elastic constants from Yukawa model. a) Energy per particle as a function of strain for a single shear strain, with second (numerical) derivative shown; the value of the second derivative at $e = 0$ gives the elastic constant c_{44}. Note that the second derivative is nearly constant over a large range of strains, indicating that the stress-strain response is quite linear. b) Energy per particle as a function of strain for an isotropic dilatation, with second (numerical) derivative; the value of the second derivative at $e = 0$ gives the bulk modulus B. Note that the second derivative varies substantially with strain, indicating a nonlinear stress-strain response; the Yukawa crystal is stiffer to compression than to dilation. For both curves, $\kappa^{-1} = 0.45\mu$m and $l = 3.34\mu$m. Energy units are arbitrary.

tions. The elastic 'constant' applies only at small strains, where a harmonic approximation is valid; at larger strains, the stress-strain relationship may soften or stiffen. I readily see the difference between positive dilation and compression in the tensile strains, by separating the distributions for positive and for negative strain (Fig. 6.12b). In this example, the 'average' elastic constant for dilation is 6.6mPa, while the 'average' elastic constant for compression is 12mPa, larger by eighty percent. Indeed, this nonlinearity is present in a simple numerical model: assuming a Yukawa interaction between particles on a perfect b.c.c. lattice, I calculate the energy per particle in a uniformly deformed lattice as a function of the strain. For shear strains, the energy is quadratic over a large range of strains, and the second derivative is quite constant (Fig. 6.14a), indicating that the stress-strain response is linear. For dilatations, the harmonic approximation is not very good at large strains, and the second derivative varies strongly with strain (Fig. 6.14b), indicating the nonlinearity of the stress-strain response to dilatation.

Let me compare these results to some of those in the literature. Crandall and Williams measured Young's modulus $Y = 1$ dyne/(cm)^2 = 100mPa for $N = 10^{12}$(cm)$^{-3}$ and suggested that, very roughly, $Y \propto N$ [10] – this would predict $Y \approx 10$mPa for my samples, which are about an order of magnitude more dilute. At the order-of-magnitude level, this

is consistent with my results for $c_{11} \approx Y \approx 20$mPa. Lindsay and Chaikin measured G' on the order of tens of dyne/(cm)^2, or a few Pa, for samples about an order of magnitude more dense than Crandall and Williams [39] – similar scaling would suggest a G' of a few tens of mPa for my system, again, consistent at the order-of-magnitude level with my results for $c_{44} \approx G' \approx 10$mPa. Hurd *et al.* measured $c_{11} \approx 7$ dyne/(cm)^2 and $c_{12} = c_{44} \approx 2$ dyne/(cm)^2 at a density very similar to that of Crandall and Williams [23], suggesting $c_{11} \approx 70$mPa and $c_{44} \approx 20$mPa for my system, also consistent. Finally, Sprakel *et al.* reported G' and c_{44} of a few to tens of mPa in the system very similar to mine [68]. All of these experiments, including my own, are consistent with one another insofar as they can be compared.

The only experimental result I am aware of concerning the anisotropy is that of Hurd *et al.*, who claim that their values of c_{11} and $c_{12} = c_{44}$ demonstrate anisotropy; yet my own calculation on their numbers yields $\mu'_{\text{shear}} = \frac{1}{2}(c_{11} - c_{12}) = 2.27$ dyne/(cm)^2 while $c_{44} = 2.43$ dyne/(cm)^2 [23], that is, the shear modulus is nearly isotropic according to their results, with $\Delta/c_{44} = 0.14$. My results demonstrate a much clearer anisotropy, that is, a larger difference in the values of μ'_{shear} and c_{44}, due to my larger value of $\lambda \equiv \kappa n^{-1/3}$ ($\lambda \approx$ 5-6 vs. $\lambda \approx 4$).

These results are, however, inconsistent with the simulations of Robbins *et al.* – while it is difficult to compare the numerical values, the relations $c_{44} < c_{12} \approx c_{11}$ reported in Robbins *et al.* [54] are markedly different from my findings that $c_{12} \lesssim c_{44} < c_{11}$, which are all of the same order of magnitude. While my system is distinctly anisotropic, the anisotropy is not so strong as that reported in Robbins *et al.* (see Fig. 2.19b) [54]. Robbins *et al.* also find results in conflict with the Cauchy relation $c_{12} = c_{44}$ – comparing this to e.g. the work of Hurd *et al.* who found all three elastic constants to be the same order of magintude [23], I question whether approximations made in the lattice dynamics simulations gave errors in Robbins *et al.*'s values of the elastic constants.

I also compare my results to my own back-of-the-envelope numerical estimates assuming a Yukawa interaction (with fixed U_0 and κ) between particles on a perfect b.c.c. lattice, taking into account the interactions with 64 nearest neighbors (the first 6 neighbor shells). I chose $\kappa^{-1} = 0.45\mu$m to tune the value of $\Delta/c_{44} \approx 1$ at $n = 0.07(\mu\text{m})^{-3}$, and $U_0 = 10^{-23}$ Jm ≈ 60 ($eV \cdot \mu$m) to tune the value of $c_{44} \approx 16$mPa at $n = 0.085(\mu\text{m})^{-3}$; the resulting computations are shown in Fig. 6.15.

These numerical estimates reproduce many aspects of our experimental results (Fig. 6.13). The increase in anisotropy with decreasing volume fraction is very similar. The elastic con-

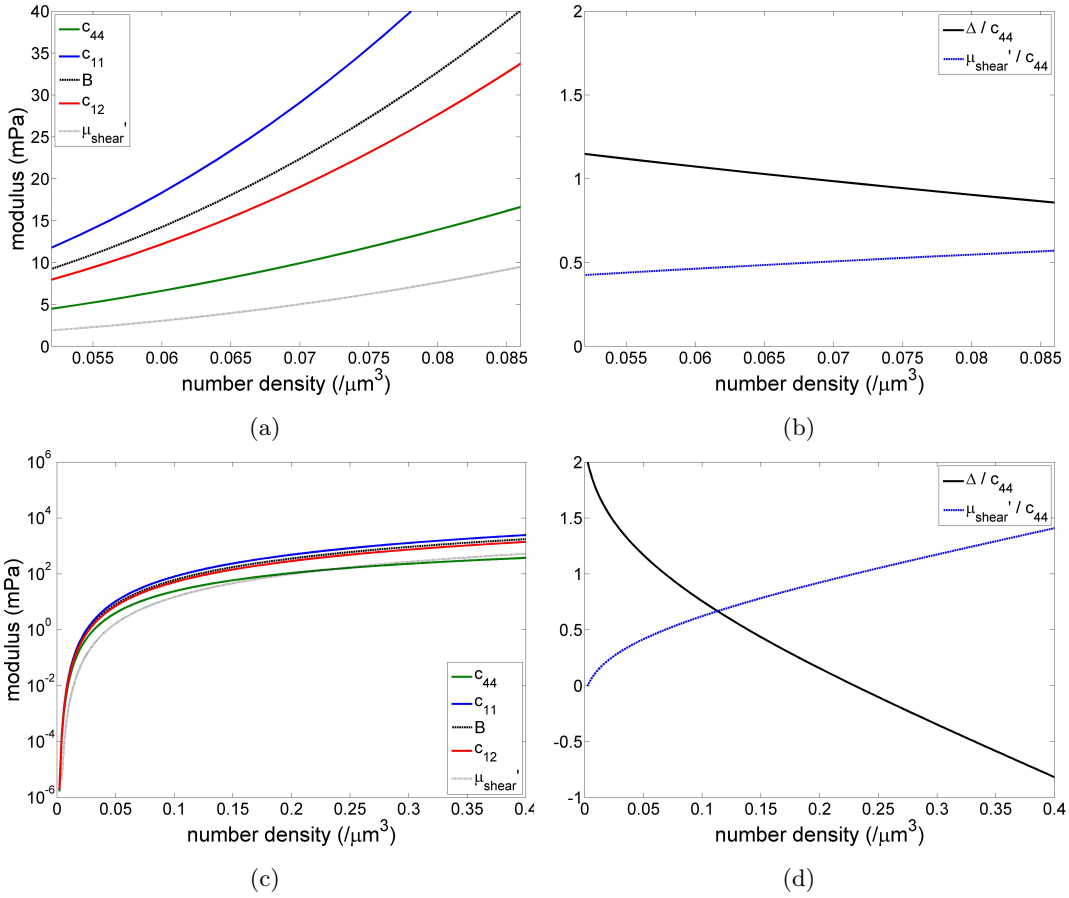

Figure 6.15: Elastic constants and anisotropy from numerical estimates of Yukawa potential. a) Elastic constants calculated as a function of volume fraction for $U_0 = 10^{-23}$Jm, $\kappa^{-1} = 0.45\mu$m, and 64 nearest neighbors considered. c_{44}, c_{11}, and B are calculated directly; c_{12} and μ'_{shear} are inferred from c_{11} and B. b) Anisotropy as a function of volume fraction; $\Delta \equiv 2c_{44} - (c_{11} - c_{12})$ as in Fig. 6.13b. In (a-b), the range of number densities is chosen to match my experimental results. c) Same calculation as in (a), but showing a larger range of volume fraction; note the log-linear scale. d) Same calculation as in (b) but again showing a larger range of volume fraction. These curves should be taken with a healthy dose of salt; assumptions such as constant U_0 and κ are not well-justified, and particularly at higher number densities, additional neighbor shells which have been discounted will be increasingly important.

stants increase with volume fraction as expected; the slower increase in the experimental results compared to the numerical estimates is potentially explained by the value of κ changing with volume fraction. The experimental results give $B \approx c_{44}$, while the numerical estimates give B about twice c_{44}; similarly, c_{11} and c_{12} have lower values relative to c_{44} in the experimental results than in the numerical estimates. Note that this holds over a larger range of volume fractions (Fig. 6.15c), that is, it does not depend on the choice of κ. While the numerical estimates give c_{11} and B in the small-strain limit, the experimental values give an ill-defined average of the elastic constants at different strain values, which may account for the discrepancy. Nonetheless, a very simple model captures the qualitative behavior of the experimental system, and in particular the variation of the anisotropy with number density.

I note the import of the values $\kappa^{-1} = 0.45$ μm and $U_0 = 10^{-23}$Jm that were chosen to obtain the best (qualitative) fits with the experimental data. The screening length is about a factor of two shorter than expected based on the added AOT concentration (and the results of [22, 28]). This expectation was very rough, so some disagreement is not surprising. I also expect the ionic strength to increase with the addition of particles, as the counterions go into solution and contribute to screening, so that the screening length may be shorter due to this effect. This also means that κ is not likely to be constant as a function of volume fraction, as we have assumed in these calculations. This change in κ, with κ^{-1} decreasing as n increases, would account for some softening at higher n, as seen in the experiments relative to the constant-κ numerical estimates.

If we estimate an *effective* particle charge from the interaction strength, we find $Z^* \approx \sqrt{U_0 \epsilon \epsilon_0} \approx 100e$. This is a very rough order of magnitude estimate, but is consistent with the effective charges reported in e.g. Refs. [22, 28, 68].

Correlations

I am also interested in the collective nature of the fluctuations in this system – particles do not simply fluctuate in a static potential well, but rather, fluctuations of one particle will affect the equilibria of its neighbors, influencing their fluctuations, and so on. This collective behavior can be quantified by the *correlations* of the fluctuations. In particular, I calculate

the *correlation field* for each strain component,

$$C_{\epsilon_{ij}}(\mathbf{\Delta r}) = \frac{\left\langle \left(\epsilon_{ij}(\mathbf{r}) - \langle\epsilon_{ij}\rangle\right) * \left(\epsilon_{ij}(\mathbf{r}+\mathbf{\Delta r}) - \langle\epsilon_{ij}\rangle\right)\right\rangle_{\mathbf{r}}}{\left\langle \left(\epsilon_{ij}(\mathbf{r}) - \langle\epsilon_{ij}\rangle\right)^2\right\rangle_{\mathbf{r}}}$$

with the average taken over all reference positions $\mathbf{r}$. Examples of these correlations are shown in Fig. 6.16. These fields show only short-range correlations of strains in the system, over about 3 lattice spacings. Correlations are related to propagating waves in the system. Longitudinal modes will be overdamped by the presence of the solvent. While some long-wavelength transverse modes have been predicted to be able to propagate through collective motion of both the particles and the solvent [23, 39], I have not seen evidence of them here, and earlier experiments have also missed them where hoped for [23].

The correlation fields are surprisingly constant across different volume fractions (Fig. 6.17). For many examples of strain component and direction, there is little variation or trend with volume fraction. The correlation fields seem to be fairly uniform characteristics of the Wigner crystals over the range of volume fraction studied.

6.3.6 Defects and diffusion through the crystal

These Wigner crystals have a remarkably low concentration of point defects: we observe grain boundaries, but within a single crystal, I have seen very few vacancies (missing particles) or interstitial particles. In this system, the energetic cost of a vacancy is dominated by the confining pressure: an external pressure estimated on the order of 10mPa is required to counteract the repulsive pressure of the crystals at these number densities, so that the added volume of a vacancy is associated with an energy cost of $PV \approx$ 20-50 k_BT.[7] About 40% of this energy cost is recovered due to the reduction of repulsive interparticle interactions around the vacancy, but the net energy cost is still on the order of $10k_BT$ at the lowest number density (and larger as number density increases), so that we expect the equilibrium population of vacancies to be on the order of a few in a hundred thousand or smaller – small enough that we do not expect to see vacancies within our limited data. Because of the soft interactions, we also do not expect many excess point defects over this small equilibrium

[7] We estimate the pressure from the numerical estimates described in the previous section: in addition to the energy of particle interactions, an energy term linear in total dilatation δ is required to stabilize a fixed-volume-fraction crystal against expansion. The coefficient of this term is determined as the first derivative of the interaction energy with respect to δ, and identified as the pressure. The pressure in this numerical estimate ranges from 4mPa at the lowest number density to 16mPa at the highest number density studied.

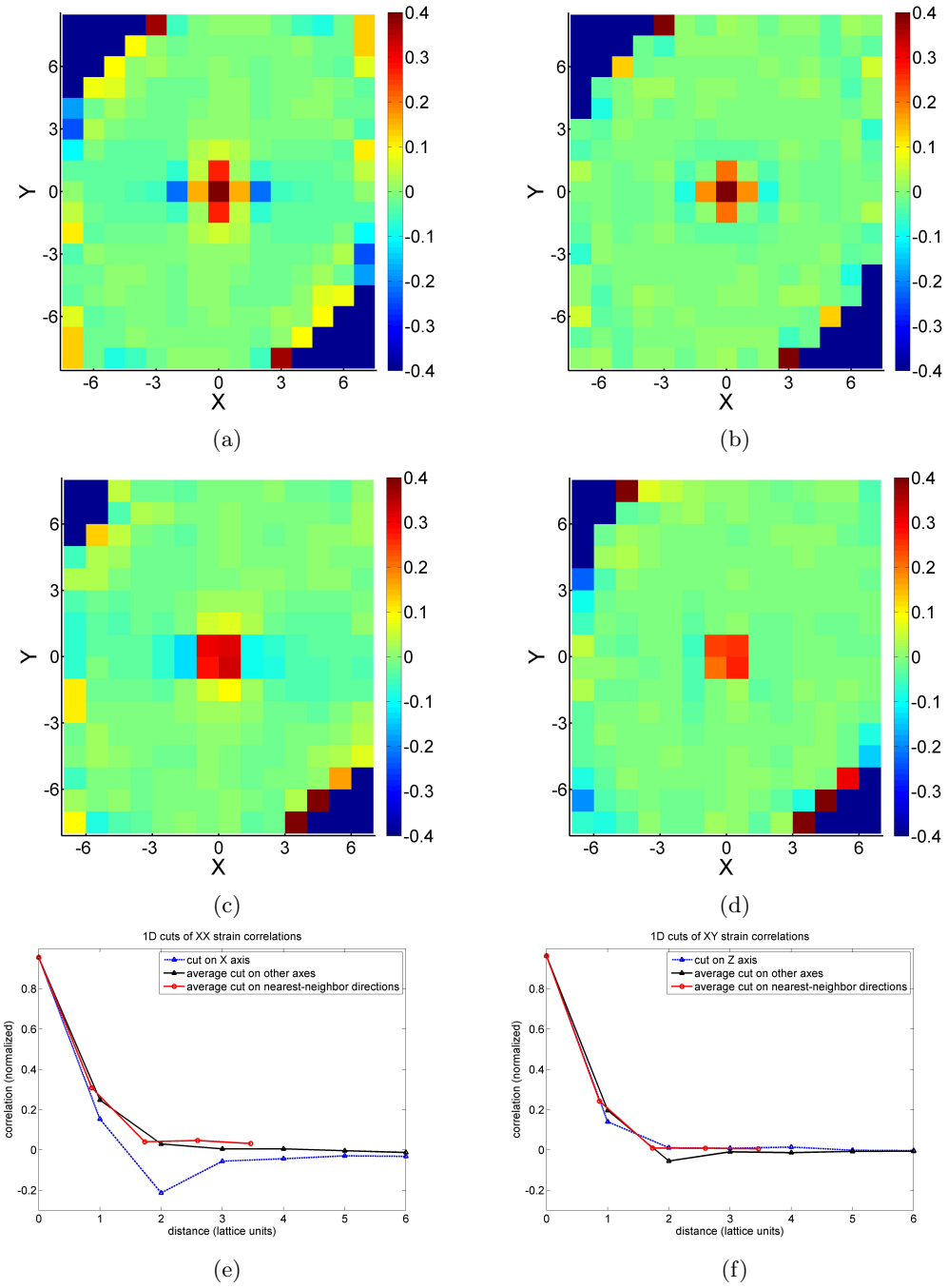

Figure 6.16: Strain correlations in an experimental Wigner crystal. (a-d) Correlation fields of a) the tensile strain e_{XX} in the XY plane; b) the shear strain e_{XY} in the XY plane; c) the tensile strain e_{XX} in the nearest-neighbor plane, parallel to but $1/2$ a lattice constant offset from the plane in (a); d) the shear strain e_{XY} in the nearest-neighbor plane, parallel to but $1/2$ a lattice constant offset from the plane in (b). (e-f) One-dimensional cuts of the correlation fields along several directions for e) the tensile strain e_{XX} correlation and f) the shear strain e_{XY} correlation. In (a-d), the dark blue regions near the corners represent regions outside the image, and the noise at large $\mathbf{\Delta r}$ is due to poor statistics with very few particle pairs contributing to the average. All plots for $n = 0.054(\mu\text{m})^{-3}$.

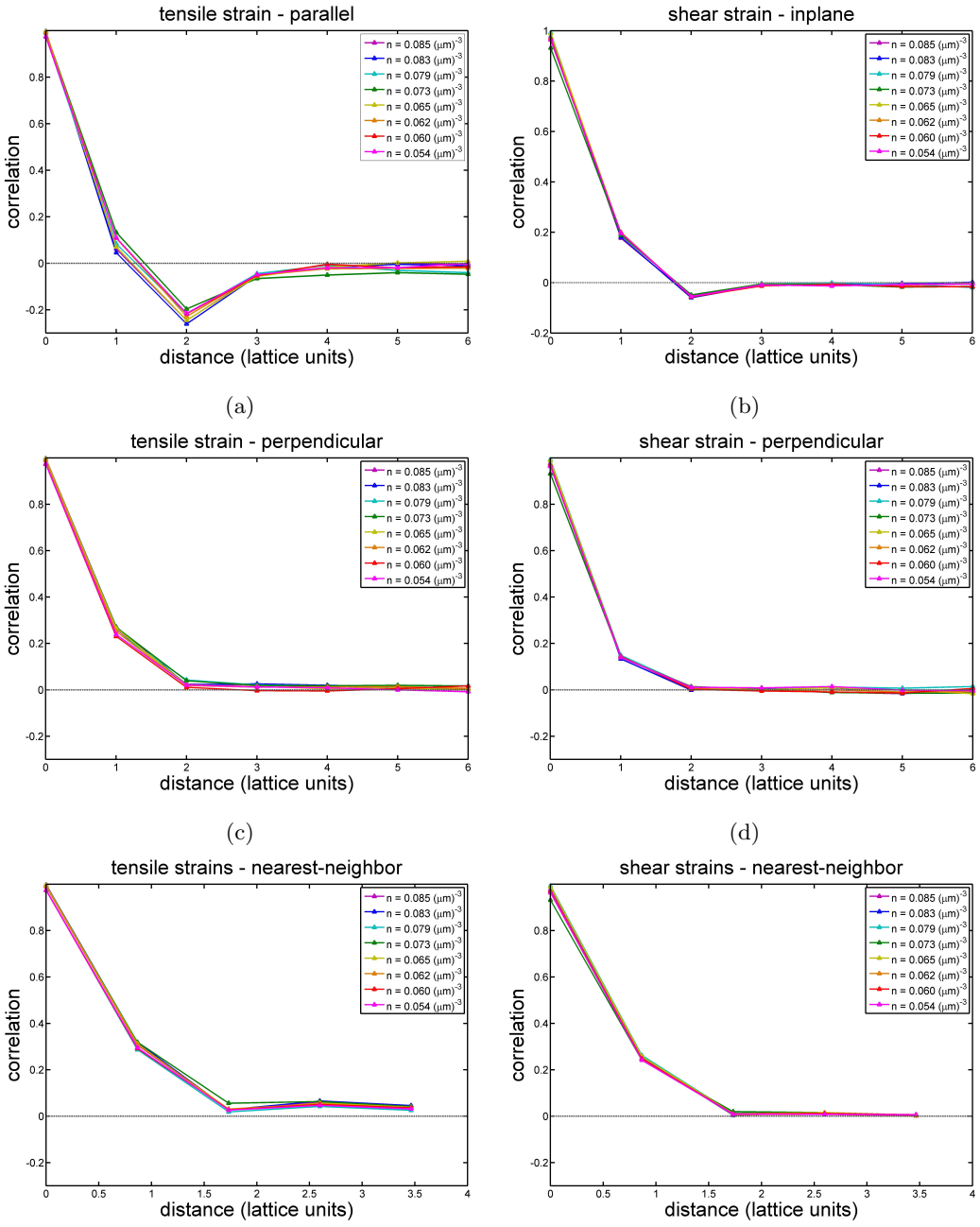

(a) (b) (c) (d) (e) (f)

Figure 6.17: Uniformity of strain correlations with volume fraction. a) Correlations of tensile strains in direction parallel to the strain component; b) Correlations of shear strains in the plane of the strain component; c) Correlations of tensile strains in the plane perpendicular to the strain component; c) Correlations of shear strains in the direction perpendicular to the strain component; e) Correlations of tensile strains in the nearest-neighbor direction; f) Correlations of shear strains in the nearest-neighbor direction. In all cases, there is little variation or trend with volume fraction.

population, as particles are easily able to rearrange to fill excess vacancies.

I do see a larger population of a particular type of defect: particle dimers. These defects arise in the nature of the constituent particles, however, rather than in the crystalline structure itself. While the particles are fairly monodisperse, a small proportion of particles were sufficiently destabilized during the synthesis or preparation processes as to fuse into dimers or small clusters. Filtering of the particles before experimentation helped remove the larger clusters and many, but not all, of the dimers. My observation was that these dimers nearly always comfortably occupied a single lattice site – at these low volume fractions, the lattice spacing was large enough to accommodate a double-particle without signficantly disrupting the lattice ordering.

To identify potential vacancies and interstitials, I performed a quick-and-dirty check of the correspondence between particles and expected lattice positions. Vacancies were identified as lattice sites in the bulk of the image (that is, not near the image boundary where particles may easily fluctuate out of the imaging volume) which did not have a particle associated to them. Multiply occupied sites were identified as lattice sites with two or more particles associated to them (note that every particle, even a potential interstitial, is associated to its nearest lattice position by my algorithm). Both types of defects typically appeared at on the order of 0.5% of lattice sites, with small variation with number density. I suspect that many of the 'extra particles' were in fact members of dimers. The vacancies may represent true vacancies; physically present particles which for some reason were not located and so were lost to the analysis; or particles which fluctuated far enough from their lattice position to be very briefly identified with another lattice position before returning 'home'. In short, these defect candidates cannot be confidently identified without further analysis.

I also see indications of particles diffusing through the crystal, not only fluctuating about a single lattice position, but hopping to a new lattice position. The slight increase of the (temporal) mean-squared displacement curves at longer times, seen in Fig. 6.7a, is suggestive, although the statistics are not good enough to be conclusive. Furthermore, I observe particles which are identified as being associated with different lattice points at different times, typically about 0.7% of particles per timestep, again with some variation across samples – examples are shown in Fig. 6.18. This has several possible explanations. First, and most interesting, that a particle has actually hopped from one lattice position to a new position, one step of diffusion through the crystal. Alternatively, the particle has

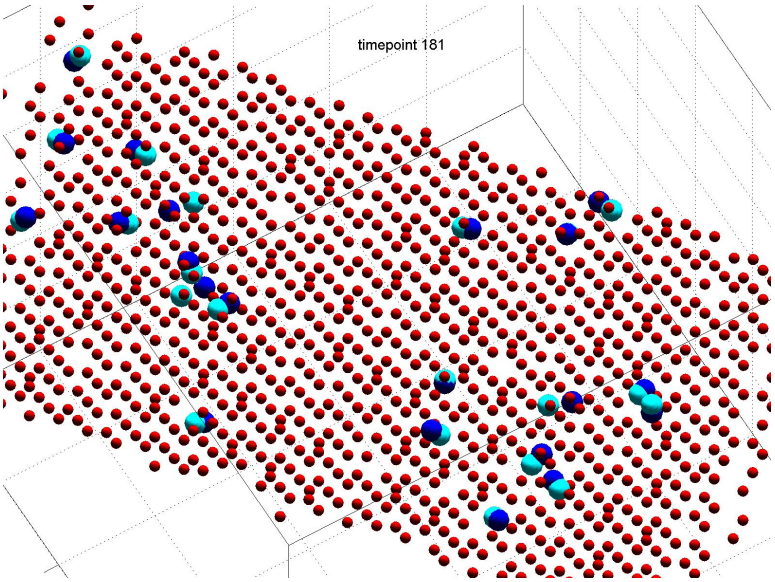

Figure 6.18: Potential particle hops, comparing particle positions at two successive timesteps. Particles which remain associated to the same lattice position are shown on that lattice position as small red spheres. Blue spheres show the true positions of particles which became associated with a new lattice position; light blue represents the position at the earlier timestep, and dark blue the position one timestep later when associated with a new lattice position. Note that these are only *potential* hops – I expect about 2/3 to be explained by tracking errors near the image boundaries, and some others to represent large excursions, particularly by members of dimers, which then return to the original lattice position. $\phi \approx 16.4\%$.

merely fluctuated particularly far from its home lattice position so as to be briefly identified with a neighboring (but occupied) lattice position, before returning to its original position. This case may be especially likely for members of a dimer, in which the member particle centers are already well off the lattice position. Finally, there may always be faults in the tracking of particles – while the algorithm is good, it is not perfect, and we are limited by the time resolution of the data collected.[8] With exquisite time resolution, this error would not be a danger – motion between time steps would be so small that there would never be confusion about the particle label. However, the time resolution in my experiments is, as mentioned, of the same order as the localization timescale of the particles, long enough for a particle to diffuse freely within its lattice potential well and move a significant distance. Thus such tracking errors are unfortunately quite possible. I expect these tracking errors to be particularly common near the boundaries of the image, where a particle may fluctuate in and out of the imaging volume; if one particle fluctuates in as another fluctuates out, tracking errors become even more likely.

A more thorough treatment of these potential hops would correlate hops with defects: dimers, vacancies, and interstitials. Further experiments including a dilute population of differently-labeled 'tracer' particles could shed light on particle defects and rearrangement, by providing a few particles which could be definitively tracked.

6.4 A teaser: sample with gravitational pressure

I will close with a brief account of the non-density-matched sample, in which a slight gravitational pressure gradient generated a gradient in structure. We observed that after two months, the particles had sedimented to the bottom of the sample cell. There was about 1cm of visibly crystalline suspension, with the volume fraction increasing markedly with depth; the upper part of this crystalline region appeared to consist of large crystals. A sharp line divided the crystal from a disordered (presumably fluid) region, with significant particle volume fraction visible for a few millimeters above this interface.

[8] Tracking errors may have either of two effects, either creating the appearance of particle swaps which did not physically occur, or missing particle swaps which did. Consider two physical particles, A and B, which at time t_1 are labeled as a and b by the tracking algorithm, and occupying neighboring lattice sites α and β. At timestep t_2, the physical particles A and B may remain on their lattice sites, but the tracking algorithm may make an error, identifying label b to physical particle A, and label a to particle B; then label b, on particle A, will be on lattice site α, and label a on site β, giving the appearance of a particle swap where none actually occured. Contrariwise, physical particles A and B may indeed swap lattice sites, while the tracking algorithm again makes an error; then label a is on particle B (due to the incorrect tracking), which has moved to lattice site α, while label b is on particle A on lattice site β. According to the tracking algorithm, both particles have remained on their original lattice position, whereas in reality they have swapped.

Confocal microscopy confirmed these qualitative observations. With a working range of 8.6mm in Z, we were able to observe about 4mm of particle fluid, with volume fraction increasing with depth; a liquid-crystal interface; about 2.5-3mm of b.c.c. crystallites; and another 1-1.5mm of f.c.c. crystallites (see Fig. 6.19). The lattice constant in the crystal changed dramatically with depth, with particles at the very top of the crystal separated by nearly a full particle diameter, while at the bottom the crystal took on a nearly-close-packed appearance.

The sample was extremely sensitive to changes in temperature and to mechanical agitation. Immediately after the sample was first moved to the confocal microscope, we observed the fluid-crystal interface to move up by about 50μm over the course of an hour; our hypothesis was that the uppermost crystal had been melted by the action of moving the sample and was re-forming. We then left the sample to equilibrate for 2.5 days before taking the majority of our data; over this time, the interface fell by about 1.5mm. Over the course of 9 hours of data collection, the interface first rose by about 50μm, then fell by 100μm, and when observing some 4mm into the fluid layer at the beginning of the data collection, an upward drift of the fluid particles was apparent. Slight temperature fluctuations would be expected to affect the solvent density, and so the relative density of the particles: the particles are relatively heavier at elevated temperature, increasing the gravitational pressure, and lighter at lower temperature, decreasing the pressure. Thus for more reliable experiments with this type of sensitive sample, we suggest more robust temperature control of the sample cell.

These data are, as mentioned, only a teaser: I have collected image sequences at a range of volume fractions (controlled by depth) in both the fluid and the crystal, but the data are recent enough that I have not yet analyzed them. I hope to carry out much of the same analysis of the elastic constants as a function of volume fraction, this time with a selection of volume fractions which may prove more interesting. This sample also gives the advantage of being able to measure the volume fractions of both crystal and fluid at the interface, and examine the dynamics of the interface itself.

6.5 Conclusion

We have observed that a charged-sphere system of colloidal particles with long-range repulsion orders into b.c.c. crystals at low volume fractions of $\phi \gtrsim 15\%$. These 'colloidal Wigner crystals' offer contrasts to more conventional colloidal hard-sphere, or effective hard-sphere

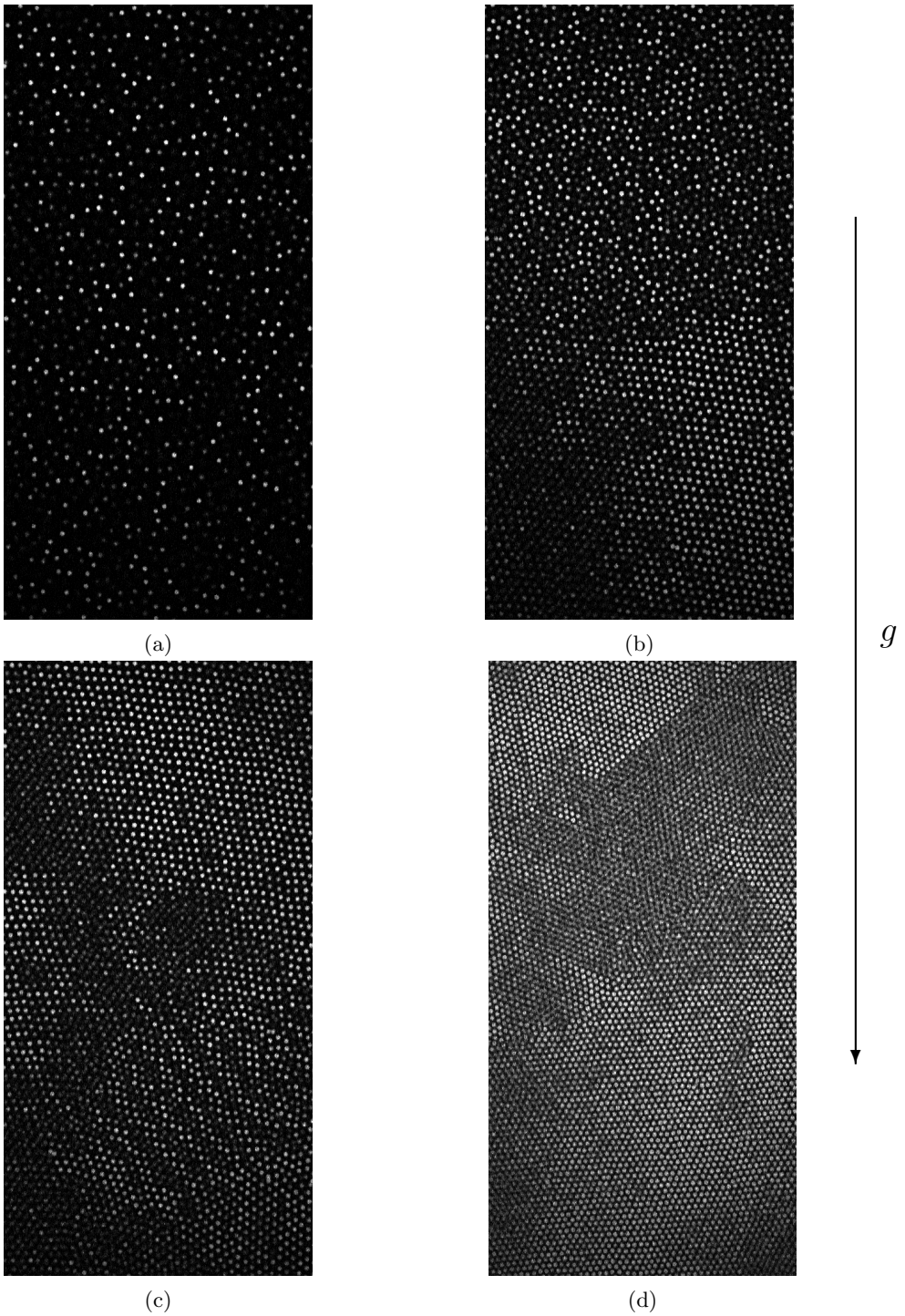

Figure 6.19: Confocal images of sample with gravitational pressure. a) Fluid 1.0mm above interface; b) crystal-fluid interface; c) crystal 200μm below interface; and d) crystal 1.8mm below interface. All images are $110 \times 220\mu$m and taken $\approx 30\mu$m from the sample boundary. Gravity is down.

crystals, which form f.c.c. structures only at much higher volume fraction.

The soft interactions in a colloidal Wigner crystal permit large fluctuations of the particles within the crystal, with typical root-mean-square displacements up to $\approx 20\%$ of the nearest-neighbor spacing (Lindemann parameter of $\delta_L \approx 0.20$). The Lindemann parameter is roughly constant over the range of volume fractions observed. We also measure the strains in the system as a meaure of the fluctuations, and find that in spite of the long-range ordering, the damping fluid restricts correlations in the fluctuations to about two to three lattice spacings; the correlations are also quite uniform with volume fraction.

We measure the crystalline elastic constants c_{11}, c_{12}, and c_{44}, and find them all to be on the order of magnitude of 10mPa, emphasizing the softness of these crystals. Our results are slightly suggestive that $c_{12} < c_{44}$, rather than equal as expected by the Cauchy relation, but inconclusive. The crystals are certainly strongly anisotropic at all volume fractions, as indicated by the nonzero values of $\Delta \equiv 2c_{44} - (c_{11} - c_{12})$. These results are qualitatively consistent with numerical estimates and with values reported in the literature.

These colloidal Wigner crystals offer the opportunity to study remarkably soft crystals with, for colloids, a relatively novel structure, and to study both the unusually large fluctuations present and the material properties of the system.

Chapter 7

Conclusions and postamble

The overall theme of my work in colloids has been to elucidate the effect of repulsive interactions on the structure and material properties of systems which have historically been understood in their absence. Both of my projects are closely related to more familiar systems, without repulsive interactions, which have been extensively studied: purely attractive colliodal gels are well known, but the introduction of charge interactions gives a binary gel in which attraction and repulsion compete; likewise, hard-sphere crystals are well characterized, but the introduction of charge repulsion allows crystallization at low volume fraction. In both of these cases, the introduction of repulsive interactions causes marked changes in structure.

This thesis is the summary of my work, collecting together what I have learned. In the first two chapters, I introduced the background to my projects – the more general systems we are hoping to model, and the work that has come before me. In the next two chapters, I gave a detailed description of both the experimental systems and procedures, and the process and methods of data analysis; I hope that these chapters may be of use to future students. Chapters 5 and 6 presented the meat of my thesis: the results concerning colloidal gelation of oppositely charged colloidal particles, and colloidal 'Wigner' crystals.

In the case of binary gels, I established an experimental state diagram for gelation of oppositely charged particles, with the three tuning parameters of total volume fraction; interaction strength (controlled via added salt concentration); and asymmetry in mixing ratio between positively and negatively charged particles. I examined the structure within the gels, and in particular the distribution of contact numbers. For shallower quenches – that

is, for gels which on the state diagram lie closer to the gel transition – the gels have a more rarified and tenuous structure, with fewer contacts; in fact, the gel line appears to coincide with the smooth decrease of average attractive bond number below 1. This is in stark contrast to the case of purely attractive colloidal gels, where the contact number increases with approach to the gel line. The difference in structure is driven by the competition between electrostatic attraction and repulsion.

In the case of colloidal crystals, long-range repulsion permits a new body-centered cubic crystalline phase, in contrast to the face-centered cubic phase found in hard-sphere colloidal crystals. These b.c.c. structures have been observed before; what is new is that I directly observed local fluctuations; measured local strains; and calculated the three independent crystalline elastic constants. Comparison of these constants demonstrated the crystal anisotropy at all volume fractions observed. The small elastic constants and large fluctuations are enabled by the repulsive interactions between particles – again, the structure and properties are markedly affected by the introduction of these interactions.

These neat summaries of course smooth over many of the details, and the mysteries still remaining. Many of these are essentially chemical in nature, as described in Chapter 3, and have to do with the true nature of the interactions between particles, and between particles and the environment. Other details are in the analysis, such as potential errors in location or the validity of approximations in the strain calculations. It seems that any science has, if not skeletons in the closet, at least a finger-bone or two.

Yet in spite of these lingering mysteries, I have learned a good deal from my studies. I hope that this work has contributed some new understanding to soft matter science: the collective entity that is 'the community' now knows something which was not known before. Although it is unsurprising that the introduction of repulsive interactions affects the structure and properties of a system, this general statement is now supported by two additional concrete and detailed colloidal examples.

Appendix

Expressions for neighbor distances as a function of strain

For an *unstrained* b.c.c. crystal with lattice cube side l, the first six neighbor shells are at distances:

$a_{1,0} = \sqrt{3}/2\ l$	at $(\pm 1/2, \pm 1/2, \pm 1/2)$	(8 neighbors)
$a_{2,0} = l$	at $(\pm 1, 0, 0)$ and cycles	(6 neighbors)
$a_{3,0} = \sqrt{2}\ l$	at $(\pm 1, \pm 1, 0)$ and cycles	(12 neighbors)
$a_{4,0} = \sqrt{11}/2\ l$	at $(\pm 1 1/2, \pm 1/2, \pm 1/2)$ and cycles	(24 neighbors)
$a_{5,0} = \sqrt{3}\ l$	at $(\pm 1, \pm 1, \pm 1)$	(8 neighbors)
$a_{6,0} = 2\ l$	at $(\pm 2, 0, 0)$ and cycles	(6 neighbors)

For a shear strain e_{xy}, the modified distances are:

$$a_{1,1} = 1/2\ l * \sqrt{2 + (1 + e_{xy})^2} \quad \text{(4 neighbors)}$$
$$a_{1,2} = 1/2\ l * \sqrt{2 + (1 - e_{xy})^2} \quad \text{(4 neighbors)}$$

$$a_{2,1} = l \quad \text{(4 neighbors)}$$
$$a_{2,2} = l * \sqrt{1 + e_{xy}^2} \quad \text{(2 neighbors)}$$

$$a_{3,1} = \sqrt{2}\ l \quad \text{(4 neighbors)}$$
$$a_{3,2} = l * \sqrt{1 + (1 + e_{xy})^2} \quad \text{(2 neighbors)}$$
$$a_{3,3} = l * \sqrt{1 + (1 - e_{xy})^2} \quad \text{(2 neighbors)}$$
$$a_{3,4} = l * \sqrt{2 + e_{xy}^2} \quad \text{(4 neighbors)}$$

$$a_{4,1} = 1/2\ l * \sqrt{10 + (1 + 3e_{xy})^2} \quad \text{(4 neighbors)}$$
$$a_{4,2} = 1/2\ l * \sqrt{10 + (1 - 3e_{xy})^2} \quad \text{(4 neighbors)}$$
$$a_{4,3} = 1/2\ l * \sqrt{10 + (1 + e_{xy})^2} \quad \text{(4 neighbors)}$$
$$a_{4,4} = 1/2\ l * \sqrt{10 + (1 - e_{xy})^2} \quad \text{(4 neighbors)}$$
$$a_{4,5} = 1/2\ l * \sqrt{2 + (3 + e_{xy})^2} \quad \text{(4 neighbors)}$$
$$a_{4,6} = 1/2\ l * \sqrt{2 + (3 - e_{xy})^2} \quad \text{(4 neighbors)}$$

$$a_{5,1} = l * \sqrt{2 + (1 + e_{xy})^2} \quad \text{(4 neighbors)}$$
$$a_{5,2} = l * \sqrt{2 + (1 - e_{xy})^2} \quad \text{(2 neighbors)}$$

$$a_{6,1} = 2\ l \quad \text{(4 neighbors)}$$
$$a_{6,2} = 2\ l * \sqrt{1 + e_{xy}^2} \quad \text{(2 neighbors)}$$

For a tensile strain e_{xx}, the modified distances are:

$$a_{1,1} = 1/2\ l * \sqrt{2 + (1 + e_{xx})^2} \qquad \text{(8 neighbors)}$$

$$a_{2,1} = l \qquad \text{(4 neighbors)}$$

$$a_{2,2} = l * (1 + e_{xx}) \qquad \text{(2 neighbors)}$$

$$a_{3,1} = \sqrt{2}\ l \qquad \text{(4 neighbors)}$$

$$a_{3,2} = l * \sqrt{1 + (1 + e_{xx})^2} \qquad \text{(8 neighbors)}$$

$$a_{4,1} = 1/2\ l * \sqrt{2 + (3 + 3e_{xx})^2} \qquad \text{(8 neighbors)}$$

$$a_{4,2} = 1/2\ l * \sqrt{10 + (1 + e_{xx})^2} \qquad \text{(16 neighbors)}$$

$$a_{5,1} = l * \sqrt{2 + (1 + e_{xx})^2} \qquad \text{(8 neighbors)}$$

$$a_{6,1} = 2\ l \qquad \text{(4 neighbors)}$$

$$a_{6,2} = 2\ l * (1 + e_{xx}) \qquad \text{(2 neighbors)}$$

For an isotropic dilatation δ ($e_{xx} = e_{yy} = e_{zz} = 1/3\,\delta$), all the undeformed distances are simply scaled by the same dilatation factor, so that

$$a_{n,1} = a_{n,0} * (1 + \delta/3)$$

Bibliography

[1] S. Alexander and J. McTague. Should all crystals be bcc? Landau theory of solidification and crystal nucleation. *Phys. Rev. Lett.*, 41(10):702–705, 1978.

[2] P. Bartlett and A. I. Campbell. Three-dimensional binary superlattices of oppositely charged colloids. *Phys. Rev. Lett.*, 95:128302, 2005.

[3] P. M. Biesheuvel and M. A. Cohen Stuart. Cylindrical cell model for the electrostatic free energy of polyelectrolyte complexes. *Langmuir*, 20(11):4764–4770, 2004.

[4] V. A. Bloomfield. DNA condensation. *Curr. Opin. Struct. Biol.*, 6(3):334–341, 1996.

[5] M. Born. Thermodynamics of crystals and melting. *J. Chem. Phys*, 7(8):591, 1939.

[6] J. B. Caballero, A. M. Puertas, A. Fernández-Barbero, and F. J. de las Nieves. Oppositely charged colloidal binary mixtures: a colloidal analog of the restricted primitive model. *J. Chem. Phys*, 121:2428, 2004.

[7] A. I. Campbell, V. J. Anderson, J. S. van Duijneveldt, and P. Bartlett. Dynamical arrest in attractive colloids: the effect of long-range repulsion. *Phys. Rev. Lett.*, 94(20):208301, 2005.

[8] M. Cerbelaud, A. Videcoq, P. Abélard, C. Pagnoux, F. Rossignol, and R. Ferrando. Self-assembly of oppositely charged particles in dilute ceramic suspensions: predictive role of simulations. *Soft Matter*, 6(2):370, 2010.

[9] L. K. Cotter and N. A. Clark. Density fluctuation dynamics in a screened coulomb colloid: comparison of the liquid and bcc crystal phases. *J. Chem. Phys*, 86(12):6616 – 6621, 1987.

[10] R. S. Crandall and R. Williams. Gravitational compression of crystallized suspensions of polystyrene spheres. *Science*, 198(4314):293–295, 1977.

[11] J. C. Crocker and D. G. Grier. Methods of digital video microscopy for colloidal studies. *J. Colloid Interface Sci.*, 179:298–310, 1996.

[12] E. Del Gado. Aggregation of model gels with directional interactions. *J. Phys.: Condens. Matter*, 22(10):104117, 2010.

[13] E. Del Gado and W. Kob. A microscopic model for colloidal gels with directional effective interactions: network induced glassy dynamics. *Soft Matter*, 6(7):1547, 2010.

[14] C. J. Dibble, M. Kogan, and M. J. Solomon. Structure and dynamics of colloidal depletion gels: coincidence of transitions and heterogeneity. *Phys. Rev. E: Stat., Nonlinear, Soft Matter Phys.*, 74:041403, 2006.

[15] A. D. Dinsmore, V. Prasad, I. Y. Wong, and D. A. Weitz. Microscopic structure and elasticity of weakly aggregated colloidal gels. *Phys. Rev. Lett.*, 96(18):185502, 2006.

[16] A. D. Dinsmore and D. A. Weitz. Direct imaging of three-dimensional structure and topology of colloidal gels. *J. Phys.: Condens. Matter*, 14(33):7581–7597, 2002.

[17] A. Eberle, N. Wagner, and R. Castañeda Priego. Dynamical arrest transition in nanoparticle dispersions with short-range interactions. *Phys. Rev. Lett.*, 106(10), 2011.

[18] D. F. Evans and H. Wennerström. *The colloidal domain: where physics, chemistry, biology, and technology meet*. Advances in interfacial engineering series. Wiley-VCH, New York, 2nd edition, 1999.

[19] M. Falk and J. Langer. Dynamics of viscoplastic deformation in amorphous solids. *Phys. Rev. E*, 57(6):7192–7205, 1998.

[20] Y. Gao and M. L. Kilfoil. Accurate detection and complete tracking of large populations of features in three dimensions. *Optics Express*, 17:4685, 2009.

[21] J.-P. Hansen and L. Verlet. Phase transitions of the Lennard-Jones system. *Physical Review*, 184(1):151–161, 1969.

[22] M. F. Hsu, E. R. Dufresne, and D. A. Weitz. Charge stabilization in nonpolar solvents. *Langmuir*, 21(11):4881–4887, 2005.

[23] A. Hurd, N. Clark, R. Mockler, and W. O'Sullivan. Lattice dynamics of colloidal crystals. *Phys. Rev. A*, 26(5):2869–2881, 1982.

[24] A.-P. Hynninen, M. Leunissen, A. van Blaaderen, and M. Dijkstra. CuAu structure in the restricted primitive model and oppositely charged colloids. *Phys. Rev. Lett.*, 96(1), 2006.

[25] M. C. Jarvis. Structure and properties of pectin gels in plant cell walls. *Plant, Cell and Environment*, 7(3):153–164, 1984.

[26] K. E. Jensen. *Structure and defects of hard-sphere colloidal crystals and glasses*. PhD thesis, Harvard University, 2013.

[27] K. E. Jensen, D. A. Weitz, and F. Spaepen. Note: A three-dimensional calibration device for the confocal microscope. *Review of Scientific Instruments*, 84(1):016108, 2013.

[28] T. Kanai, N. Boon, P. J. Lu, E. Sloutskin, A. B. Schofield, F. Smallenburg, R. van Roij, M. Dijkstra, and D. A. Weitz. in preparation.

[29] H. Kitano, S. Iwai, and N. Ise. Direct observation of association processes between polymer latex particles. *J. Am. Chem. Soc.*, 109(6):1867–1868, 1987.

[30] H. Kitano, S. Iwai, N. Ise, and T. Okubo. Kinetic analysis of association processes between oppositely charged polymer latex particles. *J. Am. Chem. Soc.*, 109(22):6641–6644, 1987.

[31] C. Kittel. *Introduction to Solid State Physics*. John Wiley & Sons, Inc., 8th edition, 2005.

[32] T. E. Kodger, R. Guerra, J. Sprakel, and D. A. Weitz. in preparation.

[33] A. H. Krall and D. A. Weitz. Internal dynamics and elasticity of fractal colloidal gels. *Phys. Rev. Lett.*, 80(4):778–781, 1998.

[34] K. Kremer, M. Robbins, and G. Grest. Phase diagram of Yukawa systems: model for charge-stabilized colloids. *Phys. Rev. Lett.*, 57(21):2694–2697, 1986.

[35] M. E. Leunissen, C. G. Christova, A.-P. Hynninen, C. P. Royall, A. I. Campbell, A. Imhof, M. Dijkstra, R. van Roij, and A. van Blaaderen. Ionic colloidal crystals of oppositely charged particles. *Nature*, 437(7056):235–240, 2005.

[36] M. E. Leunissen and A. van Blaaderen. Concentrating colloids with electric field gradients. II. Phase transitions and crystal buckling of long-ranged repulsive charged spheres in an electric bottle. *J. Chem. Phys*, 128(16):164509, 2008.

[37] T. Li, S. Kheifets, D. Medellin, and M. G. Raizen. Measurement of the instantaneous velocity of a Brownian particle. *Science*, 328(5986):1673–1675, 2010.

[38] M. Y. Lin, H. M. Lindsay, D. A. Weitz, R. C. Ball, R. Klein, and P. Meakin. Universality in colloid aggregation. *Nature*, 339(6223):360–362, 1989.

[39] H. M. Lindsay and P. M. Chaikin. Elastic properties of colloidal crystals and glasses. *J. Chem. Phys*, 76(7):3774, 1982.

[40] J. M. López-López, A. Schmitt, A. Moncho-Jordá, and R. Hidalgo-Álvarez. Stability of binary colloids: kinetic and structural aspects of heteroaggregation processes. *Soft Matter*, 2(12):1025, 2006.

[41] P. J. Lu, E. Zaccarelli, F. Ciulla, A. B. Schofield, F. Sciortino, and D. A. Weitz. Gelation of particles with short-range attraction. *Nature*, 453:499–503, 2008.

[42] S. Manley, H. M. Wyss, K. Miyazaki, J. C. Conrad, V. Trappe, L. J. Kaufman, D. R. Reichman, and D. A. Weitz. Glasslike arrest in spinodal decomposition as a route to colloidal gelation. *Phys. Rev. Lett.*, 95(23):238302, 2005.

[43] R. Mezzenga, P. Schurtenberger, A. Burbidge, and M. Michel. Understanding foods as soft materials. *Nat. Mater.*, 4(10):729–740, 2005.

[44] A. Mohraz, E. R. Weeks, and J. A. Lewis. Structure and dynamics of biphasic colloidal mixtures. *Phys. Rev. E: Stat., Nonlinear, Soft Matter Phys.*, 77(6):060403(R), 2008.

[45] M. Nikolaides. Colloids at liquid-liquid interfaces. Diploma thesis, Technische Universität München, 2001.

[46] J. T. G. Overbeek and M. J. Voorn. Phase separation in polyelectrolyte solutions. Theory of complex coacervation. *Journal of Cellular and Comparative Physiology*, 49(S1):7–26, 1957.

[47] T. Palberg. Crystallization kinetics of repulsive colloidal spheres. *J. Phys.: Condens. Matter*, 11(28):R323–R360, 1999.

[48] M. A. Piechowiak, A. Videcoq, F. Rossignol, C. Pagnoux, C. Carrion, M. Cerbelaud, and R. Ferrando. Oppositely charged model ceramic colloids: numerical predictions and experimental observations by confocal laser scanning microscopy. *Langmuir*, 26:12540–12547, 2010.

[49] W. C. K. Poon, A. D. Pirie, and P. N. Pusey. Gelation in colloid-polymer mixtures. *Faraday Discuss.*, 101:65, 1995.

[50] J. Prins and H. Petersen. Theoretical diffraction patterns corresponding to some simple types of molecular arrangement in liquids. *Physica*, 3(1-4):147–153, 1936.

[51] P. N. Pusey, A. D. Pirie, and W. C. K. Poon. Dynamics of colloid-polymer mixtures. *Phys. A*, 201(1-3):322–331, 1993.

[52] P. N. Pusey and W. van Megen. Phase behaviour of concentrated suspensions of nearly hard colloidal spheres. *Nature*, 320:340–342, 1986.

[53] X. Qiu, D. Rau, V. Parsegian, L. Fang, C. Knobler, and W. Gelbart. Salt-dependent DNA-DNA spacings in intact bacteriophage λ reflect relative importance of DNA self-repulsion and bending energies. *Phys. Rev. Lett.*, 106(2), 2011.

[54] M. O. Robbins, K. Kremer, and G. S. Grest. Phase diagram and dynamics of Yukawa systems. *J. Chem. Phys*, 88(5):3286, 1988.

[55] M. Robles, M. López de Haro, and A. Santos. Note: Equation of state and the freezing point in the hard-sphere model. *J. Chem. Phys*, 140(13):136101, 2014.

[56] S. Roldán-Vargas, F. Smallenburg, W. Kob, and F. Sciortino. Gelling by heating. *Scientific Reports*, 3, 2013.

[57] S. Roldán-Vargas, F. Smallenburg, W. Kob, and F. Sciortino. Phase diagram of a reentrant gel of patchy particles, 2013. arXiv:1310.3730 [cond-mat.soft].

[58] M. S. Romero-Cano, J. B. Caballero, and A. M. Puertas. Experimental phase diagram of symmetric binary colloidal mixtures with opposite charges. *J. Phys. Chem. B*, 110:13220–13226, 2006.

[59] C. P. Royall, M. E. Leunissen, and A. v. Blaaderen. A new colloidal model system to study long-range interactions quantitatively in real space. *J. Phys.: Condens. Matter*, 15(48):S3581–S3596, 2003.

[60] E. R. Russell, J. Sprakel, T. E. Kodger, and D. A. Weitz. Colloidal gelation of oppositely charged particles. *Soft Matter*, 8:8697–8703, 2012.

[61] L. E. Sánchez-Díaz, A. Vizcarra-Rendón, and R. Juárez-Maldonado. Ionic and Wigner Glasses, superionic conductors, and spinodal electrostatic gels: dynamically arrested phases of the primitive model. *Phys. Rev. Lett.*, 103:035701, 2009.

[62] E. Sanz, M. E. Leunissen, A. Fortini, A. van Blaaderen, and M. Dijkstra. Gel formation in suspensions of oppositely charged colloids: mechanism and relation to the equilibrium phase diagram. *J. Phys. Chem. B*, 112(35):10861–10872, 2008.

[63] E. Sanz, C. Valeriani, T. Vissers, A. Fortini, M. E. Leunissen, A. van Blaaderen, D. Frenkel, and M. Dijkstra. Out-of-equilibrium processes in suspensions of oppositely charged colloids: liquid-to-crystal nucleation and gel formation. *J. Phys.: Condens. Matter*, 20(49):494247, 2008.

[64] P. Schall, D. A. Weitz, and F. Spaepen. Structural rearrangements that govern flow in colloidal glasses. *Science*, 318(5858):1895–1899, 2007.

[65] H. Sedgwick, S. U. Egelhaaf, and W. C. K. Poon. Clusters and gels in systems of sticky particles. *J. Phys.: Condens. Matter*, 16(42):S4913–S4922, 2004.

[66] P. N. Segrè, V. Prasad, A. B. Schofield, and D. A. Weitz. Glasslike kinetic arrest at the colloidal-gelation transition. *Phys. Rev. Lett.*, 86:6042–6045, 2001.

[67] E. Sirota, H. Ou-Yang, S. Sinha, P. Chaikin, J. Axe, and Y. Fujii. Complete phase diagram of a charged colloidal system: a synchrotron x-ray scattering study. *Phys. Rev. Lett.*, 62(13):1524–1527, 1989.

[68] J. Sprakel, P. J. Lu, T. E. Angelini, F. Spaepen, P. Schall, and D. A. Weitz. in preparation.

[69] E. Spruijt, H. E. Bakker, T. E. Kodger, J. Sprakel, M. A. Cohen Stuart, and J. van der Gucht. Reversible assembly of oppositely charged hairy colloids in water. *Soft Matter*, 7(18):8281, 2011.

[70] E. Spruijt, M. A. Cohen Stuart, and J. van der Gucht. Dynamic force spectroscopy of oppositely charged polyelectrolyte brushes. *Macromolecules*, 43(3):1543–1550, 2010.

[71] E. Spruijt, J. Sprakel, M. A. Cohen Stuart, and J. van der Gucht. Interfacial tension between a complex coacervate phase and its coexisting aqueous phase. *Soft Matter*, 6:172–178, 2010.

[72] E. Spruijt, J. Sprakel, M. Lemmers, M. Stuart, and J. van der Gucht. Relaxation dynamics at different time scales in electrostatic complexes: time-salt superposition. *Phys. Rev. Lett.*, 105(20), 2010.

[73] E. Spruijt, A. H. Westphal, J. W. Borst, M. A. Cohen Stuart, and J. van der Gucht. Binodal compositions of polyelectrolyte complexes. *Macromolecules*, 43(15):6476–6484, 2010.

[74] V. Trappe, V. Prasad, L. Cipelletti, P. N. Segre, and D. A. Weitz. Jamming phase diagram for attractive particles. *Nature*, 411(6839):772–775, 2001.

[75] V. Trappe and P. Sandkühler. Colloidal gels – low-density disordered solid-like states. *Curr. Opin. Colloid Interface Sci.*, 8(6):494–500, 2004.

[76] V. Trappe and D. A. Weitz. Scaling of the viscoelasticity of weakly attractive particles. *Phys. Rev. Lett.*, 85(2):449–452, 2000.

[77] J. van der Gucht, E. Spruijt, M. Lemmers, and M. A. Cohen Stuart. Polyelectrolyte complexes: bulk phases and colloidal systems. *J. Colloid Interface Sci.*, 361(2):407–422, 2011.

[78] M. M. van Schooneveld, V. W. A. de Villeneuve, R. P. A. Dullens, D. G. A. L. Aarts, M. E. Leunissen, and W. K. Kegel. Structure, stability, and formation pathways of colloidal gels in systems with short-range attraction and long-range repulsion. *J. Phys. Chem. B*, 113(14):4560–4564, 2009.

[79] Z. Wang, F. Wang, Y. Peng, Z. Zheng, and Y. Han. Imaging the homogeneous nucleation during the melting of superheated colloidal crystals. *Science*, 338(6103):87–90, 2012.

[80] J. Weiner. *Statistical Mechanics of Elasticity*. Courier Dover Publications, 2002.

[81] D. Weitz, J. Huang, M. Lin, and J. Sung. Dynamics of diffusion-limited kinetic aggregation. *Phys. Rev. Lett.*, 53(17):1657–1660, 1984.

[82] D. Weitz, J. Huang, M. Lin, and J. Sung. Limits of the fractal dimension for irreversible kinetic aggregation of gold colloids. *Phys. Rev. Lett.*, 54(13):1416–1419, 1985.

[83] D. A. Weitz and M. Oliveria. Fractal structures formed by kinetic aggregation of aqueous gold colloids. *Phys. Rev. Lett.*, 52(16):1433–1436, 1984.

[84] Wikipedia. Turns out to be a useful resource for well-established equations and numbers.

[85] R. Williams and R. Crandall. The structure of crystallized suspensions of polystyrene spheres. *Physics Letters A*, 48(3):225–226, 1974.

[86] R. Williams, R. Crandall, and P. Wojtowicz. Melting of crystalline suspensions of polystyrene spheres. *Phys. Rev. Lett.*, 37(6):348–351, 1976.

[87] A. Yethiraj and A. van Blaaderen. A colloidal model system with an interaction tunable from hard sphere to soft and dipolar. *Nature*, 421(6922):513–517, 2003.

[88] E. Zaccarelli. Colloidal gels: equilibrium and non-equilibrium routes. *J. Phys.: Condens. Matter*, 19(32):323101, 2007.